

Electromagnetic Techniques for Analysis and Design of Ultra Sensitive Receivers for Far-Infrared Astronomy

Presented by

Colm Bracken, B.Sc.

A thesis submitted in partial fulfilment of the requirements for the degree of

Doctor of Philosophy



Department of Experimental Physics
National University of Ireland, Maynooth
Maynooth, Co. Kildare, Ireland

January 2015

Head of Department

Prof. J. Anthony Murphy, M.Sc., M.S., Ph.D.

Research Supervisor

Prof. J. Anthony Murphy, M.Sc., M.S., Ph.D.

Contents

Introduction	8
1 Far-IR Astronomy and Instrumentation	11
1.1 Science Case for Far Infra-Red Astronomy	12
1.1.1 Star and Planetary System Formation	14
1.1.2 Birth and Evolution of Galaxies and AGN	18
1.2 SPICA Space Observatory	21
1.2.1 SPICA Satellite	21
1.2.2 The SAFARI Instrument	25
1.3 Far-Infrared Imaging Fourier Transform Spectroscopy	29
1.4 VNA Measurement Techniques	31
1.5 Direct Detection Techniques	33
1.6 Transition Edge Sensors	36
1.7 Conclusions	38
2 Computational Methods for Electromagnetic and Quasioptical Design and Analysis	39
2.1 Overview of Computational Methods	40
2.2 Gaussian Beam Mode Analysis	41
2.2.1 Background	41
2.2.2 Gaussian Beam Mode Analysis of Uniformly Illuminated Apertures	44

2.2.3	Gaussian Beam Mode Analysis of EM Horns and Waveguides	49
2.2.4	Propagation Through Quasioptical Systems: Mirrors and Lenses	56
2.3	Waveguides	58
2.3.1	Background	58
2.3.2	Rectangular Waveguide	59
2.3.3	Cylindrical Waveguide	61
2.4	Electromagnetic Mode Matching	63
2.4.1	Background	63
2.5	Finite Element Method: COMSOL Multiphysics	65
2.5.1	Background	65
2.6	Conclusions	69
3	The Analysis of the SAFARI Multimode Horns	71
3.1	Rectangular Horns	72
3.1.1	Background	72
3.1.2	Approximate Method	74
3.1.3	Example Horn (Approximate Method)	76
3.1.4	Example Horn (Mode Matching Approach)	78
3.1.5	Example Horn (FEM Approach)	80
3.1.6	Inclusion of a Conducting Ground Plane	84
3.1.7	Comparing Horn to Waveguide	85
3.1.8	Directional Gain of Example Horn	86
3.1.9	External Back Scatter	89
3.1.10	Experimental Verification	89
3.2	SAFARI Horns	91
3.2.1	Far-field Radiation Patterns of SAFARI Horns	91
3.2.2	Optical Cross-talk in SAFARI Horn Array	97

3.2.3	Experimental Verification	105
3.3	Characterising Throughput of SAFARI-Like Multi-Moded Feed Horns	107
3.3.1	Background	107
3.3.2	Experimental Set-Up	112
3.3.3	Manual Optimisation of Set-Up	115
3.3.4	Alignment of the System Inside the Vacuum Tubes	118
3.3.5	Efficiency of FTS Beam Splitters	120
3.3.6	Experimental	122
3.3.7	Discussion of Results	129
3.4	Conclusions	131
4	Conical Mode Matching for Shaped Smooth-Walled CMB Horns	133
4.1	Smooth Walled Conical Horns	134
4.1.1	Background	134
4.1.2	Derivation of Spherical Harmonic Fields	136
4.1.3	Calculation of Eigenvalues	142
4.1.4	Evanescence of Modes	148
4.1.5	Cartesian Field Components	150
4.1.6	Example Horn for Comparison	151
4.1.7	Limitations of Approximate Method	152
4.2	Scattering at Conical Horn Junctions (Spherical SCATTER)	156
4.2.1	Derivation of S Parameters	157
4.2.2	Coupling Between Two Conic Sections	162
4.2.3	Coupling Between Multiple Conic Sections	168
4.3	Spherical SCATTER Program	171
4.3.1	Description of Spherical SCATTER Code	171
4.3.2	Test Horn	174

4.3.3	Experimental Verification	178
4.4	Conclusions	178
5	The Electromagnetic Design and Analysis of Cavity Coupled Absorbers for SAFARI	180
5.1	Background	181
5.2	Modelling Approaches	183
5.2.1	Mode Matching Approach	183
5.2.2	3D FEM Approach	188
5.2.3	2D FEM Approach	192
5.2.4	Comparison of Results	193
5.3	Optimisation of Absorber Position and Cavity Geometry	202
5.3.1	Optimising Absorber Position for TE_{11} Mode	202
5.3.2	Optimisation of Absorber Position for an Over-Moded System	203
5.3.3	Cavity and Absorber Size	205
5.3.4	Cavity Shape	208
5.4	SAFARI L-Band Receivers	212
5.4.1	Vacuum Gap between Neighbouring Pixel Cavities	213
5.4.2	COMSOL Model of SAFARI L-Band Detectors	224
5.4.3	Improving the SAFARI L-Band Design	228
5.5	SAFARI S-Band Receivers	234
5.5.1	Single Mode Analysis	237
5.5.2	Analysis of Higher Order Modes	238
5.5.3	Experimental Verification	240
5.6	Conclusions	249
6	Summary and Conclusions	251

Abstract

This thesis focuses on EM (electromagnetic) modelling methods for simulating the behaviour of receivers and detectors for far-IR (far-infrared) astronomy and CMB (cosmic microwave background) applications, toward an optimum design for SAFARI (the Spica Far-Infrared Instrument) on the proposed space based telescope SPICA (Space Infrared Telescope for Cosmology and Astrophysics). The computational methods required for modelling SAFARI-like receivers are described, and sophisticated conical waveguide mode matching theory is derived. Generic far-IR systems are investigated, including analysis of SAFARI-like multi-mode feed horns, and the absorber coupled superconducting TES (transition edge sensor) bolometers that are typically used in far-IR receivers. Special attention is given to the integrating cavity backshorts that serve to increase pixel efficiency, and new designs for improved cavity geometries, which provide high coupling between the detector and the incoming signal while reducing cavity losses and crosstalk, are presented. Where more than one simulation approach is employed for a particular problem, the agreement between the results served to mutually validate the approaches. Where necessary, experimental measurements were carried out for verification of the simulations, and the corresponding results are presented. The results of a measurement campaign carried out at SRON (Netherlands Institute for Space Research) during an extended visit during the summer of 2013 are presented, where a SAFARI-like horn antenna was characterised in terms of its frequency dependent throughput at THz (terahertz) frequencies. A series of cavity mounted absorber measurements are also described, where the detector components are appropriately scaled up in size to suit the frequency range of the in-house VNA (vector network analyser) system at NUIM (National University of Ireland, Maynooth). The main drivers for the work presented in this thesis were two Technology Research Programmes, both commissioned by ESA (European Space Agency).

List of acronyms used throughout the text:

Far-IR (far-infrared), CMB (cosmic microwave background), TES (transition edge sensor), Ta (tantalum), THz (terahertz: 10^{12}Hz), NEP (noise equivalent power), EM (electromagnetic), VNA (vector network analyser), SRON (Netherlands Insti-

tute for Space Research), RAL (Rutherford Appleton Laboratory), NUIM (National University of Ireland, Maynooth), SPICA (Space Infrared Telescope for Cosmology and Astrophysics), SAFARI (Spica Far-Infrared Instrument), FEM (finite element method), FIT (finite integration technique), GBM (Gaussian beam mode), ESA (European Space Agency), JAXA (Japan Aerospace Exploration Agency), ISAS (Institute of Space and Astronautical Science), TE (transverse electric), TM (transverse magnetic), AGN (active galactic nuclei), FTS (Fourier transform spectrometer), FOV (field of view), SFR (star formation rate).

Acknowledgements

The work presented in this thesis would not have been possible without the support of many people. I would like to thank my research supervisor Prof. Anthony Murphy, for all his support and assistance, who went above and beyond what is expected of a supervisor in terms of his time and effort in helping me in this pursuit.

I would also like to thank Dr. Neil Trappe, who always made time to help me with research issues, and with my teaching. Many thanks to Dr. Cr  idhe O’Sullivan and Dr. Marcin Gradziel, for their time and effort in organising our team meetings for the THz Optics Group, and for providing help any time it was needed. I give a special thank you to Ms. Gr  inne Roche, the department secretary, for all her help and good advice over the years. I also thank Mr John Kelly and Mr Derek Gleeson for all of their support with technical issues. I also appreciate the help provided to me by the other postgraduate students, in particular Niall Tynan, Darragh McCarthy, and Niamh Tobin, for their help with measurement procedures. Thank you also, to Dr Valerie Heffernan of the German department at N.U.I. Maynooth for sharing her car with me each day, and all of her great advice.

Many thanks to Dr. Gert de Lange and Dr. Damien Audley at SRON, Groningen, for hosting me during my work placement there, and helping me and my family settle into our new surroundings in the Netherlands. And thank you to Mr Willem-Jan Vreeling for his help with measurements at SRON, and for entertaining my kids during their visit to the lab.

For the financial supports provided to me throughout my studies, I thank the John and Pat Hume Scholarship fund, the Department of Experimental Physics at N.U.I. Maynooth, and ESA.

Finally, to Ciara, Hollie, and Kayla, thank you so much for your love and patience through this intensive period. Ciara, your support always made it possible for me to balance my time between work and being a dad; you have been my foundation. I am so excited about having my weekends free now to have fun with you and the girls. Thank you too, to my Mother, Susan, and my mother-in-law, Pat, for all of your love and support. And thank you to my father-in-law, Sean; you have been like a Father to me, and your guidance is what helped me to see the importance of physics, and the true beauty of Nature.

Introduction

“Imagination is more important than knowledge. For knowledge is limited to all we now know and understand, while imagination embraces the entire world, and all there ever will be to know and understand.”

- Albert Einstein

The ability to be able to predict accurately the full optical and EM performance of typical receiver systems has involved a significant research effort over the last two decades. Many previously released theses from the THz Optics Group of the Experimental Physics Department of NUIM focussed on modelling the optics that comprise the free-space path described above. Much has also been carried out on the beam patterns of corrugated feed horns, leading to the development of the highly efficient SCATTER mode matching program [Murphy *et al.*, 2010]. However, what is now required for a more complete understanding of such systems is a thorough analysis of the horn/cavity/absorber structures using EM simulation techniques. The main reason for the lack of progress in this area to date is that, without resorting to super computers, the computational power for modelling these electrically large structures was simply not available in the past. Only now is it possible to carry out a complete vector EM analysis of the integrated receiver and detector structures with a moderately powerful PC. And by employing optimisation techniques, and combining results from EM mode matching, FEM (finite element method) and FIT (finite integration technique) we can design systems with the highest coupling to the incoming signal possible, limited only by manufacturing constraints.

Due to the extremely small dimensions of the feed horns and cavities required for detection of signals in the THz frequency range, manufacturing tolerances are the main limiting factor in the design and construction of these types of detector systems. It is worth noting that, in as early as 1999, corrugated feeds had been built by RAL (Rutherford Appleton Laboratory) in the U.K. for operation at frequencies up to 2.5 THz [Wilsher *et al.*, 1999]. However, producing large numbers of such horns in array format would undoubtedly prove extremely difficult and expensive. For this reason particular attention was given to smooth walled structures in this thesis. Chapter 3 focusses on the analysis of smooth walled rectangular feed horns for the SAFARI instrument, where the far-field beam patterns are calculated using an efficient mode matching simulation method, and horn-to-horn crosstalk effects are predicted using finite element analysis.

It has been shown that, with very careful optimisation of the geometry of smooth walled feeds, similar performance to corrugated feeds can be achieved over reasonable bandwidths [McCarthy *et al.*, 2013], [Tan *et al.*, 2012]. In fact a relatively simple profile consisting of just a few straight smooth walled conic sections

can be enough to achieve the required levels of beam symmetry, low-level side lobes and low cross-polar levels, although with some restrictions of the horn profile dimensions. A complete chapter of this thesis was devoted to creating a new conical mode matching code, with the aim of producing a more exact model of smooth-walled conical feed horns. It was also hoped that the code would be more efficient than the alternative cylindrical mode matching approach. The work is also interesting from an academic point of view as there is little literature available on the subject of conical modes and conical mode matching. This work is described in detail in chapter 4.

Another main focus of the thesis is the investigation and development of new and efficient methods for modelling the interaction between the cavity and absorber of the bolometers. More efficient techniques were required for the modelling of this component, in particular due to the electrically large size of the cavity which is typically at least a few wavelengths in diameter as one moves into the THz regime. Waveguide mode matching techniques proved very efficient, and the results were checked against FEM and FIT results for verification of the approach. However the waveguide mode matching code was also limited since many real systems employ a vacuum gap between the horn array block and the detector array (see Figure 5.1 in chapter 5), which cannot be accurately modelled with waveguide modes. For this reason a discussion on the possibility of extending the NUIM in-house mode matching code “SCATTER” to account for this vacuum gap is presented in chapter 5.

Although the systems that are investigated in this thesis are for generic instruments for far infrared astronomy and CMB detection, it is mostly toward SAFARI instrument that the research is primarily aimed. The SAFARI instrument will be part of the SPICA spacecraft that is due to be launched by ESA and JAXA (Japan Aerospace Exploration Agency) in 2022/2024. The primary mission objectives of SPICA are to understand the origin and evolution of galaxies, stars and planets and for this reason some background information is given on each of these topics in sections 1.1.1 and 1.1.2. An overview of the SPICA mission as well as the SAFARI instrument are given in sections 1.2 and 1.2.2 respectively.

Chapter 1

Far-IR Astronomy and Instrumentation

“We are just an advanced breed of monkeys on a minor planet of a very average star. But we can understand the Universe. That makes us something very special.”

- Stephen Hawking

1.1 Science Case for Far Infra-Red Astronomy

It has now been accepted that in order to have a more complete understanding of our Universe and the workings within it a full panchromatic (multi-waveband) astronomical view is going to be required. Many different physical processes relating to star formation, galaxy evolution, chemical abundance variations etc. can be observed in vastly different wavelength ranges and therefore detecting radiation at all these wavelengths and performing science with the corresponding data will be essential for building a complete picture of nature on both the small and extremely large astronomical and cosmological scales. As is illustrated in Figure 1.1, a significant portion of all the photons in the universe fall within the far-IR band, thus this waveband of the EM spectrum will undoubtedly reveal many secrets of how the universe works.

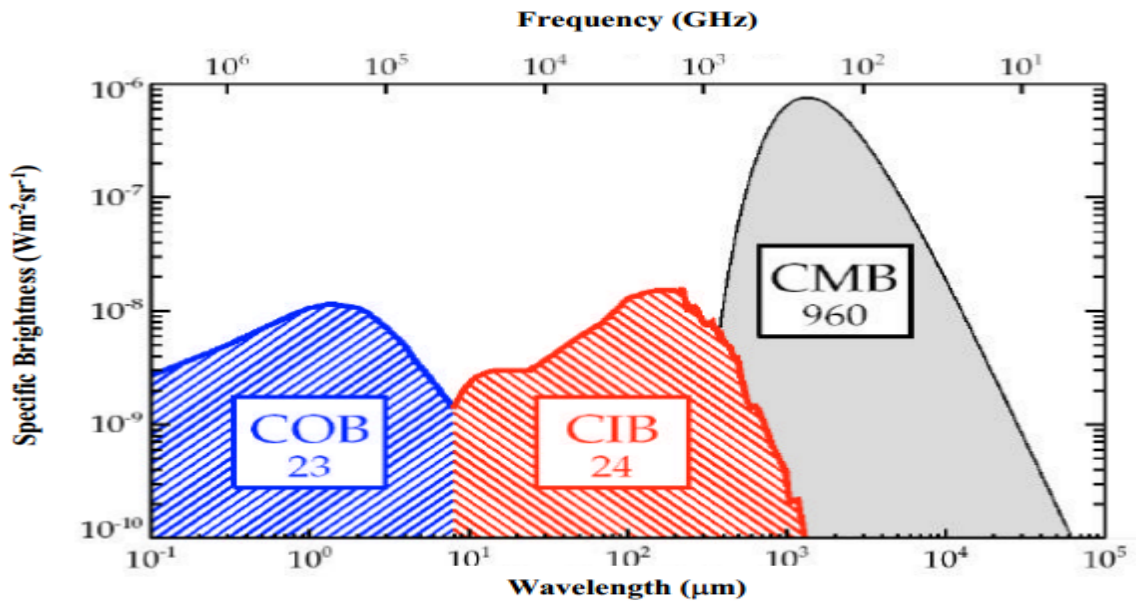


Figure 1.1: Schematic spectral energy distributions of the extragalactic background. The blue area is the cosmic optical background, the red area is the cosmic infrared background, and the grey area is the cosmic microwave background. The units of the specific brightness are Watts per metre squared per steradians [Dole *et al.*, 2006].

In October 2005 ESA announced its plans for the decade spanning 2015 to 2025 in what it called ESA’s Cosmic Vision program. This “vision” posed four questions that were to be the drivers for the objectives of future space science missions over the time period of 2015 to 2025. These questions are as follows:

- 1) What are the conditions for planet formation and the emergence of life?
- 2) How does the Solar System work?

- 3) How did the Universe originate and what is it made of?
- 4) What are the fundamental physical laws of the Universe?

The first three questions set out by ESA can be addressed with observations in the mid-IR and far-IR. As such, a next generation space based mid-to-far infrared observatory will be key in helping to fulfil this ambitious Cosmic Vision. SPICA would address the first question with its state of the art Mid-IR coronagraph [Enya *et al.*, 2008] that would provide the first direct imaging and spectroscopy of young massive planets. SPICA’s far-IR spectrometer SAFARI, which will be more than ten more sensitive times than any previous far-IR spectrometer, will be able to probe deeper into a wider range of star forming regions. SPICA will thus reveal previously hidden protostars and protoplanetary discs and allow astronomers to determine what types of stars, and which regions of the Galaxy, are the most favourable for planetary system formation.

SPICA can address the second question (how our Solar System works) by studying asteroids and comets in our Solar System. The chemical make-up of these primitive remains of the Solar nebula can provide information on the chemical mixture and initial conditions of the early nebula from which the planets formed. SPICA’s unprecedented high sensitivity spectroscopy will reveal the chemistry of these objects and will allow astronomers to compare these spectra to those of protoplanetary discs around nearby stars. By studying the formation of neighbouring stellar systems we can constrain various models of how our own Solar system formed.

The third question set out in ESA’s Cosmic Vision will also be best answered by SPICA. Understanding how the Universe originated and what is it made of will be unveiled through further resolving the far-IR background into discrete sources beyond the level achieved with Herschel [Oliver *et al.*, 2010], and by revealing the star-formation activity hidden at optical wavelengths by dust clouds. The combination of mid-IR and far-IR spectroscopy on SPICA will be essential to “Trace the formation and evolution of the super-massive black holes at galactic centres – in relation to galaxy and star formation – and trace the life cycles of chemical elements through cosmic history” [Ferlet *et al.*, 2010].

The following subsections will outline the strong science case for far-IR observations and science with a SAFARI-like instrument. The science case will be explained in terms of specific astronomical processes such as star and planetary system for-

mation, and birth and evolution of galaxies and AGN (active galactic nuclei).

1.1.1 Star and Planetary System Formation

Star formation is the process by which large clouds of gas (usually molecular clouds) collapse under gravity and coalesce, increasing in density and temperature. It is thought that the initial collapse of the previously stable gas clouds is due to two possible mechanisms. It is possible for two molecular clouds to collide with each other and this collision would cause instability leading to collapse. Another possible mechanism involves the pressure wave of a nearby supernova event causing the instability. One way or another, once the instability is generated and there is sufficient mass according to the Jeans criterion [Jeans, 1928] there is a runaway effect. As the material is compressed at the centre of collapse the density and temperature continue to rise. Eventually the density and pressure become sufficiently large that fusion of hydrogen to helium can take place. The object present just as nuclear fusion begins, and the time leading up to this, is called a protostar. A diagram depicting how the star formation process is somewhat cyclic is shown in Figure 1.2.

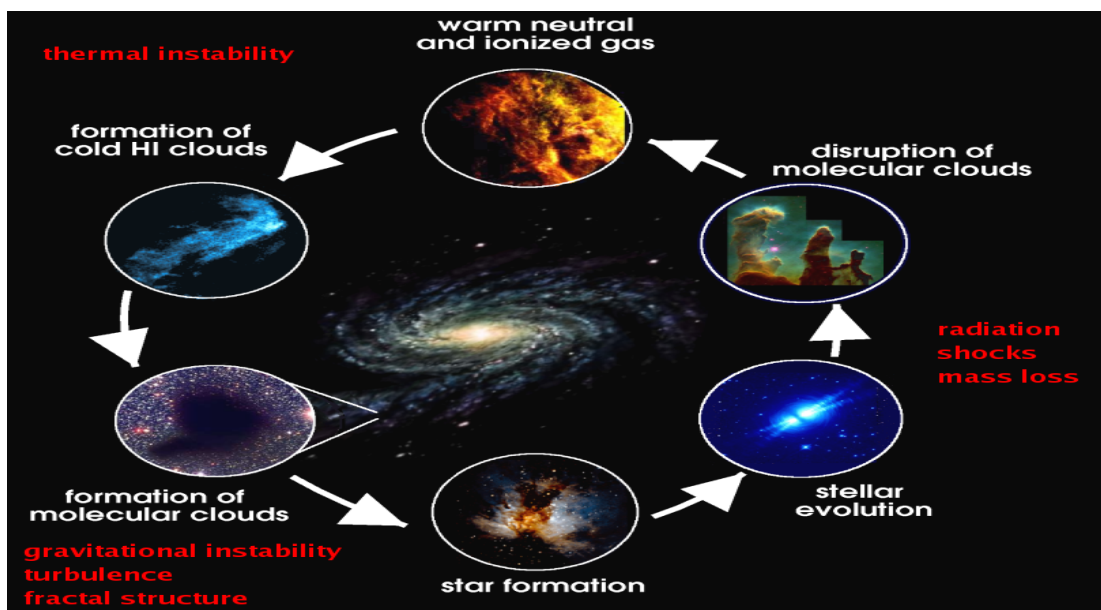


Figure 1.2: The life cycle of stars and nebulae [Kulesa, 2011].

Observing newly formed protostars and the clouds they are embedded in is crucial for understanding both how our own Solar system was formed, and the general

processes involved with star and planet formation. Although some disk shaped objects had been observed with the Very Large Array (VLA) radio telescope and some optical telescopes, the first confirmed images of protoplanetary disks that showed structure were recorded with the Hubble Space Telescope (HST) in 1992, described in a paper released on June 20th 1993 [O’Dell *et al.*, 1992]. Further ground-breaking work was done in 2003 when it was shown that dust grains within these protoplanetary disks were significantly larger than what would be expected in the interstellar medium, implying that grain growth had occurred [McCabe *et al.*, 1992]. This was achieved by analysing scattered light from the protoplanetary disk around the star HK Tau B using the 10 metre W. M. Keck telescope in Mauna Kea, Hawaii.

The far-IR and submm bands of the EM spectrum can reveal these protostars and protoplanetary disks due to the relatively long wavelength of radiation compared to the size of typical dust grains. Also the circumstellar dust and gas, that makes up the disks, emit strongly at these wavelengths. The ALMA facility will be able to image these protostellar environments in the mm and submm continuum and line emissions with unmatched angular resolution (sub-arc second) [Zapata *et al.*, 2013]. This is possible due to ALMA’s large array of 12 metre antennas that can be formatted with baselines up to 16 km. However, the far-IR, which is out of reach for ALMA due to atmospheric attenuation of signal as already indicated, can inform on younger disks that are richer in gas and less-rich in dust. This is due to transitions in H₂, H₂O and hydrides that correspond to emissions in the far-IR, and thus in order to study the youngest protostellar disks a space based far-IR observatory will be essential.

Although ALMA has the highest angular resolution of any submm facility it is not designed to map distributions of gas and dust in giant molecular clouds (GMCs) on large scales. SPICA-SAFARI would be capable of mapping these large faint regions from both the dust continuum and transition lines in the gas. The 2’×2’ large FOV (field of view) of SAFARI would allow astronomers to trace the molecular outflows in GMCs on parsec-scales as they impact the so-called “inter-clump medium” [Ferlet *et al.*, 2010]. Ground based mm and sub-mm observatories such as JCMT can map low energy emissions from molecules such as CO, CN, and C₂H, and the dust continuum emission over large spatial scales in GMCs at sub-mm wavelengths [Plume *et al.*, 2007]. However, the brightest gas cooling lines [Si

II], [OI], and [C II], at 34, 63, and $158\mu\text{m}$, respectively, are beyond the minimum wavelength range of ground based instruments such as JCMT-SCUBA 2.

Our understanding of the chemical conditions and the physical processes involved in the evolution of protostellar disks is relatively limited, in particular the transition for a stage I protostar, embedded in a substantial envelope, to a stage II configuration, with only a star and protoplanetary disk. The PACS instrument aboard the Herschel Space Observatory has recently been used to make a leap in progress by investigating the physical and chemical structure of the planet-forming regions of such disks, unveiling the major carbon and oxygen chemical species (CO, C+, H₂O, OH, O) and the mineralogy of the dust grains in these regions [Van Kempen *et al.*, 2010]. Figure 1.3 shows a spectrum that was obtained of the protostar DK Chamaeleontis with Herschel/PACS.

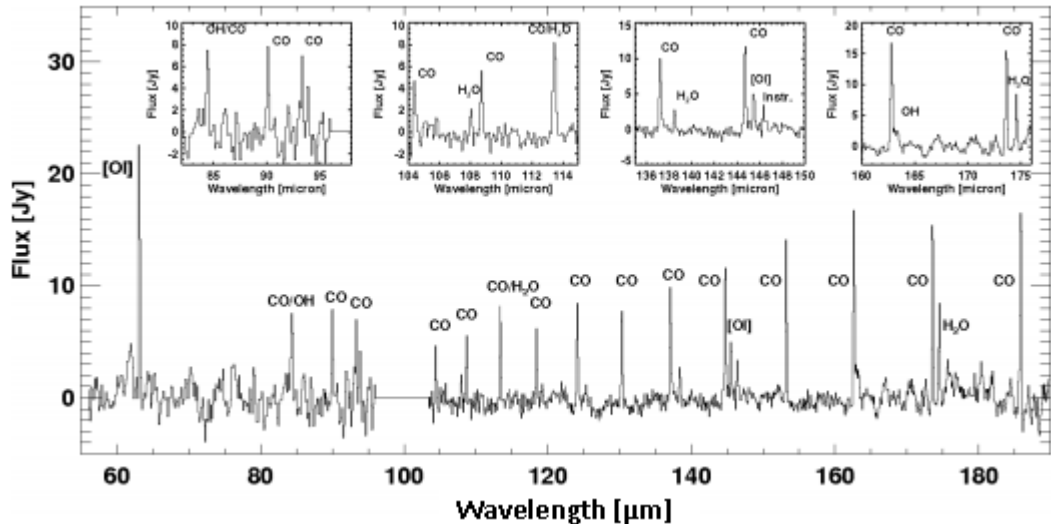


Figure 1.3: The spectrum from $55\text{--}190\mu\text{m}$ of the gas line emission spectrum of protostar DK Chamaeleontis. The inserts show expanded views of parts of the spectrum [Van Kempen *et al.*, 2010].

Although this type of spectral analysis is a significant step in our understanding of protoplanetary disks, the PACS instrument on Herschel has only been able to survey about twenty of the brightest, relatively close disks around intermediate mass stars, and due to the limited sensitivity of Herschel performing surveys of large numbers of protoplanetary disks was not possible. Furthermore disks around Sun-like stars proved to be insufficiently bright for PACS to measure. With the huge increase in sensitivity that would be provided by SPICA/SAFARI large surveys of hundreds of protoplanetary disks around T-Tauri stars could be performed. The chemistries of T-Tauri stars have been shown to be much richer than the Herbig

Ae/Be disks, with higher abundances of Polycyclic Aromatic Hydrocarbon (PAH) for example [Geers *et al.*, 2006]. Thus far-IR spectral surveys of protoplanetary disks around Sun-like stars would undoubtedly reveal many surprises in terms of the chemistry of these planet forming regions.

The importance and spectral richness of the mid to far-IR region is illustrated in Figure 1.4 where the detailed spectrum from the Infrared Space Observatory (ISO) is shown [Rosenthal *et al.*, 2007]. A simulated spectrum of a typical Milky Way-like galaxy undergoing modest SFR is then shown in Figure 1.5 where the region of the spectrum that would be covered by SPICA/SAFARI is shown together with the spectral coverage of similar facilities.

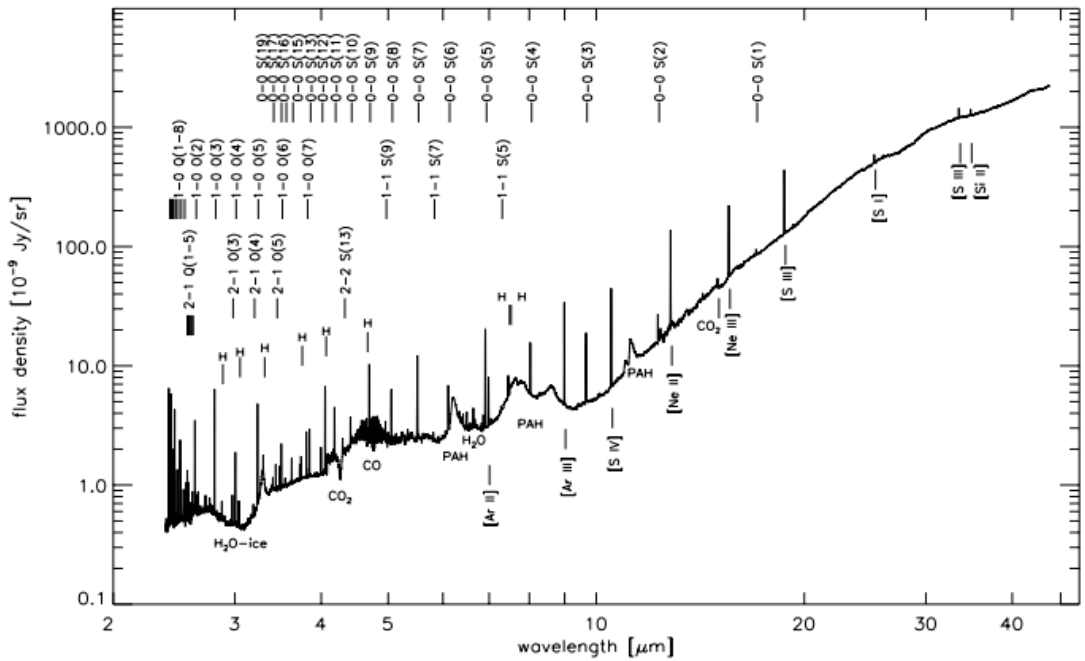


Figure 1.4: Measured spectrum from the Infrared Space Observatory (ISO) [Rosenthal *et al.*, 2007].

As can be seen in Figure 1.5 the majority of emitted radiation falls within either in the optical or in the mid to far-IR. The multitude of atomic, ionic, molecular, and fine-structure lines corresponding to carbon and oxygen, and ionic lines of neon and sulphur together with with rotational transitions of molecules such as molecular hydrogen, water, carbon monoxide, and hydroxyl demonstrate the importance of the mid and far-IR ranges for astronomy. These powerful diagnostic features can be used to study both star and planetary formation very locally, and star formation and the influence of AGN in the very distant Universe [Ferlet *et al.*, 2010]. SAFARI will be capable of measuring radiation from the proto-planetary disks of new stars

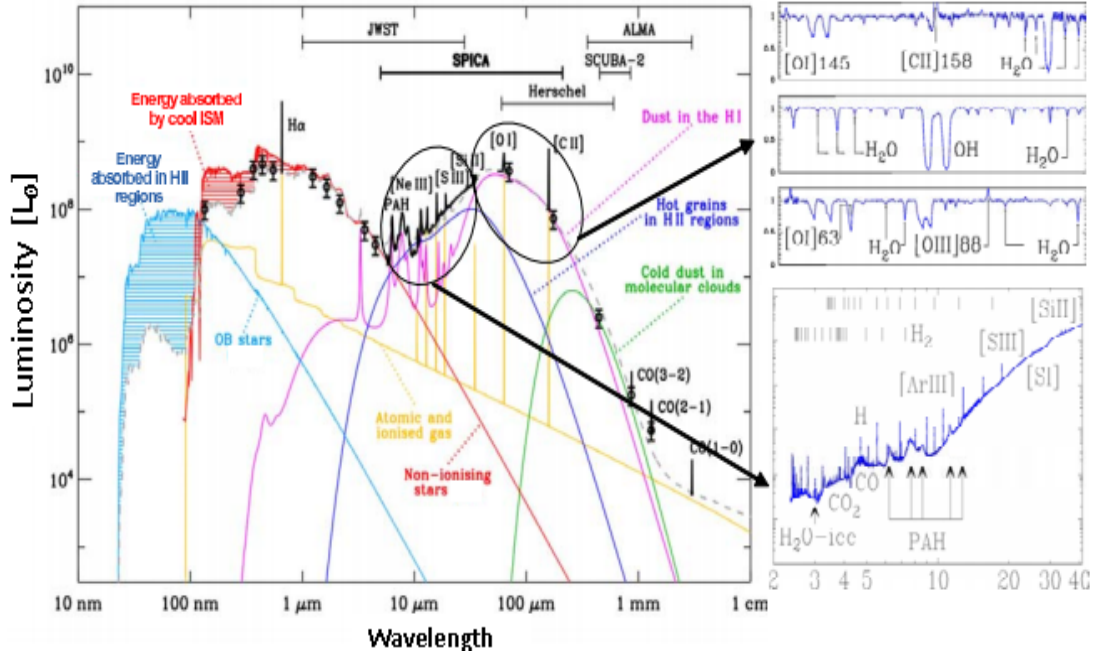


Figure 1.5: Left: A synthetic spectrum of a typical spiral galaxy undergoing modest rates of star formation showing the parts of the spectrum that will be covered by SPICA and other similar facilities [Ferlet *et al.*, 2010]. The symbol L_{\odot} in the y-axis units represents one solar luminosity. Right: Measured spectra from the Infrared Space Observatory (ISO) [Rosenthal *et al.*, 2007].

at almost all galactic distances [Goicoechea *et al.*, 2009]. Due to its unique spectral range SAFARI will perform spectral observations that include fine structure lines of atomic Oxygen ($63\mu\text{m}$ and $145\mu\text{m}$), water vapour rotational lines ($50\mu\text{m}$ and above), and features of water ice ($44\mu\text{m}$ and $62\mu\text{m}$). The water ice spectral data that will be acquired by SAFARI is essential to constrain current models of planet formation [Mayer *et al.*, 2005].

1.1.2 Birth and Evolution of Galaxies and AGN

The huge variety of galaxy morphologies has puzzled astronomers ever since the discovery that the Milky Way is but one of the hundreds of billions of galaxies populating the universe. In 1926 astronomer Edwin Hubble created a classification scheme for this morphology that separated galaxies into three basic classes [Hubble, 1926]. The diagram that demonstrates this has come to be known as Hubble's tuning fork diagram and can be seen in Figure 1.6.

The cosmological study of galaxies has undergone important changes over recent years as observational evidence is increasingly showing that galaxy formation and

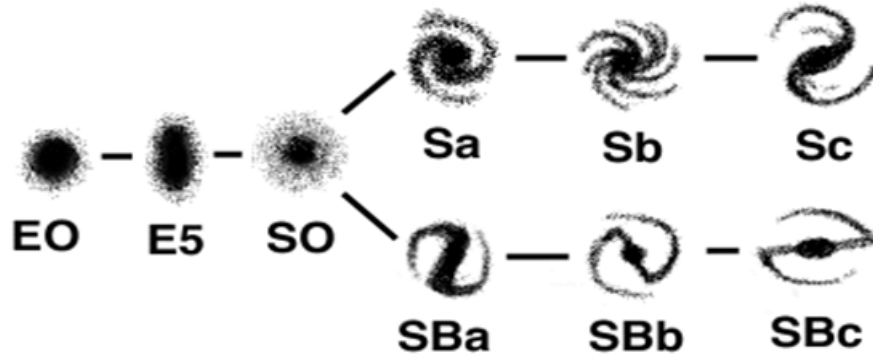


Figure 1.6: Hubble's "tuning fork" diagram illustrating the three broad classes of galaxies.

evolution is more complex than first assumed. In 1962 Eggen *et al.* put forward a theory that spiral galaxies form in a "top-down" process through a monolithic collapse of a huge gas cloud [Eggen *et al.*, 1962] in a manner similar to the collapse of a GMC in the formation of a protostar. However, more recent theories of how the first galaxies formed is based on a cold dark matter (CDM) dominated universe in which ordinary matter collected around areas of dark matter and through the process of accretion began to clump together and flatten out into a spiral shape in a "bottom-up" formation scenario. Computer simulations of galaxy formation further support the CDM, bottom-up based theories. They seem to indicate that disk galaxies such as spiral and barred spiral galaxies form as a result of accretion of intergalactic material whereas spherical and elliptical galaxies are a result of mergers between two or more separate galaxies [Steinmetz and Navarro, 2003]. The SFR (star formation rates) within galaxies across a range of cosmological distances z (where $z = (\lambda_{observed} - \lambda_{rest})/\lambda_{rest}$) can inform on how galaxies evolve. Thus, studying SFR across all values of z is clearly crucial for understanding the evolution of the Universe as a whole.

Far-IR emission is now an established tool that can be used to determine SFR within galaxies. The idea of using far-IR wavelengths to study the evolution of galaxies and to try to constrain current formation theories can be traced back to the IRAS mission that was launched on January 25th 1983. A paper released in May 1987 described how source counts with IRAS at $60\mu\text{m}$ were used to show modest levels of evolution within starburst galaxies [Hacking *et al.*, 1987]. Then in 1990 Carol J. Lonsdale confirmed the steep slope of the faint $60\mu\text{m}$ source counts discovered by Hacking *et al.* with the IRAS data, thereby re-enforcing the idea of

cosmological evolution at a rate higher than that predicted by conventional passively evolving models [Lonsdale, 1990]. The Spitzer Space Telescope then provided a big leap by allowing mid-IR surveys and spectroscopy of faint distant galaxies at high- z and revealing the star formation history of the universe to $z \approx 3$ [Soifer *et al.*, 2008]. However, the Herschel Space Observatory was again at the forefront in terms of the cutting-edge of the science being performed in the area of galaxy formation and evolution, and the breakthroughs provided by Herschel are discussed in the following paragraphs.

The infrared, and particularly the far-IR, is one of the most powerful tracers of star formation as IR luminosity directly scales with SFR [Seymour *et al.*, 2010]. The total IR output (luminosity) of a galaxy can provide an straightforward observational measure that can be used to estimate the total SFR provided care is taken when considering obscuration by dust, and AGN and recently quenched galaxies are excluded from the data [Hayward *et al.*, 2014]. The Herschel Space Observatory made it possible to directly measure the total IR luminosity of distant galaxies using rest-frame far-IR measurements of individual galaxies at wavelengths at which the IR spectral energy distribution (SED) peaks [Elbaz *et al.*, 2011]. Previous studies had relied on extrapolations from mid-IR or sub-mm photometry ([Melbourne *et al.*, 2005] for example), or indirect analysis such as stacking of far-IR data from individually undetected sources ([Zheng *et al.*, 2006] for example). The direct far-IR measurements by Elbaz *et al.* helped to clear up misconceptions of drastic evolution of IR SED due to previous incorrect extrapolations of the total IR luminosity from mid-IR ($24\mu\text{m}$) observations at $z \geq 1.5$, and the associated claim for a mid-IR excess. They demonstrated that the past incorrect extrapolations were a result of confusion between two separate star forming regimes which exhibit quite different IR SEDs; that of galaxies with extended star formation and that of galaxies with compact starbursts [Elbaz *et al.*, 2011]. Again, this was only possible through direct measurement of radiation within the far-IR band.

As already indicated in the previous section 1.1.1, the sensitivity of the Herschel Space Observatory was ultimately limited due its relatively warm 80K primary mirror. Thus Herschel was limited in the number of galaxies it could characterise using the ground-breaking far-IR measurement techniques described above. Furthermore due to the limited frequency ranges of the instruments on Herschel galaxies at very

large z were simply out of reach. The spectral coverage SPICA/SAFARI over the full THz regime will allow the above described techniques to be applied to galaxies at medium and high redshifts, thus allowing the characterisation of even the most distant galaxies. The background limited sensitivity of SPICA, and thus the much shorter integration times, coupled with the wide FOV of SAFARI ($2' \times 2'$) will make it possible to perform the first all-sky spectroscopic surveys of galaxies. These maps will be wide and deep enough to unveil the underlying physical processes that drive galaxy evolution for all sources out to $z \leq 4$, and at even higher z for the most luminous objects [Ferlet *et al.*, 2010].

Another way the SAFARI instrument can extend on the work of Herschel in determining the evolutionary mechanisms in galaxies and AGN for example is based on measurements of massive molecular outflows and negative feedback in ultra-luminous infrared galaxies (ULIRGs) performed with the Herschel/PACS instrument [Sturm *et al.*, 2011]. The authors describe how mass outflows driven by stars and AGN may produce the observed black hole-galaxy mass relation, and regulate and quench both star formation and black hole accretion in the host galaxies or AGN. Sturm *et al.* also describe how such observational evidence of these feedback processes are still scarce. Again, SAFARI could be used measure these mass outflow and feedback processes out to much higher redshifts, thus providing more extensive data spanning all cosmological epochs.

1.2 SPICA Space Observatory

1.2.1 SPICA Satellite

The SPICA space observatory is a proposed mission that had been scheduled for launch sometime in 2022, and is a joint project between JAXA and ISAS (Institute of Space and Astronautical Science) of Japan, and ESA. It will have a primary mirror of 3.5 metre diameter cooled to less than 6K which will allow background limited observation over a wavelength range of 34-210 μ m (mid to far-IR). The large aperture, monolithic mirror will provide diffraction limited performance at 34 μ m, and will enable high spatial resolution with a reasonably well controlled point spread function. SPICA, as proposed, will carry a mid infrared camera, mid-IR spectrometers and

a mid-IR coronagraph (built by JAXA institutes), a far-IR imaging spectrometer (SAFARI, provided by ESA), and a far-IR/sub-millimetre spectrometer (proposed by the U.S.A.). SPICA is planned to have a lifetime of 5 years with a 3 year minimum, and will orbit the second Lagrange point (L2) of the Earth-Sun system. It is proposed that SPICA will be launched on the H-IIA 204 in 2022 from the JAXA Tanegashima Space Centre in Tanegashima, Japan.

European involvement in SPICA was first proposed in 2007 in response to a call for missions that fit the ESA Cosmic Vision 2015-2025 programme. SPICA was selected for assessment as a candidate M-class mission, and was termed a "Mission of Opportunity". The assessment phase ran for two years from 2007 to 2009 [Ferlet *et al.*, 2010], and it included an internal ESA study of the mission concept, and 1-year industrial study programme of the SPICA cryogenic telescope assembly by both Thales Alenia Space in France and at Astrium, also in France. A study of one of the proposed main instruments for SPICA, a far-IR imaging spectrometer (SAFARI), was also carried out over the same period by a European consortium. This SAFARI study included contributions from the author of this thesis as described in chapter 5.

An updated proposal for European involvement in the SPICA project, based on the outcome of the ESA assessment study, was put forward in late 2009/early 2010. This proposal called for ESA to assume a partner agency role in SPICA, with JAXA to lead the mission ([Swinyard *et al.*, 2009] or [Nakagawa, 2010] for example), and ESA would provide the SAFARI instrument to be developed under a European Consortium led by the SRON. Then in 2013 ISAS/JAXA and ESA agreed that the scheme for SPICA was not compatible with a timely and robust implementation of the mission. Both JAXA and ESA decided that an increased ESA contribution to the mission would lead to a lower risk and more robust mission implementation [IRAP, 2014]. However, any significant extension of ESA's contribution to the SPICA mission would bring the mission into the M-Class (medium mission) range, meaning that the mission would need to be proposed to an ESA call for M-Class missions where it would need to be peer-reviewed against other proposals for the same opportunity. It was therefore decided to stop all ESA support activities on SPICA in early Autumn 2013. In spite of this, research continues on the detector technology required for a SAFARI-like instrument but under a more general far-IR

detector research effort. Strong collaboration exists between SRON in the Netherlands and the NUIM in terms of pushing the development of SAFARI-like receivers and detectors as described in chapter 5 of this thesis, and as can be seen by recent publications such as [Audley *et al.*, 2013] or [Bracken *et al.*, 2014] for example.

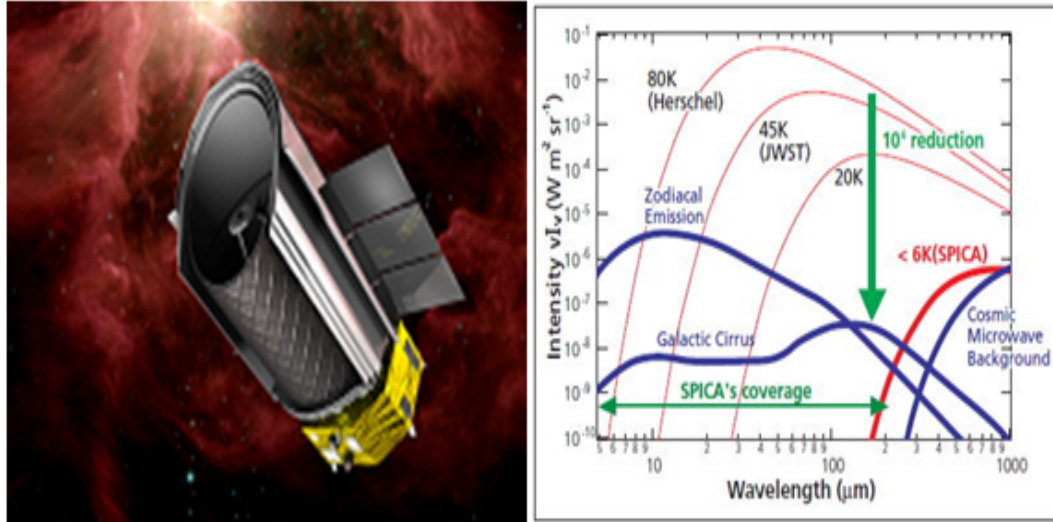


Figure 1.7: An artist’s impression of SPICA (left) and a graph showing the superior sensitivity of SPICA due to its $< 6K$ primary mirror operating temperature (right). The blue lines on the graph represent the diffuse infrared radiation emitted by some astronomical sources while the red lines show infrared radiation emitted by the telescopes themselves due to their temperature (image credit: ESA)

As already indicated the SPICA mission as proposed will build on previous work carried out using the Herschel Space Observatory (mission now finished), and will complement future work of the Atacama Large Millimetre Array (ALMA) and the James Webb Space Telescope (JWST) which is due to be launched in 2018. It will “fill in the gaps” between the lower frequency limit of JWST’s near-IR bands and the upper frequency limit of ALMA’s sub-millimetre bands. It will achieve this by extending the frequency range of Herschel to cover the full far-IR band while providing a huge improvement in sensitivity that will be at least an order of magnitude greater than Herschel.

SPICA is an ambitious project as it promises to help us understand the origin and evolution of galaxies, stars, planets, our Earth and perhaps even of life itself. To answer these questions good spatial resolution together with high sensitivity is required, but achieving both of these requirements has been a major problem in the past when observing at the mid and far-IR wavelengths. For good spatial resolution a large primary mirror is necessary, but a larger mirror means a larger observatory which would be much more difficult to cool to very low temperatures to reach

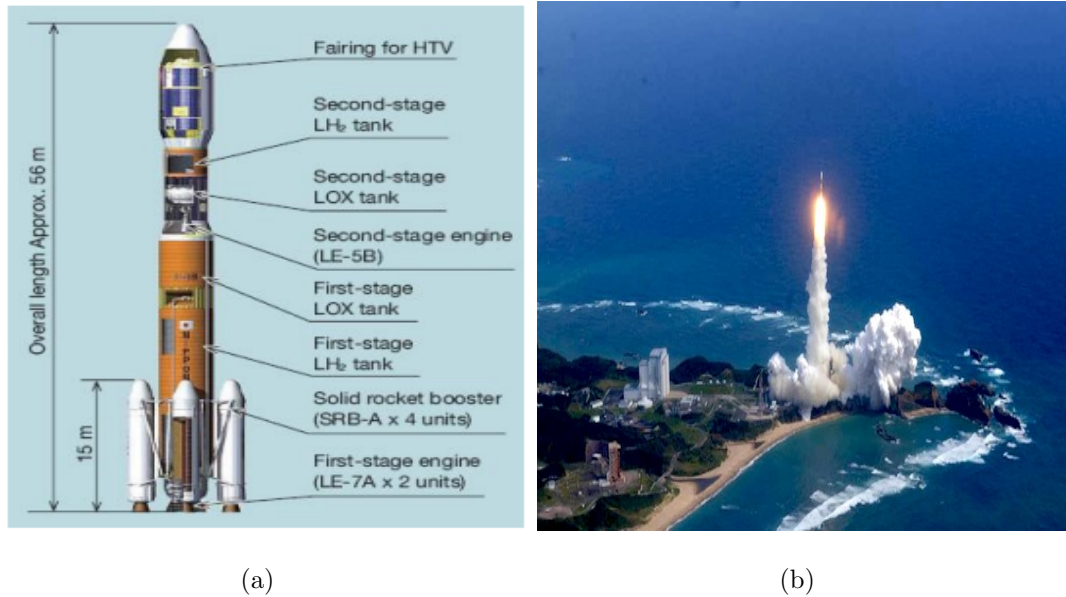


Figure 1.8: (a): H-IIA 204 launcher vehicle that will take SPICA into Earth orbit, from where SPICA will eventually transit to L2. (b): The Tanegashima Space Center (TNSC) located on Tanegashima, an island located 115km south of Kyushu, from where the H-IIA 204 rocket will launch, carrying SPICA into orbit (image credit: ESA)

the high sensitivities also required. The ESA Infrared Space Observatory (ISO), launched in November 1995, had excellent sensitivity for a facility of its time due to the relatively small 0.6m primary mirror being cooled to 1.7K by means of superfluid helium. For example the Long Wave Spectrometer (LWS) aboard ISO had a sensitivity of $\approx 10^{-16} \text{W}\sqrt{\text{Hz}}$ [Leeks *et al.*, 2003]. The ESA Herschel Space Observatory (retired as of August 2013) had a primary mirror with a diameter of 3.5m and therefore had very good spatial resolution, but the sensitivity across the 55-210 μm range was limited as the primary mirror could only be cooled to 80 Kelvin (passive cooling to ambient temperature of space). The significant improvement of SPICA compared to previous infrared observatories like Herschel comes from the combination of a large diameter mirror combined with active cooling using new technology mechanical cryocoolers [Sugitaa *et al.*, 2008] to a very low operating temperature. Thus, the primary mirror of 3.5m combined with cooling to temperatures below 6K promises to allow 10 to 100 times the sensitivity of Herschel in the far-IR band. This huge increase in sensitivity will allow integration times orders of magnitude shorter than could be achieved with Herschel thus enabling quick mapping capabilities right across the far-IR band.

1.2.2 The SAFARI Instrument

SAFARI is being developed by an international consortium led by SRON in Groningen, the Netherlands, including Cambridge University (UK), Cardiff University (Wales), and NUIM (Ireland) [Mauskopf *et al.*, 2010] or [TRP AO/1-5922/08/NL/EM, 2011]. The SAFARI detectors are split into three distinct bands corresponding to the highest frequencies that SAFARI will measure, the intermediate frequencies, and the the lowest frequencies, and the three bands have been given the names S-Band, M-Band, and L-Band, respectively. Table 1.1 presents a breakdown of the spectral coverage of each of the three SAFARI focal plane arrays, together with the number of pixels required to fully sample SAFARI’s 2’×2’ FOV. SAFARI will have various spectral resolution modes with R ranging from 10 to 10,000, for example $R \approx 2,000$ at $100\mu\text{m}$ [Goicoechea and Nakagawa, 2011], where R is defined as $\lambda/\Delta\lambda$. NUIM is involved in both the L-Band which is being investigated by Cardiff University and Cavendish Laboratory, Cambridge, [Mauskopf, 2011] and the S-Band which is under development at SRON Groningen [Audley *et al.*, 2013].

Band	Range [μm]	$F\lambda/2$ Pixel Size [μm]	Number of Pixels
S	34 - 60	480	64×64
M	60 - 110	840	38×38
L	110 - 210	1600	20×20

Table 1.1: Specifications of the three SAFARI spectral bands. Adapted from [Mauskopf *et al.*, 2010]

The baseline optical configuration of SAFARI is a Mach-Zehnder imaging FTS (Fourier transform spectrometer) [Zetie *et al.*, 2000], [Naylor *et al.*, 2006], which will provide high mapping speeds due to spatial multiplexing. It will have the ability to incorporate a photometric imaging mode and will have operational flexibility to tailor the spectral resolution to the desired science. The parts of SAFARI that were examined and modelled by the author, as described throughout this thesis, are the L-Band and S-Band detection boxes that are visible in the top-right of Figure 1.9, where each detection box consists of an array of superconducting TES bolometers mounted above an array of integrating backshorts, and fed by an array of feed horns. This part of the optical beam path is referred to as the “Waveguide Path”, and it

was discussed above in the introduction section at the beginning of this thesis. The remainder of the optics that are visible in Figure 1.9 are referred to as the “Free-Space Path”, also described above. Expanded views of the “Waveguide Path” are shown in Figure 1.10 where each sub-figure shows further zooming toward the TES bolometer.

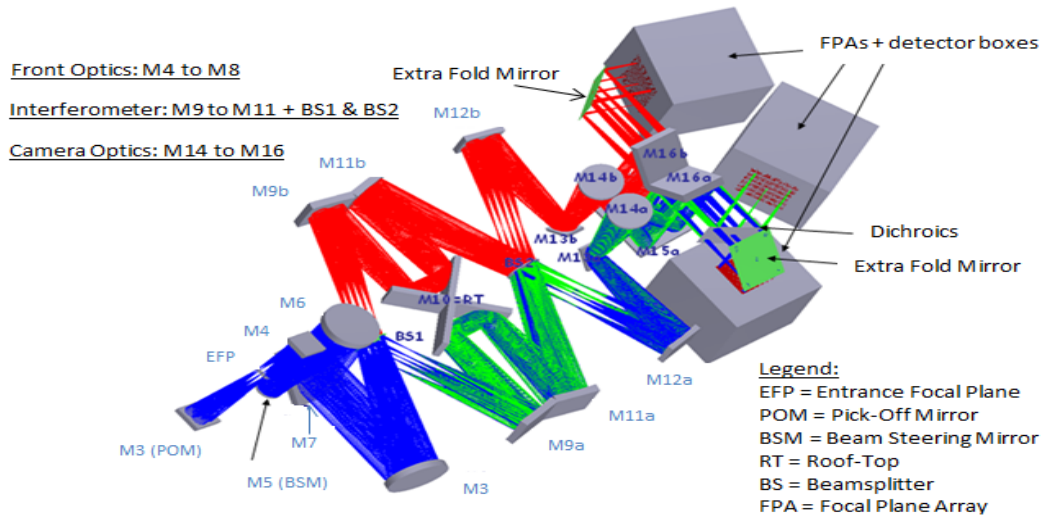
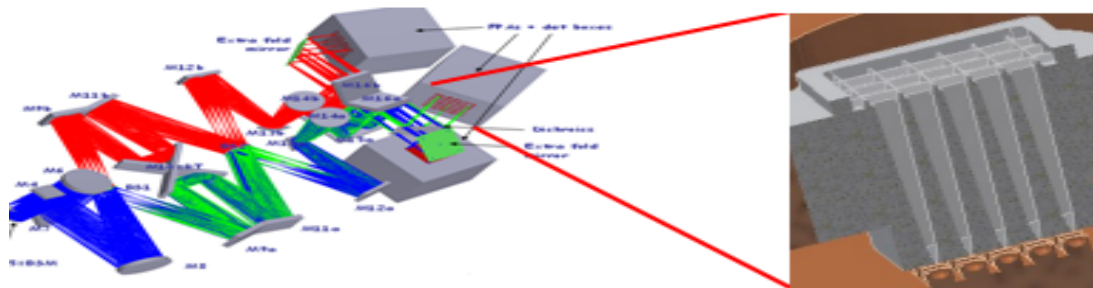
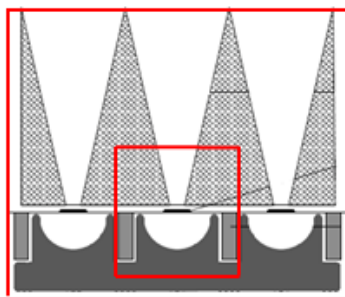


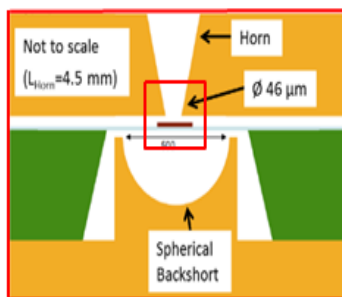
Figure 1.9: A schematic diagram of the SAFARI instrument. The detection boxes in the upper right area are the primary concern of this report (image credit: SRON).



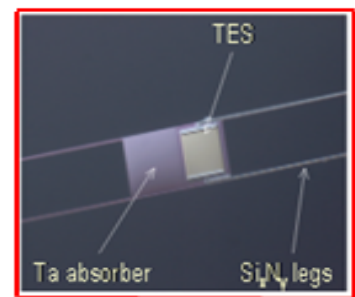
(a)



(b)



(c)



(d)

Figure 1.10: Expanded view of the “Waveguide Path” section of the SAFARI optical system. Further zooming going from (a) to (d) (image credit: SRON).

The SAFARI instrument on SPICA will exploit the power of MIR/FIR imaging spectroscopy and photometry. It will analyse radiation from processes involving galaxy evolution that are usually hidden from view due to dust. A selection of the important atomic, ionic, and fine-structure lines that will be accessible by SAFARI (and other SPICA instruments) are shown in Figure 1.11(b). SAFARI will be able to cover the full $34\text{-}210\mu\text{m}$ band in a few thousandths of the time that the photo detector array camera and spectrometer (PACS) on Herschel took to obtain a deep spectrum of comparable resolution. This is due to its broad instantaneous spectral coverage and high sensitivity. It also has a particularly wide FOV of $2' \times 2'$ making it possible to carry out spectroscopic surveys that are both wide and deep enough to analyse the underlying processes that drive galaxy evolution [Ferlet *et al.*, 2010].

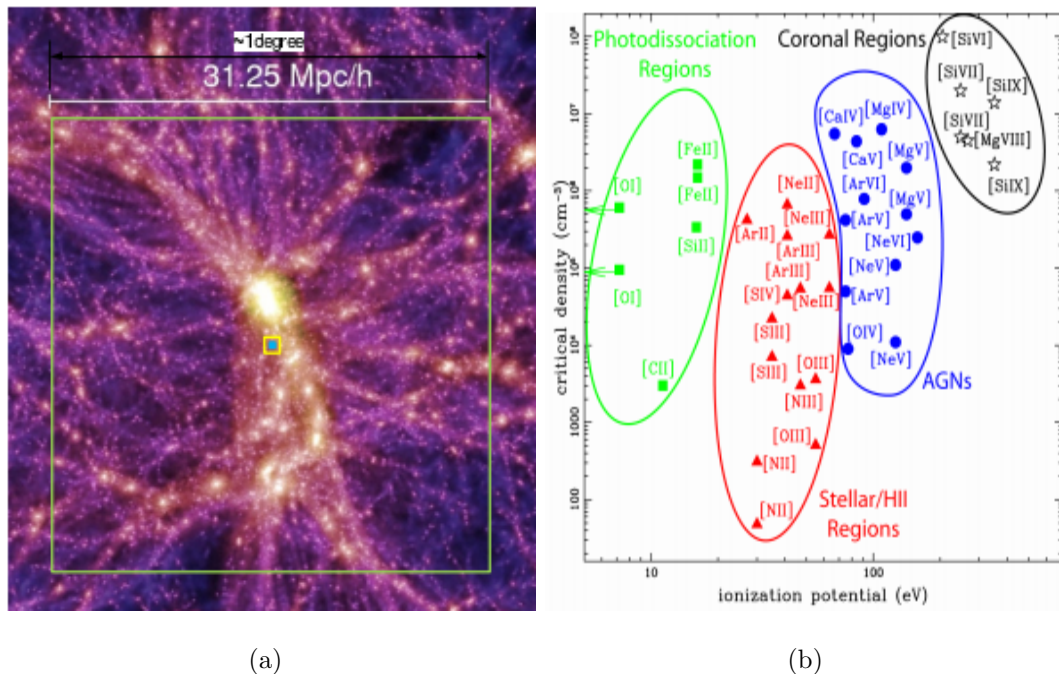


Figure 1.11: (a): Spectroscopic mapping speeds of the SAFARI Instrument compared to Herschel PACS. The mappings are shown superimposed on an output from the Millennium simulation at $z \approx 1.4$ [Springel *et al.*, 2006], [Ferlet *et al.*, 2010]. The small blue box in the centre of the image represents the footprint of the instantaneous spectroscopic FOV of Herschel-PACS, the yellow box surrounding the blue box represents the footprint of the instantaneous spectroscopic FOV of SAFARI ($2' \times 2'$), and the large green box shows the area that could be mapped by SAFARI in a 900 hour full wavelength spectral survey ($\approx (1^\circ)^2$). (b): A selection of the atomic, ionic, and fine-structure lines detectable with the proposed instruments on SPICA (including SAFARI), plotted as a function of critical density and ionisation potential [Ferlet *et al.*, 2010].

Figure 1.11(a) illustrates the mapping capabilities of SPICA-SAFARI. The large green box that marks out roughly $\approx (1^\circ)^2$ represents the area that could be mapped by SAFARI in a 900 hour full wavelength spectral survey simultaneously covering the full $34\text{-}210\mu\text{m}$ band. The large scale cosmological structure shown in

the image was taken from the Millennium project output [Springel *et al.*, 2006]. The Millennium project, or “Millennium Run”, was an N-body simulation performed at the Max Planck Society’s Supercomputing Centre in Garching, Germany, with the facility’s principal supercomputer over a one month period. It used more than 10 billion particles to trace the evolution of the matter distribution in a 2 billion light-years cubed volume of the Universe. By applying sophisticated modelling techniques to the 25 Tbytes of stored output, the team of scientists (VIRGO Consortium) were able to model the evolutionary histories of the roughly 20 million galaxies which populate the huge cube of the simulated universe. The simulations also involved the evolution of supermassive black holes which lie at the heart of most galaxies and quasars [Springel *et al.*, 2006], [Springel *et al.*, 2005].

As described in sections 1.1.1 and 1.1.2 above, SAFARI will be able to detect the key mid-IR and far-IR lines from distant galaxies by using mid-IR/far-IR diagnostics that have been revealed and calibrated by Spitzer and Herschel. At a redshift of $z = 1$ the rest-frame bandwidth of 11-35 μm , which is very rich in ionic fine structure as well as H₂ rotational lines, moves to 22-70 μm which is partially in the spectral range of SAFARI. For more distant galaxies corresponding to $z = 2$ this same bandwidth moves to 33-105 μm which can be completely covered by SAFARI. In fact galaxies out to a redshift of $z = 6$ will still be in the SAFARI spectral range. SAFARI will detect the brightest mid-IR and far-IR lines out to $z = 2$ in intermediate luminosity objects in a 1 hour integration which is a great improvement on Herschel-PACS, which only has the sensitivity to detect the very brightest mid-IR and far-IR lines in several hours of integration per line on the most luminous objects at $z \approx 1$ [Ferlet *et al.*, 2010].

SAFARI will have enough photometric sensitivity to undertake very deep large-area surveys. At 70 μm , for example, it will detect all galaxies with LIR (infrared luminosity) of $\text{LIR} \geq 10^{11}L_{\odot}$ at a redshift of $z = 2$ (where L_{\odot} is the luminosity of the sun), all those with $\text{LIR} \geq 5 \times 10^{11}L_{\odot}$ at a redshift of $z = 3$ and the most luminous IR galaxies ($\geq 10^{12}L_{\odot}$) out to $z = 4$.

1.3 Far-Infrared Imaging Fourier Transform Spectroscopy

Clearly photometric techniques can reveal the spatial and morphological details of planets, stars, and galaxies. However, spectral imaging techniques must be employed if the chemical composition and physical conditions of the same astronomical sources are to be determined. There are a number of measurement approaches that can be used for obtaining astronomical spectral information such as the familiar diffraction gratings commonly found in optical telescope systems. However, such diffractive techniques are usually quite limited in terms of the spectral coverage that can be achieved with them.

Fourier transform spectroscopy involves splitting the incoming signal beam into two, and by varying the optical path length of one of the beams before the two are recombined, an interferogram can be constructed that contains the spectral information of the signal beam. By subsequently applying sophisticated data analysis techniques the Fourier transform of the spatial intensity data can be extracted, thus revealing the signal intensity as a function of spatial frequency (wavenumber). With the high throughput, broad spectral coverage, and variable resolution possible, Fourier transform spectroscopy has been the most commonly employed spectroscopic method when dealing with the far-IR band [Naylor *et al.*, 2013].

There are in fact multiple techniques that have been demonstrated for performing Fourier transform spectroscopy. One such approach is described in chapter 3 of this thesis, where a Michelson interferometer was used to characterise a multimoded SAFARI-like feed horn. The choice of a Michelson interferometer in that case was based on the relatively short path length that can be employed with such a technique, since the entire optical system had to be mounted in a vacuum system due to the far-IR wavelengths that were under study. The drawback of the Michelson interferometer is that 50% of the signal beam will inevitably be reflected back toward the source and thus be lost (see Figure 1.18 in section 1.5 for illustration). A significant improvement on the Michelson design, in terms of efficiency, is the Mach-Zehnder (MZ) interferometer [Zetie *et al.*, 2000], [Naylor *et al.*, 2006], as illustrated in Figure 1.12. Due to its two separate output ports the full signal beam is available for analysis at the output. Figure 1.13 shows three Fourier transform spectra

[Swinyard *et al.*, 2003] and the spectrometer that is used with the SCUBA-2 instrument on JCMT [Naylor *et al.*, 2006]. The Astronomical Instrumentation Group at the University of Lethbridge, Canada has a long heritage in producing FTS's for astronomical applications at far-IR wavelengths [Naylor *et al.*, 2013] and had large involvement in the two instruments just mentioned.

1.4 VNA Measurement Techniques

The modelling approaches presented throughout this thesis often required verification, and where multiple simulation techniques are applied to the same problem the results can act to verify mutually one approach against another, assuming there is reasonable agreement between the results. Experimental verification is of course also important, and thus a number of experimental measurements were carried out as part of the work of this thesis as further verification of the modelling approaches described throughout the thesis. Section 1.5 describes the direct detection techniques that were involved in the characterisation of multi-moded SAFARI-like feed horns. In this section a description is given of the VNA and frequency extension heads that were employed for both measurement of the far-field beam pattern of a rectangular feed horn, which was used as a verification of the modelling approaches presented in chapter 3, and for cavity mounted absorber measurements, as a verification of the modelling work presented in chapter 5.

The VNA measurement approach made use of the in-house network analyser system in the department of experimental physics at NUIM. A VNA is an instrument that can perform coherent measurements of the network parameters of electrical networks, and can be used to analyse a device under test (DUT) by measuring its affect on the amplitude and phase of the coherent signal, across a swept-frequency range. In the application for the work of this thesis it was the s -parameters [Patel *et al.*, 2009] that were analysed since these parameters can provide information about the reflection and transmission of a DUT at high frequencies. Network analysers can be used to characterize networks with an arbitrary number of ports. The work presented in chapter 3 employed a two-port network, whereas the work presented in chapter 5 made use of just a one-port network.

The particular VNA used was a Rohde and Schwarz ZVA-24 system which

can generate a swept frequency range from 10-24 GHz. The VNA is operated in combination with two ZVA-Z110 W-band frequency extension heads that increase the frequency range to 75-110 GHz by using a series of frequency multipliers. This higher frequency range then allows coherent millimetre wave measurements of feed horns, cavities, and absorbers to be carried out.

In order to obtain the most accurate measurement results possible, a careful calibration must be carried out using a calibration kit that was provided by the manufacturer. The kit consists of three parts, the first of which, the short (see Figure 1.14(a)), allows for almost perfect reflection of the signal, and hence for the S_{11} and S_{22} reflection parameters to be correctly calibrated to unity (or 0 dB). The shim (Figure 1.14(b)), used in combination with the short, then contains a short transmission line causing a $\lambda/4$ phase shift around the center frequency of the converters operating range and a 180 deg phase shift of the reflection coefficient. Finally the match component (Figure 1.14(c)) allows for almost perfect absorption of the signal. The standard calibration used for a one-port network is the “off-set short, short, match” (OSM), which requires each of the above described components to be attached separately to the converter head being used. The analyzer’s “Calibration Wizard” then provides a straightforward procedure for calibration of the head. For a two-port network the same procedure is applied to both heads, one at a time, and then a “through” calibration step is performed, where the two converter heads are directly connected by a waveguide section.



Figure 1.14: The VNA calibration kit showing the three components.

The far-field beam pattern measurements used for verification of the modelling approaches described in chapter 3 also required the use of an $x - y$ plane raster scanner. The DUT was mounted on head 1, and placed on a translation stage that

could move in the direction of propagation z , while kept stationary in $x - y$. A WR-10 waveguide probe was then mounted on head 2, which itself was mounted on the raster scan assembly. The VNA scan system is shown in Figures 1.15 and 1.16.

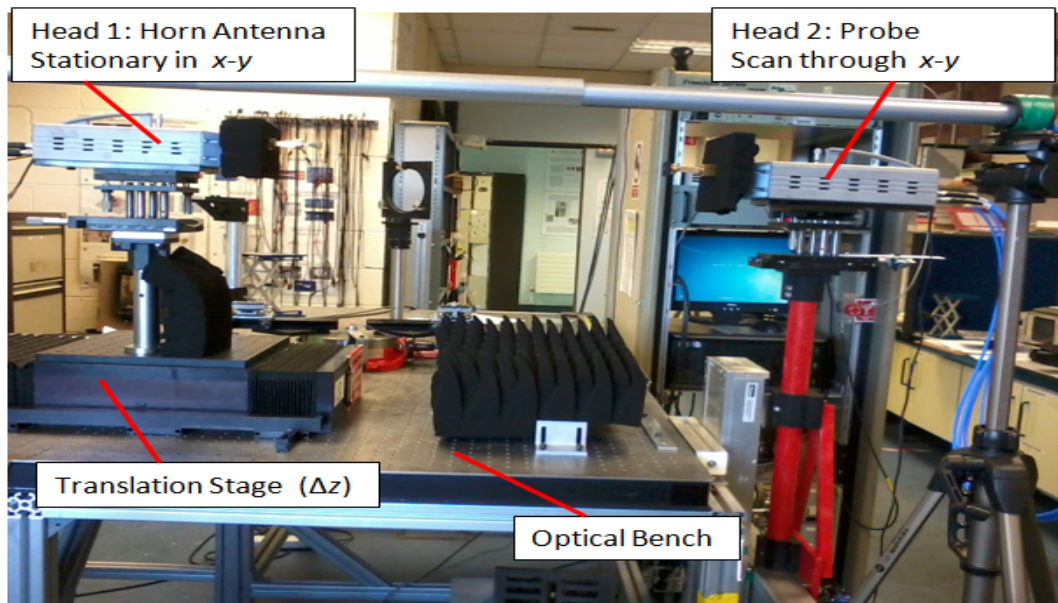


Figure 1.15: Photograph of the VNA scan system for measuring far-field beam patterns.



(a) Horn Antenna

(b) Waveguide Probe

Figure 1.16: VNA scan system showing converter heads and raster scanner.

1.5 Direct Detection Techniques

During an extended visit by the author to the SRON, Groningen, from June to September 2013, an analysis of the frequency dependent throughput of SAFARI-like

horns was carried out. The particular horn assembly that was analysed consisted of a back-to-back horn structure with a rectangular waveguide connecting the two horns. This particular format provided good beam control while also ensuring well defined cut-off frequencies for the propagating waveguide modes. The measurements and results are discussed in section 3.3 of this thesis. In this section a description of the FTS system that was used for the measurements is presented.

Fourier transform spectroscopy is the best method to analyse the frequency response of a device under test (DUT) at THz frequencies, when a broadband source is being used. An FTS based on a Michelson interferometer was set up in combination with a data acquisition device (DAQ) and a PC, and a bolometer cooled to 4K using a cryostat with liquid helium in the inner stage and liquid nitrogen in the outer stage. The FTS and cryostat are shown in Figure 1.17. A program called the Integrated Receiver Test & Control System (IRTECON) [Shitov *et al.*, 1998] was used for the control of the stepper motor in the FTS, and for compilation and initial analysis of the data corresponding to the detected power by the bolometer. The Michelson interferometer employed replaceable Mylar beam-splitters. Two different beam splitters were used separately; one with a thickness of $56\mu\text{m}$, and one with a thickness of $12\mu\text{m}$.

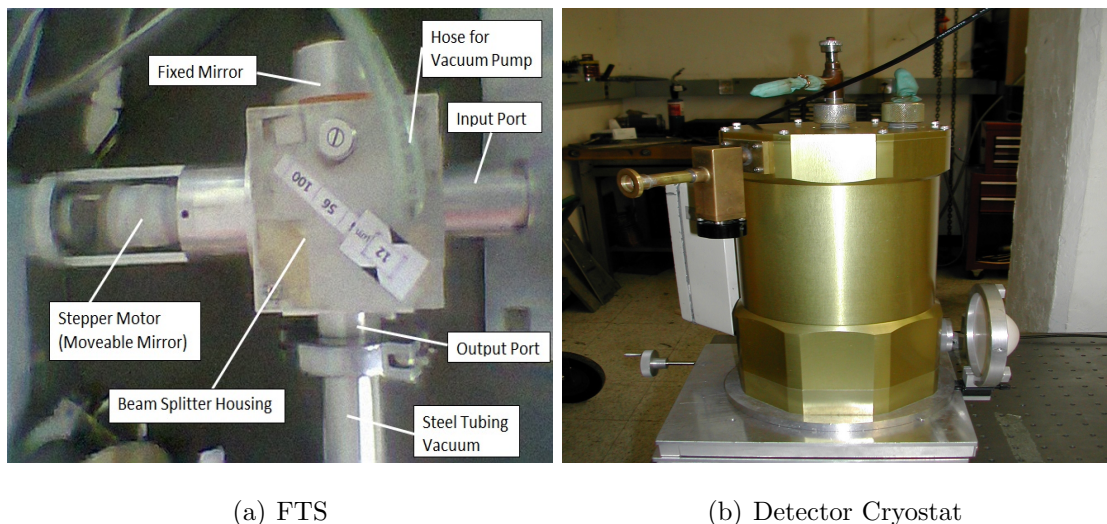


Figure 1.17: The FTS and cryostat that were used for the horn throughput experiments.

Figure 1.18 shows a schematic of an FTS and how it functions by moving one of the mirrors through a series of steps in order to vary the path length travelled by one part of the split beam, thus varying the phase of the signal beam at the end of that path. If the two parts of the beam are then combined at the detector they will

interfere in a manner that depends on the path length difference between the beam paths, and the frequency distribution within the original beam. If the path length difference is incrementally changed in uniform steps of Δx a number N times across a total scan path of $X = N\Delta x$, and the intensity of the recombined beam $f(n)$ is measured at each point, an interferogram like the one shown in Figure 1.19(a) can be created.

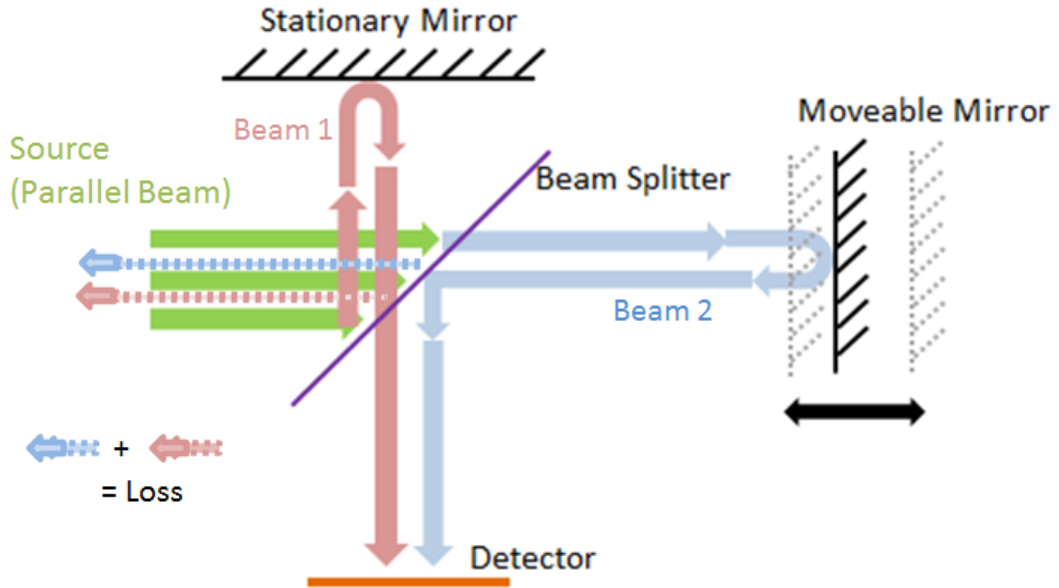


Figure 1.18: Schematic of a FTS and how it functions. The position of the moveable mirror is incrementally varied by a stepper motor which is controlled by the IRTECON software. The different colours of the separate beams is just for clarity, and should not be mistaken as different wavelengths. As is indicated, half of both beam 1 and beam 2 are lost from the system as they encounter the beam splitter for the second time.

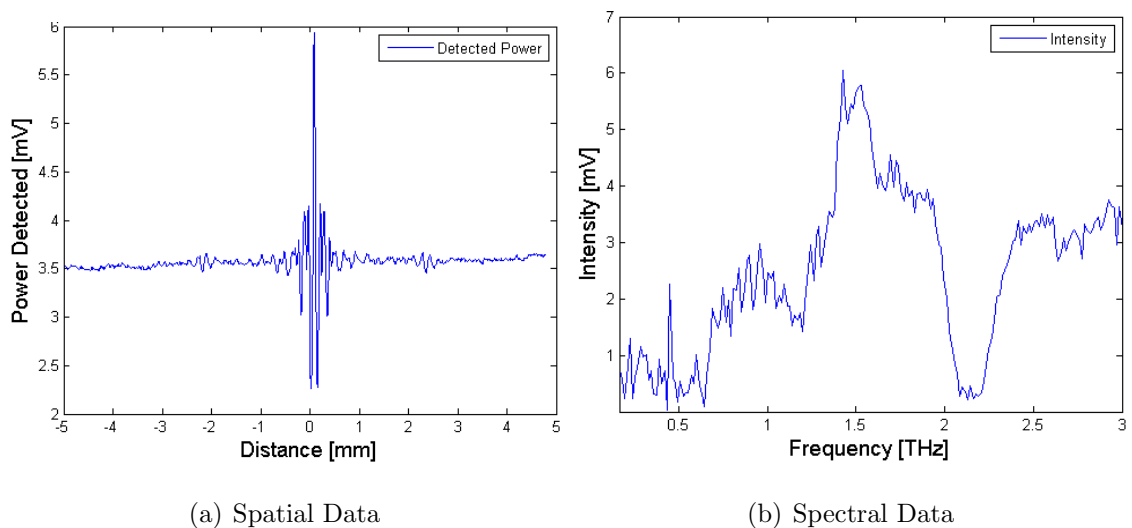


Figure 1.19: (a): Interferogram for a back-to-back horn illuminated by a glow bar in a Michelson FTS. (b): Spectral data for a back-to-back horn derived by applying a discrete Fourier transform (DFT) to the interferogram data.

The spatial data that is shown plotted in the interferogram (Figure 1.19(a)) can

then be used to obtain the frequency spectrum $F(k)$ (Figure 1.19(b)) by applying a discrete Fourier transform operation to the data as follows:

$$F(k) = \sum_{n=0}^{N-1} f(n) \exp(-2\pi ink/N) \quad (1.1)$$

where n is the n th position of the moveable mirror when it is at $n\Delta x$ from zero, and $f(n)$ is the intensity at position n .

The highest frequency that can be computed from the spatial data depends on the size of steps Δx . The smaller the steps the higher the frequencies that can be extracted, and the maximum frequency is determined by $f_{max} = f_{NQ} = \frac{1}{2\Delta x}$. f_{NQ} is known as the Nyquist frequency.

The bolometer that was housed in the cryostat could be coupled to one of three low pass filters. The 312cm^{-1} and 100cm^{-1} filters were used for the measurements. For further details of the measurements and results see section 3.3.

1.6 Transition Edge Sensors

A TES, or transition edge sensor, is essentially an extremely sensitive thermometer which is made from a material that can exhibit superconducting behaviour. Its principle of operation exploits the strong temperature dependent resistance of a superconducting material when it is at its phase transition from a superconductor to a normal metal. The material is held at its transition temperature T_c by a bias, where a very small increase in temperature causes a large increase in resistance. As can be seen by the steep curve in Figure 1.20, an increase in temperature of less than 10mK gives rise to an increase in resistance of $20\text{m}\Omega$.

The fundamental phonon noise in a TES is directly related to temperature, as described by the equation governing NEP (5.27) (see section 5.4.3). Since sensitivity is inversely related to phonon noise and thus, temperature, TES's for the far-IR are typically operated at sub-Kelvin temperatures [Khosropanah *et al.*, 2011]. The TES is usually coupled to a thin piece of metal such as Ta which is deposited on a substrate that is transparent to the radiation being detected. The thin sheet of absorbing material is ideally impedance matched to free-space in order to absorb as much radiation as possible. The TES/absorber pair is then usually thermally

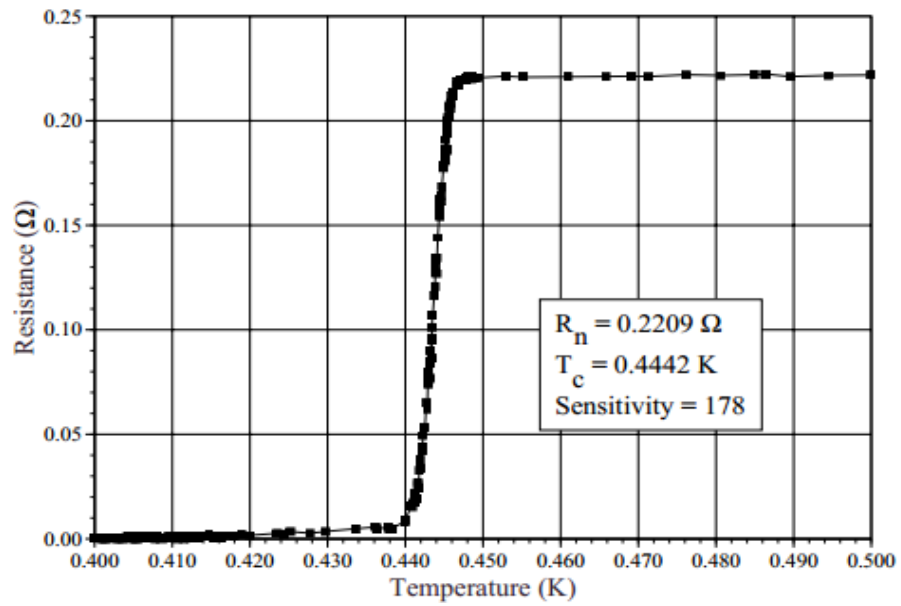


Figure 1.20: Temperature dependent resistance profile for a Mo/Au bilayer TES [Figueroa-Feliciano, 2001].

isolated from the bath by mounting it on thin silicon nitride (SiN) legs, as shown in Figure 1.21.

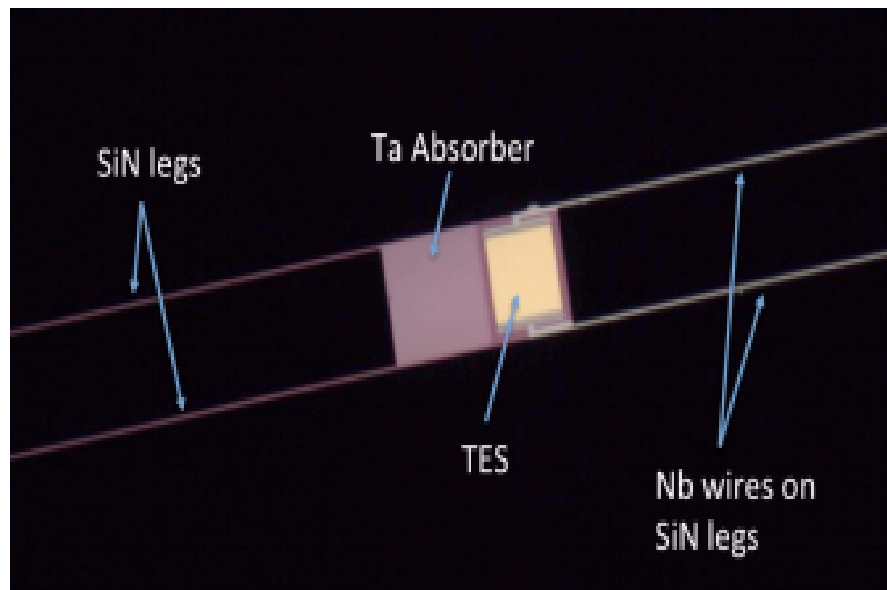


Figure 1.21: A micrograph of a TES coupled to a Ta absorber, and thermally isolated from its surroundings by SiN legs [Khosropanah *et al.*, 2011].

Over many years TES's have been shown to be powerful detectors of single photons at wavebands ranging from infrared to gamma rays [Irwin and Hilton, 2005]. More recently they have been demonstrated to operate well in close-packed array format [Iyomoto *et al.*, 2008] which will be required for the SAFARI instru-

ment. Research into the characterisation of TES's specifically for far-IR wavelengths is ongoing with projects such as the SAFARI test-bed at SRON, for example [Audley *et al.*, 2013].

1.7 Conclusions

In this chapter a strong science case for far-IR astronomy was made, where it was explained that three out of the four questions set out by ESA's Cosmic Vision could be answered by performing ultra-sensitive observations in the mid-IR and far-IR. It was shown that a next generation space based mid-to-far infrared observatory will be key in fulfilling this ambitious Cosmic Vision. The proposed JAXA/ESA space observatory SPICA was described, with particular attention given to SPICA's main instrument SAFARI, a far-IR imaging FTS. It was explained that SPICA's cooled main mirror would be key in achieving background limited sensitivity for SPICA's suite of instruments, including SAFARI, and how SAFARI's large format focal plane arrays would provide the high mapping speeds necessary for carrying out the first all sky spectroscopic surveys in the far-IR.

The principles of far-IR Fourier transform spectroscopy were outlined, including a description of the Mach-Zender interferometer format that SAFARI will be based upon. A description of the Michelson interferometer that was used for measurements presented in this thesis was given, as well as a brief overview of the VNA system that was employed for further measurements as a verification of simulation methods presented throughout this thesis.

Chapter 2

Computational Methods for Electromagnetic and Quasioptical Design and Analysis

“Somewhere, something incredible is waiting to be known.”

- Carl Sagan

2.1 Overview of Computational Methods

In this chapter the various computational modelling approaches and techniques used in the analysis of SAFARI-like receivers and detectors will be explained. Due to the electrically large multi-moded structures that make up such systems, computationally efficient methods such as EM mode matching [Wexler, 1967] and GBM (Gaussian beam mode) analysis [Wylde and Martin, 1993] are required. However due to the relatively restrictive nature of such efficient modelling techniques more flexible and exact simulation methods are also required, such as FEM employed by the COMSOL Multiphysics software [COMSOL, 2011]. The drawback of the FEM approach is that it is relatively inefficient compared to mode matching, for example.

Section 2.2 describes the GBM method which is very efficient at modelling propagation through free-space and beam transformation by optical elements such as lenses, mirrors, etc., and it was used in the analysis of the lens system that was employed for the throughput experiments carried out at SRON, as described in chapter 3. It provided a method to model the beam width of the THz radiation as it propagated from the source to the feed horn, where the model was then compared to the measured spot size. However GBM analysis is not suited to modelling fields inside conducting structures such as waveguides, horns and cavities. Thus, other techniques are required in order to characterise fully the SAFARI detectors.

Section 2.3 of this chapter summarises the theory for modelling the behaviour of EM fields inside conducting structures such as waveguides and cavities. The separated TE (transverse electric) and TM (transverse magnetic) field components are tabulated for reference in later chapters. Derivations of the modal fields can be found in [Olver *et al.*, 1994] or [Clarricoats *et al.*, 1984], for example.

The TE and TM waveguide mode field descriptions were required in many circumstances during the work presented in this thesis. For example the COMSOL software package that was used for modelling horns, cavities and absorbers (chapters 3, 4 and 5) required the mathematical descriptions of modes as inputs for port boundary conditions as a means of exciting EM fields through the structures. Although COMSOL does have some predefined mode options, if symmetry conditions in the E or H-planes are exploited in order to reduce the problem size, then the user must provide analytical field descriptions at the input ports.

The waveguide mode descriptions were also used in combination with a spherical phase cap [Clarricoats *et al.*, 1984] as a means of describing approximate solutions for aperture fields of smooth walled conical and rectangular horns for comparison with exact solutions. Examples of these approximate methods are given in chapters 3 and 4.

Throughout this thesis the waveguide mode solutions introduced above are used in EM mode matching simulation methods, so a brief description of the approach is given in section 2.4 of this chapter. The theory is described in much greater detail in chapter 4 for the specific case of conical mode matching. In general EM mode matching is a technique used to model EM fields inside conducting structures. It is similar to GBM analysis in the sense that the electric and magnetic fields are again defined as being a superposition of a set of modes, but the primary difference is the boundary conditions due to the walls of the conducting structure.

The final section 2.5 of this chapter describes the COMSOL Multiphysics package and the FEM technique upon which it is based. COMSOL Multiphysics is used throughout the work of this thesis to model a wide variety of problems relating to SAFARI-like THz receiver systems. The COMSOL software provides an interactive environment based on the proven FEM technique that can be used for modelling and solving many kinds of scientific and engineering problems. The finite element analysis is computed in combination with adaptive meshing and error control and provides multiple direct and indirect numerical solvers. The software also offers a wide range of post-processing tools for plotting data, making animations and carrying out other post-processing operations.

2.2 Gaussian Beam Mode Analysis

2.2.1 Background

Recent years have seen a fast growing interest in the application of millimetre and sub-millimetre waves (THz waves). Some examples of these applications were given in the introduction of this thesis. There are several different techniques for guiding these waves from one point or plane to another, such as EM waveguides and stripline systems. However, due to the difficulty in fabricating ever smaller components as

the desired operational frequency increases, and mass limitations for space based applications, alternative wave guiding techniques are needed. To date fibre optics techniques for the control of beams have not been possible due to no known suitable materials being available. One such alternative is quasioptics [Goldsmith, 1992], and it involves the free space propagation of narrow, quasi-collimated beams, sometimes called pencil beams when the beam opening angle is very small. This quasioptical approach relies on using EM components such as waveguides and feed horns in combination with optical elements such as lenses and mirrors. These narrow pencil beams can be mathematically described as a set of independently propagating Gaussian beam modes which are solutions to the wave equation.

GBM analysis is an alternative way of mathematically analysing the evolution of beams of EM radiation as they propagate through space. The classical approach uses Fresnel diffraction integrals to examine the radiation pattern of light at a particular location in space. This process can be computationally inefficient and is very abstract in terms of giving a physical feeling for how the beam evolves. GBMA provides a more efficient and more intuitive means of modelling such beams in terms of both their near and far field diffraction patterns. The same limitations of the paraxial approximation [Hyde, 2000] that are assumed for Fresnel diffraction apply to GBM analysis also [Murphy and Egan, 1993]. The basic approach is based on decomposing the electric or magnetic field into a set of independently propagating modes by performing an overlap integral with the field and each mode to determine the component mode amplitudes at a plane where the field is well defined. The component modes can then be independently propagated through the system or through free space, and then simply summed in a linear fashion to reproduce the evolved field at any other point or plane. The technique can be used for propagation through free-space, propagation through lenses, mirrors, polarizing grids, etc., and can be applied to more complex diffraction phenomena as described in many publications by the THz Optics group at NUIM, such as classical phase aberrations [Trappe *et al.*, 2003], GBM beam shaping [Lavelle and O’Sullivan, 2010], the quasi-optical analysis of Bessel beams in the far infrared [Trappe *et al.*, 2005].

In the following sections some examples of free-space propagation using GBM analysis are presented to demonstrate the power of the technique and to validate the GBM code written by the author. The derivation of the GBM theory can be

found in many publications, including [Goldsmith, 1998].

For a normalised field (i.e. $\int |\vec{E}|^2 dA = 1$), for example the \vec{E} field, the mathematical description can be written as [Wylde and Martin, 1993]:

$$E(x, y, z, t) = \sqrt{\frac{2}{\pi W(z)}} \exp\left[-\frac{(x^2 + y^2)}{W(z)^2}\right] \exp\left[-jk\frac{(x^2 + y^2)}{2R(z)}\right] \exp[j\phi(z)] \exp[-jkz] \exp[j\omega t] \quad (2.1)$$

where E represents one of the components of \vec{E} , $\omega = 2\pi\nu$, where ν is the frequency of radiation, $k = 2\pi/\lambda$, where λ is the wavelength of radiation, and $R(z)$, $W(z)$, and $\phi(z)$ have the following definitions:

$$R(z) = z \left[1 + \left[\frac{\pi W_0^2}{\lambda z} \right]^2 \right] \quad (\text{Phase Radius of Curvature}) \quad (2.2)$$

$$W(z)^2 = W_0^2 \left[1 + \left[\frac{\lambda z}{\pi W_0^2} \right]^2 \right] \quad (\text{Beam Width}) \quad (2.3)$$

$$\phi(z) = \arctan \left[\frac{\lambda z}{\pi W_0^2} \right] \quad (\text{Phase Slippage}) \quad (2.4)$$

where W_0 is called the beam waist, whose radius will depend on the wavelength of radiation, and corresponds to the minimum value that $W(z)$ will take. In (2.1) to (2.4) above, it is assumed that propagation is in the z direction. Figure 2.1 illustrates some of the terms in the mathematical description of a quas-optical Gaussian beam.

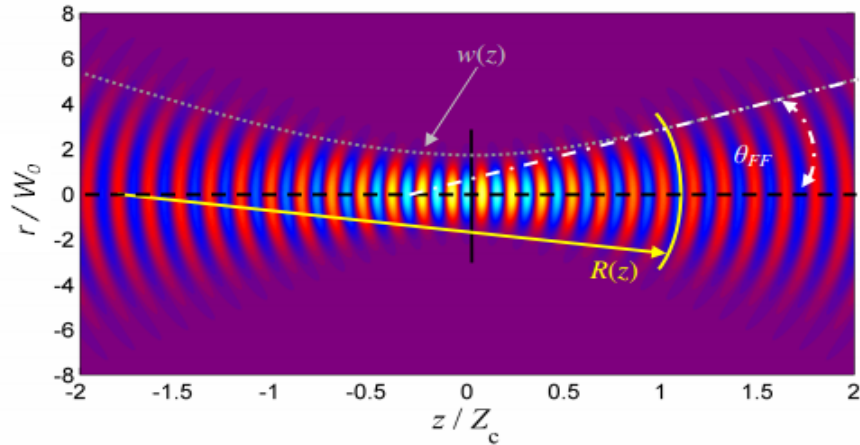


Figure 2.1: Illustration of a Gaussian beam showing the beam width and phase radius of curvature as a function of propagation distance. The propagation distance is normalised to the Rayleigh range Z_c , which is defined as $Z_c = \pi W_0^2/\lambda$. The Rayleigh range is also the distance from the position of the waist z_0 , in the direction of propagation, to the place where the value of the beam width is $\sqrt{2}W_0$. A related parameter is called the confocal distance (sometimes called the depth of focus), and is defined as $2Z_c$. *Image credit: Dr. Ronan Mahon*

Equation (2.1) describes the propagation of an ideal, purely Gaussian beam. This is called the fundamental Gaussian, or fundamental mode as higher order modes are usually also present to some degree in a propagating beam. To model accurately quasioptical systems it is usually necessary to include some of these higher order modes. This is achieved by combining (2.1) with a set of appropriate polynomials, the form of which depends on the geometry of the problem (i.e. Cartesian or cylindrical polar). Each higher order polynomial governs the structure of one particular mode while multiplication by the Gaussian term (Gaussian envelope common to all modes) “kills off” the amplitude in the transverse direction (i.e. the field has finite extent). The form of these modes in the different coordinate systems will be introduced in the simple examples considered in the following sections. It should be noted that the phase slippage term $\phi(z)$ is mode dependent as there is a different amount of phase slippage for each mode (the higher order modes fall out of phase faster than the lower order modes, relative to an infinite plane wave travelling in the same direction).

2.2.2 Gaussian Beam Mode Analysis of Uniformly Illuminated Apertures

The field that describes a uniformly illuminated circular aperture can be defined as being unity across the aperture and zero everywhere else. This is the form of the field, produced by a distant point source, at the aperture of a telescope such as SPICA for example. The image that is formed on the detector array plane then is called the point spread function [Cox and Hodge, 2006].

The current SAFARI test-bed being used at the SRON to characterise a single SAFARI pixel employs a small circular aperture between the thermal source and the conical horn that feeds the cavity coupled TES detector. A basic schematic of the source, aperture and horn layout is shown in Figure 3.35, and a detailed description of the SAFARI test-bed is given in chapter 3, section 3.3. The source, which illuminates the circular aperture, is actually a conical blackbody radiator but for simplicity in the model it will be assumed that the aperture is uniformly illuminated with monochromatic light.

It is most convenient and efficient to decompose the aperture field into modes

with similar symmetry to that of the field, i.e. cylindrical polar or Cartesian. Thus, for the example of a small circular aperture, the best suited basis set is the Laguerre-Gauss mode set. The rotationally symmetric (about the axis of propagation) higher order Laguerre-Gauss modes, travelling in the z direction, have the following form (in the appropriate cylindrical polar coordinate system) [Murphy *et al.*, 1997]:

$$E_n(r, z) = \sqrt{\frac{2}{\pi W(z)^2}} L_n(r, z) \exp\left[-\frac{(r^2)}{W(z)^2}\right] \exp\left[-jk\left(z + \frac{(r^2)}{2R(z)}\right) + j\phi(z)\right] \quad (2.5)$$

where $L_n(r)$ is a Laguerre polynomial that is a function of the propagating mode number (n), and the off-axis distance (r) perpendicular to the direction of travel of the wave. The Laguerre polynomials have the form [Pampaloni and Enderlein, 2004]:

$$L_n(r) = \frac{e^r}{n!} \frac{d^n}{dr^n} (e^{-r} r^n).$$

In order to calculate the mode coefficients A_n , an overlap integral with the aperture field and each mode was calculated [Murphy and Egan, 1993]. Since the waist position of the modes was unknown it was assumed that the aperture plane is the waist position for each mode, therefore $z = 0$, $\phi(z) = 0$ and $R(z) = R(0) = \infty$. Mathematically, this is expressed as:

$$A_n(W_0) = \sqrt{\frac{2}{\pi W_0^2}} \int_0^a \left(L_n\left(\frac{2r^2}{W_0^2}\right) \exp\left[-\frac{r^2}{W_0^2}\right] 2\pi r\right) dr \quad (2.6)$$

where n is the mode number and is an integer that goes from 1 up to the required number of modes. Note that W_0 was left as a variable so that it could be varied in order to minimise the number of modes required [Murphy and Egan, 1993]. The integration is over 0 to a where a is the radius of the circular aperture. The choice of waist radius and position is somewhat arbitrary, and non-ideal values will not necessarily result in an incorrect field description. Rather, unrealistic or non-ideal values will simply result in a larger mode set being required for a given level of accuracy.

By incrementally varying the beam width of the modes from 0 to a in steps of $0.01a$, and examining the reconstructed aperture field at each iteration, it was found that a value of $W_0 = 0.2a$ provides a reasonably accurate description of the field with relatively few modes. Figure 2.2 shows slices through the aperture “top-hat”-like truncated field for three cases, each calculated with a different number of modes. It can be seen that as more modes are used the field becomes more accurately defined with the ringing being reduced and the edges of the beam becoming sharper. The on-axis magnitude is normalised to unity in each case.

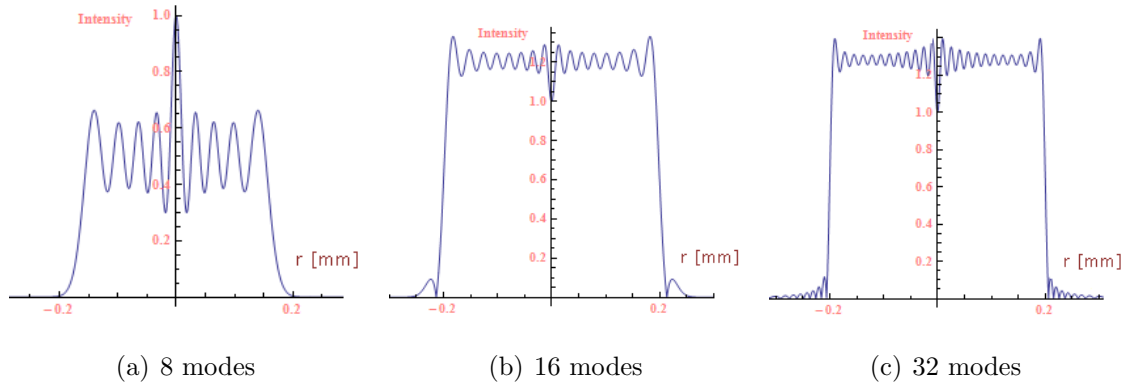


Figure 2.2: Slices through the aperture “top-hat” electric field intensity for increasing number of modes.

32 modes ($n = 32$) were then propagated to, and combined at, various locations in order to investigate how the diffraction pattern varied as propagation distance z was increased. 3D plots of the electric field are shown on Figure 2.3 for four propagation distances. As can be seen the electric field experiences a lot of change in the near field (Fresnel region) as would be expected. The far-field is reached by $z = \frac{2a^2}{\lambda}$, as can be seen by the roughly sinc profile in Figure 2.3(d). Contour plots of off-axis intensity as a function of increasing propagation distance are then shown in Figure 2.4.

Similar in a way to the example of a uniformly illuminated circular aperture, the field that describes a uniformly illuminated rectangular aperture can be defined as being unity across the aperture and zero elsewhere. Such an illuminated rectangular aperture was used in the SAFARI-like horn throughput experiments that are described in chapter 3. The equation for a Gaussian beam mode that has rectangular symmetry travelling in the z direction has the following form [Pampaloni and Enderlein, 2004]:

$$E(x, y, z) = \sqrt{\frac{1}{\pi W(z)^2 2^{2m+n-1} n! m!}} H_n(y, z) H_m(x, z) \exp\left[-\frac{(x^2 + y^2)}{W(z)^2}\right] \exp\left[-jk\left(z + \frac{(x^2 + y^2)}{2R(z)}\right) + j(m + n + 1)\phi(z)\right] \quad (2.7)$$

where $H_m(x, z)$ and $H_n(y, z)$ are Hermite polynomials that are functions of the propagating mode number (m, n) , and the off-axis distance (x, y) perpendicular to the direction of travel of the wave. The Hermite polynomials have the form [Pampaloni and Enderlein, 2004]: $H(m, x) = (-1)^m e^{x^2} \frac{d^m}{dx^m} e^{-x^2}$.

Following similar steps as before, the field at a small square aperture was decomposed in terms of such Hermite-Gauss modes, thus allowing the aperture field

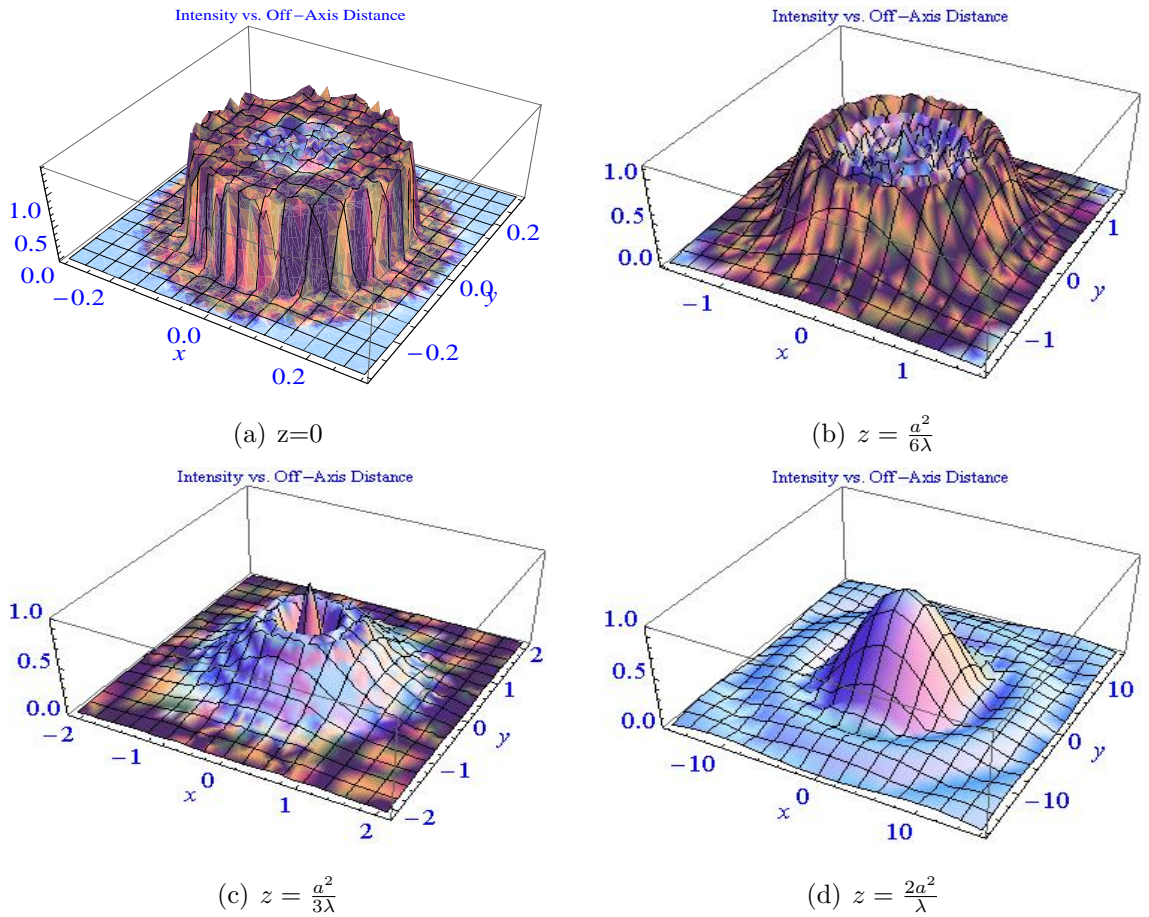


Figure 2.3: Diffraction patterns for various propagation distances from a circular aperture. 32 Laguerre-Gauss modes were used in the analysis.

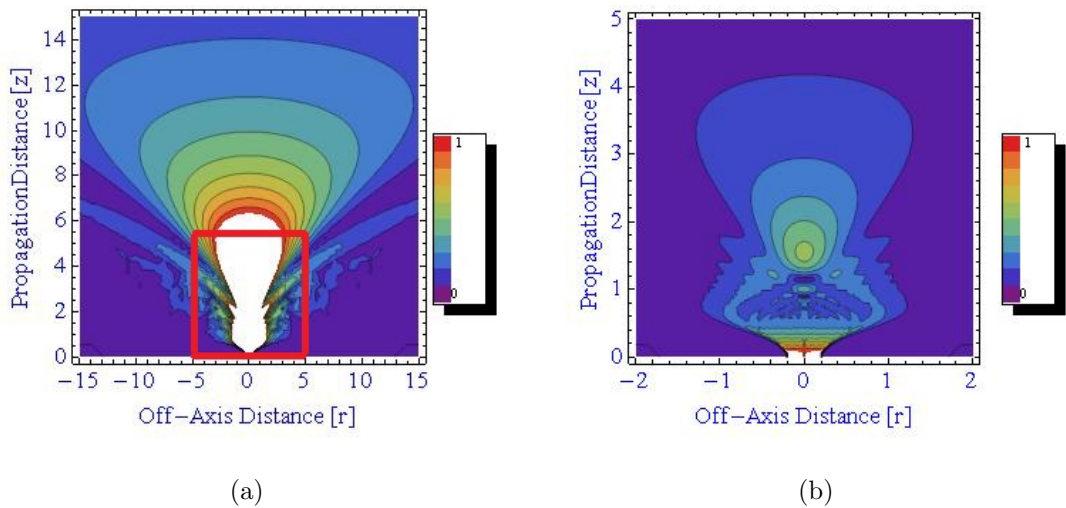


Figure 2.4: Diffraction pattern for increasing propagation distance from a circular aperture. An expanded view of the Fresnel region bounded by the red box in (a) is shown in (b). In both plots the colour legend represents electric field intensity. 32 Laguerre-Gauss modes were used.

to be reconstructed as shown in Figure 2.5(a), and the diffraction pattern to be computed at any distance from the aperture. 100 modes ($m = 10, n = 10$) were used for the analysis and the diffraction patterns for three propagation distances are

shown in Figures 2.5(b) to 2.5(d). It is clear that the far-field (Fraunhofer region) has been reached by $z = \frac{2a^2}{\lambda}$ as the sinc profile is clearly visible through the x and y centres in Figure 2.5(d). Figure 2.6 shows contour plots, illustrating how the electric field varies rapidly in the near-field before settling down in the far-field.

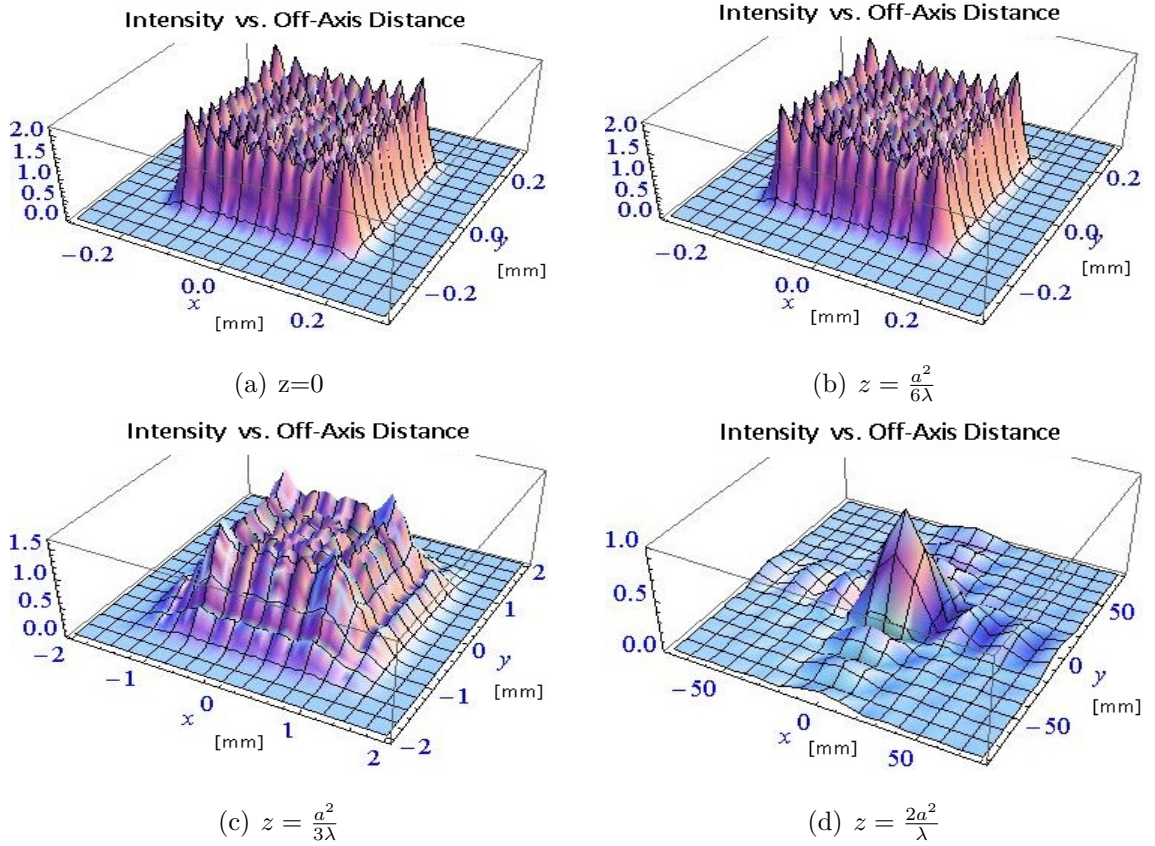


Figure 2.5: Diffraction patterns for various propagation distances from a rectangular aperture. 100 modes were used in the analysis.

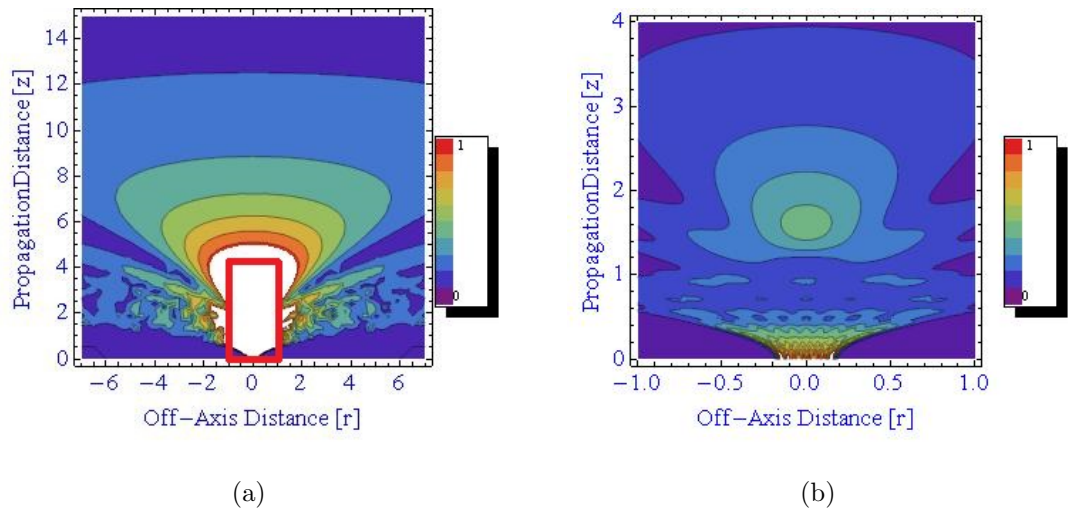


Figure 2.6: Diffraction pattern of electric field intensity for increasing propagation distance from a square aperture. An expanded view of the Fresnel region bounded by the red box in (a) is shown in (b). 100 modes were used.

2.2.3 Gaussian Beam Mode Analysis of EM Horns and Waveguides

The field at the aperture of a corrugated conical horn antenna can be approximated by a circularly symmetric zero order Bessel function [Wylde and Martin, 1993] as $|E(r)| \propto J_0(kr)$ for $r \leq a$, where $k = \frac{2.405}{a}$, a is the radius of the horn aperture, and J_0 is a zero order Bessel function of the first kind. The first root of such a Bessel function is 2.405; hence the field goes smoothly to zero at the aperture edge ($r = a$). The exact aperture fields of both rectangular and conical horns are discussed in chapters 3 and 4 and are generally calculated with rigorous mode matching calculations. For the current purposes however the Bessel function approximation is sufficient.

Again due to the circular symmetry of the aperture field, the most convenient free space modes to use are Laguerre-Gauss modes, and as always we aim to minimise the number of modes required for the analysis. In this case, because the field is quasi-Gaussian, we maximise the amplitude of the fundamental mode and thus only a few higher order modes are required to make up most the remaining field. This gives $W_0 = 0.6435a$ at the aperture of the horn, leading to a fraction of 0.9792 of the total power in the fundamental mode. For the higher order modes we again carry out overlap integrals to compute the mode coefficients, similar to the integrals used for the uniformly illuminated aperture examples.

$$A_n(W) = \sqrt{\frac{2}{\pi W_0^2}} \int_0^a (E_0 J_0(2.405r) L_n(2\frac{r^2}{W_0^2}) \exp[-\frac{r^2}{W_0^2}] 2\pi r) dr \quad \text{for } n = 1, 2, 3, \dots N \quad (2.8)$$

where E_0 is the amplitude of the aperture field, and N is the desired number of modes.

Table 2.1 shows the coefficients for the first seven modes and the corresponding fraction of power carried by each mode for an example corrugated conical horn with dimensions of $a = 1\text{mm}$, $L = 5\text{mm}$, and $\lambda = 0.5\text{mm}$. A schematic of the horn is shown in Figure 2.7(a).

Figure 2.8 shows the aperture field of the example horn reconstructed using various numbers of Laguerre-Gauss modes. It was determined that using 15 such

L_n	$n = 0$	$n = 1$	$n = 2$	$n = 3$	$n = 4$	$n = 5$	$n = 6$	$n = 7$
A_n	1.1297	-0.0001	-0.1375	-0.0491	0.0224	0.0389	0.0228	0.0002
P_n	0.9792	6.9×10^{-9}	0.0145	0.0019	0.0004	0.0012	0.0004	3.3×10^{-8}

Table 2.1: Electric field and power coefficients of a reconstructed beam from a corrugated conical horn.

modes gave rise to a reconstructed field with 99.9% accuracy.

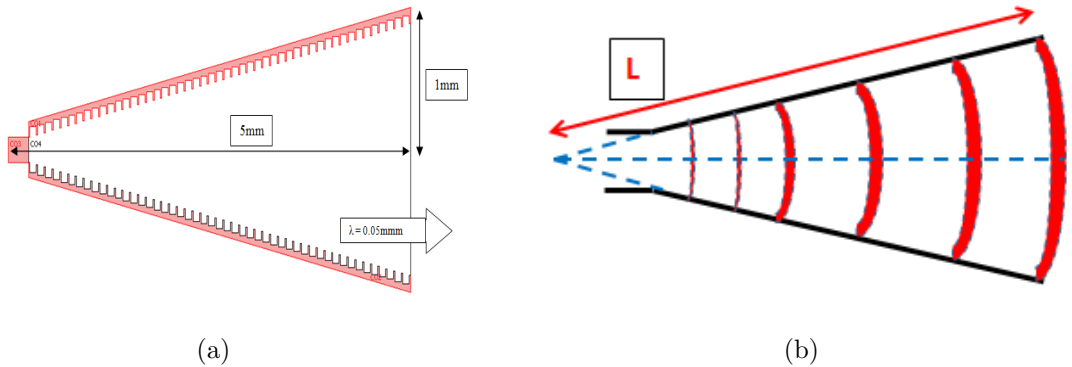


Figure 2.7: (a): Diagram of example corrugated conical horn showing dimensions. (b): Illustration of the equiphase surface of the electric field inside the horn.

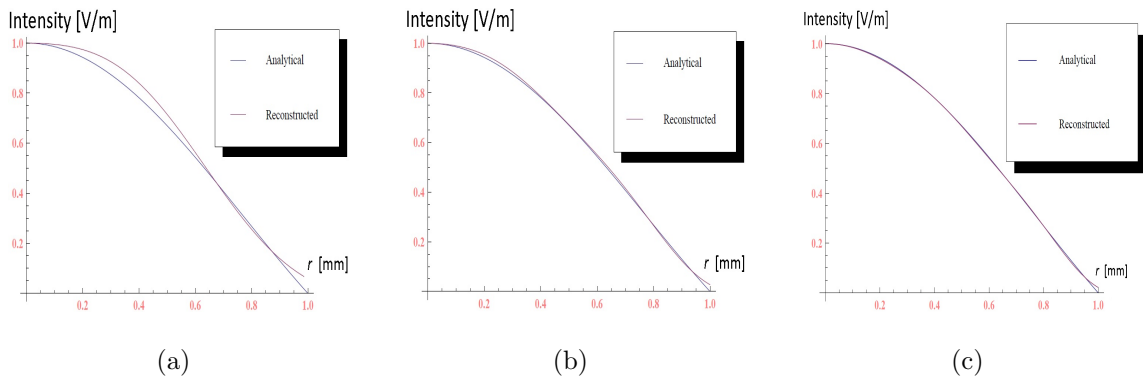


Figure 2.8: Bessel function aperture field and reconstructed aperture field for (a): 5 modes, (b): 10 modes, and (c): 15 modes.

In this example it was assumed that the beam waist and phase centre were positioned at the aperture/mouth of the horn ($z=0$), whereas in reality, the phase centre typically exists inside the horn [Goldsmith, 1998]. According to Goldsmith, for a given conical corrugated horn, both the position of the beam waist z_0 and its radius W_0 can be calculated by two relatively simple equations ((2.9) and (2.10), respectively). Thus, for a corrugated horn with the values of $a = 1\text{mm}$, $L = 5\text{mm}$, and operating at a wavelength of $\lambda = 0.5\text{mm}$, the corresponding values for the position and radius of the waist are: $z_0 = 1.0654\text{mm}$ and $W_0 = 0.5708\text{mm}$. In fact,

as demonstrated by Lucci *et al.*, the position of the phase centre of the horn can be optimised to suit the particular optical system being used [Lucci *et al.*, 2004].

$$z_0 = \frac{L}{1 + \left(\frac{\lambda L}{\pi(0.6435a)^2}\right)^2} \quad (2.9)$$

$$W_0 = \frac{0.6435a}{\sqrt{1 + \left(\frac{\pi(0.6435a)^2}{\lambda L}\right)^2}} \quad (2.10)$$

The near, mid and far-field radiation patterns (in dB) are shown in Figure 2.9 with the normalised patterns also displayed. By comparing Figure 2.9(c) to 2.9(d) it can be seen that the structure of the field does not significantly change over a distance from $z = 10\text{mm}$ to $z = 100\text{mm}$, with only the side-lobes appearing more defined. This indicates that the beam reaches the far-field within 10mm of the aperture. In fact the confocal distance (the distance from the waist at which the edge of the Fresnel region is being approached) is given by $\pi W_0^2/\lambda \approx 2\text{mm}$.

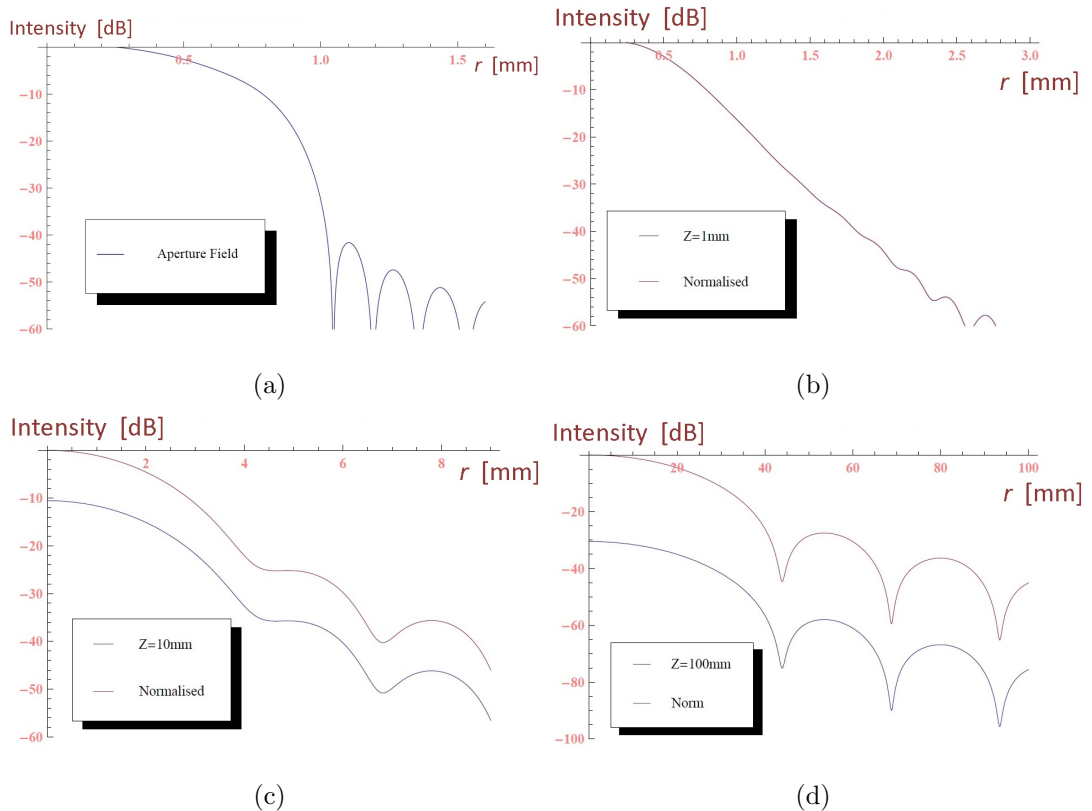


Figure 2.9: Power patterns (in dB) of a corrugated conical horn for various propagation distances. (a): Aperture field, (b): intermediate field, (c): beyond Fresnel region, and (d): far-field.

For other data that is also suited for analysis in polar cylindrical coordinates like the small circular aperture or corrugated conical horn examples above, but without the rotational symmetry that was present in those examples, a higher order

Laguerre-Gauss basis set can be used. The associated Laguerre-Gauss mode basis set L_n^α , appropriate for decomposition of fields that are not rotationally symmetric are similar to the Laguerre-Gauss modes L_n described above, but they also have azimuthal dependence governed by the order α in the superscript of L_n^α . In fact the case of the rotationally symmetric Laguerre-Gauss mode set can be considered as a special case of the more general associated Laguerre-Gauss mode set, where it is the associated Laguerre polynomial of order 0 that is used (L_n^0). The description of these free-space associated Laguerre-Gauss modes is as follows [Trappe *et al.*, 2005]:

$$\vec{\Psi}_m^\alpha(W, R, r, \phi, z) = \psi_m^\alpha(W, R, r, \phi) \exp(-ikz + i\phi_{m,\alpha}(z)) \left[\begin{matrix} \cos \alpha\phi \\ -\sin \alpha\phi \end{matrix} \right] \hat{\mathbf{i}} \pm \left[\begin{matrix} \sin \alpha\phi \\ \cos \alpha\phi \end{matrix} \right] \hat{\mathbf{j}} \quad (2.11)$$

where

$$\psi_m^\alpha(W, R, r, \phi) = \sqrt{\frac{2m!}{\pi W^2(m+\alpha)!}} \exp\left(\frac{-r^2}{W^2}\right) \left(\frac{2r^2}{W^2}\right)^{\frac{\alpha}{2}} L_m^\alpha(2r^2/W^2) \exp(-ik(r^2/2R)).$$

Such a basis set, 2.11, is well suited for the decomposition, reconstruction, and propagation of smooth walled conical horn aperture fields such as those presented in chapter 4 of this thesis. Even though smooth walled conical horn structures have rotationally symmetric apertures (generally), the fields at the horn apertures (TE_{11} mode for example) are typically asymmetric due to the different boundary conditions in the E-plane and H-plane. Of course this can be overcome by introducing carefully designed step discontinuities or change in flare angles in order to excite higher order modes (typically the TM_{11}) so that mode-mixing can build symmetry in the aperture field. Of course profiled corrugated horns can also produce symmetric fields, as demonstrated by Ade *et al.*, for example, when designing the ultra-Gaussian feed horns for the CLOVER experiment [Ade *et al.*, 2009]. Examples of EM field analysis with associated Laguerre-Gauss modes applied to multi-moded structures are presented in section 5.4.1 of chapter 5. As is shown in that section, this type of analysis is required for modelling part of the SAFARI pixel with mode matching techniques.

As an example here, the TE_{11} mode that is present at the aperture of a cylindrical waveguide feed, such as the guide that feeds the SAFARI L-Band detectors is now decomposed using the free-space associated Laguerre-Gauss mode sets $\vec{\Psi}_n^0$ to $\vec{\Psi}_n^6$ for $n = 0$ to $n = 40$. The waveguide that was modelled was given a radius of 1mm, the wavelength of radiation was set to 2mm ($f = 150\text{GHz}$), and the opti-

imum beam waist radius was found to be 1.65mm. The technique for calculating the mode coefficients is the same as in the previous examples, where overlap integrals are calculated for the waveguide aperture field with each of the free-space modes. Of course in this case the coefficients must be worked out for each mode of radial degree n and azimuthal order α . The first ten values for each azimuthal order are shown in Table 2.2.

A_n^α	$\alpha = 0$	$\alpha = 1$	$\alpha = 2$	$\alpha = 3$	$\alpha = 4$	$\alpha = 5$	$\alpha = 6$
$n = 0$	1.0908	0	0.3592	0	0	0	0
$n = 1$	0.3530	0	0.3821	0	0	0	0
$n = 2$	0.0096	0	0.3177	0	0	0	0
$n = 3$	0.1109	0	0.2279	0	0	0	0
$n = 4$	0.1178	0	0.1439	0	0	0	0
$n = 5$	0.0771	0	0.0794	0	0	0	0
$n = 6$	0.0261	0	0.0378	0	0	0	0
$n = 7$	0.0163	0	0.0170	0	0	0	0
$n = 8$	0.0431	0	0.0123	0	0	0	0
$n = 9$	0.0539	0	0.0184	0	0	0	0

Table 2.2: Coefficients of for the first 10 radial modes of various azimuthal order for decomposed cylindrical waveguide aperture field.

What is clear from Table 2.2 is that the TE_{11} waveguide mode only couples to the $\vec{\Psi}_n^0$ and $\vec{\Psi}_n^2$ free-space associated Laguerre-Gauss modes. This is simply due to the orthogonality of the modes in azimuthal dependence α , [Trappe *et al.*, 2005]. This property of the associated Laguerre-Gauss modes is very useful as it significantly reduces the number of calculations that are required for analysing the free-space propagation of the fields from multi-moded systems (see section 5.4.1 of chapter 5).

Figure 2.10(a) shows the reconstructed waveguide aperture field for 5 $\vec{\Psi}_n^0$ and 5 $\vec{\Psi}_n^2$ modes with visible differences in the data compared to the original field, which is shown for comparison. Figure 2.10(b) then shows the reconstructed waveguide aperture field for 20 $\vec{\Psi}_n^0$ and 20 $\vec{\Psi}_n^2$ modes with much better agreement now clearly displayed. Accepting this as verification that the correct mode descriptions were defined in the code, the modes were then propagated to the far-field by simply entering

a large value for the propagation distance z . The modes were then linearly summed in the usual manner and the resulting far-field patterns are shown in Figure 2.11. A FEM analysis of a similar model was carried out using COMSOL for comparison, and the FEM results are also shown in Figure 2.11. Although there is reasonable agreement in the general trend of the curves, there are some differences that require explanation.

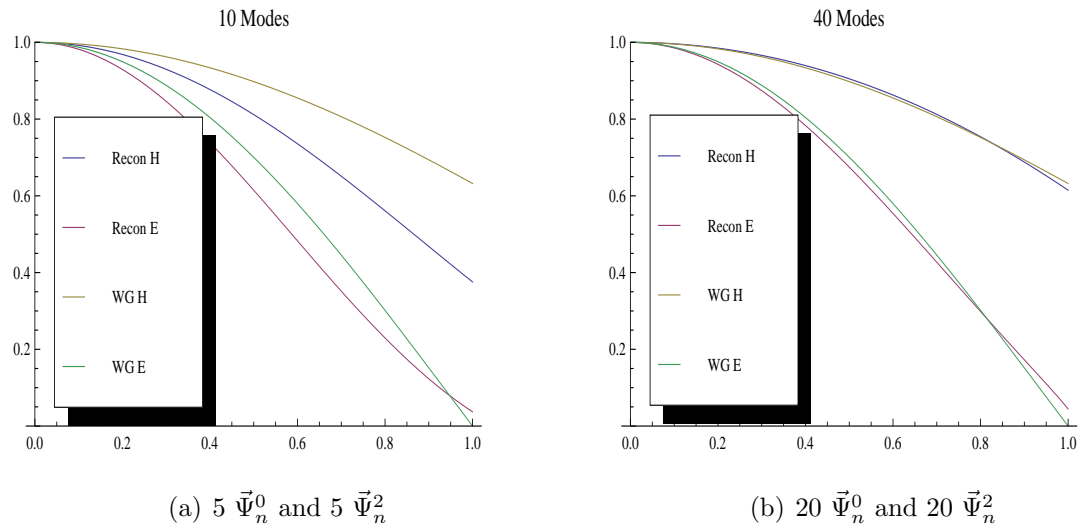


Figure 2.10: Reconstructed aperture field of a cylindrical waveguide for (a): 10 modes, (b): 40 modes.

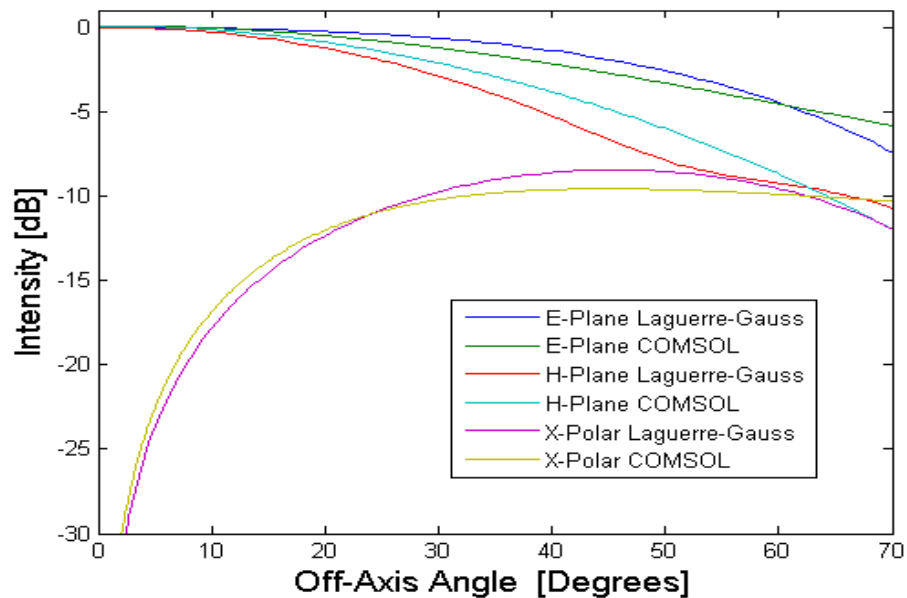


Figure 2.11: Far-field radiation patterns of a cylindrical waveguide using 40 free-space associated Laguerre-Gauss modes. Cuts are shown through $\phi = 0^\circ$ (E-Plane), $\phi = 90^\circ$ (H-Plane), and the cross-polar computed across the $\phi = 45^\circ$ plane.

The main reason for the differences in Figure 2.11 is based on the fact that the COMSOL model includes the effects of the domain around the aperture of

the waveguide, whereas the modal analysis neglects the behaviour of the fields in that domain. The COMSOL results will vary depending on whether the waveguide aperture is surrounded by a conducting ground plane or simply free-space, and in this case a conducting ground plane was used in the simulations. The effects of including such a ground plane in the FEM models is explained in detail in section 3.1.6 with more examples presented, and, as will be shown, the effect of including a conducting ground plane at the aperture of a radiating structure is only significant for a uniform waveguide. For this reason a smooth walled conical horn antenna was also modelled with the free-space associated Laguerre-Gauss modes for verification of the code. Since a ground plane has no significant effect on the radiation patterns of such a feed, better agreement between the FEM approach and modal approach was expected.

The conical horn was given a length of 3mm, an exit aperture of diameter 1mm, and an entry aperture of diameter 0.25mm, leading to a half angle of 7.2° . Due to the small entrance aperture the frequency was set to 600GHz to allow the fundamental mode to propagate through the horn. Figure 2.12 shows the far-field calculation that was achieved using 40 free-space modes with a beam waist of 1.8mm. The results of a similar simulation performed using the FEM approach with COMSOL (FEM approach to be introduced in section 2.5) are shown for comparison. As can be seen there is reasonably good agreement for the two approaches in both co-polar planes and the cross-polar distribution, thus further verifying the modal code.

The above examples of expanding asymmetric waveguide and horn fields in terms of associated Laguerre-Gauss modes are important because in order to model the full SAFARI-pixels (both S-Band and L-Band) with modal techniques the current version of NUIM's mode matching code SCATTER will need to be extended to include such free-space modes. The reason for this is due to a vacuum gap that must be included in the pixel design to allow sufficient space between the horn array block and the delicate TES detector array chip. This is explained in more detail in chapter 5, and Figure 5.1 can be referred to for an illustration.

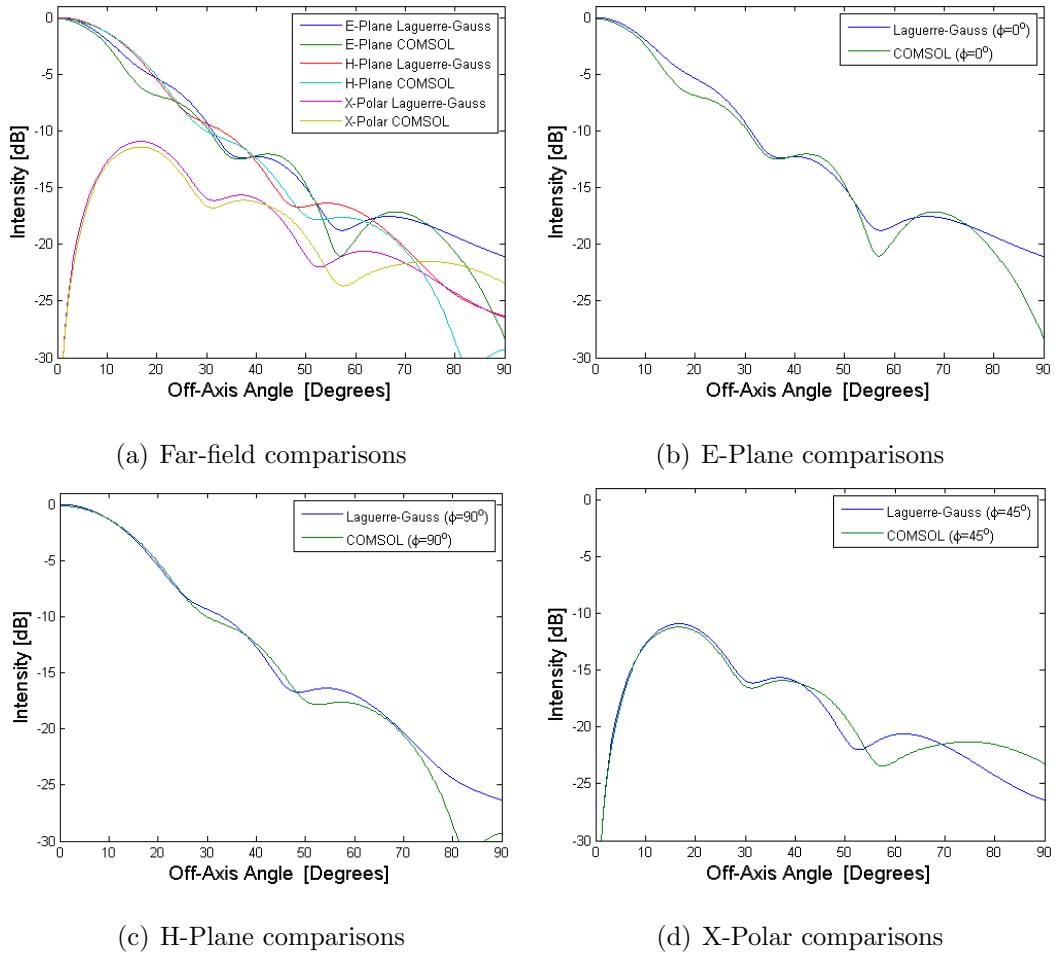


Figure 2.12: Far-field radiation patterns of a smooth walled conical horn antenna computed with 40 associated Laguerre-Gauss free-space modes, and FEM results shown for comparison. (a): All three cuts, (b): E-Plane cut ($\phi = 0^\circ$), (c): H-Plane cut ($\phi = 90^\circ$), and (d): X-Polar cut ($\phi = 45^\circ$).

2.2.4 Propagation Through Quasioptical Systems: Mirrors and Lenses

In the experimental system set up at SRON to probe the multi-mode nature of SAFARI-like horns (see chapter 3) a beam guide system was used to control the free-space propagation of THz beams through a vacuum system. This required the design of a quasi-optical lens based system. We now explain how to model such quasi-optical lens systems using the so-called ABCD matrices from ray optics.

The radius of curvature of a geometrical optics beam R is analogous to the complex beam parameter q of a Gaussian beam, so it is reasonable to assume that the effects of optical components on a Gaussian beam can be analysed in terms of the effects of the corresponding ABCD matrices on the parameter q [Goldsmith, 1998].

$$q_{out} = \frac{A \cdot q_{in} + B}{C \cdot q_{in} + D} \quad (2.12)$$

Furthermore, a single ABCD matrix representing a complete quasioptical system can be constructed by cascading the ABCD matrices representative of each element of the system. The final matrix can then be applied to the complex beam parameter at the input plane, q_{in} , with the result being the complex beam parameter at the output plane, q_{out} . This output complex parameter can then be used to calculate the beam width W , the phase radius of curvature R , and the phase slippage ϕ for each mode at the output plane. From these values the complete field can be reconstructed.

Since the complex beam parameter q is related to the propagation distance z and the confocal distance z_0 through the following relationships:

$$\frac{1}{q_0} = \frac{1}{jz_0} = -j \frac{\lambda}{\pi W_0^2} = -\frac{2}{jkW_0^2} \quad (2.13)$$

and

$$\frac{1}{z + q_0} = \frac{1}{z + jz_0} = \frac{1}{R(z)} - j \frac{\lambda}{\pi W(z)^2} = \frac{1}{q(z)} \quad (2.14)$$

where the definition of the confocal distance was used: $z_0 = \frac{\pi W_0^2}{\lambda}$, then the phase radius of curvature, beam width, and the phase slippage can be expressed as functions of q by the following relationships [Goldsmith, 1998]:

$$R(q) = \left(\text{Re} \left(\frac{1}{q} \right) \right)^{-1} \quad (2.15)$$

$$W(q) = \left(\frac{\lambda}{\pi \text{Im} \left(-\frac{1}{q} \right)} \right)^{1/2} \quad (2.16)$$

$$\phi_{out} - \phi_{in} = \Delta\phi(q) = - \left(\text{Arg} \left(A + B \left(\frac{1}{q_{in}} \right) \right) \right) \quad (2.17)$$

Based on the above definitions the GBM analysis code that was written by the author, and used to model the examples of radiating apertures and feed horns presented earlier in this section, was extended to include analysis of lenses, mirrors, and any other optical components that can be defined by an ABCD matrix. The code requires an initial complex beam parameter as an input, together with the A , B , C , and D values for each optical element that is to be modelled. A piecewise function is then defined to take account of the changing overall matrix as the propagation distance increases, and as more optical elements are encountered by the beam. Each time a new section of free-space or an optical element is encountered, the corresponding matrix is cascaded with the overall matrix up to that point. A graphical

user interface (GUI) was built into the code to allow the user to vary the parameters of the optical elements, for example the positioning or focal lengths of lenses in a system. An example of a system that was modelled with the code is presented in section 3.3, where a three lens focussing system was used in the experimental set-up for measurements of the throughput of a SAFARI-like horn antenna.

2.3 Waveguides

2.3.1 Background

The TE and TM field descriptions of EM waves in waveguide structures were required for multiple simulations as part of the work carried out for this thesis (see chapters 3 and 4). For example the FEM based software COMSOL requires the user to define the field structure of the particular mode to be excited at the input port boundary if symmetry conditions are used to reduce the problem size computationally. Also the sections of mode matching code written by the author required the normalised mode definitions to be defined so that analysis of mode-to-mode scattering could be correctly calculated (see for example chapter 4). The description of how EM fields propagate through conducting waveguide structures can be found in many sources, for example [Olver *et al.*, 1994] and [Clarricoats *et al.*, 1984]. Since the theory is well known, only a basic summary of the modal field descriptions will be outlined in this section, and some example plots of the fields will be shown to demonstrate the validity of the code written by the author. The step-by-step mode derivations are not included since they can be found in most electrical engineering textbooks [Anwane, 2007], for example.

The solutions to Maxwell's equations with PEC boundary conditions can be classified into different groups, depending on whether the electric and magnetic fields have zero or non-zero longitudinal components. The possible mode types are listed in the table below.

Electric Field	Magnetic Field	Mode Notation
$E_z = 0$	$H_z \neq 0$	TE (Transverse Electric)
$E_z \neq 0$	$H_z = 0$	TM (Transverse Magnetic)
$E_z = 0$	$H_z = 0$	TEM (Transverse Electromagnetic)
$E_z \neq 0$	$H_z \neq 0$	HE or EH (Hybrid Modes)

Table 2.3: Definitions and notation of waveguide fields.

2.3.2 Rectangular Waveguide

Excluding the case of TEM modes as they do not exist as harmonic modes of a waveguide, and excluding HE and EH modes as they can be considered as combinations of TE and TM modes, the Cartesian components of the possible transverse modes in a rectangular waveguide are listed in Table 2.4. The rectangular waveguide has width a in the x direction, and height b in the y direction. The m and n values describe the order of the TE_{mn} modes. β is the propagation constant and it is related to the free-space wavenumber k , and the waveguide wavenumber γ by $k^2 = k_c^2 - \gamma^2$, where $\gamma = j\beta$ and k_c is the cut-off wavenumber [Clarricoats *et al.*, 1984] (although slightly different notation is used in the referenced text). $Z_{\text{TE}} = Z \frac{\omega}{\beta c}$ and $Z_{\text{TM}} = Z \frac{\beta c}{\omega}$, where Z is the impedance of free space ($\approx 377\Omega$). Finally, ω is the angular frequency of radiation ($\omega = 2\pi f$).

TE Modes	TM Modes
$E_x = Z_{\text{TE}} \frac{j\beta}{k_c^2} \frac{n\pi}{b} \left(\cos \frac{m\pi x}{a} \sin \frac{n\pi y}{b} \right) e^{j\alpha}$	$E_x = -\frac{j\beta}{k_c^2} \frac{m\pi}{a} \left(\cos \frac{m\pi x}{a} \sin \frac{n\pi y}{b} \right) e^{j\alpha}$
$E_y = -Z_{\text{TE}} \frac{j\beta}{k_c^2} \frac{m\pi}{a} \left(\sin \frac{m\pi x}{a} \cos \frac{n\pi y}{b} \right) e^{j\alpha}$	$E_y = -\frac{j\beta}{k_c^2} \frac{n\pi}{b} \left(\sin \frac{m\pi x}{a} \cos \frac{n\pi y}{b} \right) e^{j\alpha}$
$E_z = 0$	$E_z = \left(\sin \frac{m\pi x}{a} \sin \frac{n\pi y}{b} \right) e^{j\alpha}$
$H_x = \frac{j\beta}{k_c^2} \frac{m\pi}{a} \left(\sin \frac{m\pi x}{a} \cos \frac{n\pi y}{b} \right) e^{j\alpha}$	$H_x = \frac{1}{Z_{\text{TM}}} \frac{j\beta}{k_c^2} \frac{n\pi}{b} \left(\sin \frac{m\pi x}{a} \cos \frac{n\pi y}{b} \right) e^{j\alpha}$
$H_y = \frac{j\beta}{k_c^2} \frac{n\pi}{b} \left(\cos \frac{m\pi x}{a} \sin \frac{n\pi y}{b} \right) e^{j\alpha}$	$H_y = -\frac{1}{Z_{\text{TM}}} \frac{j\beta}{k_c^2} \frac{m\pi}{a} \left(\cos \frac{m\pi x}{a} \sin \frac{n\pi y}{b} \right) e^{j\alpha}$
$H_z = \left(\cos \frac{m\pi x}{a} \cos \frac{n\pi y}{b} \right) e^{j\alpha}$	$H_z = 0$

Table 2.4: Mode expressions in a rectangular waveguide where $\alpha = (\omega t - \beta z)$.

Figure 2.13(a) shows the lowest order TE mode for a rectangular waveguide of width $a = 30\mu\text{m}$ and height $b = 15\mu\text{m}$, operating at a frequency of 5THz. Some higher order propagating modes are also shown in Figure 2.13(b) - 2.13(f), where the

frequency was increased for each simulation to ensure it was above cut-off frequency for each mode ($\nu = 29\text{THz}$ for TE_{42} for example). Figure 2.14(a) shows the lowest order TM mode for the same rectangular waveguide of width $a = 30\mu\text{m}$ and height $a = 15\mu\text{m}$. Some higher order propagating TM modes are also shown in Figure 2.14(b) - 2.14(f).

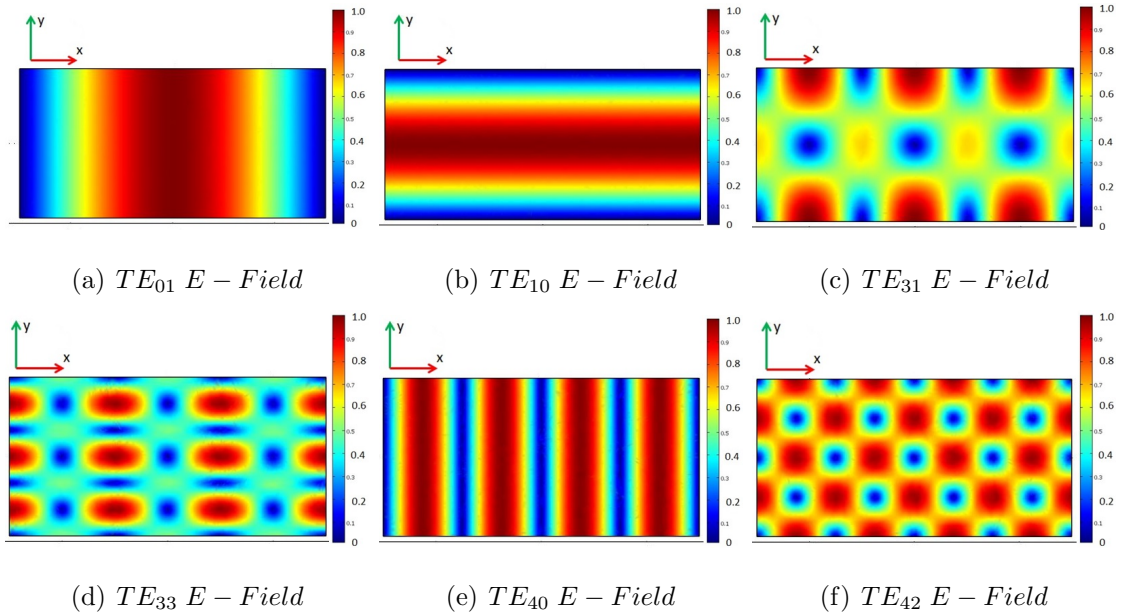


Figure 2.13: Plots of electric field intensity for TE modes of a rectangular waveguide of width $a = 30\mu\text{m}$ and height $a = 15\mu\text{m}$. (a): TE_{10} , (b): TE_{01} (c): TE_{31} (d): TE_{33} (e): TE_{40} (f): TE_{42}

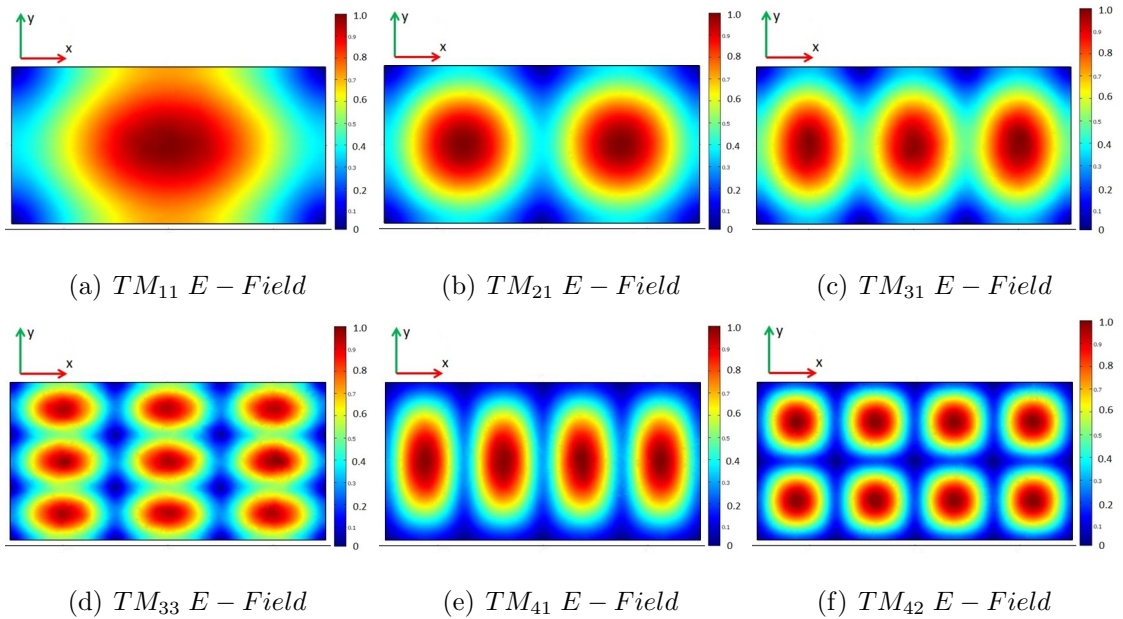


Figure 2.14: Plots of electric field intensity for TM modes of a rectangular waveguide of width $a = 30\mu\text{m}$ and height $a = 15\mu\text{m}$. (a): TM_{11} , (b): TM_{21} (c): TM_{31} (d): TM_{33} (e): TM_{41} (f): TM_{42}

2.3.3 Cylindrical Waveguide

The components of the transverse modes that can exist in a cylindrical waveguide are listed in Table 2.5. The $p'_{\nu l}$ values in the TE mode descriptions correspond to the ν^{th} roots of the derivative of the l^{th} order Bessel functions. The $p_{\nu l}$ values in the TM mode descriptions correspond to the ν^{th} roots of the l^{th} order Bessel functions. For the lowest order mode which is the TE_{11} mode, ($\nu = 1$ and $l = 1$), $p'_{11} = 1.8412$, and for the lowest order TM mode (TM_{11}) $p_{11} = 2.405$. The roots of Bessel functions and their derivatives corresponding to higher modes can be found widely in the literature, for example [Beattie, 1958]. All other symbols (β , k_c , etc.) have the same definitions as for the rectangular modes described above. The $\sin(\nu\phi)$, $\cos(\nu\phi)$, etc. terms in the mode descriptions in Table 2.5 represent two separate polarizations of the fields.

TE Modes	TM Modes
$E_r = Z_{TE} \frac{j\beta\nu}{k_c^2 r} J_\nu \left(\frac{p'_{\nu l} r}{a} \right) e^{j\alpha} \begin{Bmatrix} -\sin(\nu\phi) \\ \cos(\nu\phi) \end{Bmatrix}$	$E_r = \frac{-j\beta}{k_c^2} \frac{p_{\nu l}}{a} J_\nu' \left(\frac{p_{\nu l} r}{a} \right) e^{j\alpha} \begin{Bmatrix} \cos(\nu\phi) \\ \sin(\nu\phi) \end{Bmatrix}$
$E_\phi = Z_{TE} \frac{j\beta}{k_c^2} \frac{p'_{\nu l}}{a} J_\nu' \left(\frac{p'_{\nu l} r}{a} \right) e^{j\alpha} \begin{Bmatrix} \cos(\nu\phi) \\ \sin(\nu\phi) \end{Bmatrix}$	$E_\phi = \frac{-j\beta\nu}{k_c^2 r} J_\nu \left(\frac{p_{\nu l} r}{a} \right) e^{j\alpha} \begin{Bmatrix} -\sin(\nu\phi) \\ \cos(\nu\phi) \end{Bmatrix}$
$E_z = 0$	$E_z = J_\nu \left(\frac{p_{\nu l} r}{a} \right) e^{j\alpha} \begin{Bmatrix} \cos(\nu\phi) \\ \sin(\nu\phi) \end{Bmatrix}$
$H_r = \frac{-j\beta}{k_c^2} \frac{p'_{\nu l}}{a} J_\nu' \left(\frac{p'_{\nu l} r}{a} \right) e^{j\alpha} \begin{Bmatrix} \cos(\nu\phi) \\ \sin(\nu\phi) \end{Bmatrix}$	$H_r = \frac{1}{Z_{TM}} \frac{j\beta\nu}{k_c^2 r} J_\nu \left(\frac{p_{\nu l} r}{a} \right) e^{j\alpha} \begin{Bmatrix} -\sin(\nu\phi) \\ \cos(\nu\phi) \end{Bmatrix}$
$H_\phi = \frac{j\beta\nu}{k_c^2 r} J_\nu \left(\frac{p'_{\nu l} r}{a} \right) e^{j\alpha} \begin{Bmatrix} -\sin(\nu\phi) \\ \cos(\nu\phi) \end{Bmatrix}$	$H_\phi = -\frac{1}{Z_{TM}} \frac{j\beta}{k_c^2} \frac{p_{\nu l}}{a} J_\nu' \left(\frac{p_{\nu l} r}{a} \right) e^{j\alpha} \begin{Bmatrix} \cos(\nu\phi) \\ \sin(\nu\phi) \end{Bmatrix}$
$H_z = J_\nu \left(\frac{p'_{\nu l} r}{a} \right) e^{j\alpha} \begin{Bmatrix} \cos(\nu\phi) \\ \sin(\nu\phi) \end{Bmatrix}$	$H_z = 0$

Table 2.5: Mode expressions in a cylindrical waveguide where again $\alpha = (\omega t - \beta z)$.

Figure 2.15(a) shows a cross-sectional cut through the lowest order mode (TE_{11}) for a cylindrical waveguide of radius $a = 50\mu\text{m}$, operating at a frequency of 1.8THz which is just above the cut-off frequency of 1.76THz. Figure 2.15(b) shows E-plane and H-plane cuts through the same TE_{11} mode. The electric field intensity for some higher order propagating TE modes is shown plotted in Figure 2.16, where the frequency was increased in each simulation to ensure propagation of the mode (18.4THz for the TE_{54} mode, for example). The electric field intensity for some higher order propagating TM modes is shown plotted in Figure 2.17. Again, the frequency was increased for each simulation to ensure propagation of the mode being analysed (19.9THz for the TM_{54} mode, for example).

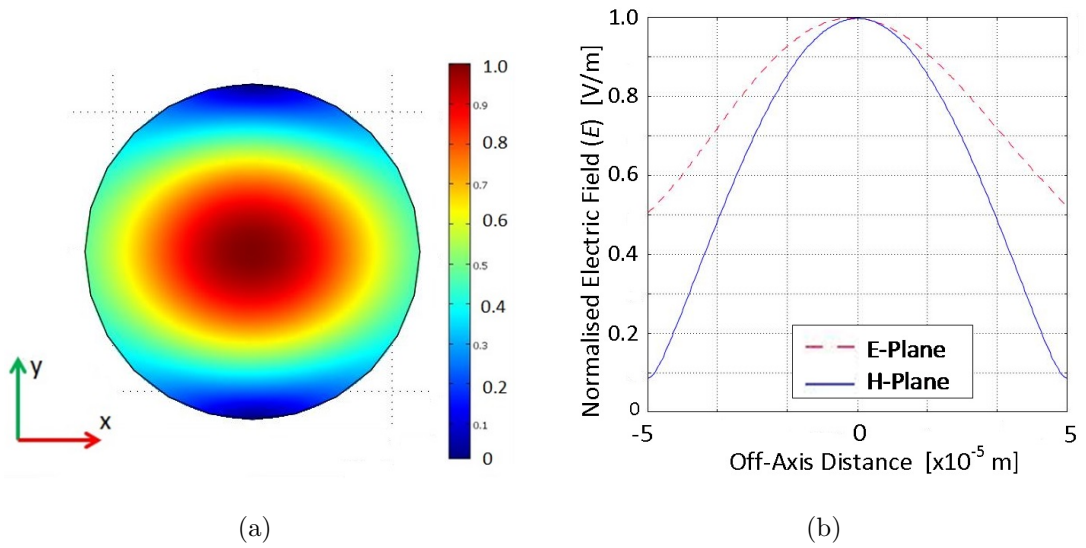


Figure 2.15: Plots of TE_{11} electric field intensity for a cylindrical waveguide of radius $a = 60\mu\text{m}$. (a): 2D planar slice plot, and (b): 1D cuts through E and H-planes.

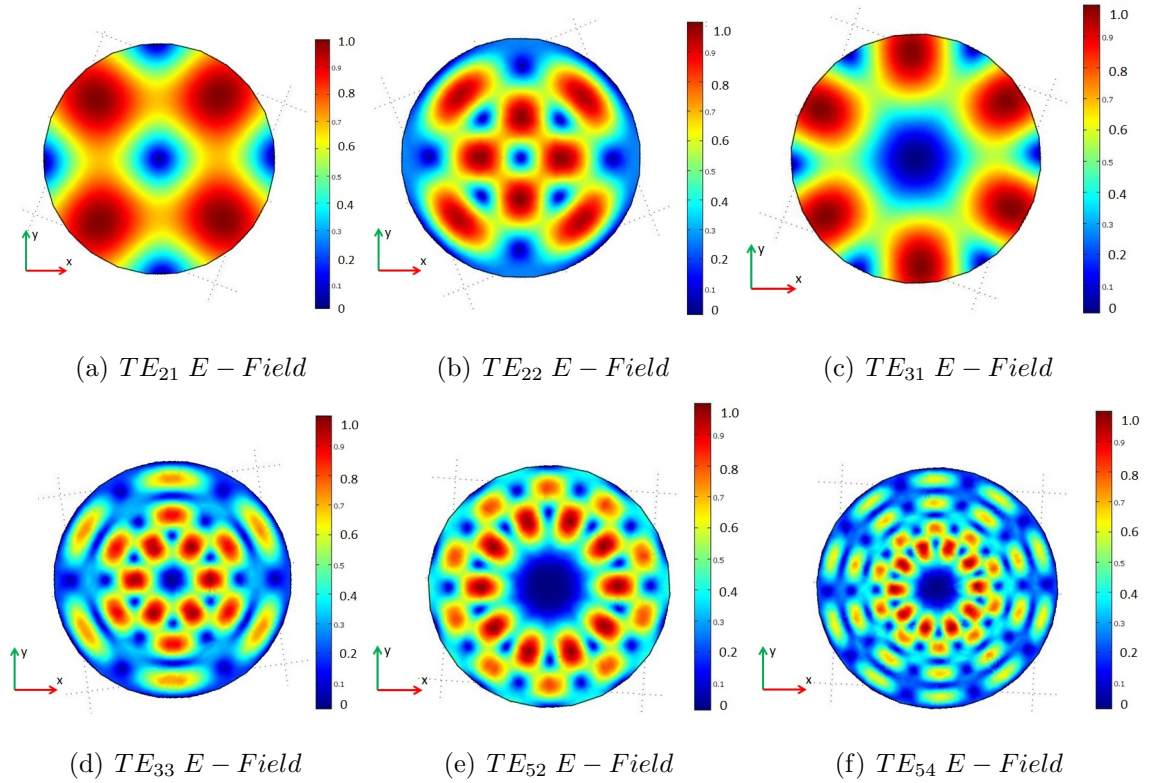


Figure 2.16: Plots of electric field intensity for higher order TE modes of a cylindrical waveguide of radius $a = 6\mu\text{m}$. (a): TE_{21} , (b): TE_{22} (c): TE_{31} (d): TE_{33} (e): TE_{52} (f): TE_{54} .

As was already indicated, the theory presented in this section is widely accessible in the literature [Olver *et al.*, 1994], [Clarricoats *et al.*, 1984]. The simulation work presented throughout this thesis (chapters 3, 4 and 5) required code to be written that was capable of modelling the modal fields, thus the mode descriptions were required to be defined computationally. In contrast to the readily available

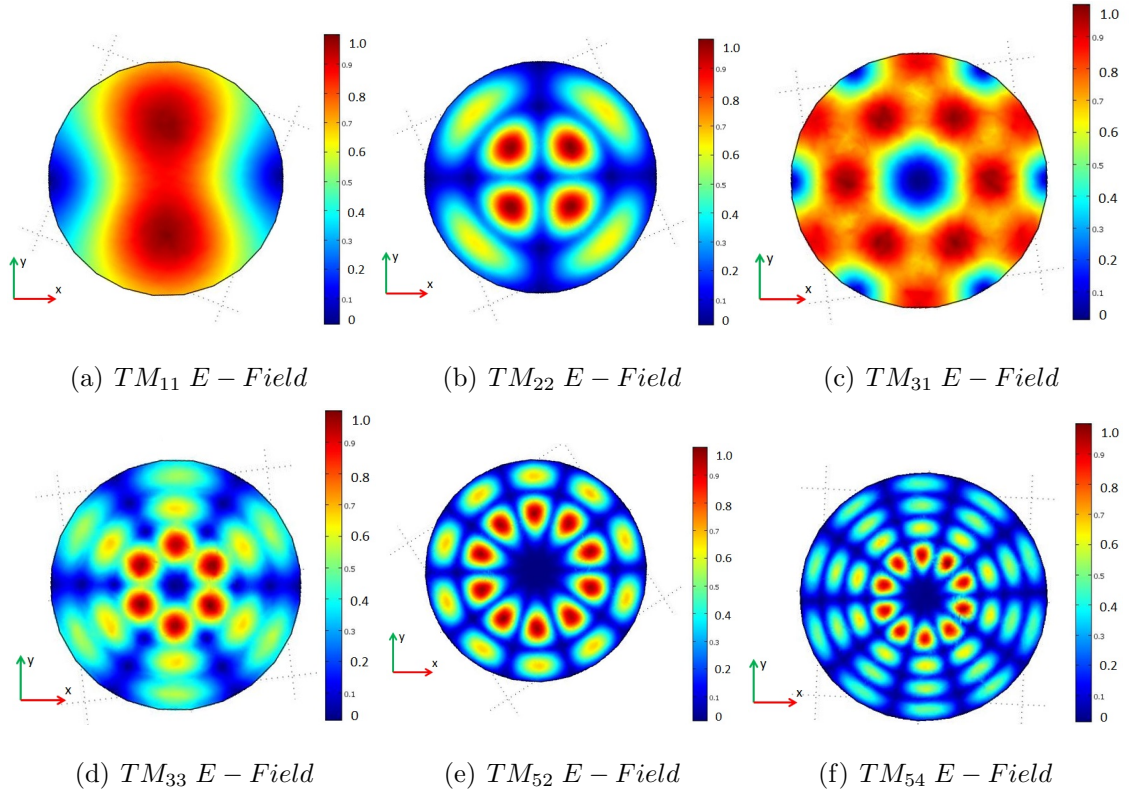


Figure 2.17: Plots of electric field intensity for higher order TM modes of a cylindrical waveguide of radius $a = 6\mu\text{m}$. (a): TM_{11} , (b): TM_{22} (c): TM_{31} (d): TM_{33} (e): TM_{52} (f): TM_{54} .

rectangular and cylindrical coordinate solutions, conical mode solutions were much harder to find in the literature. Thus, conical EM modes are derived in chapter 4.

2.4 Electromagnetic Mode Matching

2.4.1 Background

In the mode matching technique a corrugated or profiled waveguide structure is regarded as a sequence of short uniform waveguide segments which step in radius (cylindrical) or width and height (rectangular) at the junctions between the segments. For each segment the natural modes of propagation are the usual TE and TM modes of a uniform waveguide, and the mathematical description of such fields for both polar cylindrical and Cartesian geometries were presented in section 2.3 of this chapter. The theory of EM mode matching is already well established and it is described in detail in many texts [Olver *et al.*, 1994], [Clarricoats *et al.*, 1984]. NUIM has a strong heritage in the subject of mode matching, where previous graduate students have developed code that is suited for modelling conical feed horn

structures, both smooth walled and corrugated [Gleeson, 2004], [Colgen, 2001]. The result was a highly efficient simulation tool called Cylindrical SCATTER, and it has been used to model complex horn structures such as the HIFI (High Frequency Instrument) horns on the Planck observatory [Murphy *et al.*, 2010]. More recently a Cartesian based mode matching code was written [Doherty, 2012] that is suited to modelling the behaviour of smooth walled or corrugated rectangular horns, and is flexible enough to account for both straight or profiled geometries.

The topic of EM mode matching is introduced here as it is used throughout this thesis as a means of comparing results with other simulation methods such as the FEM approach. Also, the author was involved in verifying a new section of cylindrical mode matching code that was developed with the aim of including cavity mounted absorbers in the models. This work is discussed in chapter 5. The mode matching theory was then extended further by the author through the development of a new mode matching program. The new Spherical SCATTER code was aimed at modelling smooth walled conic section horns in a more exact way compared to Cylindrical SCATTER. It was also aimed at increasing the computational speed at which conical horn can be modelled. Work pertaining to conical modes and Spherical SCATTER is presented in chapter 4.

Figure 2.18 shows an example of a typical EM feed horn structure that is ideally suited for analysis with the mode matching technique. It is a profiled “super-Gaussian” corrugated feed horn from the CLOVER instrument [Ade *et al.*, 2009], and due to the many small corrugations throughout its geometry, modelling such a structure with the FEM, for example, proves very computationally demanding. The tiny mesh that is required for a FEM simulation, in order to correctly map the sub-wavelength corrugations, results in a huge number of degrees of freedom, and thus a large problem size. The mode matching approach is a much more efficient simulation tool for such problems due to the well behaved fields in each uniform section, and the cylindrical symmetry of the overall structure. Figure 2.19 shows the far-field radiation patterns for the CLOVER horn, calculated with the mode matching code SCATTER, and with FEM software COMSOL.

The FEM approach required just over four hours to calculate the radiation patterns, compared to just 10.5 minutes for the mode matching method. Clearly, mode matching is hugely advantageous over FEM techniques when dealing with

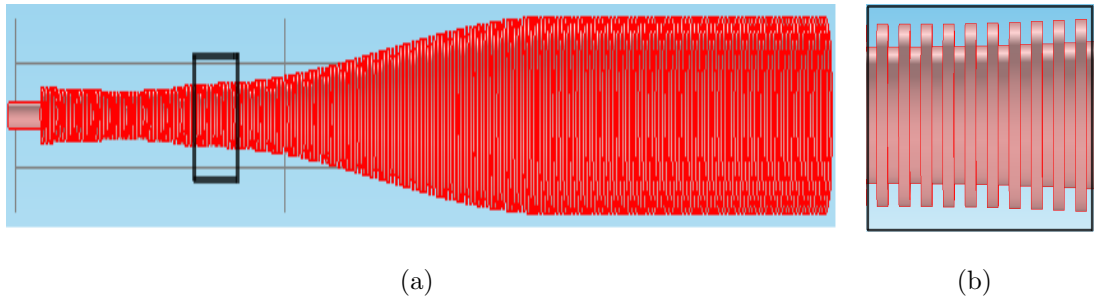


Figure 2.18: FEM screen-shot of CLOVER profiled corrugated horn. (a): Full Horn, (b): Zoomed view of section highlighted in (a) by black box.

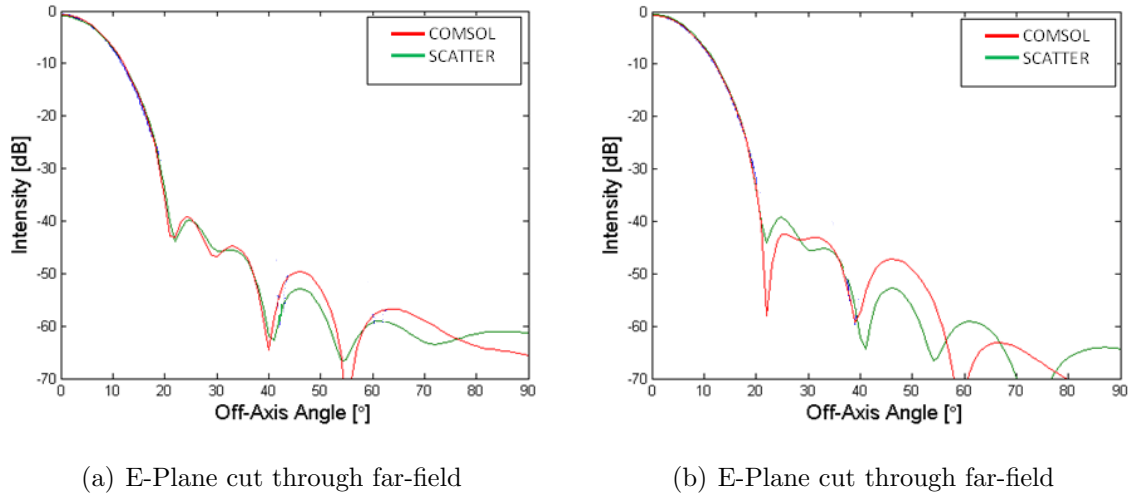


Figure 2.19: Far-field radiation patterns of a corrugated feed horn at an operational frequency of 100GHz.

structures with high symmetry such as the CLOVER horn. However, when the structure to be modelled is lacking such symmetry then other techniques (such as FEM) will clearly be required. The following section (2.5) presents a brief description of the FEM method, with an example model described to illustrate the approach.

2.5 Finite Element Method: COMSOL Multiphysics

2.5.1 Background

The FEM technique is a numerical analysis approach used by many commercially available software packages for modelling a range of science and engineering problems. COMSOL Multiphysics uses the FEM approach and any FEM analysis that is presented in this thesis was carried out with the COMSOL Multiphysics package. The main benefit of using the FEM approach is its versatility in terms of the types

of problems that can be modelled with it.

While some progress is being made in terms of combining waveguide and free-space techniques, as presented in chapter 5 of this thesis, the FEM approach allows more complex models with multiple sub-domains, each with different boundary conditions, to be solved. There is also virtually no restriction on the shape of the problem domain. There is of course the disadvantage that the FEM approach is relatively inefficient, and compared to waveguide and free-space modal techniques, FEM typically has computation times that are orders of magnitude larger.

The FEM approach is based on finding approximate solutions to boundary value problems for differential equations, for example Maxwell's equations for EM field calculations. FEM employs variational methods to produce a stable solution by minimizing an error function. Similar to the way a circle can be approximated by a series of small straight connected lines, a problem domain Ω can be broken into many smaller elements Ω^e and then reconnected through nodes as shown in Figure 2.20. There are a number of different mesh types available with COMSOL but the most commonly used is a tetrahedral mesh in the 3D modelling environment, and a triangular mesh in the 2D environment (shown in Figure 2.20).

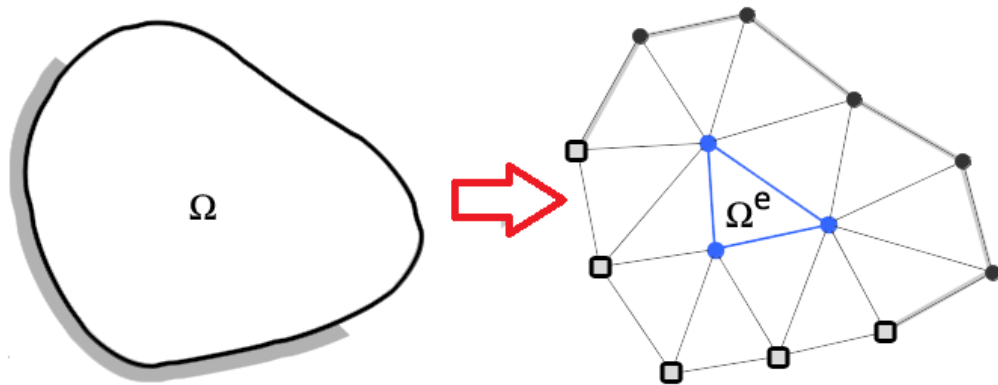


Figure 2.20: Triangular mesh that is used to approximate a problem domain.

The PDEs (partial differential equations) that describe the nature of the problem must then be discretised over the meshed problem domain. The manner in which Maxwell's equations are handled by COMSOL is now described as an example of the general COMSOL FEM approach. Assuming harmonic time dependence

($e^{j\omega t}$) Maxwell's equations can be written as:

$$\begin{aligned}
\vec{D} &= \epsilon'_r \epsilon_0 \vec{E} \\
\vec{B} &= \mu_r \mu_0 \vec{H} \\
\vec{\nabla} \times \vec{E} &= -j\omega \vec{B} \\
\vec{\nabla} \times \vec{H} &= \vec{J}_S + \sigma \vec{E} + j\omega \vec{D}
\end{aligned} \tag{2.18}$$

The vector wave equations for \vec{E} and \vec{H} can then be written as:

$$\begin{aligned}
\vec{\nabla} \times \left(\frac{1}{\mu_r} \vec{\nabla} \times \vec{E} \right) - k_0^2 \epsilon_r \vec{E} &= -jk_0 \eta_0 \vec{J}_S \\
\vec{\nabla} \times \left(\frac{1}{\epsilon_r} \vec{\nabla} \times \vec{H} \right) - k_0^2 \mu_r \vec{H} &= \vec{\nabla} \times \left(\frac{1}{\epsilon_r} \vec{J}_S \right)
\end{aligned} \tag{2.19}$$

where \vec{J}_S is the source current density and $\epsilon_r = \epsilon'_r - j\frac{\sigma}{\omega\epsilon_0}$.

From (2.19) above the weak form [Tio *et al.*, 2004] of the vector wave equations can be formulated, which for \vec{E} is:

$$\int_V \frac{1}{\mu_r} \left(\vec{\nabla} \times \vec{E} \right) \cdot \left(\vec{\nabla} \times \vec{W} \right) dV - k_0 \int_V \epsilon_r \vec{E} \cdot \vec{W} dV = -jk_0 \eta_0 \int_V \vec{J}_S \cdot \vec{W} dV \quad \text{for all } \vec{W} \tag{2.20}$$

It is these weak form vector equations that are formulated for each element in the problem domain, resulting in a set of simultaneous equations that must then be solved.

Using COMSOL's built-in meshing functions, the problem domain is broken up into the finite mesh elements, where the number of elements depends on the physics of the problem. For example an EM problem will typically require a minimum of 5 mesh elements per wavelength to reach a solution, however at least 6 mesh elements per wavelength are recommended in the COMSOL literature [COMSOL, 2011] for a reasonably high level of accuracy. An advantage of the FEM approach over other finite analysis techniques, such as the finite difference method for example, is that there is very little restrictions on the type of geometry that the problem domain represents. The finite difference method is limited to rectangular geometries due to the fact that the mesh must be uniform. The mesh of the FEM problem domain can be irregular and take almost any closed form. Care should be taken however of very small sections of a problem domain, ensuring that the mesh size is sufficiently small to map these sections. This is particularly important for EM devices such as corrugated horn structures as the corrugations are typically on scales corresponding to a fraction of a wavelength.

The COMSOL user must specify material properties and boundary conditions for each sub-domain of the overall problem domain, and any scalar variables such as the frequency of radiation to be modelled, etc. must also be defined. The software has multiple built-in solvers, both direct solvers such as PARADISO, SPOOLES, and MUMPS, and iterative solvers such as Conjugate Gradient, GMRES, and FGMRES for example, and COMSOL will usually select the optimum solver based on the chosen space dimension, the physics of the problem and the type of study being carried out, however the user can alternatively select any of the other solvers that are available.

An example FEM model is illustrated in Figure 2.21, where the model was built using the COMSOL Multiphysics computer aided design (CAD) package (Figure 2.21(a)). The TE_{11} mode was excited at the entry port, and a perfectly matched layer was defined at the output port to simulate propagation into free-space. Both ports were given the same dimensions as the WR-10 waveguides that were used in combination with the VNA for measurements described in chapters 3 and 5: $a = 1.27\text{mm}$ and $b = 2.54\text{mm}$. The walls of the structure were defined as being perfect electric conductors (PEC) and a tetrahedral mesh was then defined for the entire geometry, as shown in Figures 2.21(b) and 2.21(c), with an element size of 0.45mm corresponding to $\lambda_{min}/6$, where λ_{min} is the minimum wavelength of the frequency range to be analysed. The time harmonic wave equation ($E \propto e^{i\omega t}$) was then solved for the electric field over the frequency range of the VNA system (75-110GHz) in steps of 1GHz.

COMSOL allows a frequency sweep to be easily performed due to its ability to automatically increment the frequency in user defined steps while saving the solutions for each step. COMSOL also allows similar parametric sweeps for other variables such as changing spatial distances, etc. to be carried out. Figure 2.21(d) shows a screen shot of the COMSOL post-processing environment, where the z component of the electric field is depicted as a raised colour plot. The post-processing module can also be used for evaluating parameters such as the transmitted signal (S_{21}), the return signal (S_{11}), integrated Ohmic losses across a particular surface, etc.

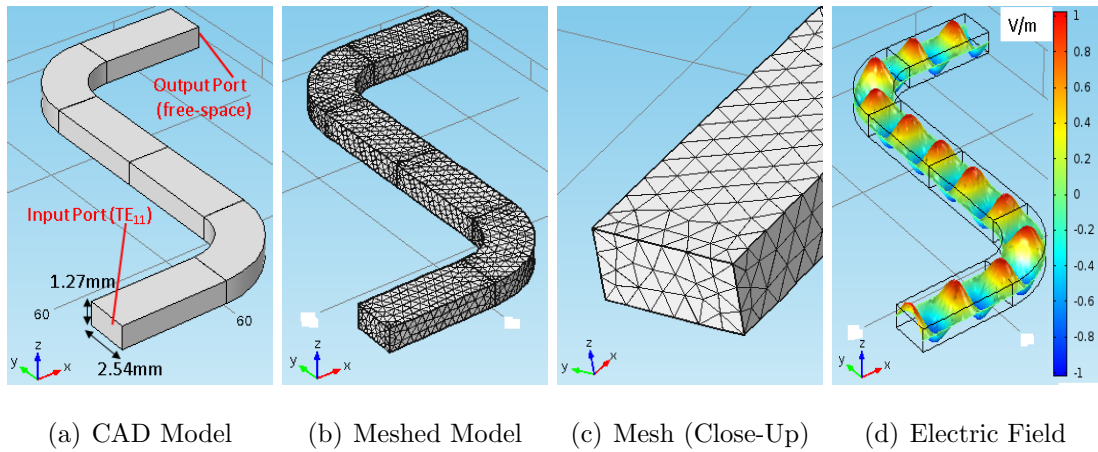


Figure 2.21: Steps in solving a FEM problem.

2.6 Conclusions

In this chapter the computational approaches that were employed for the work presented throughout this thesis were described. The first section 2.2 of the chapter presented methods for modelling free-space propagation of radiation, with examples provided for both Cartesian and polar cylindrical reference frames. GBM analysis provides an efficient means of modelling free-space propagation when dealing with a signal with relatively low divergence, such as that from a horn antenna with shallow flare angle. This limitation is based on the paraxial approximation from which the theory is derived. Relatively good agreement was found for a conical horn antenna with a half angle of 7.2° when compared to a similar FEM model. An alternative approach for modelling fields with significant divergence, and which is not based upon the paraxial approximation, is spherical wave expansion [Olver *et al.*, 1994]. This vector based approach is similar to the scalar GBM analysis in the manner in which the field is decomposed into a basis set of modes. When dealing with radiation with significant beam divergence or horns with large flare angles (low F-number optics) spherical wave expansion would likely be required in place of GBM methods [Clarricoats *et al.*, 1984],[Olver *et al.*, 1994].

In sections 2.3 and 2.4, simulation methods specific to fields in conducting structures (PEC boundaries) were described. The mode matching code SCATTER was shown to be a very efficient tool for modelling corrugated feed horn structures in terms of analysing far-field radiation patterns, throughput, and return power, etc. However, it was explained that SCATTER is relatively limited in terms of the types of problems it can be used to model.

In section 2.5 a description of the FEM approach was given, which is the basis of the commercially available COMSOL Multiphysics package and which was used extensively in the work presented throughout this thesis. FEM was shown to be a versatile simulation tool that is capable of modelling problems relating to both free-space propagation and waveguide propagation, as well as a host of other multiphysics problems. This versatility comes at a cost however, and the approach is relatively inefficient computationally. It was shown that solving a problem with the FEM approach can take orders of magnitude longer than the mode matching approach.

It will be shown throughout this thesis that in order to accurately model the receivers and detectors of far-IR instruments, such as the SAFARI S-Band for example, a combination of the computational approaches presented in this chapter is required. The efficiency of mode matching techniques is essential for SAFARI receivers due to the large electrical size of the structures, and the flexibility of the FEM method is necessary when dealing with asymmetric structures or problems involving multiple sub-domains, where free-space propagation may be required in one sub-domain and PEC boundary conditions may be present in an adjacent sub-domain.

Chapter 3

The Analysis of the SAFARI Multimode Horns

“I hear and I forget.

I see and I remember.

I do and I understand.”

- Confucius

3.1 Rectangular Horns

3.1.1 Background

Smooth walled horns, both conical and rectangular, are becoming increasingly utilised in sub-millimetre and far-IR systems. As we continue to design instruments with feed horn coupling structures for higher operational frequencies the size of the horns and waveguides become increasingly smaller. Manufacturing these feed structures with dimensions on the order of a few microns is proving difficult for the manufacturers, particularly when arrays of such feeds are required. In the true THz regime (approximately 3 to 10 THz) the components typically have dimensions on the order of tens of microns, and building corrugated structures on these scales is simply not possible with current manufacturing techniques. For this reason smooth walled feeds are proving to be the only feasible option.

The current design of the SAFARI horns are two sectioned smooth walled rectangular horns consisting of a short 0.54mm length section with a flare angle of 20° , and a longer 4.84mm section with a softer flare angle of 4.5° (see Figure 3.1 (a)). The horns are sufficiently wide to allow higher order modes to propagate through them and therefore the overall throughput will be increased compared to a single mode horn. However due to both the smooth walled nature of the horns and the fact that they are multi-moded, the quality of the beam patterns will not compare to corrugated conical feeds such as those typically used in CMB experiments. This will not be an issue however since qualities such as high beam symmetry will not be required as the SPICA telescope will not be aimed at performing ultra-sensitive polarisation experiments like those of, say, the Planck CMB telescope.

Extremely low side-lobes are not required either as the focal plane arrays will be contained in an extremely low temperature (dark) area, illuminated only by a pinhole as shown in Figure 3.1 (b) during testing. This means that the side-lobes in the beam patterns of the horns will only “see” a cold baffle. Therefore the side-lobes of the SAFARI horns will essentially only see a cold baffle and will not pick up artefacts that more exposed horns arrays may detect in other telescope systems. The priority of the SAFARI horn design is for maximum throughput which led to the multi-moded design. Each propagating mode is capable of carrying power through the horn and onto the TES detectors, so a multi-moded system allows for

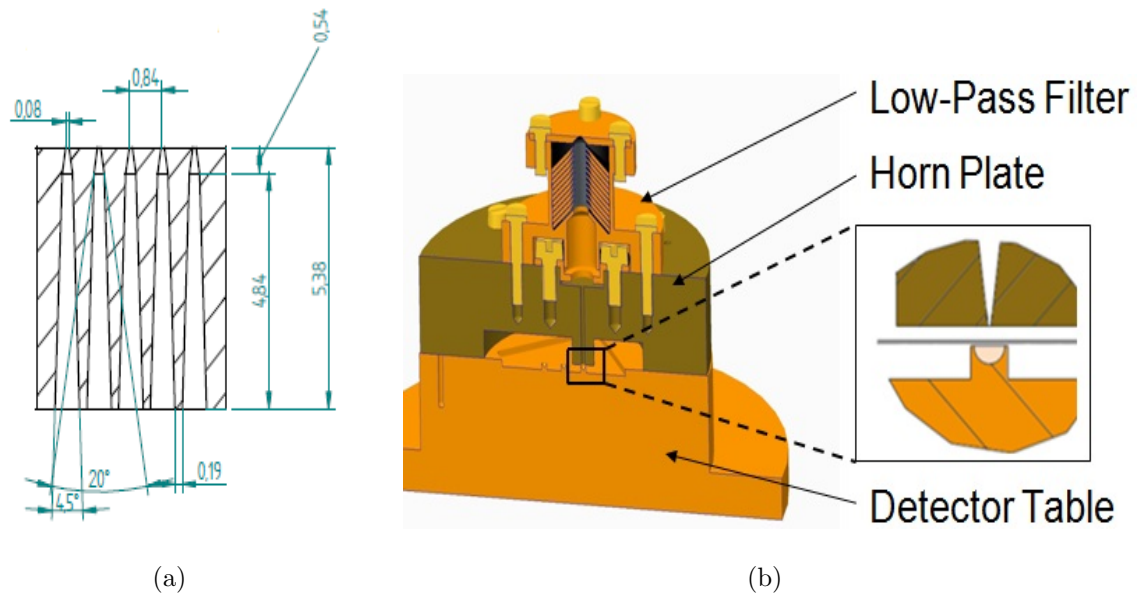


Figure 3.1: (a): Layout of the Safari horn array block showing dimensions and angles. Only five horns from one row are shown (b): Part of the SRON SAFARI testbed for characterising single pixels for the future detector array. A conical horn and hemispherical backshort are shown in the expanded window (image credit: SRON).

a significant increase of total throughput and therefore an increase in sensitivity. Careful design of the smooth walled horn structures can still produce relatively good quality beams in terms of beam symmetry and low side-lobe levels.

In the first section of this chapter various techniques for modelling smooth walled pyramidal horns will be described. The results from the different approaches will be compared to each other and to measurements performed with the VNA facility. Three methods for calculating far-field beam patterns of pyramidal horns will be discussed, and it will be shown that there is excellent agreement between the three approaches. The driving force behind these experiments was to examine how far the simulations could be taken, taking into account aspects of the radiating horns that have thus far not been included in the models. Such progressions in the models include analysis of the fields at the mouth of the horn in order to determine if significant power propagates behind the horn, including a conducting ground plane between horn apertures to examine if induced surface currents can influence the far-field patterns of the horns, and quantifying the levels of optical cross-talk between horns in a SAFARI-like horn array.

As will be demonstrated the best modelling approach for these SAFARI-type horns depends on the particular problem being considered. For example analysis of the far-field radiation patterns at the high operating frequencies of the SAFARI in-

strument requires the rectangular mode matching technique, as EM FEM approaches are simply too inefficient for such electrically large, multi-moded structures. On the other hand if optical cross-talk between horns, or induced surface currents on the horn array block are being investigated, then the FEM approach is required as the current mode matching software is relatively restricted in terms of these broader questions. By employing multiple simulation methods, antenna feed horns such as the current SAFARI design can be accurately modelled in terms of their far-field radiation patterns, and more subtle effects such as optical cross-talk.

3.1.2 Approximate Method

In this section the fields inside, and at the aperture, of smooth walled pyramidal horns are described. The derivation is almost identical to the case of a rectangular waveguide with the inclusion of a phase slippage term to account for the extra distance covered by the field at the horn's sides. The equiphase surface of the field forms a spherical cap (quadratic phase cap) that extends beyond the mouth of the horn. This quadratic approximation works well for horns of small flare angle [Milligan, 2005]. To analytically derive the fields at the mouth of such horns, Maxwell's equations can be solved in spherical coordinates with the appropriate PEC boundary conditions. This method is discussed in section 4.1.2, where the fields inside conical horn structures are derived.

The coordinates and parameters of a typical pyramidal horn are shown in Figure 3.2(a), and Figure 3.2(b) shows the extra distance Δ_L travelled by the fields which results in the quadratic phase error at the aperture. The equiphase surface at the mouth of the horn is shown as a dotted line.

The structure of the field amplitude at the mouth of a rectangular/pyramidal feed horn is defined by the input waveguide mode. The phase distribution is approximately quadratic across the aperture, with each aperture coordinate having a separate quadratic phase distribution constant (R_X and R_Y in this case for the H -plane and E -plane respectively). The constant R_X for the H -plane is formulated as follows:

By applying Pythagoras' theorem to the sides L , $\frac{a}{2}$ and L_X of figure 3.2(b), the length L_X can be defined as $L_X = \sqrt{(L)^2 + (r_a)^2}$, or $L = \sqrt{(L_X)^2 - (\frac{a}{2})^2}$. It is

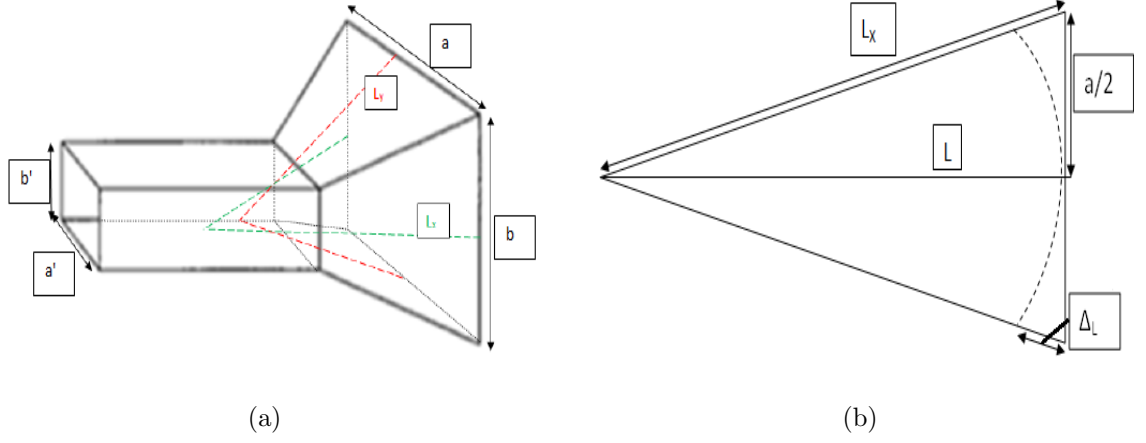


Figure 3.2: Pyramidal horn diagrams showing typical parameters used to describe such horns. (a): Primary horn and waveguide parameters. (b): Illustration of the equiphase surface in the H-plane of the horn.

clear from figure 3.2 that $\Delta_L = L_X - L$, therefore: $\Delta_L = L_X - \sqrt{(L_X)^2 - \left(\frac{a}{2}\right)^2}$

$$\Rightarrow \Delta_L = L_X \left(1 - \sqrt{1 - \frac{(a/2)^2}{(L_X)^2}} \right) \approx L_X \left(1 - \left(1 - \frac{(a/2)^2}{2(L_X)^2} \right) \right) = \frac{a^2}{8L_X} \quad (3.1)$$

$$\Rightarrow \Delta_L = \frac{a^2}{8L_X} \quad (3.2)$$

where Δ_L is the extra distance travelled by a field near the walls of the horn in the H -plane (with respect to the on-axis field). Multiplying both sides of (3.2) by the free-space wavenumber k gives the dimensionless constant R_X of the quadratic phase distribution:

$$\Delta_L k = \frac{ka^2}{8L_X} = R_X \quad (3.3)$$

By applying the same reasoning to the E -plane the dimensionless constant of the quadratic phase distribution for the E -plane was calculated as:

$$\frac{kb^2}{8L_Y} = R_Y \quad (3.4)$$

Using the two constants R_X and R_Y in combination with the definitions for the transverse fields of rectangular waveguides given in section 2.3.2, the aperture fields for pyramidal/rectangular horns can be completely defined. Each field component for both TE and TM modes is defined as the rectangular waveguide field component multiplied by $\exp\left(-j\left[R_X\left(\frac{2x}{a}\right)^2 + R_Y\left(\frac{2y}{b}\right)^2\right]\right)$, for example:

$$E_x = Z_{\text{TE}} \frac{j\beta}{k_c^2} \frac{n\pi}{b} \left(\cos \frac{m\pi x}{a} \sin \frac{n\pi y}{b} \right) \exp(j(\omega t - \beta z)) \exp\left(-j\left[R_X\left(\frac{2x}{a}\right)^2 + R_Y\left(\frac{2y}{b}\right)^2\right]\right).$$

3.1.3 Example Horn (Approximate Method)

The aperture field and far-field distributions are calculated for an example horn with a rectangular waveguide section acting as a mode filter (as for example if a waveguide feeds an integrating cavity) with dimensions such that only the fundamental mode (TE_{10}) can propagate. The waveguide has transverse dimensions of a standard WR-10 guide section, $a' = 2.54\text{mm}$, $b' = 1.27\text{mm}$, and its length is defined as $l = 5\text{mm}$. The horn section has aperture dimensions of $a = 15.08\text{mm}$, and $b = 10.80\text{mm}$, with an axial length of 20.69mm , giving rise to slant lengths of $L_x = 24.88\text{mm}$, and $L_y = 23.06\text{mm}$.

This particular small horn was chosen because its beam pattern can be experimentally measured with the VNA and it is small enough to be modelled through FEM analysis on a reasonably powerful PC. In fact the size of the example horn with respect to the operational wavelength is just within the limits of what can be solved with the FEM technique on a PC with 16 gigabytes of RAM if symmetry conditions are exploited to minimise the problem size. Symmetry conditions are put in place for the E-plane and H-plane of the model resulting in a 75% reduction in the geometry size and therefore a 75% reduction in the number of mesh elements and the number of degrees of freedom.

While there are no limitations on the size of the horn that can be modelled with the approximate method, the FEM approach is limited by the power of the PC being used and the amount of RAM available. The mode matching approach is only limited by the amount of computation time available since it calculates in a stepwise fashion and each section can be calculated independently.

The central operating frequency of the VNA system ($\nu = 100\text{GHz}$) is below the cut-off of any higher order modes. So considering the expressions in Table 2.4 for the x and y components of the fundamental TE mode, where the subscripts 1 and 0 denote that $m = 1$ and $n = 0$, then E_x and E_y can be calculated over a cut through the aperture of the horn by keeping y constant, say at $y = b/2$. Similarly to calculate E_x and E_y through a cut perpendicular to the previous one then the x coordinate should be kept constant, say at $x = a/2$. The magnitude of the total electric field can of course be calculated across either of the aperture cuts by calculating $|\vec{E}| = \sqrt{E_x^2 + E_y^2}$ and keeping either x or y constant.

Now using the two expressions for R_X and R_Y defined in 3.3 and 3.4, and combining all constants such as Z_{TE} , β , etc. that appear in the TE_{10} mode description into one arbitrary amplitude E_0 (since only the general structure of the field is of interest at this point), then the aperture field for the TE_{10} mode of a rectangular horn can be written as:

$$E_y(x, y) = \sin\left(\frac{\pi x}{a}\right) \exp\left(-j\frac{k}{2}\left[\frac{x^2}{L_x} + \frac{y^2}{L_y}\right]\right) \quad (3.5)$$

Equation 3.5 above corresponds to a reference frame where the aperture is defined as going from 0 to a which is the usual convention in textbooks. A similar expression is defined for the aperture field going from $-\frac{a}{2}$ to $\frac{a}{2}$ as:

$$E_y(x, y) = \cos\left(\frac{\pi x}{a}\right) \exp\left(-j\frac{k}{2}\left[\frac{x^2}{L_x} + \frac{y^2}{L_y}\right]\right) \quad (3.6)$$

The far-field radiation pattern can then be calculated from the aperture field by deriving the Fourier transform of either of the two equations 3.5 and 3.6 above. For the case of evaluating the field from $-\frac{a}{2}$ to $\frac{a}{2}$ the result is:

$$E_{FF}(\theta, \phi) = \frac{k}{4\pi r} (1 + \cos\theta) \int_{-\frac{b}{2}}^{\frac{b}{2}} \int_{-\frac{a}{2}}^{\frac{a}{2}} E_{NF}(x, y) \exp[jk(x \sin\theta \cos\phi + y \sin\theta \sin\phi)] dx dy \quad (3.7)$$

Using the expressions just outlined for the aperture field and far-field distributions the following graphs were plotted.

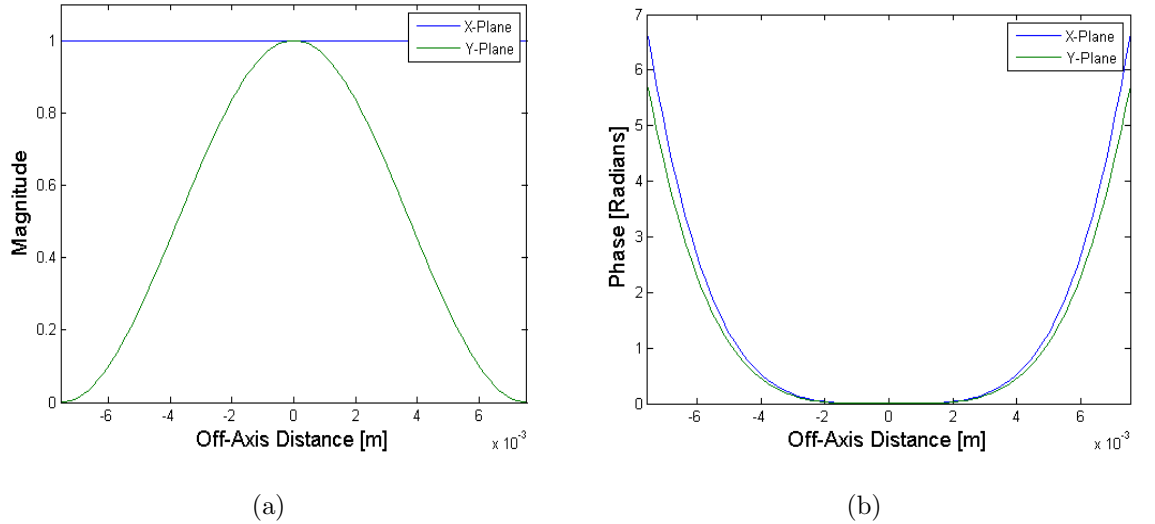


Figure 3.3: Small rectangular VNA horn modelled with approximate theory, where the aperture field phase is approximated as quadratic. (a): The magnitude of the normal electric field across the aperture. (b): The phase of the electric field across the aperture.

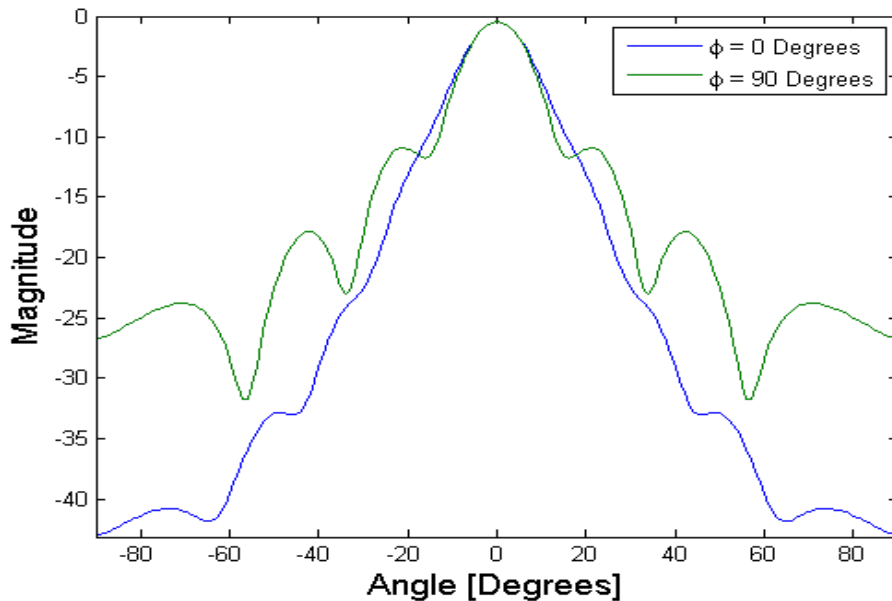


Figure 3.4: Far-field of small rectangular VNA horn modelled with approximate theory, where the aperture field phase is approximated as quadratic. Cuts are shown for 0 and 90 degrees about the azimuthal angle ϕ corresponding to the E and H -planes, respectively. The magnitude was normalised to the on-axis value.

3.1.4 Example Horn (Mode Matching Approach)

The general mode matching theory will not be discussed in great detail in this section, as it is explained in depth for spherical geometries in chapter 4 and an overview of the general theory is given in chapter 2. The theory specific to rectangular/Cartesian geometries is detailed in Stephen Doherty’s PhD thesis mentioned above [Doherty, 2012] and the approach is based on approximating the smooth walled pyramidal geometry as a series of rectangular sections with increasing size in a stepwise fashion, as is shown in Figure 3.5. The fields in each uniform section are defined as the Cartesian modal solutions set out in chapter 2 of this thesis and mentioned again in the discussion on the approximate method above.

Using the basis set of modes appropriate for Cartesian geometries, scatter matrices are formulated for analysing how much power scatters between modes on either side of each junction so that complex power is conserved, and then the scatter matrices are cascaded for the total number of sections. The term complex power is used since the scattering is calculated by integrating the product of the complex electric and magnetic fields over the cross-section of the waveguide junction. A detailed description of complex power is given in [Morgenthaler, 2011]. The scatter matrices are constructed from three power coupling integrals (or overlap integrals) $P, Q,$ and R which are derived from taking cross products between either the \vec{E} or

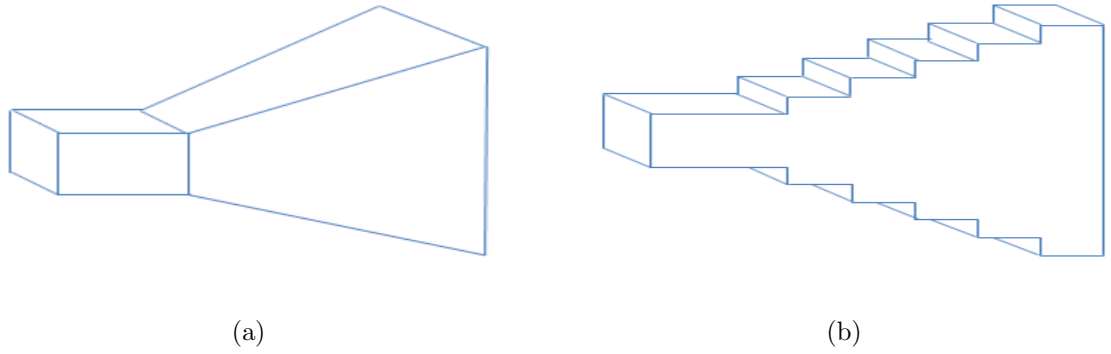


Figure 3.5: Simplified illustration of a smooth walled rectangular horn showing stepwise approximation. (a): A smooth walled horn with regular flat walls. (b): A cut through the horn when it is represented in a stepwise fashion. The steps are shown exaggerated for clarity.

\vec{H} field on one side of the junction with the complex conjugate of either the \vec{H} or \vec{E} field on the opposite side of the junction for cross-coupled power scattering, or else cross products between fields on the same side of the junction for self-coupled power scattering. The exact formulation of the P,Q, and R integrals are described in chapter 2.

By running the Rectangular SCATTER program with an input geometry file corresponding to a horn and waveguide with the same dimensions described in the approximate method, the following graphs were generated for the aperture field and far-field patterns. The horn's geometry was split into 400 steps each with a length of $0.05173mm$, or $\lambda/58$. 58 steps per wavelength was most likely over-kill but the program is very fast so calculation time was not an issue. A study into the minimum requirement for step number was not investigated in this study.

Examining the figures corresponding to both the approximate solutions of the fields and the mode matching results it is clear that there is relatively good agreement in the E-plane for the aperture fields, particularly for the magnitude. The SCATTER results for the H-plane are very different than the constant unity magnitude shown across the aperture in the approximate method. The phase also exhibits large differences in the H-Plane, however the far-field patterns of both techniques agree very well in both planes. A more detailed comparison will be shown after the next section and it will include results from yet another approach, namely the FEM technique.

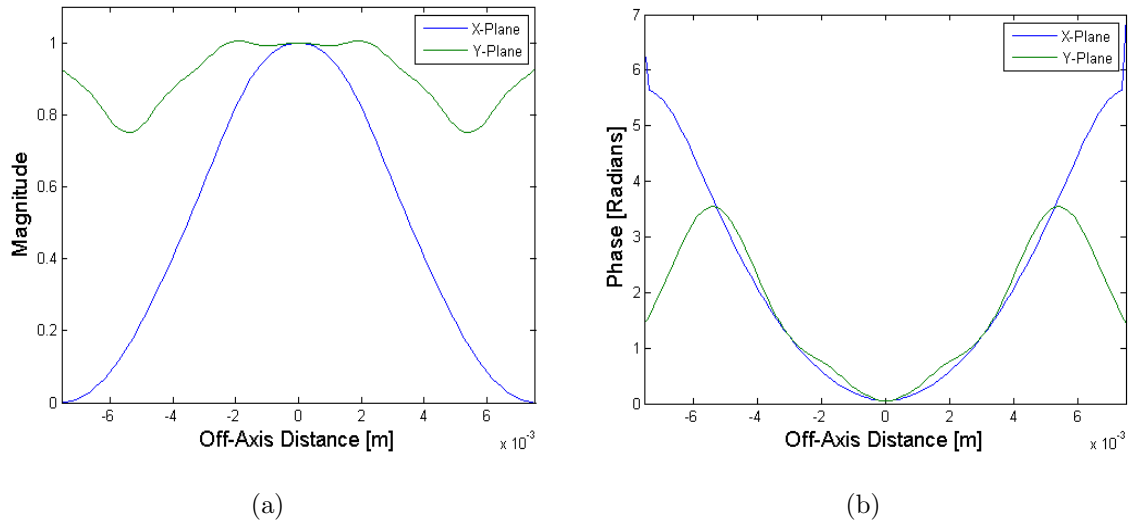


Figure 3.6: Small rectangular VNA horn modelled with mode matching algorithms. The X-plane (blue) corresponds to the H-plane, and the Y-plane (green) corresponds to the E-plane, in both graphs. (a): The magnitude of the electric field $|\vec{E}|$ across the aperture. (b): The phase of the electric field across the aperture.

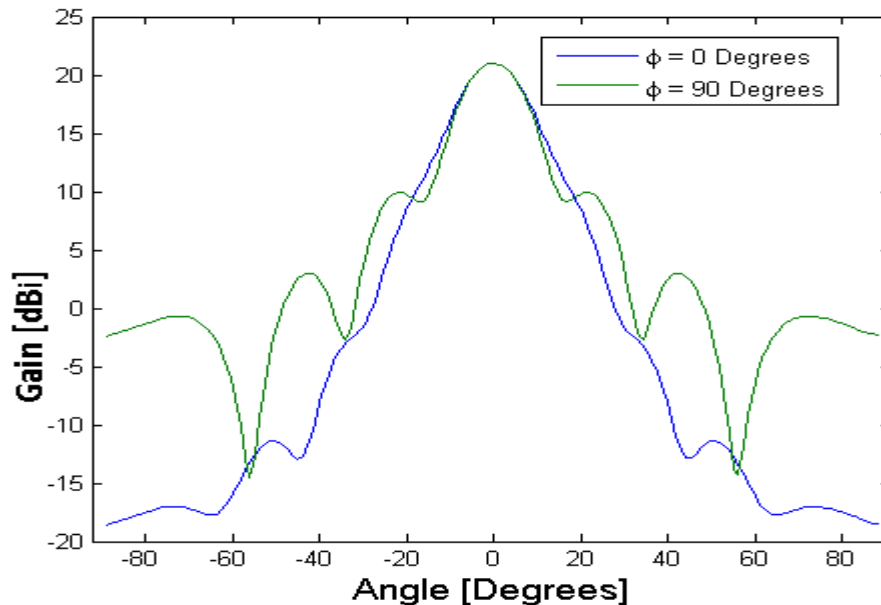


Figure 3.7: Far-field of small rectangular VNA horn modelled with mode matching algorithms. Two cuts through the far-field pattern are shown for 0 and 90 degrees about the azimuthal angle ϕ corresponding to the E and H -planes respectively. The gain (dBi) is relative to an isotropic radiator.

3.1.5 Example Horn (FEM Approach)

Figure 3.8 shows the model that was created in COMSOL to simulate the behaviour of the same feed horn that was analysed with both the approximate and the mode matching methods. The quarter section of the horn is shown in (a) and the model after meshing is shown in (b). The symmetry boundary in the E-plane was defined as a perfect magnetic conductor (PMC), while the symmetry boundary in the H-plane was defined as a perfect electric conductor (PEC). The input waveguide was

excited with the lowest order rectangular waveguide mode (TE_{10}), and the quarter-hemispherical cap that extends beyond the mouth of the horn and the quarter-cylindrical section that runs adjacent to the horn were defined as the far-field domain.

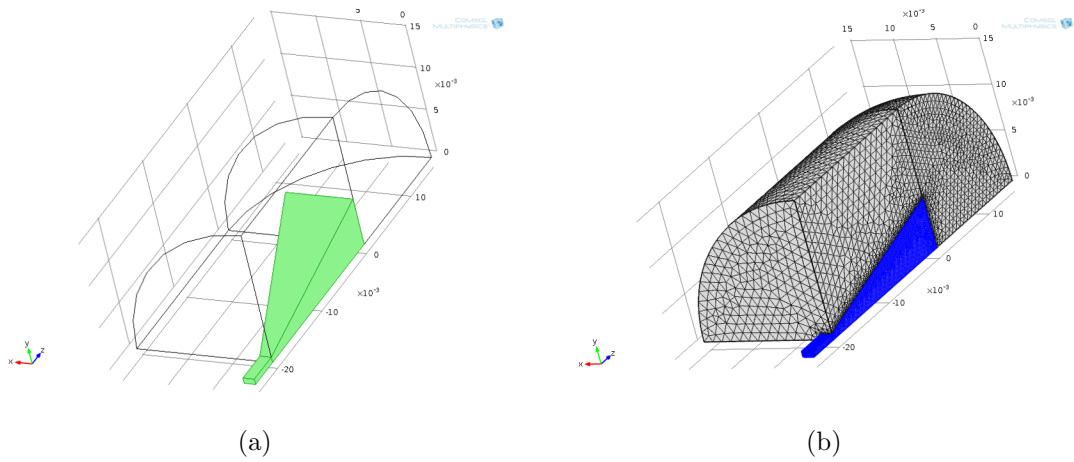


Figure 3.8: Small VNA horn modelled with COMSOL. (a): A quarter of the full horn was sufficient to model due to the symmetry of the geometry and the field in the E and H-planes. (b): The model completely meshed.

Figure 3.9 shows the default model solution. It is a surface plot for the log of the electric field for the full model at two separate viewing angles. 2D slice plots and 1D line plots can also be generated for the electric and magnetic fields, for example, using post-processing. The post-processing environment in COMSOL also allows analysis of many other parameters such as current densities, resistive heating, S parameters, etc. and the latest version of COMSOL (version 4.3) also provides a polar plot option for graphing data such as far-field patterns.

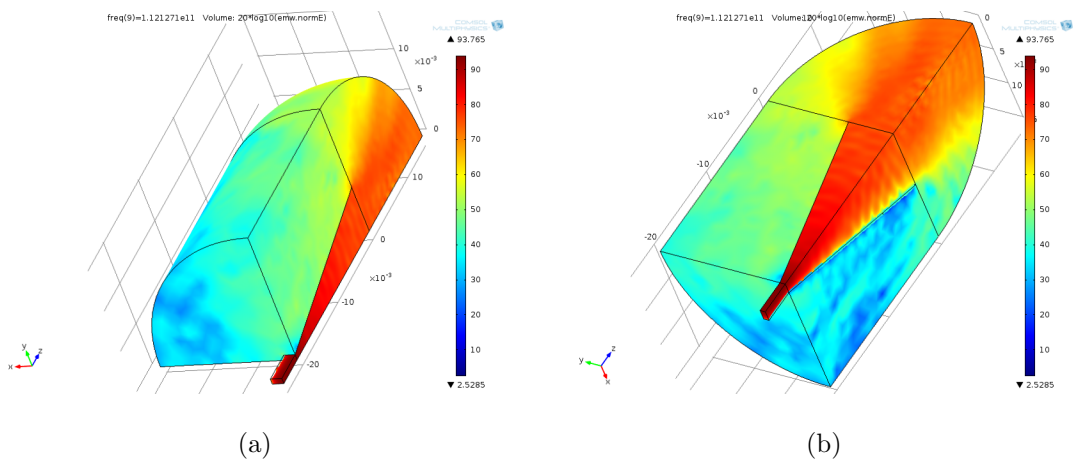


Figure 3.9: Electric field of a small VNA horn modelled with COMSOL.

Following calculation of the aperture fields \vec{E}_A and \vec{H}_A across the surface that makes up the aperture of horn, and the plane surrounding the aperture, S , the

Stratton-Chu formula [Volakis and Sertel, 2012] is applied to the near field data in order to calculate the far electric field \vec{E}^{FF} at each point on a sphere infinitely far from the aperture of the horn. The Stratton-Chu formula for calculating the far-field at each point P on the sphere has the following form:

$$\vec{E}_P^{FF} = \frac{ik}{4\pi} \vec{r}_0 \times \int \left[\vec{n} \times \vec{E}_A - \eta \vec{r}_0 \times (\vec{n} \times \vec{H}_A) \right] \exp(ik\vec{r} \cdot \vec{r}_0) dS \quad (3.8)$$

where \vec{E}_A and \vec{H}_A are the tangential fields on the surface S across the aperture of the horn, \vec{n} is the unit normal to the surface S , η is the impedance, and k is the wavenumber ($k = \frac{2\pi}{\lambda}$). Finally, \vec{r}_0 is the vector pointing from the centre of the horn aperture to the field point P . The geometry of the problem is illustrated in Figure 3.10.

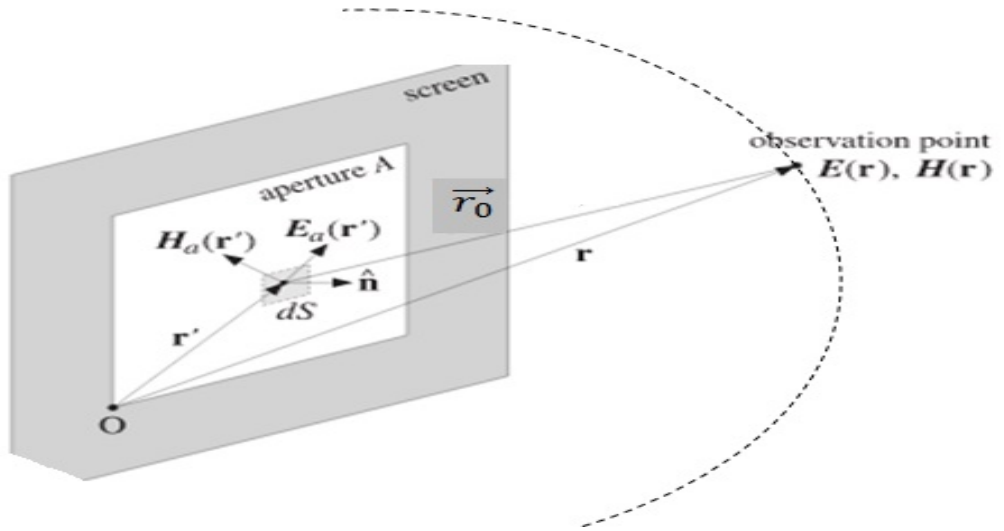


Figure 3.10: Illustration of COMSOL far-field calculation [Orfanidis, 2002].

According to Volakis and Serte, the Stratton-Chu integral formulae for field representations are in fact among the most popular in scattering and antenna related problems [Volakis and Sertel, 2012]. And the COMSOL support literature states that the COMSOL far-field calculation is identical to what is known as the “scattering amplitude” in an EM scattering problem [COMSOL, 2011]. In deriving the waveguide modes in chapter 3 the starting point was the homogeneous Helmholtz equation, usually just called the Helmholtz equation $(\nabla^2 + k^2) \vec{\psi}(\vec{r}) = 0$, since we were dealing with the source free case. However since the aperture of the horn acts as a source for the far-field the inhomogeneous Helmholtz equation is required as a starting point for deriving the relationship between the aperture field and far-field:

$$(\nabla^2 + k^2) \vec{\psi}(\vec{r}) = -f(x) \text{ in } \mathbb{R}^n \quad (3.9)$$

where $n = 1, 2, 3$, and f is some function yet to be defined.

The way to solve the above equation uniquely is to specify a boundary condition at infinity. The boundary condition typically used is the Sommerfeld radiation condition [Schot, 1992]. The solution then to the inhomogeneous Helmholtz equation is:

$$(\nabla^2 + k^2) G(\vec{r}, \vec{r}') = -\delta(\vec{r} - \vec{r}') \text{ in } \mathbb{R}^n \quad (3.10)$$

where $\delta(\vec{r} - \vec{r}')$ is the Dirac delta function, and $G(\vec{r}, \vec{r}')$ is the Green's function, the form of which depends on the dimension of the space n . For $n = 3$ the Green's function has the following form:

$$G(\vec{r}, \vec{r}') = \frac{e^{ik\vec{r}}}{4\pi\vec{r}} \quad (3.11)$$

where the boundary condition that the Green's function is an outgoing spherical wave for $|\vec{r}| \Rightarrow \infty$ was chosen.

Finally, using this particular Green's function, and applying Green's theorem to the spherical surface that bounds the far-field domain in the model, we obtain an important expression relating the values of the fields in the interior of the surface to those at the closed surface, that of equation 3.8.

There are two reasons for allowing a small amount of propagation beyond the mouth of the horn. The first is to allow the field to freely propagate away from the aperture of the horn. This serves to avoid unwanted reflections that could occur if the model geometry was truncated right at the aperture of the horn. If the surface of the quarter sphere that bounds the propagation region is given appropriate boundary conditions (Scattering Boundary or Perfectly Matched Layer) then no reflections will occur. The second reason is to create a surface that has points with well-defined angular position (θ, ϕ) with respect to the horn aperture for the far electric field to be analysed across.

This transformation process using the Stratton-Chu formula generates a new variable (E_{far}) with three components ($E_{far\hat{r}}$, $E_{far\hat{\theta}}$ and $E_{far\hat{\phi}}$) that represent the collection of far-field data points \vec{E}_P^{FF} across the spherical surface.

The results of the COMSOL model are shown together with the results from the other two methods discussed previously.

As can be seen in Figure 3.11, there is excellent agreement between the three different simulation techniques particularly out to about 40 degrees which corresponds

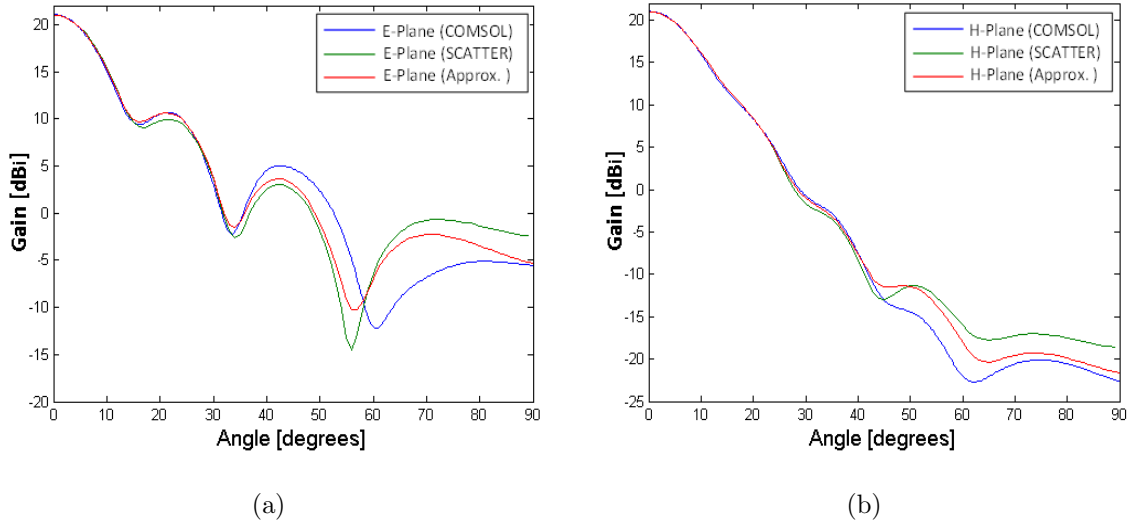


Figure 3.11: Comparisons of the far-field beam patterns for three simulation methods, the approximate phase-cap method, the rectangular mode matching method, and the FEM approach. (a): The beam pattern in the plane with the azimuthal angle set equal to zero ($\phi = 0$, or E -plane), (b): The beam pattern in the plane with the azimuthal angle set equal to 90 degrees ($\phi = 90$, or H -plane)

to approximately $-20dB$ in the E-plane and $-32dB$ in the H-plane. However beyond 40 degrees there is still reasonably good agreement considering the FEM technique is a very different computational approach than the mode matching technique.

3.1.6 Inclusion of a Conducting Ground Plane

The COMSOL results displayed so far have assumed free-space surroundings at the aperture of the horn. The mode matching technique does not consider the surroundings of the horn at all, and the same is true for the phase-cap approximate method. However the horns on the SAFARI instrument will be combined in an array with conducting material (gold coated) between them (see Figure 3.1(a) at the start of this chapter). Any induced surface currents across this adjoining plane could possibly act as sources for the far-field radiation leading to increased side-lobes for example. For this reason COMSOL simulations were run again with the boundary adjacent to the horn aperture defined as a perfect electric conductor (PEC) boundary condition. These results were again compared to the mode matching results and they are displayed in Figure 3.12.

As can be seen there are small differences between the COMSOL results when the conducting ground plane is included, however the effect is so small it would be considered negligible. What is interesting though is that the small deviation is in the

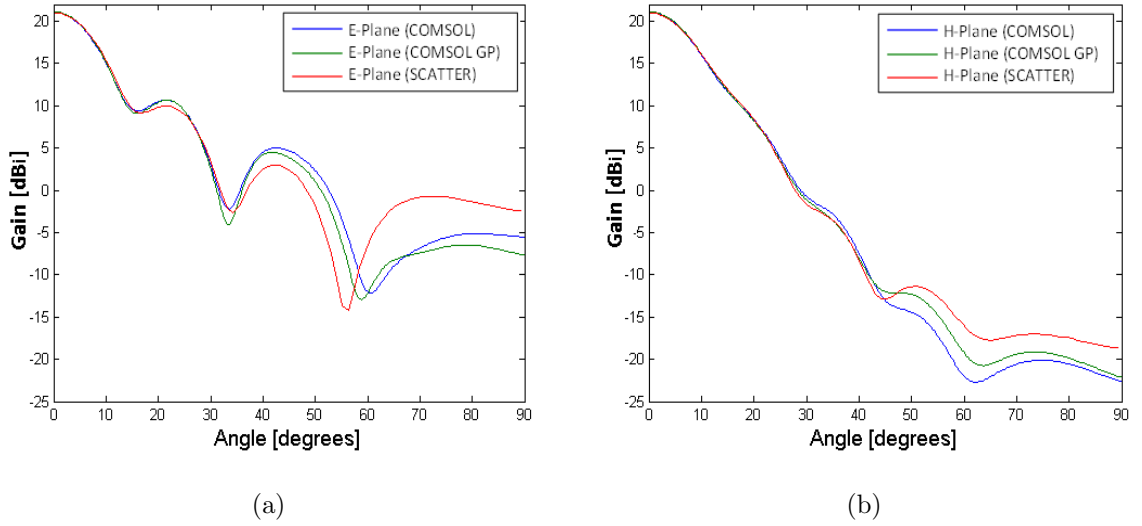


Figure 3.12: Comparisons of the far-field beam patterns for the effect of inclusion of a conducting ground plane. (a): The beam pattern in the plane with the azimuthal angle set equal to zero ($\phi = 0^\circ$, or E-plane), (b): The beam pattern in the plane with the azimuthal angle set equal to 90 degrees ($\phi = 90^\circ$, or H-plane)

direction of bringing the results into better agreement with the SCATTER results, in both planes. Because there was a small visible change in the beam patterns an analysis of the induced surface currents across the ground plane was carried out.

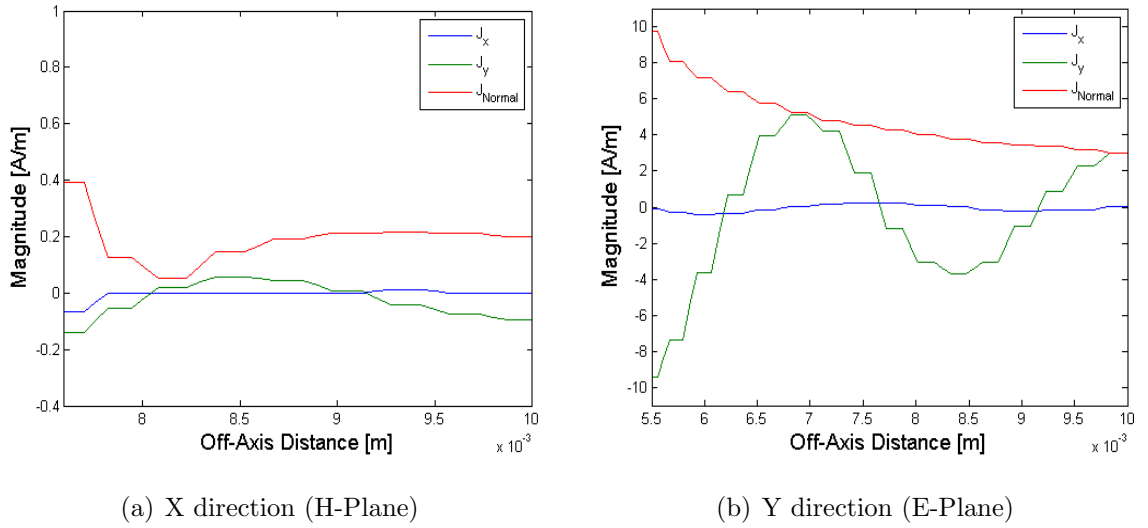


Figure 3.13: 1D cuts of the surface current density across the conducting ground plane adjacent to the horn aperture. The off-axis distance is from the edge of the horn aperture to the edge of the propagation zone

3.1.7 Comparing Horn to Waveguide

In order to investigate the most extreme case of the possible effect of the conducting ground plane on the far-field, a simple waveguide was modelled. The far-fields were

calculated for both the case of a free standing waveguide and one embedded in a ground plane. A straight waveguide was chosen because it has poor directionality and would therefore likely lead to significant induced currents across the ground plane. The waveguide was given the same transverse dimensions as the waveguide section of the horn model (WR-10), and the same length as that of the horn.

Figure 3.15 shows the far-field radiation patterns for both a waveguide in free-space and a waveguide connected to a ground plane. As can be seen there are significant differences in both far-field planes when the ground plane is included. The effect is much more obvious in the case of a waveguide than it was for a rectangular horn, as would be expected. The data corresponding to the surface current density is also shown plotted in Figure 3.14. When compared to the surface current density generated across the ground plane from the horn it is clear that it is much greater for a waveguide. These induced currents act as sources for the far-field.

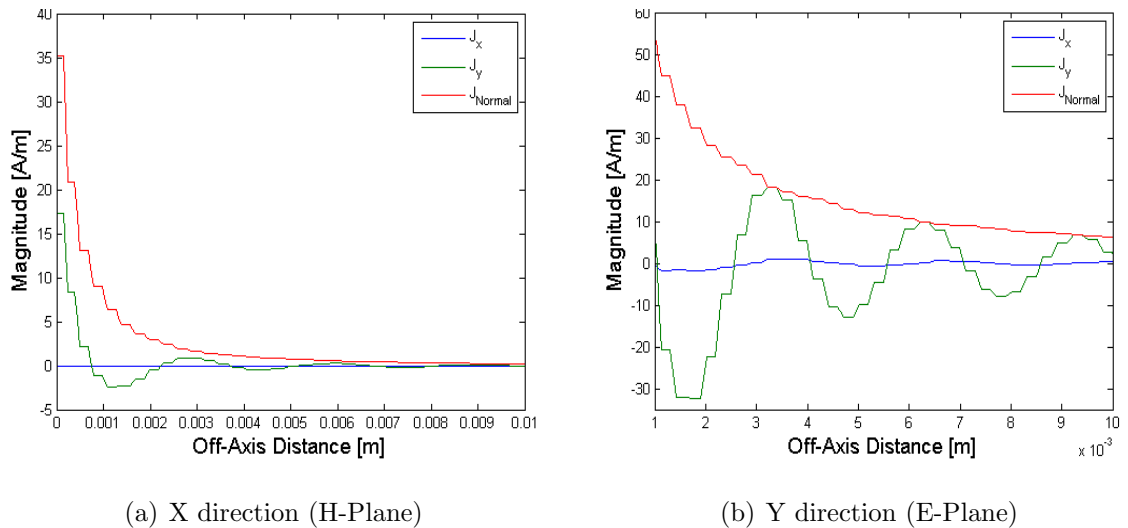


Figure 3.14: 1D cuts of the surface current density across the conducting ground plane adjacent to waveguide aperture. Off-axis distance is from the edge of the waveguide aperture to the outer edge of the propagation zone.

3.1.8 Directional Gain of Example Horn

In the far-field patterns shown for the COMSOL FEM simulations and those of the mode matching approach, the data on the vertical axis was directional gain. While the aim of plotting the far-field data was to compare the structure of the far-field patterns for the different computational approaches, the calculation of gain can also be a very useful parameter for describing the performance of a horn antenna. The

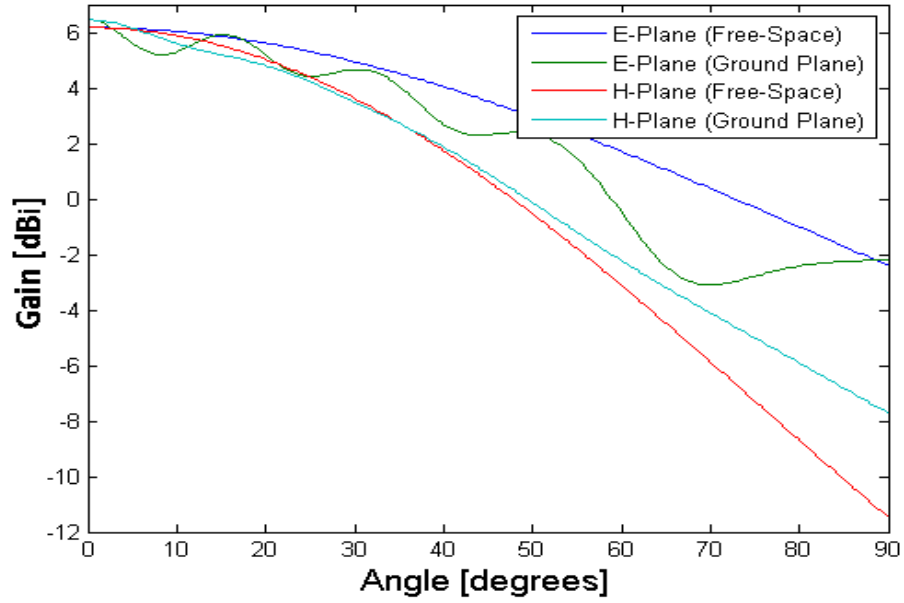


Figure 3.15: Far-field patterns of a waveguide in free-space and connected to a conducting ground plane.

measure of directional gain provides important information about the directivity of the beam compared to an isotropic radiator. However there is no built-in option in the COMSOL software to calculate the gain so the author derived an expression that would allow it to be calculated.

The directivity of the horn can be defined as $10\text{Log}_{10}(I(\theta, \phi)/I_{iso})$, where $I(\theta, \phi)$ is the power flux or power density at a point P , and I_{iso} is the power flux of an ideal isotropic radiator at the same point P on a sphere with radius r , which is of course is defined as $I_{iso} = P_0/4\pi|r|^2$, where P_0 is the total input power at the horn aperture. Now $I(\theta, \phi)$ can also be defined as $|\vec{E}|^2/2Z$, where Z is the impedance of free space and is equal to 377Ω , so the directivity can be defined as:

$$\mathbb{G} = 10\text{Log}_{10}\left(\frac{4\pi|r|^2|\vec{E}|^2}{2ZP_0}\right) \quad (3.12)$$

Now the default value for the input power P_0 in the RF module of COMSOL is 1 Watt. Also, strictly speaking the value of $|r|$ in the far-field is infinity, however if this was allowed to be the case then the fields would all go to zero in the far-field. For this reason COMSOL defined r to be unity in the definition of the far-field. So setting $P_0 = 1$ and $|r| = 1$ the above expression for the directive gain reduces to:

$$\mathbb{G} = 10\text{Log}_{10}\left(\frac{2\pi|\vec{E}|^2}{Z}\right) \text{dBi} \quad (3.13)$$

where the i in dBi denotes that the gain is with respect to an ideal isotropic radiator.

To be more precise the directive gain should really be computed with respect to an ideal isotropic radiator with power equal to that at the mouth of the horn rather than the power input at the entry port. If there is no significant back scatter then the result will be almost identical, but if there are significant losses due to back scatter (S_{11}) then the correct definition should be:

$$\mathbb{G} = 10 \text{Log}_{10} \left(\frac{2\pi |\vec{E}|^2}{Z} (1 - |S_{11}|^2) \right) \text{ dBi} \quad (3.14)$$

It was Equation 3.14 that was used for calculating the gain in the previous far-field plots. Then using the same definition an analysis was carried out to investigate the gain of the example horn across the frequency range of the VNA system, namely 65 to 110GHz, in steps of 6GHz. The same analysis was also performed for the waveguide described above so that the benefit of using a horn instead of a waveguide would be highlighted. Figure 3.16 shows the gain plotted as a function of frequency for both the horn and waveguide.

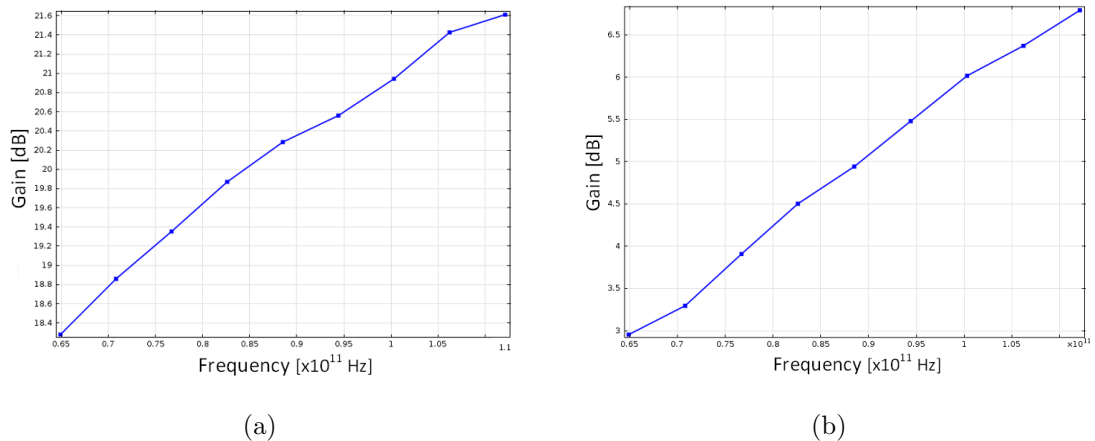


Figure 3.16: Gain plotted as a function of increasing frequency for (a): a small pyramidal horn, and (b): a waveguide with similar dimensions.

The gain is significantly higher for the horn, as can be seen in Figure 3.16. The trend of the gain graphs is similar for both cases, with the gain increasing steadily as frequency increases. However the value at each frequency point is much higher for the horn. It can be concluded that using a horn in place of a simple waveguide provides greater directionality with less back scatter. This would clearly be expected based on λ/d considerations, where d is the size of the aperture which is significantly larger for the horn, and λ is the wavelength of radiation.

3.1.9 External Back Scatter

The ability to include a propagation analysis domain with COMSOL made it possible to model external back scatter around the back of the horn. It has always been assumed that the power levels in this direction would be insignificant, but it is a question of interest all the same. In fact the Planck CMB satellite had some problems when an artefact in the detector data could not be explained. The source of the problem was eventually traced to some of the horns being able to see a warm part of the satellite behind the horns. Being able to model the beam patterns of horns right through the full 360° field will allow more careful design of systems that can avoid such problems.

By extending the propagation region through 180° it was possible to perform a far-field transformation on the field data behind the horn using the same Stratton-Chu method described above. Figures 3.17(a) and 3.17(b) show the co-polar and cross-polar far-field beam patterns for both a WR-10 waveguide and the example pyramidal horn from before. As can be seen for the case of the horn, the gain does begin to increase for angles greater than 90° , but not to significant levels. However, for very sensitive receiver horns such as those required for CMB polarisation experiments, these levels could become significant. A very strong source behind the horns, such as the Sun for example, could become noticeable if sufficient shielding is not employed.

The 180° plot for the waveguide is also interesting, particularly the cross-polar field. It shows a very smooth distribution that is almost symmetric about the 90° angle. Careful analysis of the behaviour of the fields in the vicinity of a waveguide aperture may be important for modelling the VNA set-up in the future as short waveguide sections are being increasingly used as probes for examining the far-field patterns of radiating feed horns. Tests to date seem to show that while a waveguide probe is well suited for measuring the co-polar fields of radiating components, they are not ideal for analysing cross-polar distributions.

3.1.10 Experimental Verification

In order to verify the computational approaches presented in this section, a series of beam pattern measurements were carried using the VNA system at NUIM. Neil

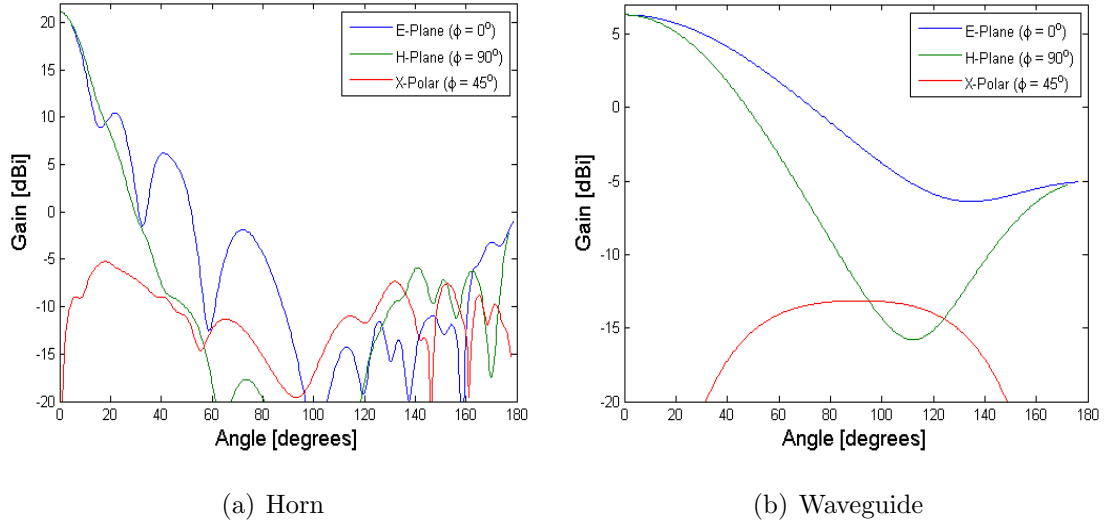


Figure 3.17: Cuts through the far-field beam patterns of a small pyramidal horn and a WR-10 waveguide in free space. The far-field data is plotted over the full 180° , thus including the space behind the radiating component.

Tynan of the Department of Experimental Physics at NUIM provided assistance with the experimental set-up and the alignment procedures. The experimental set-up is illustrated in Figures 1.15 and 1.16 in section 1.4 of chapter 1. The particular pyramidal horn that was analysed had the same dimensions as the example horn described in this section, and the details can be found in subsection 3.1.3 above.

A two-port network was used for the analysis, where port one was used in combination with a frequency converter head (head one) as the transmitter. Port two, also used in combination with a frequency converter head (head two), was employed as the receiver. The waveguide probe was mounted head one of the VNA system, which was fixed to the $x - y$ raster scanner. The pyramidal horn was then mounted head two, which was fixed and a z translation stage. The distance (Δz) between the horn aperture and the waveguide probe aperture was set to 450mm using the translation stage. The maximum off-axis angle at which the beam pattern could be measured was limited by the range of the raster scanner in the $x - y$ plane. The limits of the scan in x and y were both -140mm to $+140\text{mm}$, leading to a maximum off-axis angle range of -17.28° to $+17.28^\circ$ in both the E-plane and H-plane.

Figure 3.18 shows the E-plane ($x = 0$) and H-plane ($y = 0$) cuts through the measured far-field beam pattern. The COMSOL FEM and SCATTER mode matching simulation results are shown again for comparison, and as can be seen there is very good agreement between measurement and model.

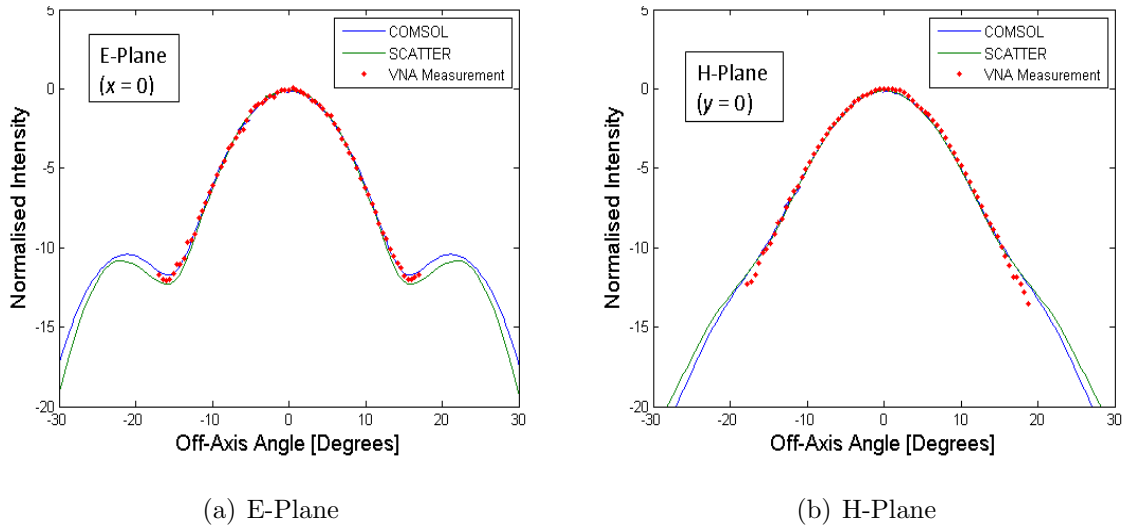


Figure 3.18: Far-field beam pattern measurements of a pyramidal horn using a VNA.

3.2 SAFARI Horns

The current feed horn being used in the SAFARI test bed at SRON is a smooth walled conical design. However the current design for the SAFARI feed horns in array format is a two angled pyramidal horn as shown in Figure 3.21. The reason for the choice of a pyramidal geometry over a conical one is down to limitations in the manufacturing process. For horns on these micrometer scale the most accurate method of manufacture is to start with a block of material (usually aluminium) and to first fashion rows of horns through one dimension as shown in Figure 3.20 (b). The same process is then carried out in the perpendicular direction to reveal an array of pyramidal mandrels as shown in Figure 3.20 (c). RAL in the U.K. have built monolithic arrays of 388 pyramidal horns as shown in Figure 3.19 (b) and (c). The horns are electroformed in copper on wire-eroded aluminium mandrels (see Figure 3.19 (a)). During the wire erosion process it becomes difficult to transfer heat away from the tip of the mandrels due to the extremely small dimensions of the horn apertures. The sudden change from the softer angle (4.5°) to a much steeper angle (20°) solves this problem and this is what leads to the design shown in Figure 3.21.

3.2.1 Far-field Radiation Patterns of SAFARI Horns

The frequency range the SAFARI S-Band instrument is designed for is 4.3THz to 10THz ($\lambda = 30 - 70\mu\text{m}$) meaning that the dimensions of the horns correspond to many wavelengths. Standard computers will not be able to fully model these

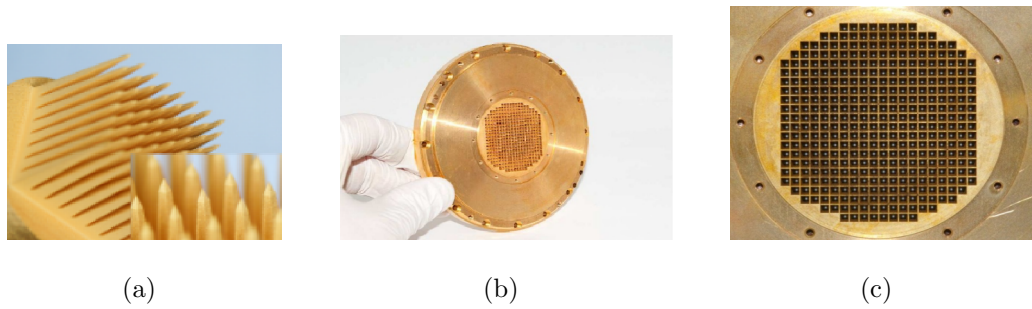


Figure 3.19: SAFARI horn array and mandrel. (a): A mandrel for construction of an 8×8 pyramidal horn array, (b): An array of 388 pyramidal horns with a hand to demonstrate the small scale of the structures, and (c): The same array of 388 pyramidal horns shown enlarged a face-on.

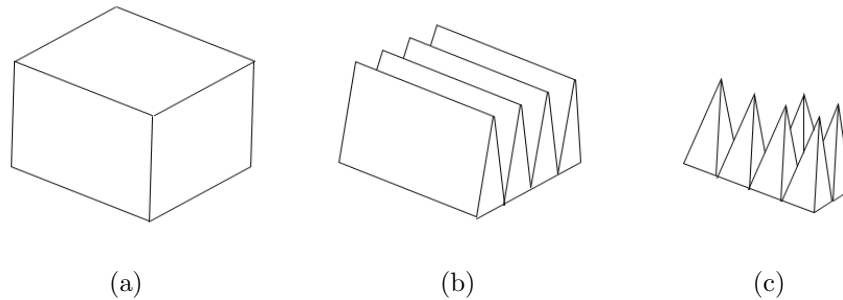


Figure 3.20: Illustration of the wire-erosion process for micro horn array manufacture. (a): A solid block of material. (b): The block following wire-erosion in one dimension, and (c): The block following wire-erosion in two perpendicular directions revealing pyramidal horn mandrels.

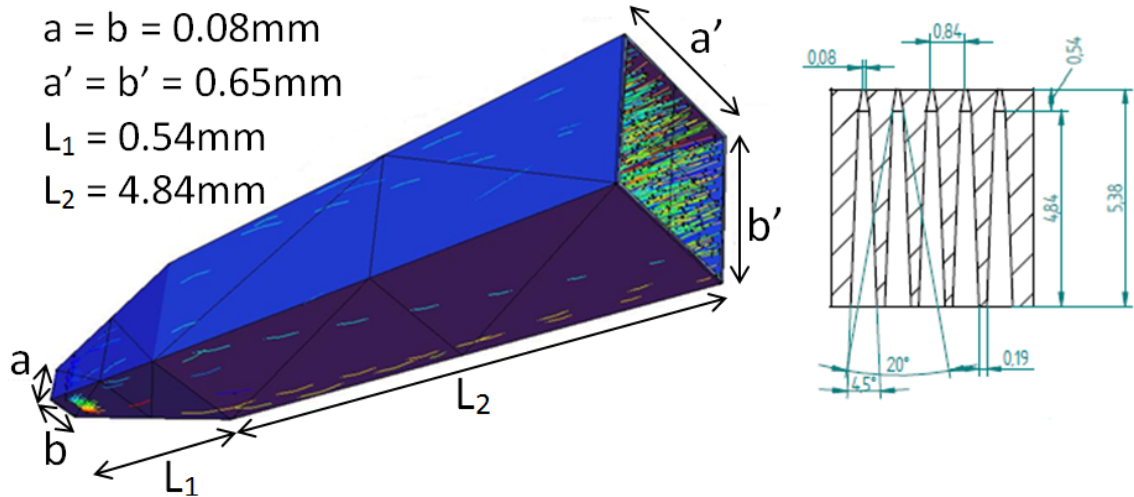


Figure 3.21: *left*: 3D model of curret SAFARI horn design. *right*: Curret SAFARI horn design showing the dimensions of the horns in a slice through the array, where all dimensions are in mm.

large horn structures using FEM or FIT techniques, particularly at the highest frequencies. The pyramidal mode matching approach will be essential in order to characterise these feed horns across the desired frequency range.

Using a particularly powerful computer with 64 gigabytes of RAM, and taking advantage of symmetry conditions in both the E-plane and H-plane, it was possible

to use COMSOL to perform a FEM simulation of a SAFARI S-Band horn at the lowest operational frequency of 4.3THz. The beam patterns at azimuthal cuts of $\phi = 0^\circ$ and $\phi = 90^\circ$ are shown in Figure 3.22. The same horn was simulated using the Pyramidal SCATTER program for comparison. As can be seen in the comparison plot there are large differences in the far-field patterns calculated by COMSOL and SCATTER.

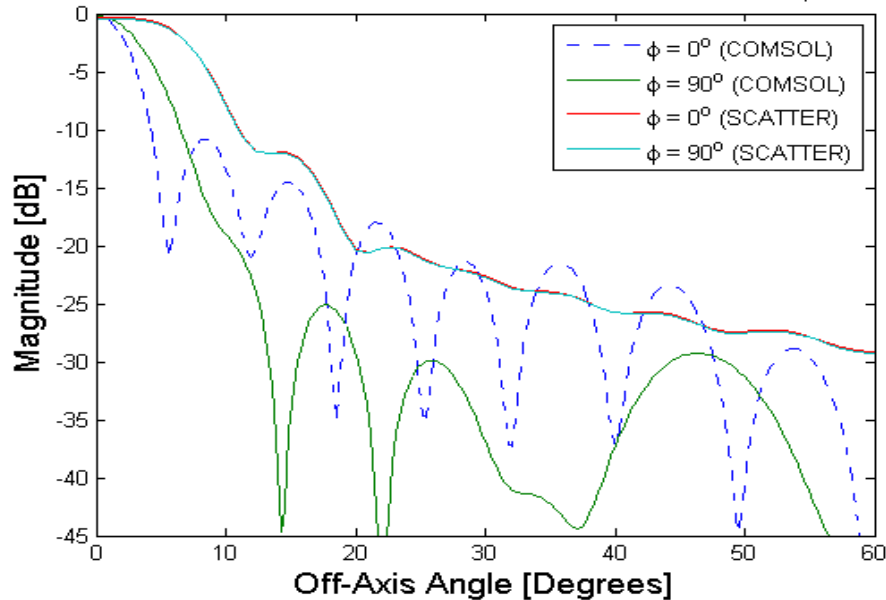


Figure 3.22: Far-field pattern of a SAFARI horn at 4.3THz ($70\mu\text{m}$) modelled with COMSOL and SCATTER.

The main beam in the SCATTER data is clearly much wider than the COMSOL data. Upon comparing the approaches of COMSOL and SCATTER in terms of mode excitation at the input waveguide feed, the large differences are expected. COMSOL only allows a single mode to be defined for each simulation (the TE_{01} mode in this case with the electric field polarised in the y direction, or $\phi = 90^\circ$, leading to the higher side-lobes in the $\phi = 90^\circ$ far-field cut), thus the higher order propagating modes were not included. In contrast, SCATTER is including the power contribution from all possible propagating modes. The symmetry in the E-plane and H-plane for the SCATTER results is due to the horn being square rather than rectangular, and since all propagating modes are included in the calculation, then both polarisations of each mode will also be included, for example the TE_{10} and TE_{01} modes, leading to the observed symmetry.

COMSOL does account for power scattering from the input mode to higher order modes when a step discontinuity or change in flare angle is encountered, for example the change in angle in the SAFARI horn in this case. This scattering

behaviour is clear in the example of the spline fit conic section horn modelled with COMSOL in chapter 4 of this thesis. In that case the horn is fed by a rectangular WR-10 waveguide excited with only the fundamental TE_{01} mode with the resulting horn aperture field exhibiting a combination of modes that is evident from the symmetric Gaussian field observed at the output. As can be seen in the analysis presented in section 4.3.2 both COMSOL and SCATTER in cylindrical coordinates agree very well for that particular example, and this is due to the fact that the first section of the spline fit conic horn supports only a single mode. However, the difference in the present case of the SAFARI horn is that the first waveguide section is itself over-moded, meaning that the large number of modes generated by the SCATTER code will each carry power through the horn and contribute to the far-field pattern.

An attempt to encourage the FEM and mode matching results to agree was made by independently simulating higher order modes with COMSOL and then summing them during post-processing analysis. Only modes with cut-off frequencies below 4.3 THz were considered since any modes with higher cut-off frequencies would be highly attenuated through the horn. Table 3.1 shows the cut-off frequencies for some of the higher order rectangular modes, and thus the modes that were considered in the FEM analysis. The far-field data corresponding to each propagating mode was summed in a linear fashion and the resulting far-field pattern is shown in Figure 3.23 with the SCATTER result shown again for comparison.

Mode	Cut-Off (THz)	Behaviour	Mode	Cut-Off (THz)	Behaviour
TE_{10}	1.875	Propagating	TE_{21}	4.193	Propagating
TE_{01}	1.875	Propagating	TE_{12}	4.193	Propagating
TE_{11}	2.652	Propagating	TM_{21}	4.193	Propagating
TM_{11}	2.652	Propagating	TM_{12}	4.193	Propagating
TE_{20}	3.750	Propagating	TE_{22}	5.303	Evanescent
TE_{02}	3.750	Propagating	TM_{22}	5.303	Evanescent

Table 3.1: Cut-off frequencies of some of the higher order modes at the input aperture of a SAFARI horn.

As can be seen there is now much better agreement between the two results, but there are still some differences in far-field distributions for the SCATTER and COMSOL models. In the COMSOL analysis each propagating mode was excited

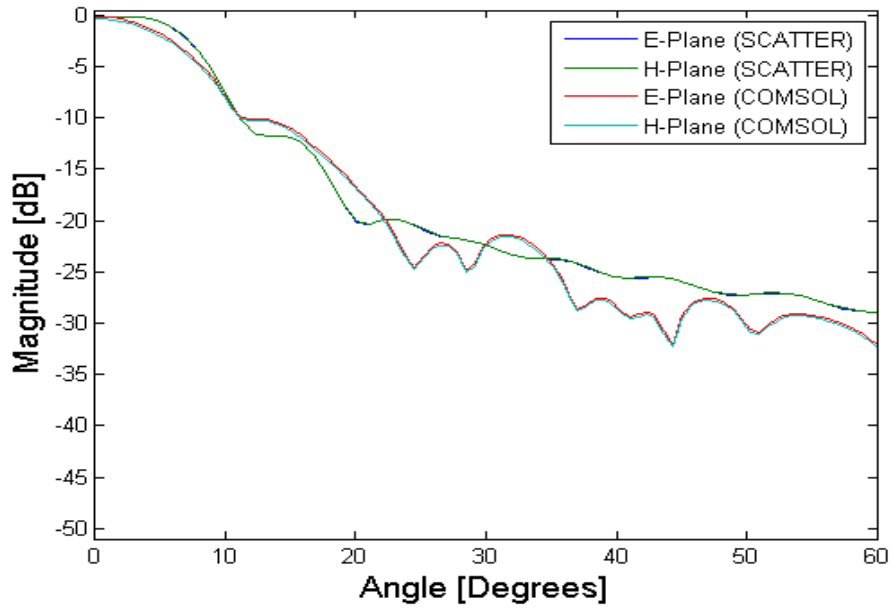


Figure 3.23: Far-field pattern of a SAFARI horn at 4.3THz ($70\mu\text{m}$) modelled with COMSOL and Pyramidal SCATTER. In this example the TE_{10} , TE_{01} , and TM_{11} modes were analysed separately with COMSOL and then summed.

with equal power at the input port while no consideration was given to evanescent modes. The SCATTER mode matching code excites all modes (up to the number defined by the user) including evanescent modes, some of which may eventually become significant since the SAFARI horn widens relatively quickly and therefore these modes may actually contribute to the far-field, thus leading to differences between the two results. It may also be possible that simulating each mode independently with COMSOL is missing more subtle modal cross-coupling effects that SCATTER is so good at capturing.

Following the analysis at the lowest frequency of 4.3THz, and having pushed the limits of the COMSOL FEM approach with the highest powered PC available, the SAFARI horns were then modelled at both an intermediate frequency (7.15 THz) and the highest operational frequency (10 THz) with the SCATTER mode matching code in order to examine the aperture fields and far-field patterns of the current horn design. The calculation time at 7.15 THz and 10 THz was 21.49 hours and 92.70 hours respectively. The near field and far-field patterns are shown in Figures 3.25 and 3.24 below for the three frequencies that were examined, corresponding to the start, middle, and end of the operational frequency range of the SAFARI S-Band horn array.

The aperture field plots shown in Figure 3.25 show interesting field distribution

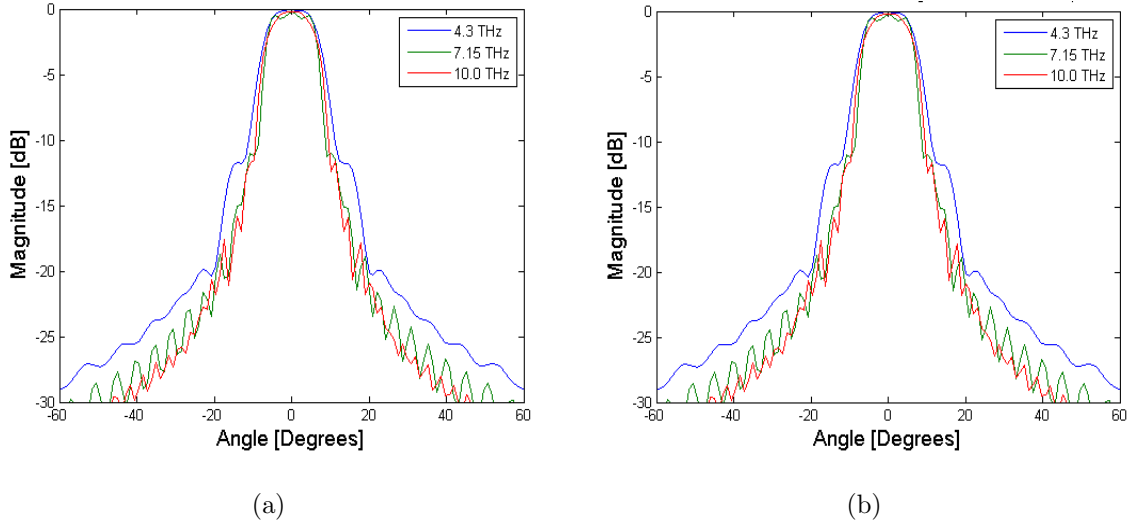


Figure 3.24: Far-field patterns of a SAFARI horn at three spot frequencies. (a): The E-plane ($\phi = 0^\circ$) cut at 4.3, 7.15, and 10.0THz, and (b): The H-plane ($\phi = 90^\circ$) cut at 4.3, 7.15, and 10.0THz. It is clear that the E and H-plane cuts are identical, as would be expected.

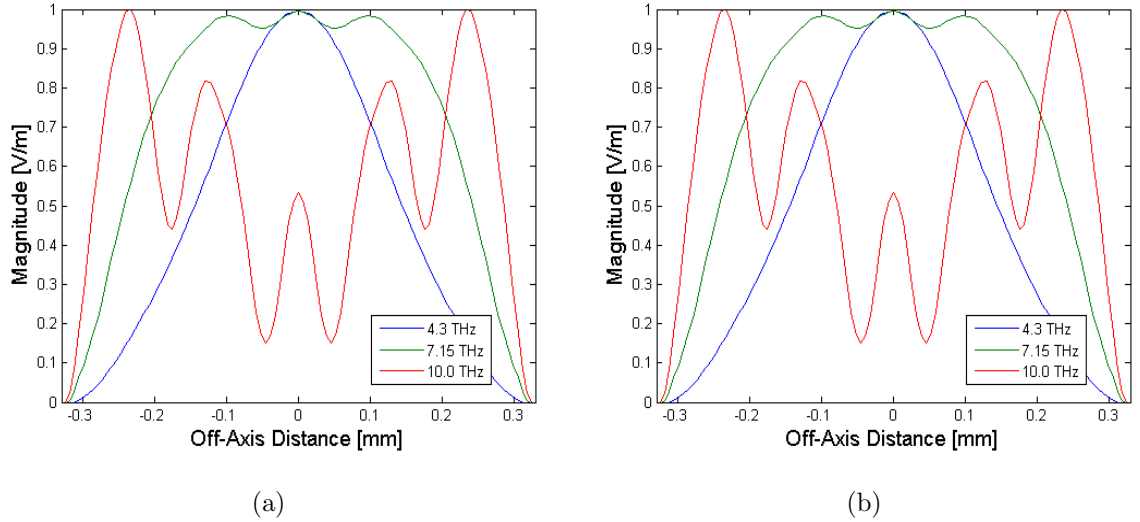


Figure 3.25: Aperture fields of a SAFARI horn at three spot frequencies. (a): The E-plane ($\phi = 0^\circ$) cut at 4.3, 7.15, and 10.0THz, and (b): The H-plane ($\phi = 90^\circ$) cut at 4.3, 7.15, and 10.0THz. It is clear that the E and H-plane cuts are identical, as would be expected. The off-axis distance is plotted for the extent of the aperture of the horn (-0.325 to 0.325 mm).

across the aperture of the horn compared to a typical single mode rectangular horn. The aperture field distributions vary significantly for the various frequencies. The far-field patterns however show much more similarity for different frequencies but are again very different from what would be seen by a single mode horn. The main beam has a large width which indicates the higher levels of throughput that are possible with such multi-moded horns.

As efficient as the mode matching approach is compared to the FEM approach for example, the computation times for modelling the SAFARI horns are still very

long for the higher frequencies. A brief discussion is now given on a possible method for significantly increasing the efficiency of the mode matching technique used.

A huge reduction in computation time would be possible if conical modes could be employed in the mode matching code in place of the rectangular modes. The difficulty that arises of course is that the SAFARI horns are rectangular in nature meaning that conical modes do not fit naturally with the horn geometry. However it would still be possible to describe the fields by conical waveguide modes by means of coordinate transformations since a rectangular horn with a spherical phase cap at the aperture is just as much a section of a sphere as a conical horn.

The reason this would be useful is because the only place where scattering of power occurs is at the plane where there is a change in flare angle, meaning that power scattering overlap integrals would only be required to be calculated at one junction rather than a few hundred. In fact the only modes that can actually carry significant power through the horn are the modes that can propagate through the cross sectional area at the plane of angle change. The current rectangular mode matching code continues performing overlap integrals for the sections making up the entire length of the horn, and since the cross section of the horn becomes very large toward the aperture a huge number of modes are included in the calculation that in reality will carry little to no power.

The highest mode index at the intermediate frequency of 7.15 THz is $m = 31$. This gives rise to 1,984 modes that must be accounted for in the scattering calculations, and is determined by $4 \times \sum_{i=1}^N i$ since each index i can correspond to TE_{mi} , TE_{in} , TM_{mi} , or TM_{in} . The highest mode index at the high end of the frequency band (10 THz) is $m = 45$, giving rise to 4,140 modes.

A detailed description of conical and spherical modes, and the theory of conical mode matching is given in chapter 4. It is the same techniques that could be applied to modelling the SAFARI rectangular horns but with some alterations to account for the rectangular pyramidal PEC boundaries in place of the conical PEC boundaries.

3.2.2 Optical Cross-talk in SAFARI Horn Array

In this section the term ‘optical cross-talk’ will define the amount of power detected at the entry aperture of a horn (smaller aperture of the SAFARI horns) that is

adjacent to a transmitting horn. More specifically it is defined as a ratio of the total detected power at Port 2 to the total input power at Port 1 (see Figure 3.26). The SAFARI instrument that is being investigated in this thesis is purely a receiving system. However, it is still desirable to quantify the crosstalk effects between feed horns in the SAFARI horn array in a manner that assumes one feed horn to be transmitting and the rest of the neighbouring feed horns to be in the receiving mode, as this represents an extreme case that can be taken as an upper limit on cross-talk levels. This is because any receiving system will always reflect a small amount of the incident power, effectively making it a weak transmitter.

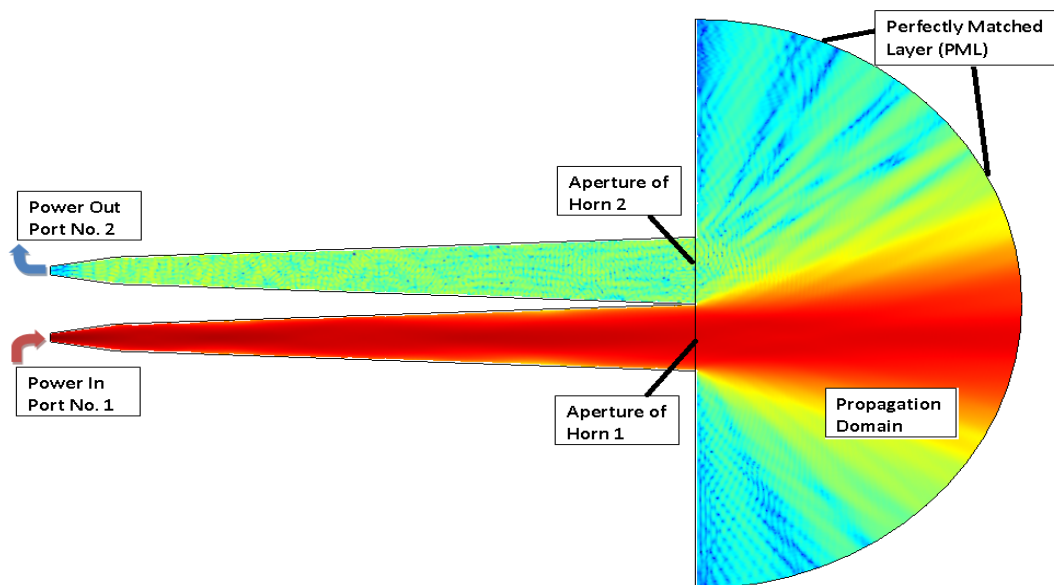


Figure 3.26: Screen shot of COMSOL model of optical cross-talk in the SAFARI horn array.

Figure 3.26 shows a screen shot of a 2D model of the transmit/receive problem just described that was built with COMSOL multiphysics modelling software. As can be seen from the image the COMSOL software is ideal for this analysis due to the ability to include a propagation domain that serves to link neighbouring feed horns together through free-space. However, as mentioned already the FEM approach that COMSOL employs is very computationally demanding, so modelling multiple horns even at the lowest frequencies would be impossible without some sort of super computer. In fact, as was shown in the previous section, modelling even one SAFARI horn at the lowest frequency of 4.3 THz was just about manageable if the PEC and PMC symmetry boundaries were used to reduce the problem size to one quarter of the original full horn model.

The most computationally efficient way to model this optical cross-talk problem

for the SAFARI horns using FEM analysis, and without resorting to the use of a super computer, was to take advantage of the 2D modelling environment available with COMSOL. This 2D simulation format is very computationally efficient but it was unclear how accurate it would be. In order to investigate the accuracy of the 2D approach two smaller horns were modelled in both the 3D and 2D COMSOL environments and the results were compared. Figure 3.27 shows a cut through the E-plane of the 3D COMSOL model. The same VNA example horn from the previous section was used again for this analysis in which the distance between the radiating and receiving horns was incrementally increased.

It was considered important to examine how the cross-talk levels changed with separation distance in both the E-plane and the H-plane as the fields behave very differently in each plane unless some sort of mode mixing is carried out by using corrugations or some sort of smart profile. In a straight, non-profiled, smooth walled horn the electric field will smoothly approach zero toward the boundary of the horn in the H-plane, whereas the field will be significantly greater than zero at the horn boundary in the E-plane; usually approximately 65% of the on axis intensity. Therefore it would be expected that the levels of cross-talk will be greater in the E-plane both through radiative processes and possibly through induced surface currents across the boundary joining the apertures of the two horns.

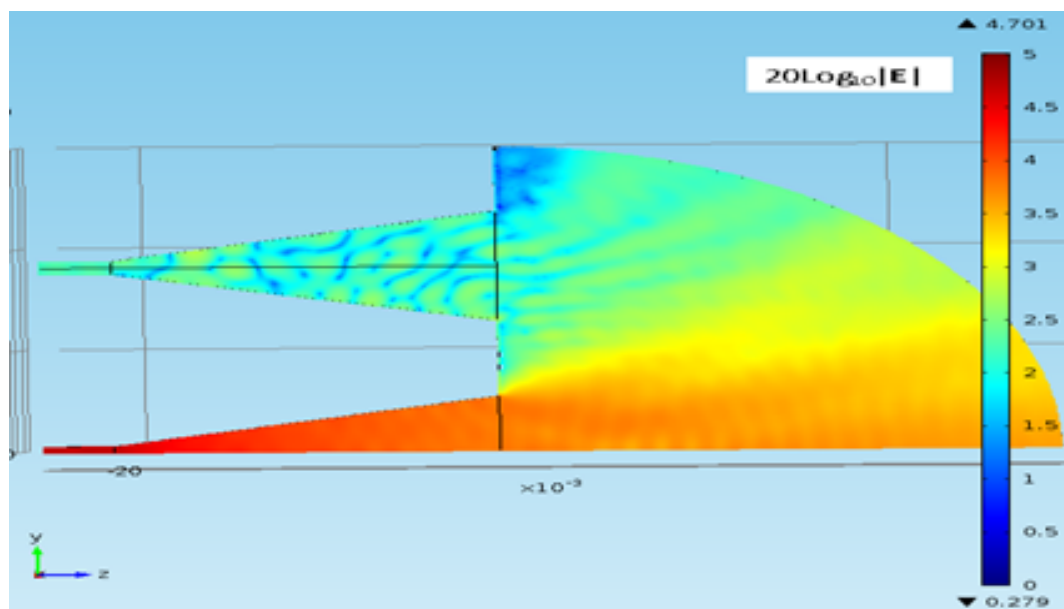


Figure 3.27: Screen shot of the example horn cross-talk model showing a cut through the E-plane.

The level of cross-talk can be calculated in the post-processing mode of COMSOL following the completion of the solver. It is calculated by integrating the power

across the surface of the detector port 2 and then dividing the result by the total input power; usually 1 Watt in the form of a particular TE or TM mode. This method will give an upper limit on the cross-talk level for the particular arrangement since not all this power will couple into the waveguide that will typically join the horn to the detector cavity. A more accurate method for calculating the cross-talk is to examine how much of the power detected at port 2 actually couples to the eigenmodes of the waveguide. This is the S_{21} parameter and is defined as follows:

$$S_{21} = \frac{\int_{Port2}(E_c \cdot E_2^*)dA_2}{\int_{Port2}(E_2 \cdot E_2^*)dA_2} \quad (3.15)$$

where E_c is the total electric field across port 2, and E_2 is the electric field eigenmode of the rectangular waveguide that has the same transverse dimensions as the exit aperture of the receiving horn. The overlap integral is then normalised with respect to E_2 . The subscript 21 represents power that will couple to port 2 from the input field at port 1.

The value of the return power S_{11} can also be calculated in a similar manner by:

$$S_{11} = \frac{\int_{Port1}((E_c - E_1) \cdot E_1^*)dA_1}{\int_{Port1}(E_1 \cdot E_1^*)dA_1} \quad (3.16)$$

The subscript 11 represents power detected at port 1 from port 1.

Figure 3.28 shows the predicted results of incrementally increasing the separation distance between the two example feed horns. As was expected the levels of cross-talk are indeed significantly higher in the E-plane data. What is also clear is that there is relatively good agreement between the 2D and 3D data, at least in terms of the general trend. There are some differences between the two but the general trends are in agreement, and they are of the same order of magnitude. Based on these results it can be assumed that a 2D analysis of optical cross-talk for the SAFARI horns can be relied upon to give an approximate result that is of the correct order of magnitude.

As was done with the analysis of the effect of induced surface currents on far-field patterns, the most extreme possible case was examined so that an upper limit on cross-talk could be calculated. As before a uniform waveguide was considered to have to the lowest directionality of any waveguide component (ignoring instruments such as isotropic radiators). A similar cross-talk analysis to that performed for the small horn was carried out for two uniform waveguides in an array. As was expected

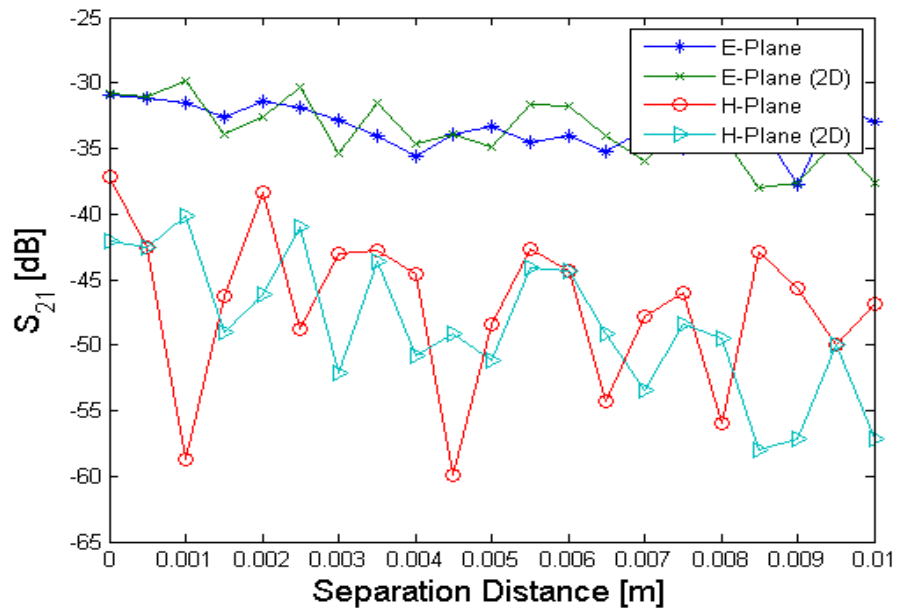


Figure 3.28: Predicted optical cross-talk levels between two small pyramidal VNA horns at 100GHz. It is clear that the levels are significantly greater in the E-plane.

the levels of detected power by the neighbouring waveguide were significantly greater than the case of a horn, and a neighbouring waveguide in the E-plane again gave rise to much higher levels than one in the H-plane. Figure 3.29 shows how the cross-talk between two rectangular waveguides varied over a range of separation distances in both the E-plane and H-plane.

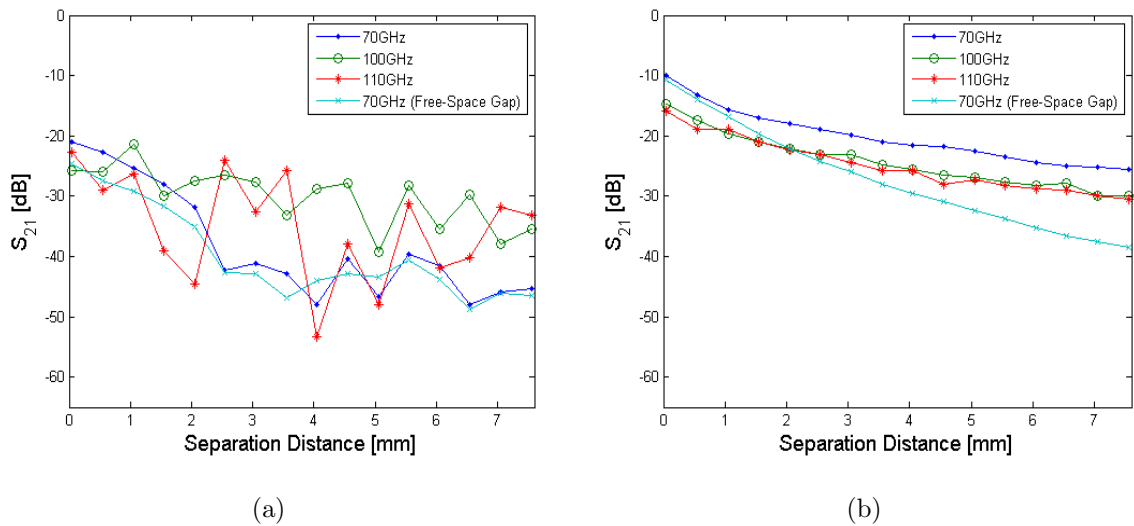


Figure 3.29: Predicted optical cross-talk levels between two WR-10 waveguides at three test frequencies in (a): the H-plane, and (b): the E-plane. The 70GHz frequency was first modelled with a conducting plane separating the horns, and then a free-space plane.

An interesting feature of the waveguide cross-talk plots is how much smoother the fall-off of detected power is in the E-plane compared to the H-plane as the waveguides are separated. The maximum levels were found at the lowest frequency

of 70GHz, so this frequency was chosen for an investigation into the difference between including a conducting boundary between horns or a free-space boundary. Employing a PEC boundary is representative of waveguides in an array, whereas a free-space boundary represents the waveguides in free-space and therefore not connected through currents. The aim of this analysis was to try to determine if the cross-talk effects were the result of radiative processes through coupling of EM fields, or induced surface currents across the boundary that separates the guides.

The plot shown in Figure 3.29(a) for a neighbouring waveguide in the H-plane seems to indicate that a conducting boundary can affect the levels of cross-talk by as much as 5dB when the horns are very close together. As the separation distance is increased the effects of the conducting boundary decrease. This would be expected as the electric field goes to zero at the aperture of the guide in the H-plane meaning that few surface currents would be expected to be induced across the adjoining boundary. Figure 3.29(b) shows that as the separation distance between two waveguides in the E-plane is increased the conducting boundary has a greater effect. Again this would be expected due to the relatively large magnitude of the electric field at the aperture of the waveguide in the E-plane. The electric field can excite surface currents across the adjoining boundary meaning that removing the PEC condition reduces the levels of cross-talk detected.

With a good understanding of the processes governing cross-talk between neighbouring waveguide structures, two SAFARI horns were then modelled in a similar manner to that described above but only in the 2D COMSOL environment due to electrical size of the horns. Three spot frequencies corresponding to the lowest, intermediate, and highest end of the S-Band were examined for various TE and TM modes. The structure of the field in the third (unaccounted for) dimension, which would be in and out of the screen in the z direction since the model plane on-screen represents the $x - y$ plane, is assumed to be constant. The transverse fields can be thought of as having subscript $m = 0$ in a TE_{0n} mode or $m = 1$ in a TM_{1n} mode that would exist in a three dimensional model. However it is again an approximation since with the real 3D horn the presence of conducting walls bounding the fields in the z direction will have an effect on the field structure in the other two directions, particularly if the mode is close to cut-off.

Another issue with the 2D environment is that for any TE_{0n} mode analysed

in the on-screen ($x - y$) plane, the analysis is always carried out in the H-plane. In other words the 2D model of TE modes represents two horns side-by-side in the H-plane. However the 3D cross-talk study performed on the example horn in the previous section demonstrated that the cross-talk levels are significantly higher in the E-plane. In order to analyse cross-talk in the E-plane using the 2D environment TM modes were considered as this allowed post-processing analysis of power flow in the E-plane. Before the analysis was carried out a separate investigation was performed in order to determine if different mode orders gave rise to varying levels of cross-talk. If the cross-talk proved to be independent of mode order then 2D analysis of the TM_{11} mode would provide a means for determining an approximate value of the SAFARI horn cross-talk in the E-plane, accurate to within an order of magnitude. Likewise, 2D analysis of the TE_{01} mode would provide a means of evaluating the cross-talk in the H-plane to within an order of magnitude.

The first simulations involved examining cross-talk levels for multiple propagating modes in the SAFARI horn array. Three frequencies were simulated at two values of separation distance corresponding to the most extreme case of $d = 0\text{mm}$, and the value of the current SAFARI horn array design of $d = 0.19\text{mm}$. Figure 3.30 shows that the TE_{01} , TE_{02} and TE_{03} modes gives rise to almost identical levels of cross-talk at each of the test frequencies. The TM modes are also in very good agreement with the largest difference of about 2dB at the intermediate frequency. What is clear is that analysis of the TM modes results in much larger levels of cross-talk as was expected since the TM mode analysis represents two horns in the E-plane. The post-processing analysis of the TE modes carried out in the H-plane shows significantly lower levels of spill over as expected.

With confidence that there is relatively low dependence on mode number for cross-talk levels, the next analysis that was performed was a parametric sweep for separation distance between two SAFARI horns for the lowest frequency of 4.3 THz and the highest frequency of 10 THz. Figure 3.31(a) shows the results. Again it can be seen that there are significantly higher levels in the E-plane data compared to the H-plane data as would be expected, however even when the horn apertures are allowed to touch the levels do not exceed -30dB. The cross-talk levels are then lower for the higher frequency data which again would be expected since bore-sight gain generally increases with frequency, and since gain is related to directivity then

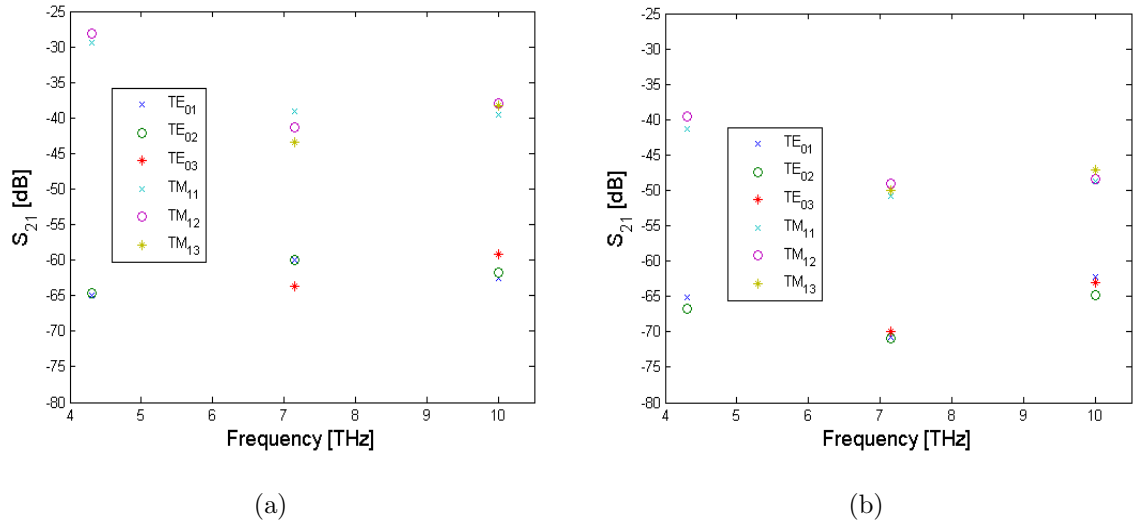


Figure 3.30: Levels of cross-talk in SAFARI horn array for various propagating modes. Three test frequencies were examined in each instance. (a): Cross-talk levels for zero spacing between horn apertures. (b): Cross-talk levels for 0.19mm spacing between horn apertures.

the higher frequency beams would be expected to have less power off-axis.

Figure 3.31(b) shows the results of a frequency sweep that was analysed across the full operational range of the SAFARI S-Band array. The sweep was across 4.3 to 10THz for 50 spot frequencies at 0.114THz intervals. Again there are significantly higher cross-talk levels in the E-plane, but it is below -30dB right across the band. It should be again pointed at that these results only provide an approximation. This is due to the analysis being carried out in the 2D COMSOL modelling environment which was shown to sometimes yield inaccurate results, some of which can be significant as can be seen at certain frequency values in Figure 3.28. A final verification using the 3D COMSOL package on a super computer would be required for complete confidence that cross-talk levels would not be an issue in terms of the required sensitivity of SAFARI.

The levels of cross-talk that were calculated from the simulations described in this section are not considered to be of concern for a SAFARI-like instrument. Even though -30dB is a significant level for some aspects of the instrument such as the magnitude of the far-field beam at large angles, the optical cross-talk will only be due to reflections of power from a horn rather than a radiating horn. Therefore the initial emitted power at the 'radiating' horn will already be very small, so -30dB of an already low-level source will have little to no effect compared to the incoming source signal.

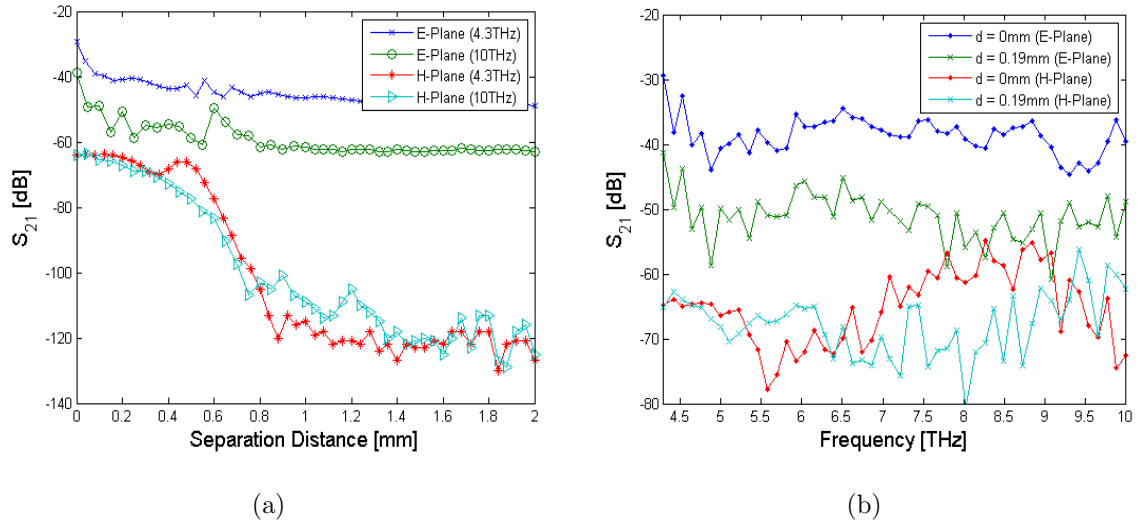


Figure 3.31: Predicted cross-talk levels in SAFARI horn array. (a): Predicted levels for various separation distances. (b): Predicted levels for a frequency sweep from 4.3 to 10THz.

3.2.3 Experimental Verification

In order to verify the optical cross-talk simulations presented in this section a series of measurements were carried out using the VNA at NUIM. Two WR-10 waveguides were chosen rather than two horns since the poor directionality of uniform waveguides allows for a stronger detectable signal, as was shown in the simulations in this section. A single separation distance was chosen with its value constrained by the dimensions of the waveguide flange sizes, as shown in Figure 3.32.

A frequency sweep from 75 to 100 GHz was carried out in both the E-plane and H-plane. The results of the measurements are shown in Figure 3.33, where the results of a corresponding FEM model are also shown for comparison. It is clear that there is excellent agreement in the E-plane, and relatively good agreement in the H-plane considering the very low levels measured. What should be noticed though is that the H-plane data in the FEM simulation appears to indicate an upper limit on the level of crosstalk since the levels in the measured data are consistently lower than the model across the band. This indicates that the models can be trusted as they appear to represent a worst case scenario.

The optical crosstalk tests presented here are clearly trivial measurements to perform. However, they were important nevertheless since they served to verify the simulations presented throughout section 3.2.2. It would also have been possible to cut the waveguides, and sacrifice the flanges. However, because this would have rendered the waveguides useless afterwards, and because of the previous good

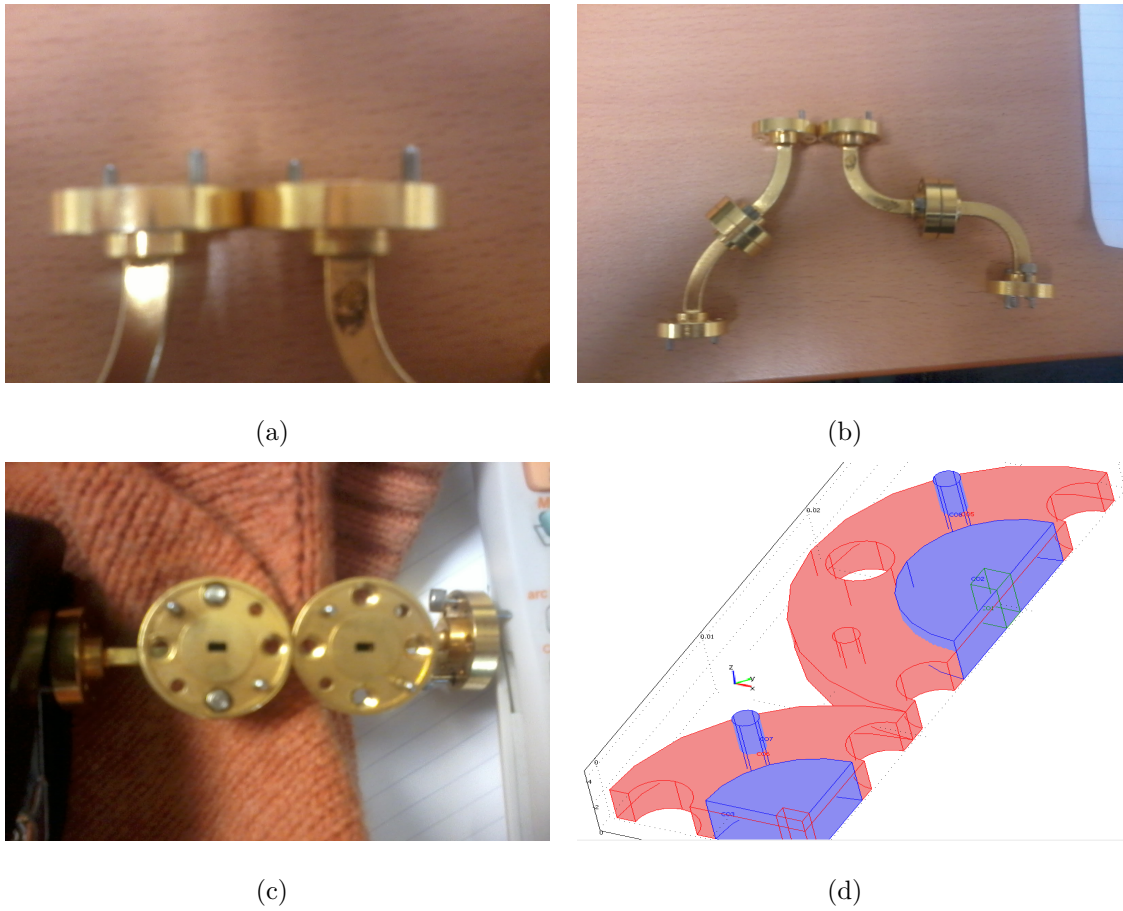


Figure 3.32: Photographs of WR-10 waveguides (a) to (c), and CAD model of WR-10 waveguide face. The holes and connecting dowels were included in the COMSOL simulations so as to match the experimental set-up (d).

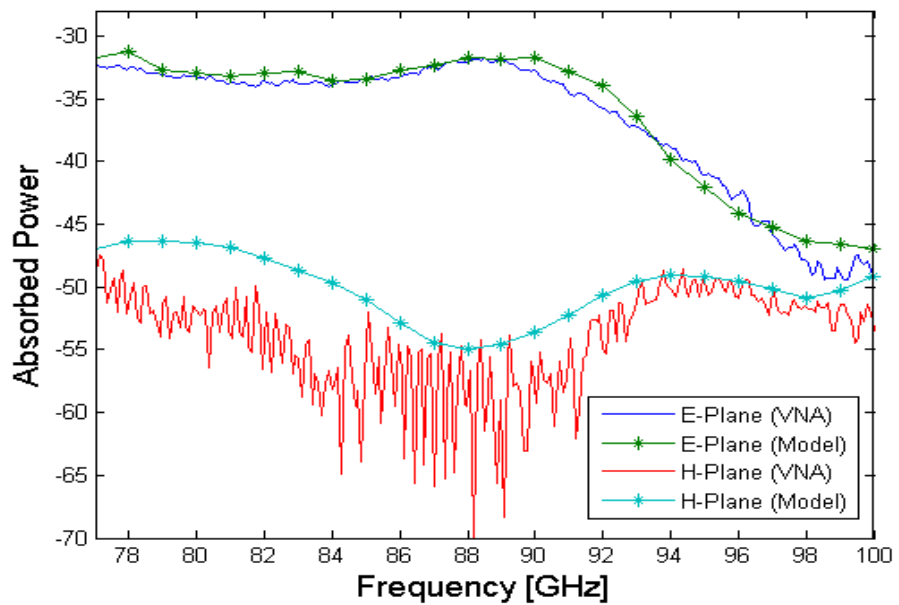


Figure 3.33: Optical crosstalk between two WR-10 waveguides measured with the VNA at NUIM. The simulation results shown were performed using COMSOL.

agreement reported, it was chosen not to take the destructive route.

3.3 Characterising Throughput of SAFARI-Like Multi-Moded Feed Horns

3.3.1 Background

The SAFARI research team at the SRON is currently performing a detailed analysis of a single SAFARI-like pixel in what they are calling the SAFARI testbed [Audley *et al.*, 2013]. Figure 3.34 shows a schematic that highlights the main components of the system. The testbed is an ultra-low background test facility that consists of a multi-stage refrigerator that is pre-cooled by a Cryomech PT-415 pulse-tube cooler which is attached to the 50-K and 3-K stages. The SRON team report base temperatures below 8 mK on the mixing chamber, and describe operating detectors in the dark with bath temperatures as low as 15 mK. The primary aim of the SAFARI testbed is to characterize and qualify the SAFARI focal plane arrays and readout before they are integrated into the SAFARI instrument, and the testbed is now being used routinely for measurements of prototype SAFARI detectors.

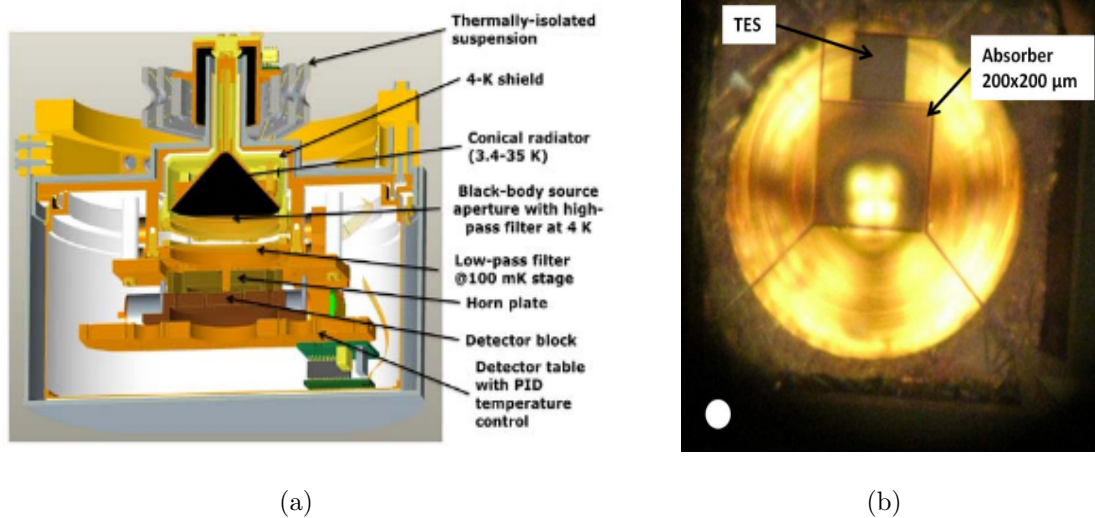


Figure 3.34: (a): A schematic of the SRON SAFARI S-Band testbed that is currently being used to characterise a single SAFARI-like pixel. (b): A micrograph of the TES coupled to the Ta absorber in front of the hemispherical backshort. The white circle in the lower left of the image represents the footprint of the $46\mu\text{m}$ exit aperture of the conical horn (image credit: SRON).

The measurements involve characterising the optical response of the TES detectors designed for SAFARI's short-wave band (S-Band) focal plane array (FPA) that is designed for operation across a frequency range of $30\text{--}70\ \mu\text{m}$. However if the optical response of the TES is to be precisely characterised, then the effects of

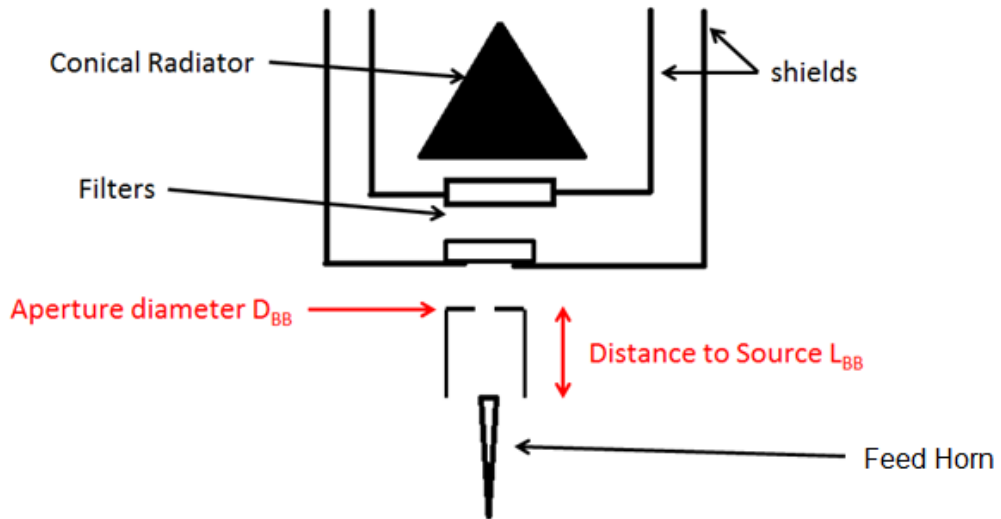


Figure 3.35: Schematic showing the positioning of the horn, aperture, source, etc. of the SRON SAFARI S-Band testbed (image credit: SRON).

all other components in the optical system must be taken into account. For example the spectrum of the blackbody source must be known and the throughput of the horn as a function of frequency should be well understood.

In this section an experiment to try to characterise the frequency dependent throughput of a SAFARI-like horn is described. The aim of the experiment was to prove the concept that such a method, as will be discussed, could be used to measure the increase in throughput as a function of increasing frequency as more modes begin to propagate as the 'cut-on' frequencies of the higher order modes are reached. The detectors of the SAFARI imaging FTS will require such multi-moded feed horns (i.e. feed horns fed by oversized waveguides) to direct the signal toward the TES's that will be housed inside integrating cavities.

These feed horns will have their own frequency profile along with the profile of the imaging FTS and the detector itself. This is because the number of modes that can propagate through a waveguide structure depends on the transverse dimensions of the structure relative to the wavelength of the radiation. The larger the cross sectional area of the guide compared to the wavelength, the more modes it will allow to propagate through it. And since each propagating mode can carry power through the structure then we would expect the throughput of the horn to increase as a function of increasing frequency. It will therefore be important to take account of the effect of all the components of the instrument as a function of frequency to fully understand the detected power by the TES's. In this regard it is the frequency

response of SAFARI-like feed horns that is discussed in this section.

What can be expected for a multi-moded horn with a straight smooth walled waveguide section is that as the frequency is increased the amount of power passing through the horn should also increase. In fact due to the waveguide section the increase should occur in steps as each higher order mode 'cuts on'. This is because each propagating mode has a particular cut-off frequency, below which the mode will not propagate. The cut-off frequency f_{co} for a given mode depends on the dimensions of the waveguide and is described by 3.17

$$f_{co} = \frac{c}{2\pi} \sqrt{\left(\frac{n\pi}{a}\right)^2 + \left(\frac{m\pi}{b}\right)^2} \quad (3.17)$$

where c is the speed of light, a and b are the width and height of the waveguide in the transverse direction, n is an integer corresponding to the variation of the electric field in the x direction, and m is an integer corresponding to the variation of the electric field in the y direction.

The SAFARI testbed described above is currently using a smooth walled conical feed horn with no waveguide section for coupling the radiation to the detectors at frequencies ranging from 4.3THz to 9THz. The throughput characterisation experiment described in this section is concerned with the analysis of a smooth walled back-to-back rectangular horn configuration with a rectangular waveguide section of width $250\mu\text{m}$ and height $125\mu\text{m}$ between the two horns, but in principle the same technique could be applied to any type of feed horn. Figure 3.36(a) shows the dimensions of the horn that was chosen for characterisation. Figure 3.37 is a micrograph taken of the waveguide section of the back-to-back horn structure. As the right side of the image shows there is an excellent finish on the structure even at these extremely small scales. Figure 3.36(b) displays a human hair that is approximately $100\mu\text{m}$ in width which is just slightly smaller than the width of the waveguide section of the back-to-back structure.

Figure 3.38 shows a simple geometrical analysis of propagating mode number as a function of frequency for a waveguide with the dimensions described above. The expected number of modes based on a $1/\lambda^2$ approximation is shown for comparison. In fact if there was no uniform waveguide section to act as a mode filter the expected throughput as a function of frequency would be expected to look more like the smoothly increasing $1/\lambda^2$ profile. The reasons for this are explained in detail in

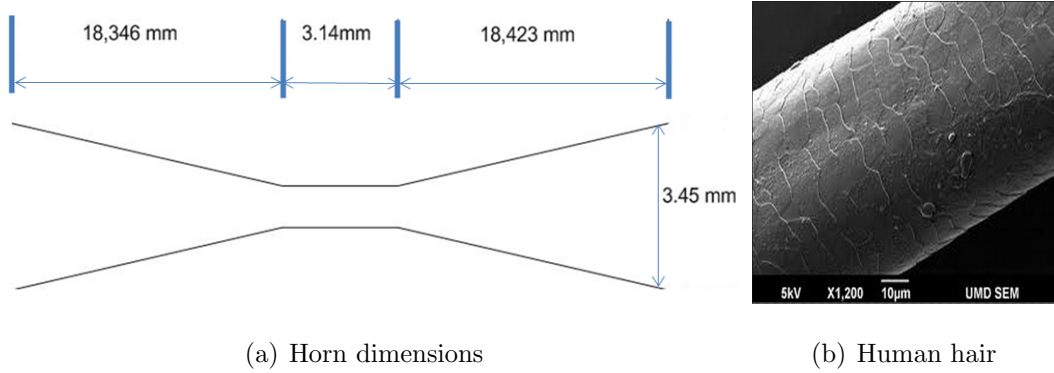


Figure 3.36: (a): Dimensions of back-to-back horn that was characterised at SRON. (b): Micrograph of a human hair for a reference of micron scales.

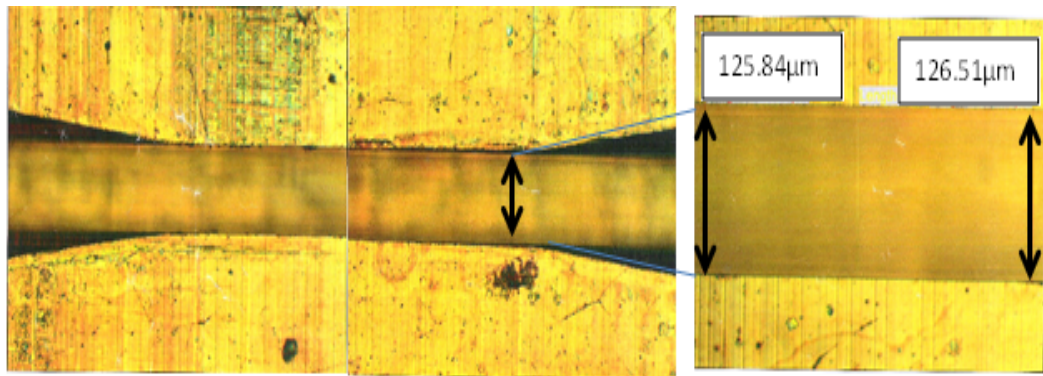


Figure 3.37: Dimensions of waveguide section of horn that was characterised at SRON. The expanded image on the right shows how good the etching process is at achieving a smooth finish on the structure. Two separate precision measurements were made of the height of the waveguide section showing $125.84\mu\text{m} \pm 10\text{nm}$ and $126.51\mu\text{m} \pm 10\text{nm}$.

chapter 4 and it arises due to the partially evanescent behaviour of conical modes when they are close to cut-off. The presence of the waveguide section between the two horn sections is expected to yield a much more quantized or stepped profile, similar to the geometric solution in the plot.

It can be seen that the waveguide has a 'switch-on' frequency of 600GHz, and if it is assumed that each propagating mode carries equal power then the graph can be interpreted as throughput vs. frequency. The frequency of the sources ranged from 200GHz to 4THz, and the cut-on frequencies of the first 20 modes within this range are shown in Table 3.2.

Some of the issues that inevitably arise during an analysis of such tiny feed horns at THz frequencies are the high absorption due to water vapour in the air, the noise generated by the detector itself at temperatures above liquid Helium levels, and the tiny size of the actual horns leading to difficulties in alignment and reduced throughput levels. The solutions to all of these issues are discussed in the next

Cut-Off Freq. (THz)	Mode	Total No. of Modes	Cut-Off Freq. (THz)	Mode	Total No. of Modes
0.6	TE_{10}	1 ('Switch-On')	2.4	TE_{02}	11
1.2	TE_{20}	2	2.4	TE_{40}	12
1.2	TE_{01}	3	2.474	TE_{12}	13
1.342	TE_{11}	4	2.474	TM_{12}	14
1.342	TM_{11}	5	2.683	TE_{22}	15
1.697	TE_{21}	6	2.683	TM_{22}	16
1.697	TM_{21}	7	2.683	TE_{41}	17
1.8	TE_{30}	8	2.683	TM_{41}	18
2.163	TE_{31}	9	3.0	TE_{32}	19
2.163	TM_{31}	10	3.0	TM_{32}	20

Table 3.2: Cut-on frequencies of the first 20 modes in the waveguide linking the back-to-back horn. The 'switch-on' frequency, based on the transverse dimensions of the rectangular waveguide section, is 600GHz.

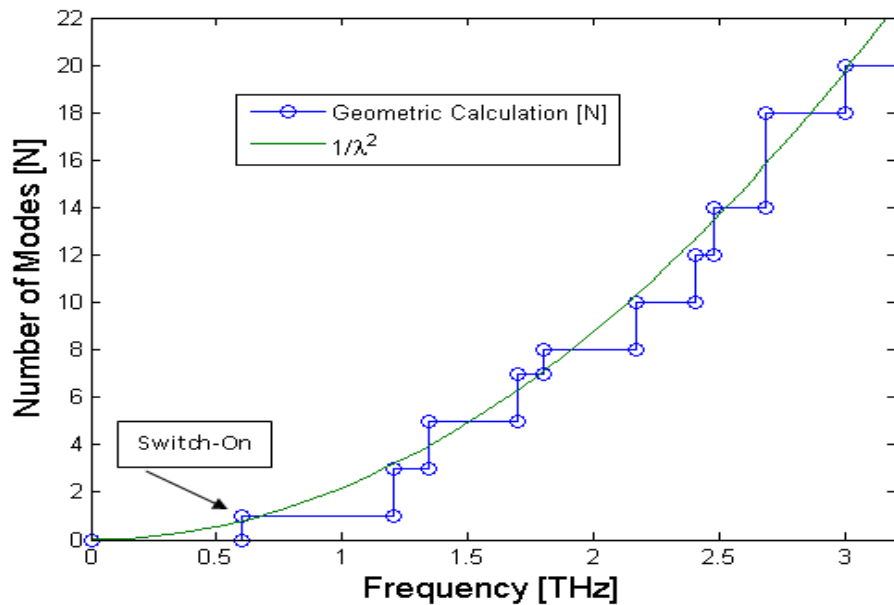


Figure 3.38: Increasing number of propagating modes as a function of frequency. If each mode is considered to carry equal power then the graph can be thought as throughput as a function of frequency also. A scaling factor of $2 \times 10^{-7} \text{m}^2$ was used to plot the $1/\lambda^2$ fit.

subsection.

3.3.2 Experimental Set-Up

An FTS based on a Michelson interferometer was used for the analysis of the horn. A detailed description of the FTS system is presented in section 1.5 of this thesis. Two different sources were employed; a high voltage mercury (Hg) arc lamp and a glow bar [Shumyatsky and Alfano, 2011]. Hg arc lamps are commonly used in a wide range of scientific experiments ([Yuana *et al.*, 2014], for example), so no description was deemed necessary. A glow bar (or globalbar) is a resistively heated rod, typically made of silicon carbide. It is somewhat similar to a tungsten filament in an incandescent light bulb. Of course any object will emit radiation with a peak intensity at a wavelength that depends on its temperature. Wien's displacement law can be used to show that for a light bulb aimed at producing visible light ($\lambda \approx 500\text{nm}$) the blackbody temperature required for the tungsten filament is $T_{BB} \approx 5,800\text{K}$. Based on Wien's displacement law then, it would appear that for the desired THz frequencies, say for example, 3THz ($\lambda \approx 0.1\text{mm}$), the temperature of the glow bar should be set to $T_{BB} = 28.98\text{K}$ for the emission spectrum to peak at 3THz and exhibit an overall intensity distribution that follows a blackbody spectrum as that shown by the green line in Figure 3.39. However, this assumes that the surroundings are cooler than the globalbar, which is not typically the case. Rather, the globalbar is usually operated at a high temperature, and then emits over a very wide spectrum, some of which covers the THz regime, but with a relatively weak output power at the THz frequencies [Shumyatsky and Alfano, 2011]. This is the scenario under which the globalbar was operated for the experiment described in this section. Research into the spectra of globalbars can be found in [Pozela *et al.*, 2013], for example.

The spectrum of the Hg lamp was not accurately known, but it was assumed to have more discrete features and also having high emission in the ultra violet (UV) requiring protective glasses to be worn. Both sources produced a large amount of low frequency noise so a beam chopper and lock-in amplifier were used to cut out these low frequencies. The beam chopper was set to 16.67Hz and the lock-in amp was set to match the frequency of the chopper.

To overcome the absorption due to water vapour in the air a vacuum system was used that completely housed the source, the FTS, the horn, the detector, and the lenses (which will be discussed shortly) as illustrated in the schematic in Figure 3.40. The vacuum tube system, FTS, and pump are shown in Figure 3.41.

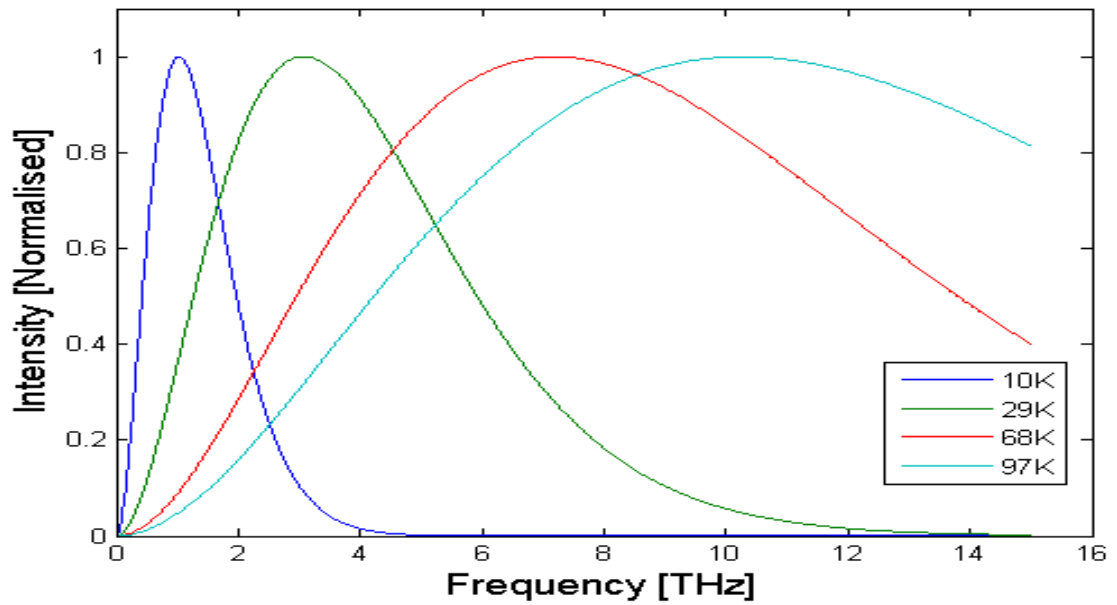


Figure 3.39: Predicted blackbody emission for radiating sources of various temperatures.

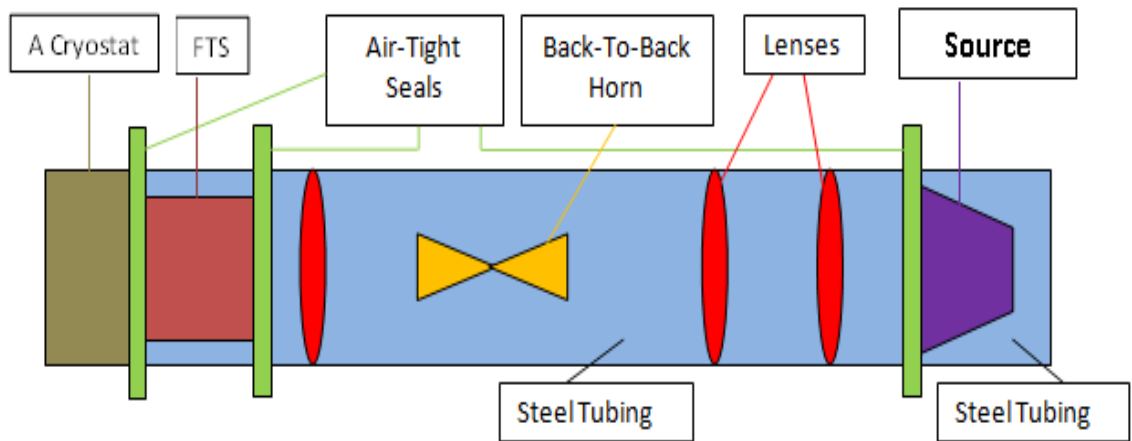


Figure 3.40: Schematic of the vacuum system used to house the horn, lenses, and FTS for throughput experiment. Each section of steel tubing was connected together with air-tight seals before pumping commenced.

To deal with the thermal emission of the bolometer [Hulbert and Jones, 1955] (which would lead to noise in the signal detected) it was housed in a two-stage cryostat and cooled to near absolute zero. Liquid nitrogen was first used to cool the central stage of the cryostat to 77 K. The liquid nitrogen was then pumped out of the central stage and liquid helium was pumped in, thereby reducing the temperature to 4.3 K. Liquid nitrogen was then pumped into the second (outer) stage of the cryostat to maintain the low temperature of the detector by reducing the boil-off rate of the liquid He. The signal detected by the bolometer was fed to an amplifier which amplified it by a factor of either 200 or 1,000 (depending on the setting). The cryostat also had three low pass filters built into it which cut off frequencies above

either 3THz, 9.4THz, or 18THz, depending on the setting chosen.

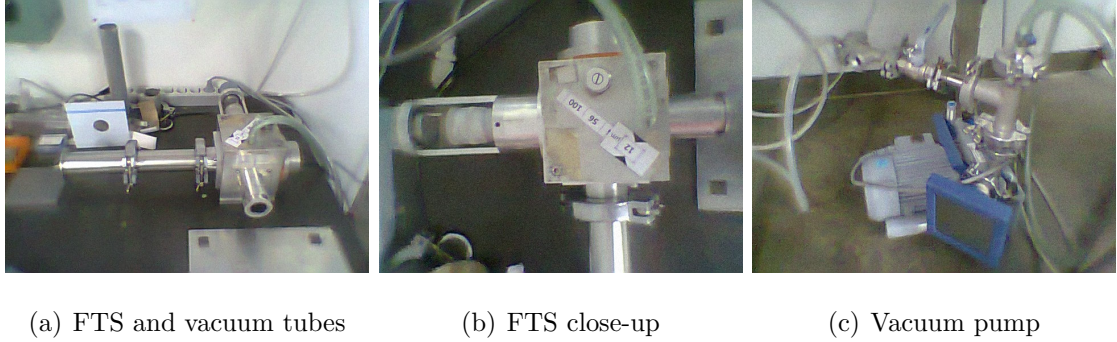


Figure 3.41: FTS and vacuum system.

In order to focus the source onto the aperture of the horn a three lens telescope design was decided upon, where high-density polyethylene (HDPE) lenses were chosen as the HDPE material is well suited for control of radiation at THz frequencies due to its excellent clarity, chemical stability, and the fact that it is easily machinable [Lee, 1979]. HDPE is also particularly suited for THz radiation due to its low loss. The design was comprised of three lenses with three different focal lengths, two of which were positioned between the source and the horn, and one positioned between the horn and the FTS (see Figure 3.42). The optical modelling package ZEMAX was used for the design of the lens system. The optimisation tool was used to find the optimal foci of the lenses and their positioning. The result was an 80mm focal length lens positioned 80mm (d_1) from the source, a 180mm lens at 40mm (d_2) from the first lens, the horn positioned 180mm from the 180mm lens (d_3), and finally a 60mm lens located 60mm from the exit aperture of the horn (d_4). It should be noted that the 180mm lens is focussed on the entry aperture of the horn as the phase centre was unknown. All the lenses had diameters of 40mm.

The first lens (L1) was a relatively fast lens ($f/2$) that served to parallelise quickly the source. The 180mm lens ($f/4.5$) labelled as L2 was designed to slowly focus the beam to match the slow angle of the feed horn. The fast 60mm ($f/1.5$) lens labelled as L3 was aimed to capture the light emerging from the horn and parallelise the beam before it entered the FTS; (if a good interferogram is to be observed it is important to have a parallel beam entering the FTS as this is assumed by optical design). The entry port of the FTS was positioned at 70mm from the third lens. The cryostat housing the detector was connected to the output port of the FTS.

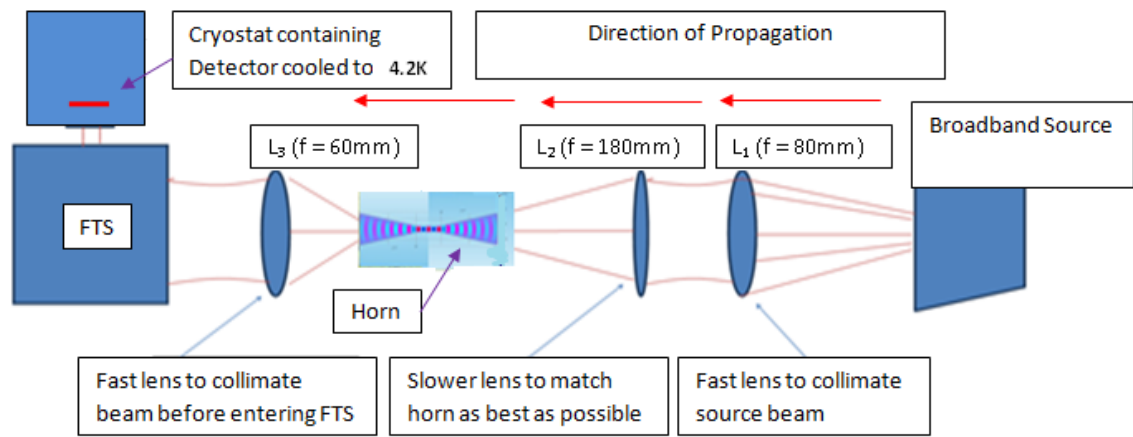


Figure 3.42: Diagram showing the placement of the horn and lenses.

3.3.3 Manual Optimisation of Set-Up

Before the system was put under vacuum it was decided to experiment with the positioning of the lenses and horn to verify that the prescribed separation distances based on the lens focal lengths were indeed optimised. This was to ensure that there were no minor errors in the curvature of the lenses, etc. due to manufacture tolerances. If the curvature of any lens deviated from the prescription then the focal length would also deviate from the expected value. Also the refractive index of the lens material was not accurately known so again the focal lengths of the lenses came into question to some degree.

An optical bench was set up with the horn and lenses positioned at the distances calculated by ZEMAX. The set-up was the same as described above but without the vacuum system. Also the FTS was not used as at this point the aim was just to optimise the positions of the components for maximum throughput of the horn. The glow bar that was described above was used as a source and placed 80mm from the first lens L1. 5 V was supplied to the glow bar with a current of 3.92 A. The cooled detector was placed at 60mm from the third lens L3. The initial positions of the back-to-back horn and lens L2 were as shown in Figure 3.42.

The lenses were attached to metal screens with apertures that had the same dimensions as the lenses, and the horn was attached to a similar screen with an aperture the same size as the horn opening. The optical bench was set up such that the transverse positions (x) of the horn and lenses were aligned and fixed by keeping the edges of the lens/horn holders tight against a metal straight edge that

was itself aligned perpendicular to the direction of axial propagation. The optical components were free to move in the direction of axial propagation (z). The heights (y) of the components were set equal to each other and kept fixed by manufacturing the lens/horn holders appropriately. Part of the set-up can be seen in Figure 3.43, although the transverse alignment bar (straight edge) and the detector are not in the image at that point. In retrospect some absorber material should have been used to coat the metal parts of the screens as standing waves could possibly arise in such a set up.

As the lenses and horn were incrementally moved, one at a time, the value of the detector voltage was monitored. An audio device was connected to the output of the lock-in amplifier so that as the detector power increased an audio signal could be heard to increase in pitch. This allowed the positions to be varied with real time audible feedback indicating increase or decrease of received signal.

Through the method described above it was discovered that indeed there were errors on the assumed focii of the lenses. The 60mm lens was found to have a focal length of 64mm, the 80cm lens had a focal length of 82mm, and the largest deviation was on the 180mm lens which actually had a focal length of 167mm. However it should be noted that a small amount of the apparent error on the 180mm lens (L2) is likely due to the phase centre of the horn being located inside the horn. It would therefore make sense that the lens would be better positioned closer to the horn since the focal point/plane should ideally be situated at the phase centre of the horn. The same might be true for the error on the 60mm lens L3 since this was directly coupled with the horn also.

Another test that was carried out at this point was an analysis of the spot size of the beam at the position of the entry aperture of the horn. Obviously the aim was to have as small a spot size as possible in order to focus the maximum amount of power into the horn. Although the method used did not give a direct measure of the spot size, it did give a good indication of the order of the size of the beam width. The method involved replacing the horn with a pinhole (small circular aperture ($r \approx 0.5\text{mm}$) in a metal screen) located at the previous position of the entry aperture of the horn. This was also the position of the beam waist which was verified in the procedure just described above. The pinhole was at the same height as the horn aperture and this height was kept fixed.

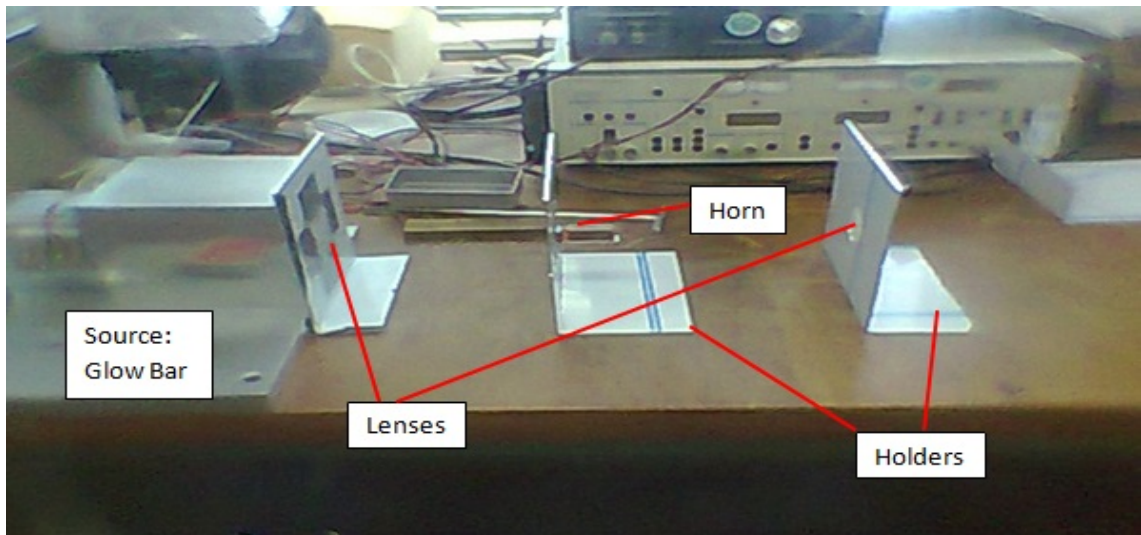


Figure 3.43: Set-up of lenses and horn for verification of optimal positioning.

Starting at the central location the position of the pinhole was varied in the horizontal transverse direction in increments of 0.5mm, out to a distance of 20mm. The pinhole was then returned to the central location and then incrementally varied in the opposite direction. At each position the detector voltage was measured and recorded and the results can be seen in the graph in Figure 3.44. The power fell to $\frac{1}{e^2}$ of the on-axis power at a distance of approximately 6mm on each side of the maximum, indicating a beam width of approximately 12mm at the beam waist. This was not ideal since the aperture of the horn was only 3.45mm×3.45mm, but it was the best that could be achieved.

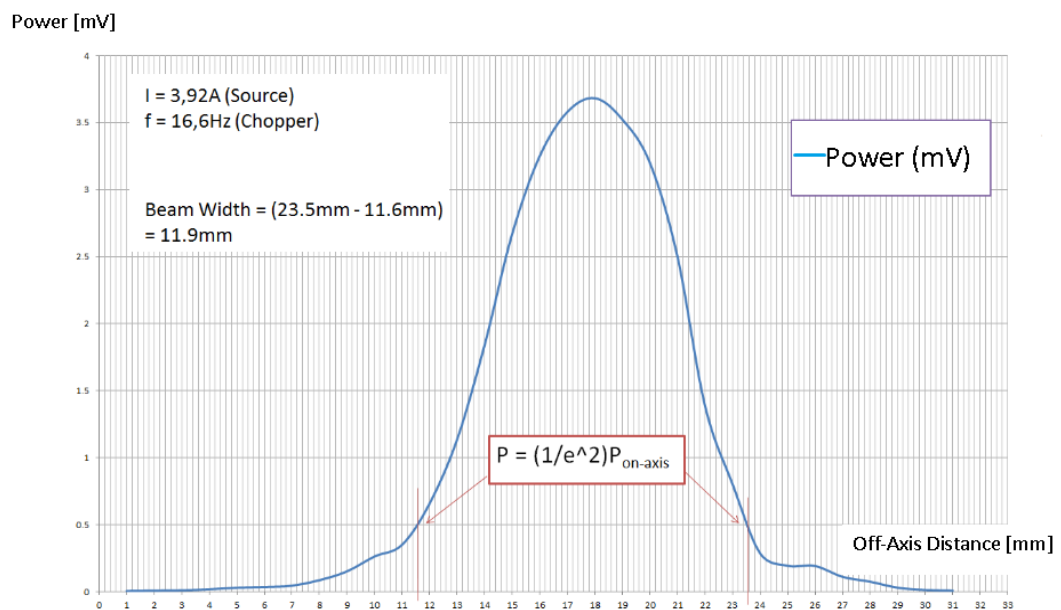


Figure 3.44: Beam width of a focussed broadband beam at the focal point of the 180mm lens.

The lens system with the pinhole in place of the horn was modelled with the GBM analysis code described in chapter 2. It was found that by including a source field corresponding to a horn with a wide flare angle a spot size of approximately 10mm in diameter was formed at the location of the pinhole. The model assumes monochromatic light as a source, and the input beam width and phase radius of curvature (input q) are somewhat arbitrary. Thus, as it stands the model is only an approximation. Further work will be required to account more accurately for the spacial and spectral distribution of the source. Figure 3.45 shows two screen shots from the Gaussian beam program that was developed by the author for modelling free-space propagation.

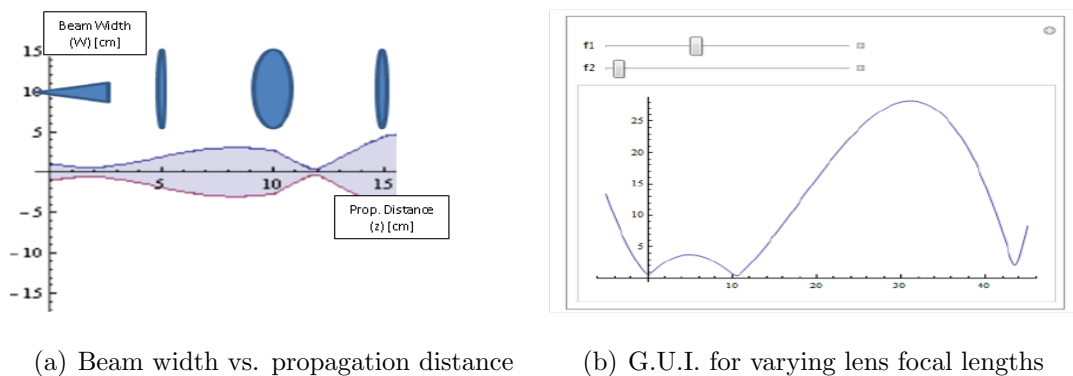


Figure 3.45: (a): Screen shot of beam width calculation from GBM analysis code. (b): Graphical user interface (G.U.I.) for varying the focal lengths of two of the lenses. The separation distances are automatically recalculated when the focal lengths are changed.

3.3.4 Alignment of the System Inside the Vacuum Tubes

An issue that arose when packing the horn and lenses into the vacuum tubes was how to rigidly fix each component in the correct position such that it would remain there and stay completely perpendicular to the direction of propagation. An earlier attempt had been made that used three thin threaded guide wires that were inserted through each component, with small nuts tightened at each surface to hold the components in place. This set-up had too much movement in it and it was very difficult to ensure that the lenses and horn were completely perpendicular to the beam once the vacuum system was sealed. An exaggerated example diagram is shown in Figure 3.46.

An improvement on this system was achieved using PVC plumbing pipes. A length of pipe was found that had almost exactly the same outer diameter as the

inner diameter of the vacuum tubing system. The diameter of the PVC pipe was just slightly too large so it was trimmed down in the workshop using a lathe. The result was a pipe that fit snugly inside the vacuum tubes. The pipe was then cut into various lengths relating to the various spacings that were required between the lenses and horn. The lenses and horn mount had diameters just slightly less than the inner vacuum tube diameter so they could be held in position by being pressed between sections of the PVC piping and then inserted into the vacuum system (see Figure 3.47).



Figure 3.46: An exaggerated diagram of how the guide wires might bend as the components are pushed through the vacuum tubing.



(a) PVC piping cut to sizes (b) Vacuum tube and PVC pipe (c) Tube with ring insert pipe



(d) Pipe section in tube (e) Optical components shown separated (f) Optical components shown snugly clamped

Figure 3.47: Some components of the set-up showing how the system was aligned and kept fixed.

3.3.5 Efficiency of FTS Beam Splitters

As will be shown in the results of the throughput experiments described in the next section, a particularly strong spectral effect in any FTS data can arise from the beam splitter if the material is too thick compared to the wavelength of the signal. A beam splitter of any thickness will give rise to reduced efficiency at certain frequencies due to destructive interference between different parts of the beam travelling different path lengths within the beam splitter material. Any signal radiation that reflects off the inner boundary of the beam splitter twice will interfere with signal propagating straight through the material. Since the phase of the doubly reflected part will be shifted with respect to the direct part of the beam some sort of interference will occur either constructive, destructive, etc.

The type of interference described above is known as the Fabry-Perot effect. Figure 3.48 shows the transmission profile of a $12\mu\text{m}$ and a $56\mu\text{m}$ Mylar beam splitter based on this Fabry-Perot effect. The data for the graphs were calculated from equations given in a paper by James and Ring [James and Ring, 1967] (see also page 256 of Goldsmith [Goldsmith, 1998]). The analysis by James and Ring was for a thin film of Melinex but the same principles can be applied to the Mylar thin film used for this experiment by simply using the correct refractive index.

The efficiency of a beam splitter in a Michelson interferometer is given by the depth of modulation of the interference fringes:

$$\eta(\sigma) = 4RT \quad (3.18)$$

where R and T are the reflection and transmission intensity coefficients respectively. If absorption of the Mylar material is neglected then $T = 1 - R$, leading to:

$$\eta(\sigma) = 4R(1 - R) \quad (3.19)$$

James and Ring (see also page 62 of [Born and Wolf, 1999]) showed that the intensity reflection coefficients could be described by [James and Ring, 1967]:

$$R_s = \frac{2r_{1s}^2(1 - \cos 2\delta)}{1 + r_{1s}^4 - 2r_{1s}^2 \cos 2\delta} \quad R_p = \frac{2r_{1p}^2(1 - \cos 2\delta)}{1 + r_{1p}^4 - 2r_{1p}^2 \cos 2\delta} \quad (3.20)$$

where the subscripts s and p refer to the two planes of polarisation of the electric field relative to the plane of incidence. δ is the relative phase difference between adjacent

emerging beams and is defined as $\delta = \frac{2\pi}{\lambda}nd\cos\phi_1$, where d is the film thickness, n is the refractive index and ϕ_1 is the angle of the beam inside the film relative to the surface normal. Finally r_{1s} and r_{1p} are the well known Fresnel amplitude reflection coefficients, and are defined as [James and Ring, 1967]:

$$r_{1s} = \frac{n_0\cos\phi_0 - n_1\cos\phi_1}{n_0\cos\phi_0 + n_1\cos\phi_1} \quad r_{1p} = \frac{n_0\cos\phi_1 - n_1\cos\phi_0}{n_0\cos\phi_1 + n_1\cos\phi_0} \quad (3.21)$$

where ϕ_0 is the angle of incidence, ϕ_1 is the angle of refraction, and n_0 and n_1 are the refractive indices of the initial medium and the final medium, respectively. Figure 3.48 shows the transmission T of a Mylar beam splitter ($n \approx 1.76$ at 1THz) for a thickness of $12\mu\text{m}$ and $56\mu\text{m}$. It is clear that the $12\mu\text{m}$ film has significantly less of an effect on the throughput of the signal over the frequency range of interest.

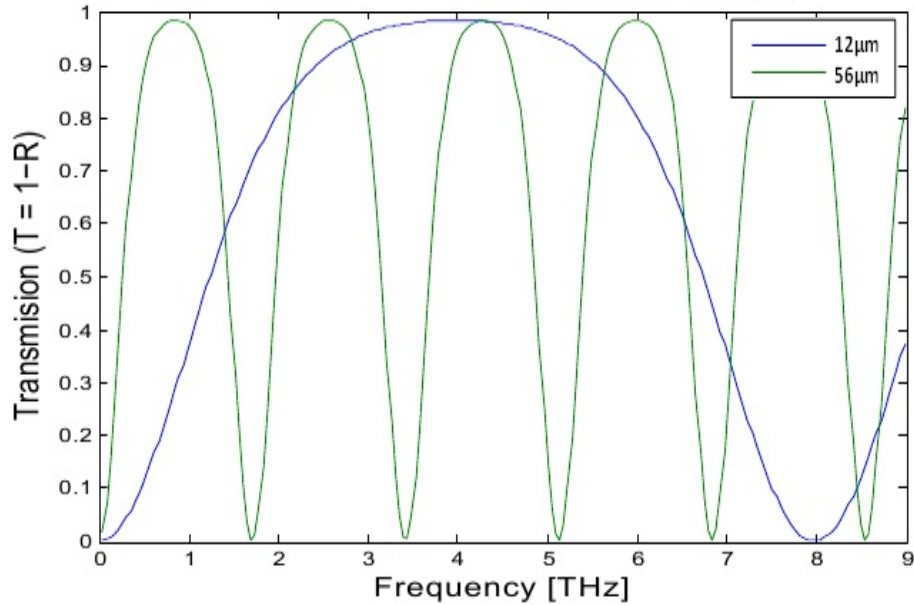


Figure 3.48: Power transmission for Mylar beam splitters of different thicknesses.

For the experimentalist interested in performing Fourier transform spectroscopy across the entire IR range using such Mylar (PET) beam splitters, a variety of beam splitter films would be required, each with a different thickness in order to access a series of discrete frequency regions, which could then be merged to form a continuous spectrum. In a paper by Homes *et al.* they explain how thick silicon beam splitters can offer numerous advantages over Mylar films [Homes *et al.*, 2007].

3.3.6 Experimental

With the lenses and horn sandwiched snugly between the pipe sections and inserted into the vacuum tubes the pump was switched on to evacuate the system. The power supply for the glow bar was switched on and ten minutes was allowed for the bar to heat up. The chopper and lock-in amplifier were switched on and the phase of the lock-in amp was locked such that it and the chopper were completely in phase (as described above). A series of scans were performed with the FTS with varying resolution and varying frequency range. Performing a scan over a longer distance range results in higher resolution in the Fourier transformed data, whereas performing a scan with smaller step size ensures higher frequencies are reached in the Fourier transformed data (see Nyquist frequency [Oppenheim *et al.*, 1999]). A number of different beam splitters were used also with the best results being obtained with the $12\mu\text{m}$ Mylar beam splitter.

Each scan that was performed for the back-to-back horn was repeated keeping all the parameters the same except with a metal screen with a small aperture in place of the horn. The aperture was given the same dimensions as the horn, and an extra length of PVC pipe was cut and placed in the vacuum system to account for the length of the horn.

The aim of doing the scans with an aperture in place of the horn was to obtain a calibration data set for each horn scan. Then by dividing the data from the aperture scans into the data from the horn scans, any spectral features not specific to the horn would be cancelled out. Such effects include the frequency response of the detector itself, the spectrum of the source, the efficiency of the FTS beam splitter, and any frequency dependent absorption profile of the PVC lenses. For example the spectra of both the glow bar and the Hg arc lamp were not accurately known, and if they were to be characterised then a well understood measurement system would be required with a detector whose spectral response was accurately characterised. The response of the bolometer that we were using was not well understood so it could not be used to properly investigate the spectra of the sources.

Figure 3.49(a) shows a plot of the back-to-back horn throughput data, and the corresponding aperture throughput data that would be used for calibration is shown in Figure 3.49(b). Figure 3.50 then shows the result of dividing the back-to-

back horn data by the aperture data in an attempt to remove all undesired spectral artefacts. The recorded noise levels in the bolometer were approximately 0.1mV, where the source was removed but everything else remained the same, including the level of vacuum.

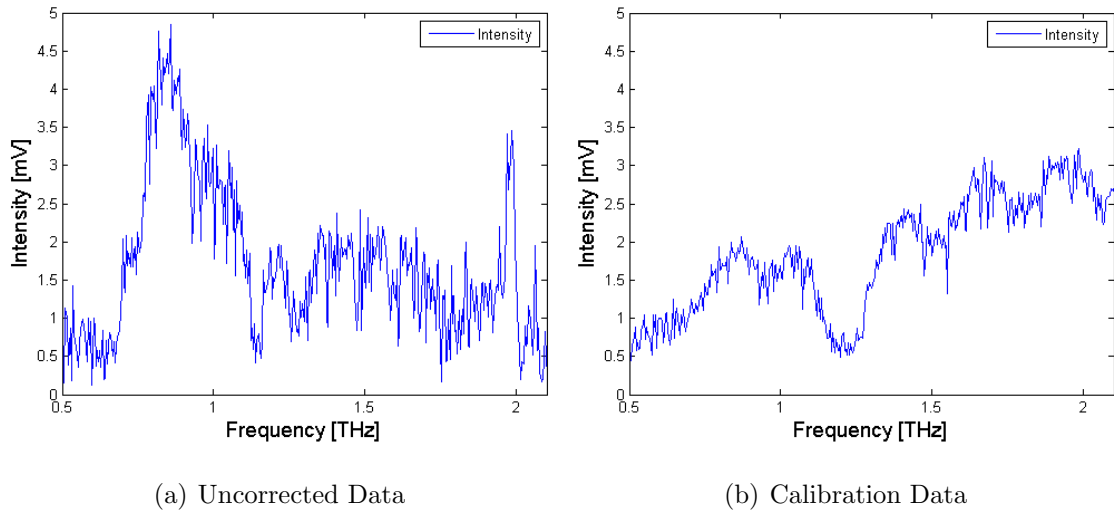


Figure 3.49: (a): Uncorrected throughput for a back-to-back horn antenna illuminated by a glow bar in a Michelson FTS. (b): Throughput of a small rectangular aperture illuminated by a glow bar in a Michelson FTS. This data was used to correct the back-to-back horn throughput data.

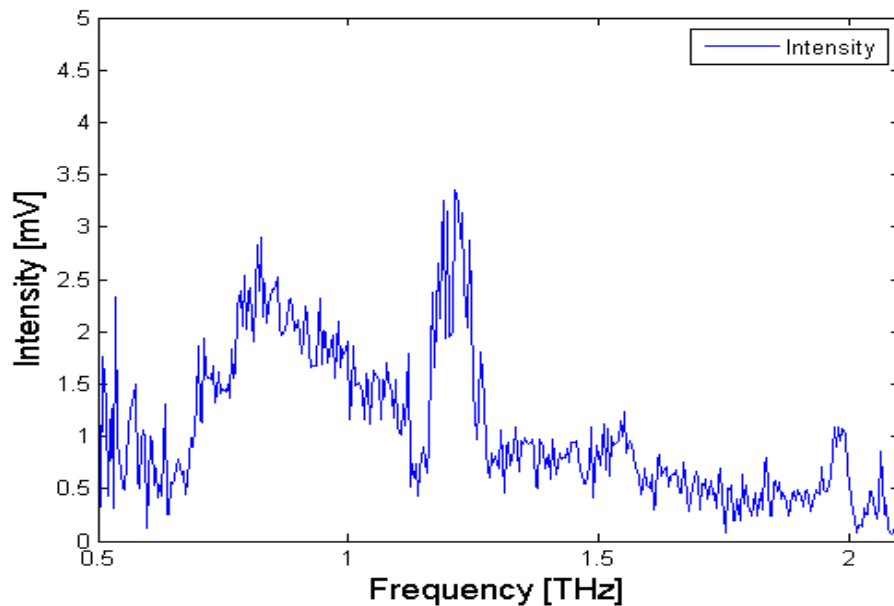


Figure 3.50: Corrected throughput for a back-to-back horn antenna illuminated by a glow bar in a Michelson FTS. The rectangular aperture data was used to correct the data plotted in Figure 3.49(a).

What should be noticed when comparing Figures 3.49(a) and 3.49(b) is that the aperture data in 3.49(b) displays a continuous increase in throughput as the frequency is increased whereas the same is not true for the back-to-back horn data

in 3.49(a). This results in the corrected throughput profile shown in Figure 3.50 exhibiting a general fall-off of power as frequency increases. As will be shown in the following results this was an ongoing phenomenon that was observed throughout the measurement campaign. The reason for this is still unclear, however some discussion on the matter is provided at the end of this section.

Performing identical scans with the rectangular aperture is analogous to using a flat field in astronomy imaging with a CCD. The flat field is aimed at correcting the image for differences in pixel efficiency from pixel to pixel. Of course we were attempting to account for a lot more variables with the aperture scans used in this experiment, however it was deemed the most accurate method with this particular set up for removing the unwanted spectral features described above.

Scan 1:

The first scan performed was with the horn in the centre of the evacuated tubing system without any lenses (see Figure 3.42). The glow bar was used as a source and the beam chopper was set to 16.67Hz with the sensitivity on the lock-in amplifier at 20mV and the time constant set to 1 second. The $56\mu\text{m}$ Mylar beam splitter was used in the FTS and a scan of 10mm was carried out with a step size of $7.5\mu\text{m}$. The 100cm^{-1} filter was selected on the detectors filter wheel, with the gain set to $200\times$. The Fourier transformed data are shown in Figure 3.51. As can be seen there is very little transmission, resulting in mostly noise in the plot. As before, the recorded noise levels (source removed) were approximately 0.1mV.

Scan 2:

The second scan carried out included the three lenses, with two of them serving to focus the source radiation onto the horn aperture and the third one positioned after the horn with the aim of forming a parallel beam for entry into the FTS (see again Figure 3.42). All the scan parameters were the same as the previous scan (Scan 1). The Fourier transformed data are shown in Figure 3.52. It is clear that there is much higher throughput when the lenses are used, and there is a sudden jump at 600GHz which is exactly the position of the 'switch-on' frequency of the waveguide section between the two horn sections. The data shown have not yet been corrected for the

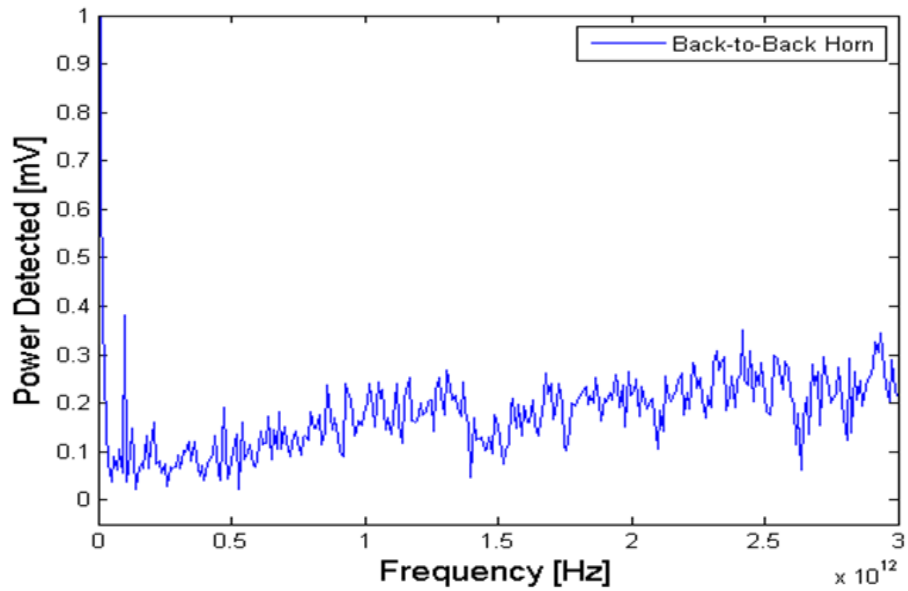


Figure 3.51: Throughput of the back to back horn with no lenses.

efficiency of the Mylar beam splitter, or any of the other undesirable effects outlined above (i.e. the data has not yet been divided by the corresponding aperture scan data). Nonetheless the 'switch-on' frequency is quite obvious and even some of the higher order propagating modes can be seen to 'switch on', for example the TE_{20} & TE_{01} at 1.2THz, and some indication of the TE_{11} & TM_{11} at 1.4THz. The positions (in terms of frequency) of the cut-on frequencies of some of the higher order modes are shown superimposed on the same graph.

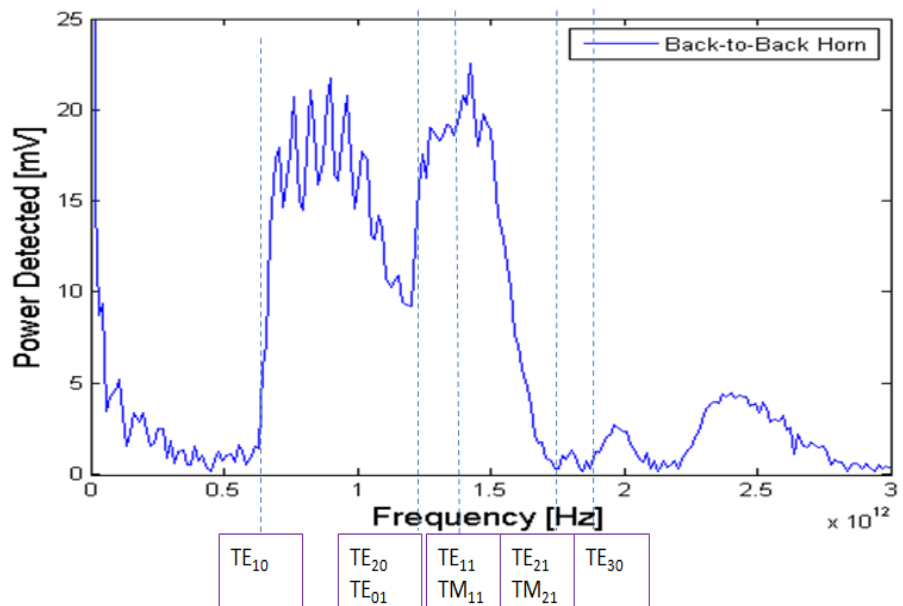


Figure 3.52: Throughput of the back to back horn with three lens optical system included.

The next graph shown in Figure 3.53 has the efficiency function of a $56\mu\text{m}$ Mylar beam splitter shown superimposed on the previous plot data. This demonstrates the strong modulating effect that such a beam splitter will have on the result. As can be seen the null in the throughput data at 1.8THz coincides exactly with the position of complete destructive interference in the beam splitter.

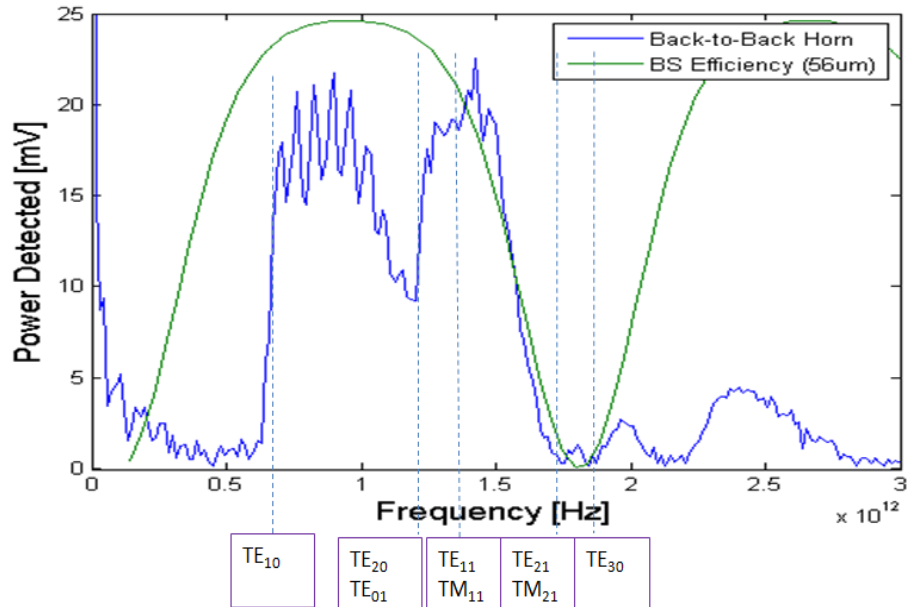


Figure 3.53: Throughput of back to back horn with three lens system, and $56\text{ }\mu\text{m}$ beam splitter efficiency.

Scan 3:

The $56\mu\text{m}$ beam splitter film was replaced with the $12\mu\text{m}$ film and another scan with the same parameters as before was carried out. A second identical scan was then performed but with the rectangular aperture replacing the horn. The back-to-back horn throughput data was then divided by the aperture throughput data for calibration. The corrected Fourier transformed data is shown in Figure 3.54 and this represents the highest quality result that was achieved using the 100cm^{-1} filter and the glow bar source during the measurement campaign at SRON.

Again the switch-on of the fundamental mode can be seen at 600GHz and some of the higher order propagating modes can be seen to 'switch on'. The TE_{20} & TE_{01} are again recognisable at 1.2THz , and the TE_{11} & TM_{11} are assumed to be the source of the increase in detected signal at 1.4THz . In fact there is also some indication of the cut-on of the TE_{21} & TM_{21} modes at about 1.7THz (both should

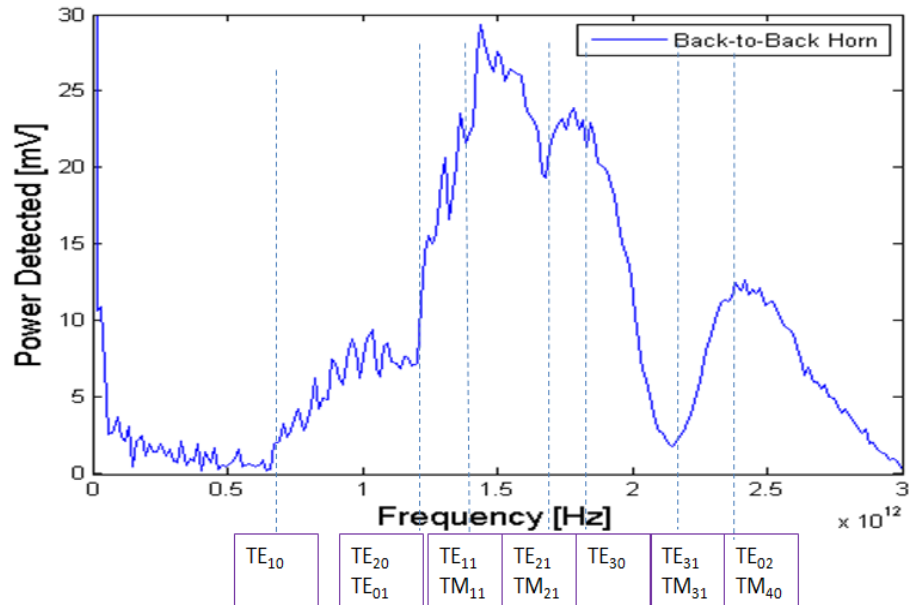


Figure 3.54: Normalised throughput of the back to back horn with a $12\mu\text{m}$ beam splitter replacing the $56\mu\text{m}$ one.

cut-on at 1.697THz), and the TE_{31} & TM_{31} modes at about 2.2THz (these two should cut-on at 2.163THz).

While it can be seen that the reduced beam splitter film thickness has improved the result, there are still some details in the data that do not agree with what is expected for the throughput as a function of increasing frequency for a horn with a smooth walled waveguide section acting as a mode filter. Figure 3.54 shows that there is a steady fall-off of detected signal beyond approximately 1.5THz . This is possibly a result of the aperture having better coupling to the FTS than the back-to-back horn does. A sophisticated modelling software that could simulate the full optical system would likely be very informative on the observed spectral profiles. Such a computational tool, capable of modelling the FTS, the quasioptical lens beam path, the broadband source, and the horn and aperture would make for an interesting and very useful thesis.

Scan 4:

A final set of measurements was performed with the aim of achieving higher detectable frequencies. The 9.4THz filter was selected on the filter wheel (in front of the bolometer), the step size of the scan was set to $4\mu\text{m}$ allowing frequencies up to almost 6THz to be resolved, and the source was changed to a Hg arc lamp as it was thought that it would have stronger emission at the higher frequencies than the

glow bar. The thinner $12\mu\text{m}$ beam splitter was again used.

The uncorrected Fourier transformed data of the final scan for the back-to-back horn can be seen in Figure 3.55, where the calibration data corresponding to the scan for the rectangular aperture is also shown in the plot. What is clear straight away is that there appears to be better agreement between the horn and the aperture in terms of throughput at the higher frequencies. The previously observed higher throughput for the aperture is not present in this scan.

Figure 3.56 shows the corrected throughput plotted as a function of frequency. As can be seen the switch on at 600GHz is not clear and in fact there is a high level of noise at frequencies lower than 600GHz that was not observed in the previous scans. It is interesting however that the high levels of noise seem to dissipate once the switch on frequency is reached.

Even though there is not a clear rise in throughput at the expected 600GHz, there is an evident rise in detected signal between 1.2 and 1.3THz which can be attributed to the TE_{20} & TE_{01} modes which have a switch on frequency at 1.2THz, and the TE_{11} & TM_{11} which are expected to switch on at 1.342THz. The next jump that is observed at approximately 1.7THz is attributed to the TE_{21} & TM_{21} modes ($f_{cut-on} = 1.697\text{THz}$) and some contribution from the single TE_{30} mode ($f_{cut-on} = 1.8\text{THz}$). There is then another significant step in signal just before 2.2THz which again fits with two more modes with switch on frequencies at 2.163THz, namely the TE_{31} & TM_{31} . The next modes are expected to cut-on at 2.4THz but again there is a fall off of signal at these higher frequencies so these modes are not visible switching on.

The final plot shown in Figure 3.57 is the same data as that in 3.56 but the theoretical throughput profiles are also shown for comparison. The geometrical analysis based on the transverse dimensions of the waveguide assumes that each mode carries equal power and contributes 0.25mV to the corrected signal. This appeared to provide a good fit with the measured data. The continuous red line is again the expected profile based on a $1/\lambda^2$ approximation.

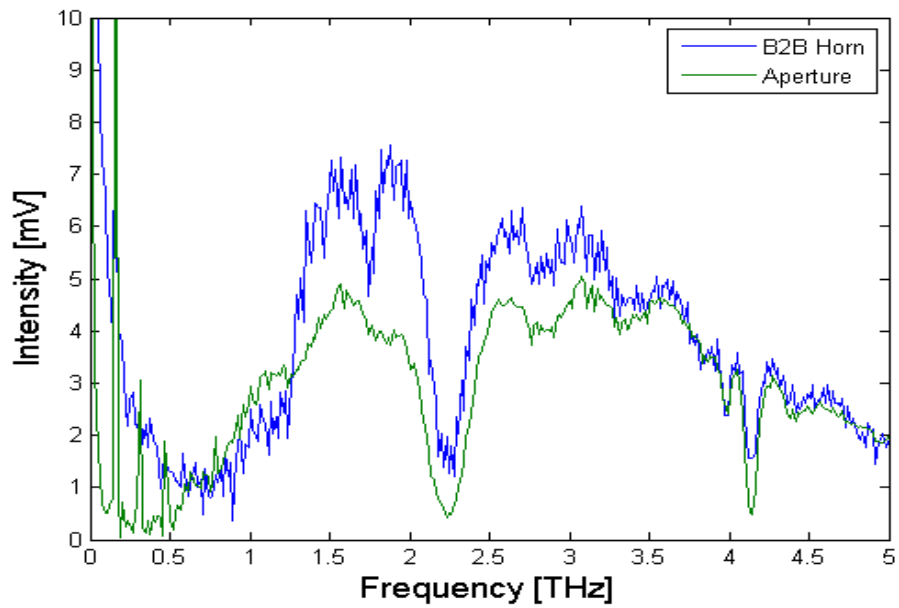


Figure 3.55: Throughput of the back to back horn and aperture for the Hg arc lamp using the 312cm^{-1} filter.

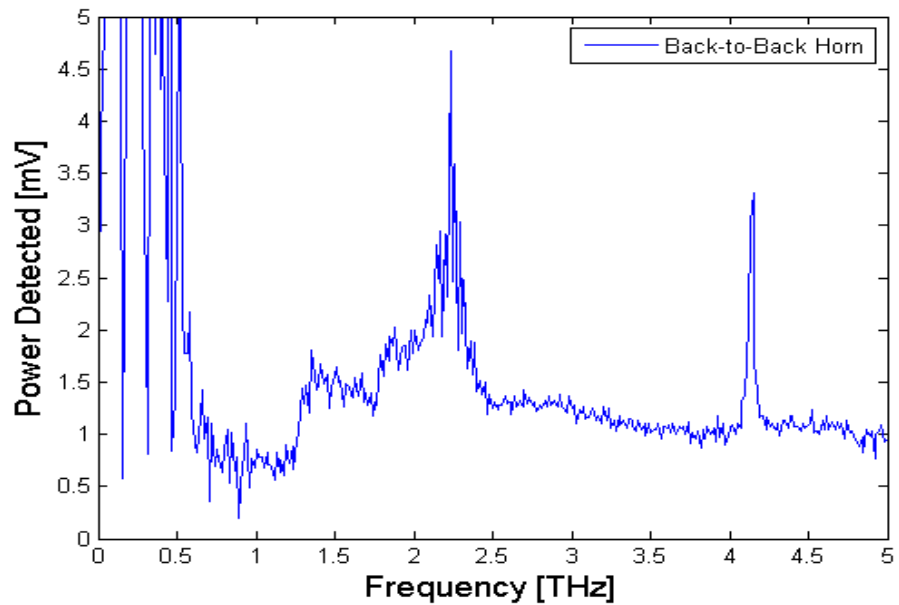


Figure 3.56: Corrected throughput of the back to back horn for the Hg arc lamp using the 312cm^{-1} filter.

3.3.7 Discussion of Results

The results presented in this section show clear evidence that the multi-mode behaviour of tiny feed horns can be measured at THz frequencies. There are still some effects in the system that have not been taken care of as can be seen in each of the graphs, particularly the general fall off of power as higher frequencies are approached especially when using the glow bar and 100cm^{-1} filter. Future work will aim to characterise accurately the spectrum of the glow bar source, the Hg arc lamp

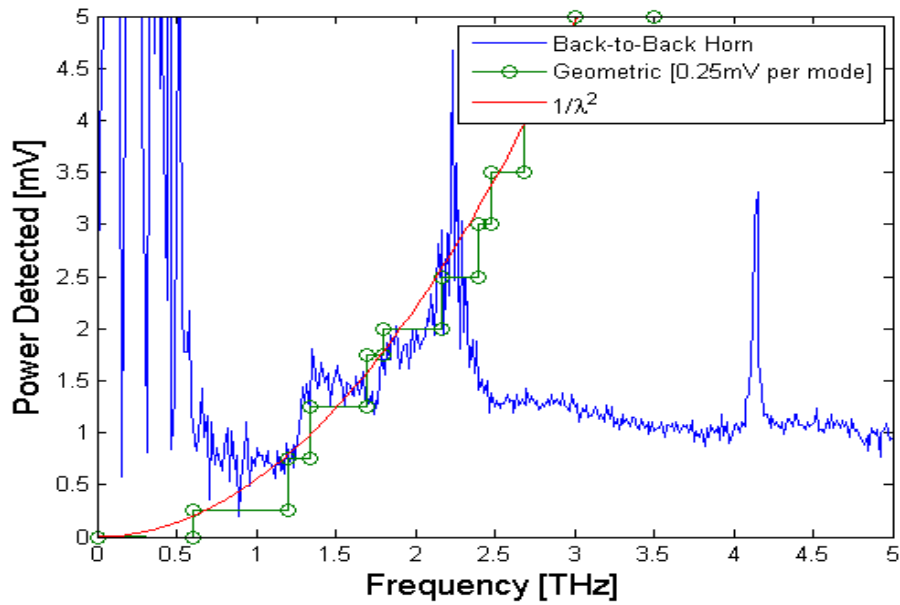


Figure 3.57: Corrected throughput of the back to back horn with theoretical plots shown also. It was assumed that each mode carries equal power and contributes 0.25mV to the corrected signal. This scaling provides a good fit to the measured data.

source, the bolometer, and the frequency dependence of the absorption of the lens material. Once these factors are known the data can be more accurately reduced and corrected.

Another option for future work would be to redesign the optical system with mirrors replacing the lenses. The benefits of this type of set-up would be easier alignment and focus of the system, and there would be a large reduction in the losses that occur due to absorption by the lens material. A mirror system would be more difficult to manufacture due to the limited space within the vacuum tubes, but the benefits would be worth it.

Although the back to back horn structure analysed in this report was larger than the horn currently being used in the SAFARI testbed, the principle of the technique has been successfully demonstrated. With sufficient care and precision the same method could be applied to characterising the smaller horns presently being employed by the testbed.

3.4 Conclusions

In the first section of this chapter three simulation methods were compared for modelling smooth walled rectangular horns and calculating the corresponding far-field beam patterns. The COMSOL model included a propagation region beyond the mouth of the horn that allowed for analysis of a conducting ground plane adjacent to the mouth of the horn. It was shown that the effects of such a ground plane are negligible unless the extreme case of a poor directional antenna is considered, such as a uniform waveguide for example.

Through the comparison study the results of the Pyramidal SCATTER program were verified which is significant as the SCATTER program will be necessary for modelling large SAFARI horn designs in the future. This necessity for SCATTER is because the mode matching technique allows for the analysis of electrically large, multi-moded structures in a very computationally efficient manner. High frequency, multi-mode analysis of SAFARI-like horns was shown not to be possible with the FEM approach on a computer with moderate processing power.

The optical cross-talk between neighbouring SAFARI horns in an array was shown to be negligible. This is an important result due to the unprecedented sensitivity requirements of SAFARI. It was shown that the cross-talk levels are considerable only for instruments with poor directivity, such as two uniform waveguides which are quite close together, for example.

The final section of this chapter detailed the measurement work that was carried out by the author at SRON during a three month visit there from June 2013 to September 2013. The work was aimed at measuring the throughput of SAFARI-like rectangular feed horns as a function of frequency. The measurement technique was shown to be successful, and results were presented which displayed clear evidence of modes ‘switching on’ at the correct frequencies leading to increasing throughput as frequency was increased. The experimental difficulties with such measurements were discussed, and solutions to some of these issues were described. However, the data presented was still quite noisy, and the falloff of signal at the higher frequencies was difficult to explain. For these reasons some ideas on how to improve the system in the future were given at the end of the section.

The techniques discussed in this chapter for characterising multi-moded feed

horns, both the experimental measurements and the modelling techniques, will be essential for understanding and predicting the behaviour of future SAFARI horn designs and similar multi-moded structures, and will help in maximising the sensitivity of these far-IR receivers.

Chapter 4

Conical Mode Matching for Shaped Smooth-Walled CMB Horns

“An investment in knowledge pays the best interest.”

- Benjamin Franklin

4.1 Smooth Walled Conical Horns

4.1.1 Background

Smooth walled sectional horns are becoming increasingly popular due to the simplicity of their geometry which leads to easier manufacture and therefore lower cost compared to corrugated structures, for example. In fact at the operational wavelengths of the SAFARI short wave (SW) band ($\lambda = 30\mu\text{m}$ to $70\mu\text{m}$) manufacturing arrays of corrugated structures is not possible with current technologies. Therefore high performance smooth walled horns, that can have similar performance to corrugated horns, are currently in high demand for far-IR and sub-millimetre systems.

Of course smooth walled geometries will never completely match the excellent performance of corrugated feeds, particularly for wide-band systems, but with optimisation of the profile similar performance can be achieved for most of the important parameters across smaller bandwidths. An excellent example of this is described in a paper by the THz Optics Group at NUIM [McCarthy *et al.*, 2013]. The genetic algorithms that can be used for optimisation of the profile of a smooth walled feed horn are outlined and the authors then go on to describe a final design that was optimised, modelled, and then built for testing. The optimisation routines were based on an adapted version of the in-house mode matching code SCATTER. The details of the EM theory for mode matching in waveguides that SCATTER is based upon are given in a number of publications ([Murphy *et al.*, 2010] and [Murphy *et al.*, 2001] for example) and the theory was discussed in chapter 2 of this thesis.

The cylindrical mode matching theory is well established and the SCATTER code for modelling systems in cylindrical coordinates that is based on this theory has proved accurate and efficient for modelling a wide range of horn antennas. Due to its high efficiency and short computational time for modelling even electrically large structures, SCATTER was a good choice for the optimisation of the profile of smooth walled horns due to the requirement that the calculations must be performed a very large number of times. Although SCATTER is primarily aimed at simulating the behaviour of corrugated horns it can be adapted for modelling smooth walled horns quite easily by simply approximating the smooth-wall geometry by a large number of very small steps. A screen shot of an example horn is shown in Figure 4.1.

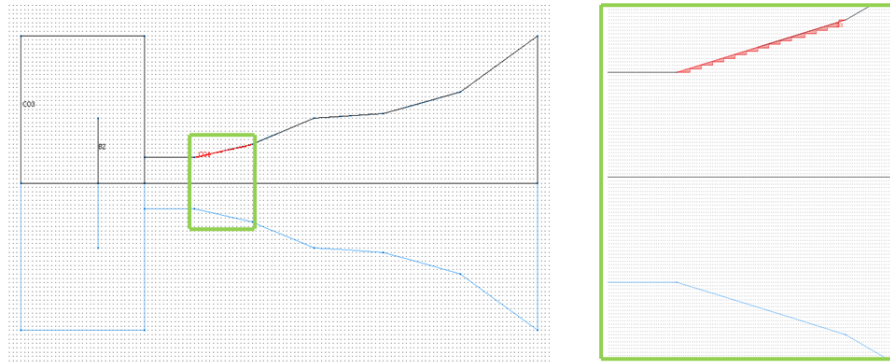


Figure 4.1: Diagram showing how a smooth wall of a feed horn can be approximated by a series of small steps. The green boxed-off section on the left is shown magnified on the right hand side so that the small steps are visible.

As efficient as this approach is, as demonstrated in chapter 2 where it was compared to the FEM approach, it was thought that there is still room for improvement in the speed of computation. The solution is quite obvious and it involves ignoring the steps that approximate the smooth walls. This can be achieved by deriving a basis set of *conical* modes through solving Maxwell's equations in spherical coordinates and by applying appropriate boundary conditions. Theoretically the only scattering of power occurs when there is a change of flare angle, and there should be no scattering of power occurring throughout a section of constant flare angle. This assumption is based on the spherical Helmholtz equation having analytical solutions for conic sections with PEC walls, where it will be shown in the following section 4.1.2 that the modal solutions, and the corresponding eigenvalues, depend directly on the flare angle of the conic section. This implies that power coupling integrals need only be performed at the relatively few junctions corresponding to change of angle rather than the few hundred steps required for approximating even a small horn.

It is this approach that is described in this chapter, starting with a derivation of the conical modes. A description is then given of the new software entitled Spherical SCATTER that was coded by the author using Mathematica. Finally, the results for comparisons between the already existing Cylindrical SCATTER code and the Spherical SCATTER will be shown, and then both methods will be compared to experimental data corresponding to far-field beam measurements of a smooth walled sectional horn performed using a VNA system. Excellent agreement will be demonstrated between both theoretical approaches and measured data.

There were many drivers for this work with the primary motivation being the requirement to design and produce a smooth walled Gaussian horn that compared well with similar corrugated horns, as part of an ESA Announcement of Opportunity (AO) programme [RFQ 3-6418/11/NL/CBi]. Another driver was based on the fact that when the author began to investigate the theory for conical waveguide modes it became clear that the existing literature on the subject is sparse and incomplete. A number of publications discuss the ideas of conical mode matching to some degree, most notably those of [Olver *et al.*, 1994] and [Clarricoats *et al.*, 1984], but the mathematical description of the spherical modes are only stated, with no derivation of the theory in these texts. Furthermore the book by Clarricoats for example limits the discussion to conical waveguide modes of degree 1 ($m = 1$) and gives no description on how to deal with modes of higher azimuthal dependence ($m > 1$). The theory required to account for the higher order modes is essential for the design and analysis of multi-moded feeds and it was therefore necessary to develop the theory further.

4.1.2 Derivation of Spherical Harmonic Fields

The electric field of a particular mode of degree $m = 1$ and order l at the mouth of a smooth walled conical horn antenna for the TE_{1l} mode is described by [Gleeson, 2004] as having the following structure:

$$\vec{E}(x, y) = \left(\left(J_0 \left(p'_{1,l} \frac{r}{a} \right) + J_2 \left(p'_{1,l} \frac{r}{a} \right) \cos(2\phi) \right) \hat{i} + \left(J_2 \left(p'_{1,l} \frac{r}{a} \right) \sin(2\phi) \right) \hat{j} \right) \exp \frac{-jkr^2}{2L} \quad (4.1)$$

where $p'_{1,l}$ is the l^{th} root of $\frac{\partial}{\partial z} J_1(z) = 0$. For the TE_{11} mode $p'_{1,1} = 1.841$.

Equation 4.1 is an approximation that has proven to be very accurate for horns of moderate flare angle, however it is not completely analytically derived. It is calculated by taking the analytically derived solution of the field inside a cylindrical waveguide (see chapter 2.3) and adjusting the phase based on the flare angle of the horn. It is assumed that the amplitude profile is unaffected when the waveguide develops a uniform flare angle, meaning that the only effect is on the phase front which becomes spherical, with its apex coinciding with the apex of the cone of the horn. An extra term is thus included in the field definition to account for this effect ($\exp \frac{-jkr^2}{2L}$). A similar quadratic approximation can be exploited for smooth walled

rectangular horns, as shown in chapter 3.

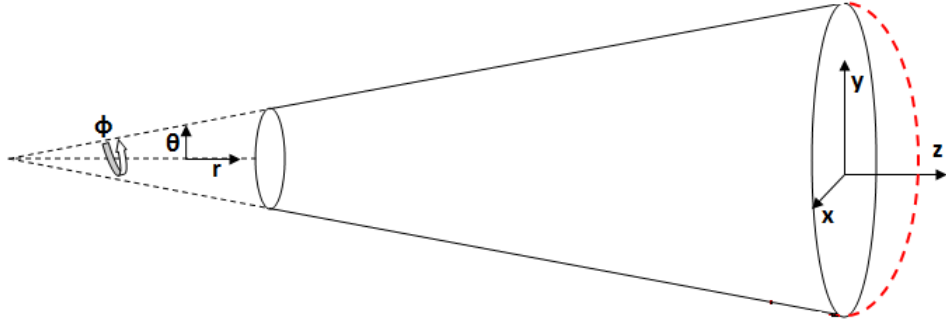


Figure 4.2: Smooth walled conical horn showing the extension back to its virtual apex where there will typically be a cylindrical waveguide section adjoining the horn. The spherical phase cap is also shown at the aperture.

To derive an analytical solution without approximations that includes the phase automatically, the fields must be expanded in terms of conical modes which have the natural symmetry of a cone. These modes can be derived by looking for separable solutions to Maxwell's equations in spherical coordinates, and considering the boundary condition at the walls of the horn, i.e. that the tangential component of the electric field must be zero (perfect electric conductor (PEC) boundary). The resulting solutions can be partitioned into the usual TE modes and TM modes. The starting point is to solve the electric Helmholtz equation ($\nabla^2 E + k^2 E = 0$) in spherical coordinates. One such solution is:

$$E(r, \theta, \phi) = \sum_{\nu}^{\infty} \sum_{m=-\nu}^{\nu} \gamma_{\nu m} [j_{\nu}(k_c r) + y_{\nu}(k_c r)] P_{\nu}^m(\theta, \phi) \quad (4.2)$$

where $\gamma_{\nu m}$ is just some constant, $P_{\nu}^m(\theta, \phi)$ are Legendre functions of order ν and degree m , and $j_{\nu}(k_c r)$ and $y_{\nu}(k_c r)$ are spherical Bessel functions of the first and second kind respectively, and they are related to the radial Bessel functions $J_{\nu}(k_c r)$ and $Y_{\nu}(k_c r)$ by:

$$j_{\nu}(k_c r) = \sqrt{\frac{\pi}{2k_c r}} J_{\nu+\frac{1}{2}}(k_c r) \quad \text{and} \quad y_{\nu}(k_c r) = \sqrt{\frac{\pi}{2k_c r}} Y_{\nu+\frac{1}{2}}(k_c r) \quad (4.3)$$

There are in fact a number of other solutions to the spherical Helmholtz equation, but the most general solutions that are convenient here are:

$$\begin{aligned} E(r, \theta, \phi) &= \sum_{\nu}^{\infty} \sum_{m=-\nu}^{\nu} \gamma_{\nu m} [j_{\nu}(k_c r) + iy_{\nu}(k_c r)] P_{\nu}^m(\theta, \phi) \\ E(r, \theta, \phi) &= \sum_{\nu}^{\infty} \sum_{m=-\nu}^{\nu} \gamma_{\nu m} [j_{\nu}(k_c r) - iy_{\nu}(k_c r)] P_{\nu}^m(\theta, \phi) \end{aligned} \quad (4.4)$$

where i is just the imaginary unit.

$j_\nu(k_c r) + iy_\nu(k_c r)$ is sometimes called a Bessel function of the third kind, or more commonly a Hankel function of the first kind denoted by $h_\nu^{(1)}(k_c r)$, and $j_\nu(k_c r) - iy_\nu(k_c r)$ is sometimes called a Bessel function of the fourth kind, or more commonly a Hankel function of the second kind denoted by $h_\nu^{(2)}(k_c r)$ (see figure 4.3). Using this notation for Hankel functions together with the relations in (4.3) gives:

$$E(r, \theta, \phi) = \sum_{\nu} \sum_{m=-\nu}^{\nu} \gamma_{\nu m} \left[\sqrt{\frac{\pi}{2k_c r}} J_{\nu+\frac{1}{2}}(k_c r) + i \sqrt{\frac{\pi}{2k_c r}} Y_{\nu+\frac{1}{2}}(k_c r) \right] P_{\nu}^m(\theta, \phi) \quad (4.5)$$

$$\Rightarrow E(r, \theta, \phi) = \sum_{\nu} \sum_{m=-\nu}^{\nu} \gamma_{\nu m} h_{\nu}^{(1)}(k_c r) P_{\nu}^m(\theta, \phi) \quad (4.6)$$

where $h_{\nu}^{(1)}(k_c r) = j_{\nu}(k_c r) + iy_{\nu}(k_c r)$.

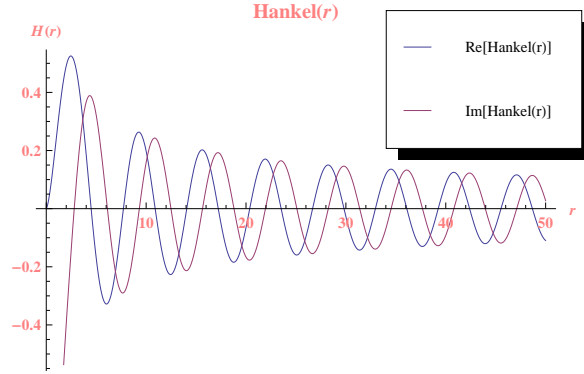


Figure 4.3: Real and imaginary parts of the Hankel function of the first kind. Notice that as r goes to zero the amplitude of the imaginary part of the Hankel function goes to minus infinity, i.e. a singularity.

Equation 4.6 represents a random component of the electric field that is neither specifically TE or TM. However, it is more convenient to begin with the radial component of either the TE or TM modal field. Nagelberg gives a definition for the radial component of the electric field for the TM modes, assuming harmonic time dependence ($e^{-i\omega t}$), as [Nagelberg, 1967]:

$$E_r = A \frac{\mu(\mu + 1)}{ikr^2} h_{\mu}^{(1)}(kr) P_{\mu}^m(\cos \theta) e^{im\phi} \quad \text{and} \quad H_r = 0 \quad (4.7)$$

and for the TE modes the radial component of the magnetic field [Nagelberg, 1967]:

$$H_r = B \frac{\nu(\nu + 1)}{ikr^2} y_0 h_{\nu}^{(1)}(kr) P_{\nu}^m(\cos \theta) e^{im\phi} \quad \text{and} \quad E_r = 0 \quad (4.8)$$

The above expressions are valid for waves travelling away from the apex and toward the aperture of the horn (forward going waves). For waves moving in the

opposite direction back toward the apex of the cone (backward going waves) the mathematical descriptions are very similar but with the radial component being governed by a Hankel function of the second kind:

$$E_r = A \frac{\mu(\mu+1)}{ikr^2} h_\mu^{(2)}(kr) P_\mu^m(\cos\theta) e^{im\phi} \quad \text{and} \quad H_r = 0 \quad (4.9)$$

and for the TE modes:

$$H_r = B \frac{\nu(\nu+1)}{ikr^2} y_0 h_\nu^{(2)}(kr) P_\nu^m(\cos\theta) e^{im\phi} \quad \text{and} \quad E_r = 0 \quad (4.10)$$

In fact the above field components can be further separated into two polarizations. For the forward going TM modes:

$$E_r = A \frac{\mu(\mu+1)}{ikr^2} h_\mu^{(1)}(kr) P_\mu^m(\cos\theta) \begin{Bmatrix} \cos(m\phi) \\ \sin(m\phi) \end{Bmatrix} \quad \text{and} \quad H_r = 0 \quad (4.11)$$

And for the forward going TE modes:

$$H_r = B \frac{\nu(\nu+1)}{ikr^2} y_0 h_\nu^{(1)}(kr) P_\nu^m(\cos\theta) \begin{Bmatrix} \sin(m\phi) \\ -\cos(m\phi) \end{Bmatrix} \quad \text{and} \quad E_r = 0 \quad (4.12)$$

A similar separation of polarisations holds for the backward going waves also. Knowing the radial components of the electric and magnetic fields should allow the remaining components of the fields to be calculated. This is straightforward in the case of constant radius cylindrical waveguides, where the equivalent component is the longitudinal 'z' component, due to the $e^{-\gamma z}$ dependence, but it becomes much more difficult for the case of a conical horn due to the spherical geometry. Since the radius continually changes with length the $e^{-\gamma z}$ dependence has been replaced with Hankel functions of either the first or second kind that account for the diffusion or concentration of the field as it fills ever increasing or decreasing cross sections, respectively, as r increases.

The transverse components (θ and ϕ) of the TE and TM modes can be derived from Maxwell's curl equations:

$$\vec{\nabla} \times \vec{E} = \frac{-\partial \vec{B}}{\partial t} = -\mu \frac{\partial \vec{H}}{\partial t} = -i\omega\mu \vec{H} \quad (4.13)$$

$$\vec{\nabla} \times \vec{H} = \epsilon \frac{\partial \vec{E}}{\partial t} = i\omega\epsilon \vec{E} \quad (4.14)$$

And the curl of \vec{H} , for example, in spherical coordinates is:

$$\vec{\nabla} \times \vec{H} = \frac{1}{r^2 \sin\theta} \det \begin{vmatrix} \hat{r} & r\hat{\theta} & r\sin\theta\hat{\phi} \\ \frac{\partial}{\partial r} & \frac{\partial}{\partial \theta} & \frac{\partial}{\partial \phi} \\ H_r & rH_\theta & r\sin\theta H_\phi \end{vmatrix} \quad (4.15)$$

Thus 4.14 yields:

$$i\omega\epsilon\vec{E} = \left[\frac{1}{r \sin \theta} \frac{\partial(\sin \theta H_\phi)}{\partial \theta} - \frac{1}{r \sin \theta} \frac{\partial(H_\theta)}{\partial \phi} \right] \hat{r} + \left[\frac{1}{r \sin \theta} \frac{\partial H_r}{\partial \phi} - \frac{1}{r} \frac{\partial(r H_\phi)}{\partial r} \right] \hat{\theta} + \left[\frac{1}{r} \frac{\partial(r H_\theta)}{\partial r} - \frac{1}{r} \frac{\partial(H_r)}{\partial \theta} \right] \hat{\phi} \quad (4.16)$$

And rearranging the above equation, the components for \vec{E} are then given by:

$$E_r = \frac{1}{i\omega\epsilon} \left[\frac{1}{r \sin \theta} \frac{\partial(\sin \theta H_\phi)}{\partial \theta} - \frac{1}{r \sin \theta} \frac{\partial(H_\theta)}{\partial \phi} \right] \quad (4.17)$$

$$E_\theta = \frac{1}{i\omega\epsilon} \left[\frac{1}{r \sin \theta} \frac{\partial H_r}{\partial \phi} - \frac{1}{r} \frac{\partial(r H_\phi)}{\partial r} \right] \quad (4.18)$$

$$E_\phi = \frac{1}{i\omega\epsilon} \left[\frac{1}{r} \frac{\partial(r H_\theta)}{\partial r} - \frac{1}{r} \frac{\partial(H_r)}{\partial \theta} \right] \quad (4.19)$$

Applying similar analysis to equation 4.13, which relates the magnetic field to the curl of the electric field, yields for the components of \vec{H} :

$$H_r = -\frac{1}{i\omega\mu} \left[\frac{1}{r \sin \theta} \frac{\partial(\sin \theta E_\phi)}{\partial \theta} - \frac{1}{r \sin \theta} \frac{\partial(E_\theta)}{\partial \phi} \right] \quad (4.20)$$

$$H_\theta = -\frac{1}{i\omega\mu} \left[\frac{1}{r \sin \theta} \frac{\partial E_r}{\partial \phi} - \frac{1}{r} \frac{\partial(r E_\phi)}{\partial r} \right] \quad (4.21)$$

$$H_\phi = -\frac{1}{i\omega\mu} \left[\frac{1}{r} \frac{\partial(r E_\theta)}{\partial r} - \frac{1}{r} \frac{\partial(E_r)}{\partial \theta} \right] \quad (4.22)$$

Substituting the expression 4.22 for H_ϕ into the expression 4.18 for E_θ yields:

$$rE_\theta = -\frac{i\omega\mu}{k^2 \sin \theta} \frac{\partial H_r}{\partial \phi} - \frac{1}{k^2} \frac{\partial^2(r E_\theta)}{\partial r^2} + \frac{1}{k^2} \frac{\partial}{\partial r} \frac{\partial(E_r)}{\partial \theta} \quad (\text{using } k^2 = \omega^2 \mu \epsilon) \quad (4.23)$$

which can be rewritten as:

$$rE_\theta - \frac{\partial^2(r E_\theta)}{\partial (kr)^2} = -\frac{i\omega\mu}{k^2 \sin \theta} \frac{\partial H_r}{\partial \phi} + \frac{1}{k} \frac{\partial}{\partial \theta} \left[\frac{\partial(E_r)}{\partial kr} \right] \quad (4.24)$$

Similar analysis applied to substituting the expression 4.21 for H_θ into the expression 4.19 for E_ϕ yields the result:

$$rE_\phi + \frac{\partial^2(r E_\phi)}{\partial (kr)^2} = \frac{i\omega\mu}{k^2} \frac{\partial H_r}{\partial \theta} + \frac{1}{k \sin \theta} \frac{\partial}{\partial \phi} \left[\frac{\partial(E_r)}{\partial kr} \right] \quad (4.25)$$

TE Mode Solutions

If at this point only the TE modes are considered then $E_r = 0$. Assuming equation 4.24 for H_r of the form $H_r = B \frac{\nu(\nu+1)}{ikr^2} y_0 h_\nu^{(1)}(kr) P_\nu^m(\cos \theta) \left\{ \begin{matrix} \sin(m\phi) \\ -\cos(m\phi) \end{matrix} \right\}$ (see (4.12)) implies:

$$\Rightarrow rE_\theta + \frac{\partial^2(r E_\theta)}{\partial (kr)^2} = -\frac{\omega\mu y_0 B}{k^2 r \sin \theta} \left[\frac{\nu(\nu+1)}{kr} h_\nu^{(1)}(kr) P_\nu^m(\cos \theta) m \left\{ \begin{matrix} \cos(m\phi) \\ \sin(m\phi) \end{matrix} \right\} \right] \quad (4.26)$$

Using the relationship on page 445 of Abramowitz and Stegun, the spherical Hankel functions satisfy the following differential equation [Abramowitz and Stegun, 1972]:

$$\frac{\partial^2(z.h_\nu^{(1)}(z))}{\partial z^2} + \left[1 - \frac{\nu(\nu+1)}{z^2}\right] (z.h_\nu^{(1)}(z)) = 0 \quad \text{where } z.h_\nu^{(1)}(z) = \sqrt{\frac{\pi z}{2}} H_{\nu+0.5}^{(1)}(z) \quad (4.27)$$

Then with some rearranging and substitution it can be shown that:

$$\frac{\nu(\nu+1)}{r} h_\nu^{(1)}(kr) = r h_\nu^{(1)}(kr) + \frac{1}{k^2} \frac{\partial^2}{\partial r^2} [r h_\nu^{(1)}(kr)] \quad (4.28)$$

Substituting the right side of the above expression into equation 4.26:

$$r E_\theta + \frac{\partial^2(r E_\theta)}{\partial (kr)^2} = -\frac{m\omega\mu y_0 B}{k \sin \theta} \left[\left(r h_\nu^{(1)}(kr) + \frac{\partial^2 r h_\nu^{(1)}(kr)}{\partial (kr)^2} \right) P_\nu^m(\cos \theta) \begin{Bmatrix} \cos(m\phi) \\ \sin(m\phi) \end{Bmatrix} \right] \quad (4.29)$$

and therefore we obtain

$$\Rightarrow r E_\theta = -\frac{m\omega\mu y_0 B}{k \sin \theta} \left[h_\nu^{(1)}(kr) P_\nu^m(\cos \theta) \begin{Bmatrix} \cos(m\phi) \\ \sin(m\phi) \end{Bmatrix} \right] \quad (4.30)$$

Finally by using the fact that $\frac{\omega\mu}{k} = \sqrt{\frac{\mu}{\epsilon}} = \frac{1}{y_0}$, this simplifies to:

$$E_\theta = -\frac{mB}{r \sin \theta} h_\nu^{(1)}(kr) P_\nu^m(\cos \theta) \begin{Bmatrix} \cos(m\phi) \\ \sin(m\phi) \end{Bmatrix} \quad (4.31)$$

Applying the same TE conditions to equation 4.25 for E_ϕ , and with similar analysis and substitutions, an expression for E_ϕ can be derived that is independent of any other field components.

$$r E_\phi + \frac{1}{k^2} \frac{\partial^2}{\partial r^2} (r E_\phi) = \frac{i\omega\mu}{k^2} \frac{\partial H_r}{\partial \theta} \quad (4.32)$$

giving

$$r E_\phi + \frac{\partial^2(r E_\phi)}{\partial (kr)^2} = \frac{i\omega\mu}{k^2} \left[B \frac{\nu(\nu+1)}{i k r^2} y_0 h_\nu^{(1)}(kr) \frac{\partial P_\nu^m(\cos \theta)}{\partial \theta} \begin{Bmatrix} \sin(m\phi) \\ -\cos(m\phi) \end{Bmatrix} \right] \quad (4.33)$$

which yields in a similar manner that:

$$\Rightarrow E_\phi = \frac{B}{r} h_\nu^{(1)}(kr) \frac{\partial P_\nu^m(\cos \theta)}{\partial \theta} \begin{Bmatrix} \sin(m\phi) \\ -\cos(m\phi) \end{Bmatrix} \quad (4.34)$$

In order to derive the transverse components of the magnetic field (H_θ and H_ϕ) for the TE solutions the expressions above derived for E_θ and E_ϕ (4.31 and 4.34) can be substituted into equations 4.22 and 4.21 respectively, setting $E_r = 0$ to satisfy the TE conditions. Starting with 4.22:

$$H_\phi = -\frac{1}{i\omega\mu} \left[\frac{1}{r} \frac{\partial(rE_\theta)}{\partial r} \right] = \frac{mkB}{i\omega\mu r \sin\theta} \frac{\partial h_\nu^{(1)}(kr)}{\partial kr} P_\nu^m(\cos\theta) \begin{Bmatrix} \cos(m\phi) \\ \sin(m\phi) \end{Bmatrix} \quad (4.35)$$

$$\Rightarrow H_\phi = -\frac{imBy_0}{r \sin\theta} \frac{\partial h_\nu^{(1)}(kr)}{\partial kr} P_\nu^m(\cos\theta) \begin{Bmatrix} \cos(m\phi) \\ \sin(m\phi) \end{Bmatrix} \quad (4.36)$$

Similarly, for H_θ :

$$H_\theta = \frac{1}{i\omega\mu} \left[\frac{1}{r} \frac{\partial(rE_\phi)}{\partial r} \right] = -\frac{iBy_0}{r} \frac{\partial h_\nu^{(1)}(kr)}{\partial kr} \frac{\partial P_\nu^m(\cos\theta)}{\partial\theta} \begin{Bmatrix} \sin(m\phi) \\ -\cos(m\phi) \end{Bmatrix} \quad (4.37)$$

TM Mode Solutions

The transverse components of both the electric and magnetic fields for the case of TE modes have been derived above. If the same starting point of equations 4.24 and 4.25 are taken, but this time allowing the radial component of the *magnetic* field to be zero ($H_r = 0$) thereby satisfying the conditions of TM modes, then a similar analysis can be applied to derive the transverse field components of the TM solutions. The resulting expressions are:

$$E_\theta = -\frac{iA}{r} \frac{\partial h_\nu^{(1)}(kr)}{\partial kr} \frac{\partial P_\nu^m(\cos\theta)}{\partial\theta} \begin{Bmatrix} \cos(m\phi) \\ \sin(m\phi) \end{Bmatrix} \quad (4.38)$$

$$E_\phi = \frac{imA}{r \sin\theta} \frac{\partial h_\nu^{(1)}(kr)}{\partial kr} P_\nu^m(\cos\theta) \begin{Bmatrix} \sin(m\phi) \\ -\cos(m\phi) \end{Bmatrix} \quad (4.39)$$

$$H_\theta = -\frac{mAy_0}{r \sin\theta} \left[h_\nu^{(1)}(kr) P_\nu^m(\cos\theta) \begin{Bmatrix} \sin(m\phi) \\ -\cos(m\phi) \end{Bmatrix} \right] \quad (4.40)$$

$$H_\phi = -\frac{Ay_0}{r} \left[h_\nu^{(1)}(kr) \frac{\partial P_\nu^m(\cos\theta)}{\partial\theta} \begin{Bmatrix} \cos(m\phi) \\ \sin(m\phi) \end{Bmatrix} \right] \quad (4.41)$$

Expressions for the complete set of electric and magnetic field components have now been derived for both the TE and TM mode solutions and they are summarised in Table 4.1 below. Note that the eigenvalues for the TM modes are now denoted by subscript μ rather than ν as before. This is to differentiate them from the TE mode eigenvalues. This notation will be used from this point onwards.

4.1.3 Calculation of Eigenvalues

One of the complications that arises when trying to calculate the fields of a smooth walled conical horn in spherical coordinates is that the eigenvalues of the Legendre

TE Modes
$E_r = 0$
$E_\theta = -\frac{mB}{r \sin \theta} h_\nu^{(1)}(kr) P_\nu^m(\cos \theta) \begin{Bmatrix} \cos(m\phi) \\ \sin(m\phi) \end{Bmatrix}$
$E_\phi = \frac{B}{r} h_\nu^{(1)}(kr) \frac{\partial P_\nu^m(\cos \theta)}{\partial \theta} \begin{Bmatrix} \sin(m\phi) \\ -\cos(m\phi) \end{Bmatrix}$
$H_r = B \frac{\nu(\nu+1)}{ikr^2} y_0 h_\nu^{(1)}(kr) P_\nu^m(\cos \theta) \begin{Bmatrix} \sin(m\phi) \\ -\cos(m\phi) \end{Bmatrix}$
$H_\theta = -\frac{iBy_0}{r} \frac{\partial h_\nu^{(1)}(kr)}{\partial kr} \frac{\partial P_\nu^m(\cos \theta)}{\partial \theta} \begin{Bmatrix} \sin(m\phi) \\ -\cos(m\phi) \end{Bmatrix}$
$H_\phi = -\frac{imBy_0}{r \sin \theta} \frac{\partial h_\nu^{(1)}(kr)}{\partial kr} P_\nu^m(\cos \theta) \begin{Bmatrix} \cos(m\phi) \\ \sin(m\phi) \end{Bmatrix}$
TM Modes
$E_r = A \frac{\mu(\mu+1)}{ikr^2} h_\mu^{(1)}(kr) P_\mu^m(\cos \theta) \begin{Bmatrix} \cos(m\phi) \\ \sin(m\phi) \end{Bmatrix}$
$E_\theta = -\frac{iA}{r} \frac{\partial h_\mu^{(1)}(kr)}{\partial kr} \frac{\partial P_\mu^m(\cos \theta)}{\partial \theta} \begin{Bmatrix} \cos(m\phi) \\ \sin(m\phi) \end{Bmatrix}$
$E_\phi = \frac{imA}{r \sin \theta} \frac{\partial h_\mu^{(1)}(kr)}{\partial kr} P_\mu^m(\cos \theta) \begin{Bmatrix} \sin(m\phi) \\ -\cos(m\phi) \end{Bmatrix}$
$H_r = 0$
$H_\theta = -\frac{mAy_0}{r \sin \theta} \left[h_\mu^{(1)}(kr) P_\mu^m(\cos \theta) \begin{Bmatrix} \sin(m\phi) \\ -\cos(m\phi) \end{Bmatrix} \right]$
$H_\phi = -\frac{Ay_0}{r} \left[h_\mu^{(1)}(kr) \frac{\partial P_\mu^m(\cos \theta)}{\partial \theta} \begin{Bmatrix} \cos(m\phi) \\ \sin(m\phi) \end{Bmatrix} \right]$

Table 4.1: Mode expressions in spherical coordinates for a conical feed horn.

functions are not integers as is the case for spherically symmetric systems such as the electron in the spherically symmetric potential of the proton (Hydrogen). This is because the conical horn is only a conic section of a sphere, rather than a complete sphere, so the boundary condition on the polar coordinate θ is determined by the flare angle of a cone instead of the requirement that the solution be finite everywhere from $\theta = 0$ to $\theta = \pi$. Therefore the values for ν and μ must be calculated by considering the boundary conditions at the walls of the horn where ($\theta = \theta_h$). Thus, for TM modes, $E_r = 0$ and $E_\phi = 0$ when $\theta = \theta_h$, leading to $P_\mu^m(\cos \theta_h) = 0$, while for TE modes, $E_\phi = 0$ when $\theta = \theta_h$, leading to $\left[\frac{d}{d\theta} [P_\nu^m(\cos \theta)] \right]_{\theta=\theta_h} = 0$.

Values for ν and μ were calculated for the case of $m=1$ by finding the roots of the two equations above for particular values of horn half angle θ_h . The values are listed in tables 4.2 and 4.3, and the values for a horn of half angle of $\theta_h = 5^\circ$ are highlighted as this is appropriate for the example horn that is most commonly discussed in this section. It is clear from the tables that as the half angle of the horn gets larger the eigenvalues get smaller. In fact the eigenvalues approach integers for very large values of half angle as would be expected as one goes smoothly over to

the free space case.

Horn Half Angle (θ_h)	μ_1	μ_2	μ_3	μ_4	μ_5
1°	219.041	401.464	582.397	762.891	943.198
2°	109.271	200.482	290.949	381.196	471.349
3°	72.6819	133.489	193.800	253.964	314.066
4°	54.3874	99.9921	145.225	190.348	235.425
5°	43.411	79.8943	116.081	152.179	188.240
6°	36.0935	66.4958	96.6508	126.733	156.784
7°	30.8669	56.9255	82.7725	108.557	134.315
8°	26.9471	49.7479	72.3638	94.9252	117.463
9°	23.8985	44.1654	64.2682	84.3227	104.356
10°	21.4598	39.6995	57.7918	75.8408	93.8711

Table 4.2: Tabulated results for the first five eigenvalues for TM modes for horns of various opening half angles.

Horn Half Angle (θ_h)	ν_1	ν_2	ν_3	ν_4	ν_5
1°	104.995	304.970	488.596	670.205	851.121
2°	52.253	152.237	244.049	334.853	425.311
3°	34.674	101.326	162.533	223.070	283.375
4°	25.887	75.871	121.776	167.178	212.407
5°	20.616	60.599	97.322	133.643	169.826
6°	17.103	50.417	81.019	111.287	141.439
7°	14.594	43.145	69.375	95.318	121.163
8°	12.714	37.692	60.642	83.342	105.955
9°	11.252	33.450	53.849	74.027	94.128
10°	10.084	30.057	48.416	66.575	84.666

Table 4.3: Tabulated results for the first five eigenvalues for TE modes for horns of various opening half angles.

If a mode matching simulation tool based on these field definitions was to be developed it would obviously require a technique for automatically calculating the eigenvalues of horn sections with arbitrary flare angles. Various approximations can

be applied for the Legendre functions and their derivatives, including one described on page 62 in [Clarricoats *et al.*, 1984]. That particular approximation states that for small angles (and therefore large μ and ν) the Legendre function for $m=0$, and its derivative, can be written as:

$$P_\mu(\cos \theta) \approx J_0 \left(\left(\mu + \frac{1}{2} \right) \theta \right) \quad (4.42)$$

$$\left[\frac{d}{d\theta} [P_\nu(\cos \theta)] \right]_{\theta=\theta_h} \approx - \left(\nu + \frac{1}{2} \right) J_1 \left(\left(\nu + \frac{1}{2} \right) \theta \right) \quad (4.43)$$

But $P_\mu^1(\cos \theta_h) = \left[\frac{d}{d\theta} [P_\nu(\cos \theta_h)] \right]$ therefore the Legendre function for $m=1$, and its derivative, can be written as:

$$P_\mu^1(\cos \theta) \approx - \left(\mu + \frac{1}{2} \right) J_1 \left(\left(\mu + \frac{1}{2} \right) \theta \right) \quad (4.44)$$

$$\left[\frac{d}{d\theta} [P_\nu^1(\cos \theta)] \right]_{\theta=\theta_h} \approx - \frac{1}{2} \left(\nu + \frac{1}{2} \right)^2 \left[J_0 \left(\left(\nu + \frac{1}{2} \right) \theta \right) - J_2 \left(\left(\nu + \frac{1}{2} \right) \theta \right) \right] \quad (4.45)$$

where J_0 , J_1 and J_2 are the zero order, first order and second order Bessel functions, respectively, and the relationship $J_n'(x) = \frac{1}{2} (J_{n-1}(x) - J_{n+1}(x))$ was used.

The above approximations are very convenient since the roots of the Bessel functions are well known and they can be automatically generated in some mathematical programming environment such as Mathematica. The required eigenvalues of the Legendre functions (and their derivatives) can then be calculated by a “find root” function with the approximation just described as a starting point for the search.

Comparisons for the Legendre functions and the Bessel function approximations are shown below for a range of angles. It is clear from figure 4.4 that the approximation (4.44) only begins to deviate for angles approaching 50° . There is greater deviation at smaller angles for the approximation (4.45) ($\approx 30^\circ$), but since these approximate solutions will only be used as an initial search point for the Legendre function eigenvalues then the agreement is considered sufficiently good. Furthermore, feed horns for the purposes of SAFARI-like multimode systems will generally consist of relatively shallow flare angles that would certainly not exceed 30° . In fact for horns that lie within these limits the approximations could actually be used for describing the fields and could therefore be employed in the mode matching algorithms. Analytical solutions for power coupling integrals involving Bessel

functions are what are used in the Cylindrical SCATTER program so they are well understood. Of course this close relationship between the Legendre functions and Bessel functions is related to the good approximation of representing the fields of a conical horn by a waveguide mode. The $P_\nu^1(\cos \theta)$ function for the conical horn determines the amplitude as it varies with θ , but with a spherical wavefront that is represented by the Hankel function $h_\mu^{(1)}(kr)$, which is constant as θ varies. This is taken care of by the $\exp\left(\frac{-ikr^2}{2L}\right)$ term in the waveguide mode approximation.

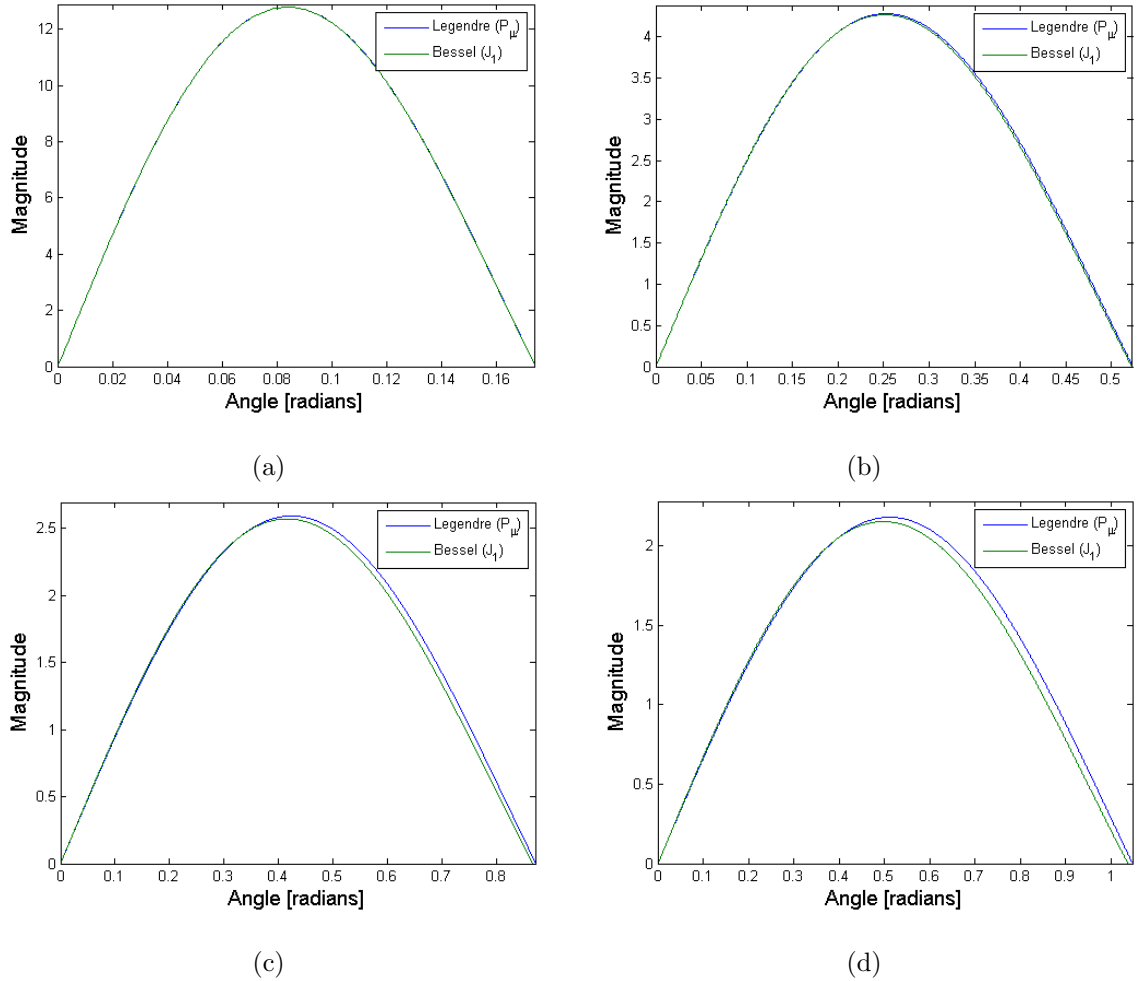


Figure 4.4: Comparison of Legendre function ($P_\mu^1(\cos \theta)$) and first order Bessel function ($-(\mu + \frac{1}{2}) J_1((\mu + \frac{1}{2}) \theta_h)$) for increasing angle. (a): $\theta_h = 10^\circ$, (b): $\theta_h = 30^\circ$, (c): $\theta_h = 50^\circ$, and (d): $\theta_h = 60^\circ$.

Equations 4.42 to 4.45 show that if the zeros of the corresponding Bessel functions can be calculated then the dependence of the Legendre function eigenvalues on the horn opening angle can be calculated analytically and plotted. For the case $m = 0$ for example, the dependence of ν for the TE_{1l} modes, on the horn half angle can be written as:

$$\nu_l^1 \approx \left(\frac{p'_{1l}}{\theta_h} \right) - \frac{1}{2} \quad (4.46)$$

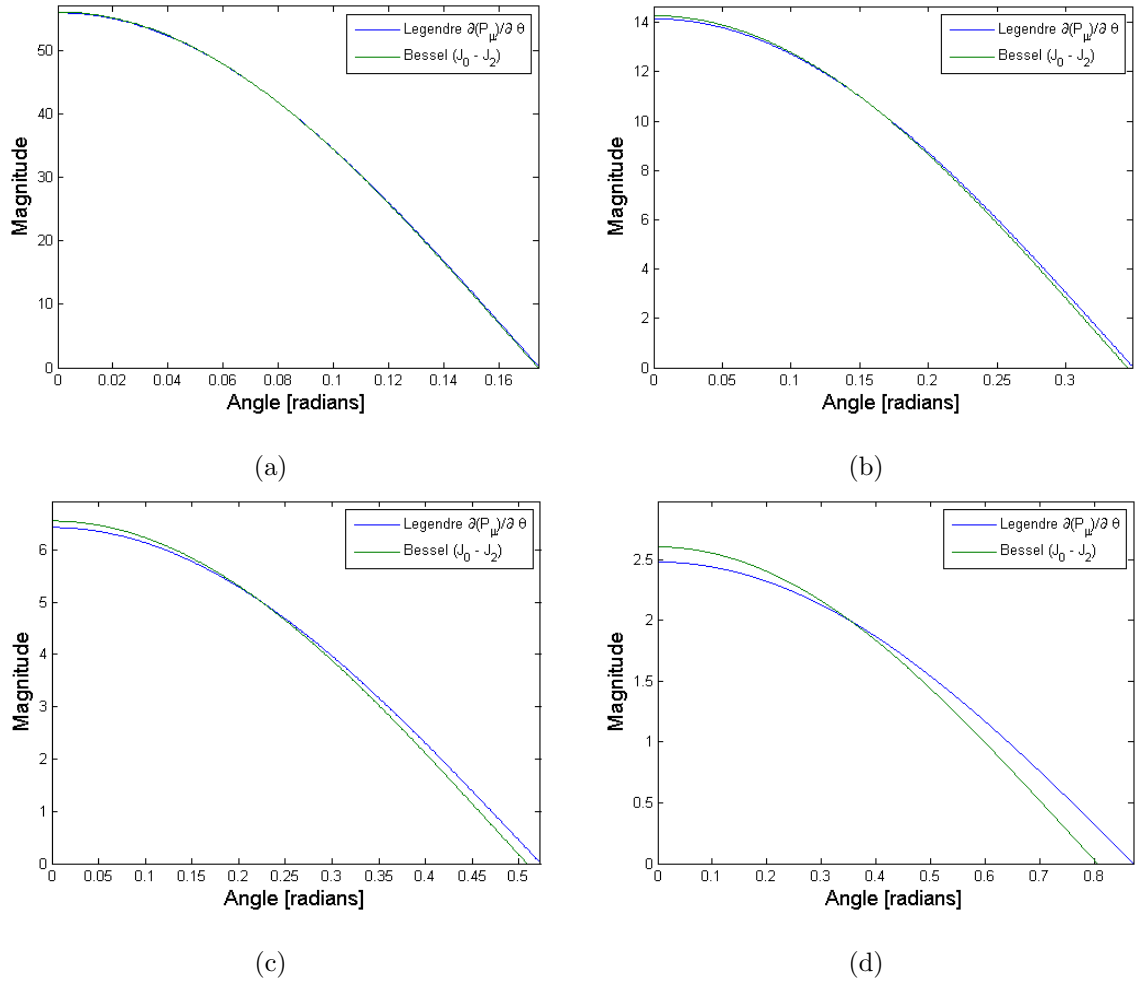


Figure 4.5: Comparison of derivative of the Legendre function $\left(\left[\frac{d}{d\theta} [P_\nu^1(\cos \theta_h)] \right]_{\theta=\theta_h} \right)$ and Bessel approximation $\left(-\frac{1}{2} (\nu + \frac{1}{2})^2 [J_0((\nu + \frac{1}{2})\theta_h) - J_2((\nu + \frac{1}{2})\theta_h)] \right)$. (a): $\theta_h = 10^\circ$, (b): $\theta_h = 20^\circ$, (c): $\theta_h = 30^\circ$, and (d): $\theta_h = 60^\circ$.

where p'_{1l} is the l^{th} root of the derivative of the first order Bessel function (J'_1), and θ_h is the horn half flare angle in radians. The ν values can then be plotted as a function of horn flare angle as shown in Figure 4.6.

For the case of higher order modes, i.e. those with azimuthal dependence $m > 1$, a recursive relationship can be applied to equations 4.44 and 4.45 to yield:

$$P_\mu^m(\cos \theta) \approx (-1)^m \left(\mu + \frac{1}{2} \right)^m J_m \left(\left(\mu + \frac{1}{2} \right) \theta \right) \quad (4.47)$$

and

$$\begin{aligned} & \left[\frac{d}{d\theta} [P_\nu^m(\cos \theta_h)] \right]_{\theta=\theta_h} \\ & \approx \frac{(-1)^m}{2} \left(\nu + \frac{1}{2} \right)^{(m+1)} \left[J_{m-1} \left(\left(\nu + \frac{1}{2} \right) \theta \right) - J_{m+1} \left(\left(\nu + \frac{1}{2} \right) \theta \right) \right] \end{aligned} \quad (4.48)$$

A more useful approximation however is found on page 362 of Abramowitz and

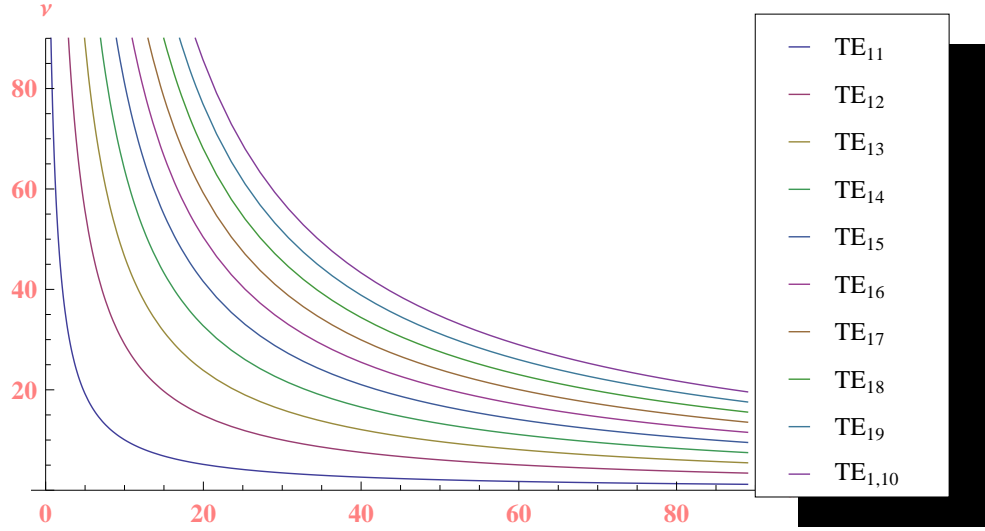


Figure 4.6: Graph of eigenvalue (ν) as a function of horn half angle (θ) for the first ten modes assuming the approximation $\nu_l^1 = \left(\frac{p_l \mu}{\theta_h}\right) - \frac{1}{2}$. The azimuthal order is fixed at $m = 1$.

Stegun [Abramowitz and Stegun, 1972] of the form:

$$\mu^m P_\mu^{-m} \left(\cos \frac{\theta_h}{\mu} \right) \cong J_m(\theta_h) \quad (4.49)$$

which leads to the relationship:

$$P_\mu^m(\cos \theta_h) \cong (-1)^m \mu^m J_m(\theta_h \mu) \quad (4.50)$$

where the $(-1)^m$ is brought in to account for the fact that $P_\mu^{-m} = -P_\mu^m$.

Equation 4.50 then leads to

$$\begin{aligned} P_\mu^m(\cos \theta_h) \cong 0 \quad \text{when} \quad \mu &= \frac{p_{ml}}{\theta_h} \\ \Rightarrow \mu_{ml} &= \frac{p_{ml}}{\theta_h} \end{aligned} \quad (4.51)$$

where p_{ml} correspond to the l^{th} root of the m^{th} order Bessel function, which are always the same and therefore are easily tabulated for functions to call upon. Tabulated roots of Bessel functions and their derivatives can be found widely in the literature, for example [Beattie, 1958], and Figure 4.7 illustrates the trends of some of the calculated roots. It is these values that can be used to estimate initial search points for the eigenvalues of the Legendre functions.

4.1.4 Evanescence of Modes

A very interesting feature of the conical mode approach is how the evanescence of modes is governed. When analysing modal power flow and power coupling in

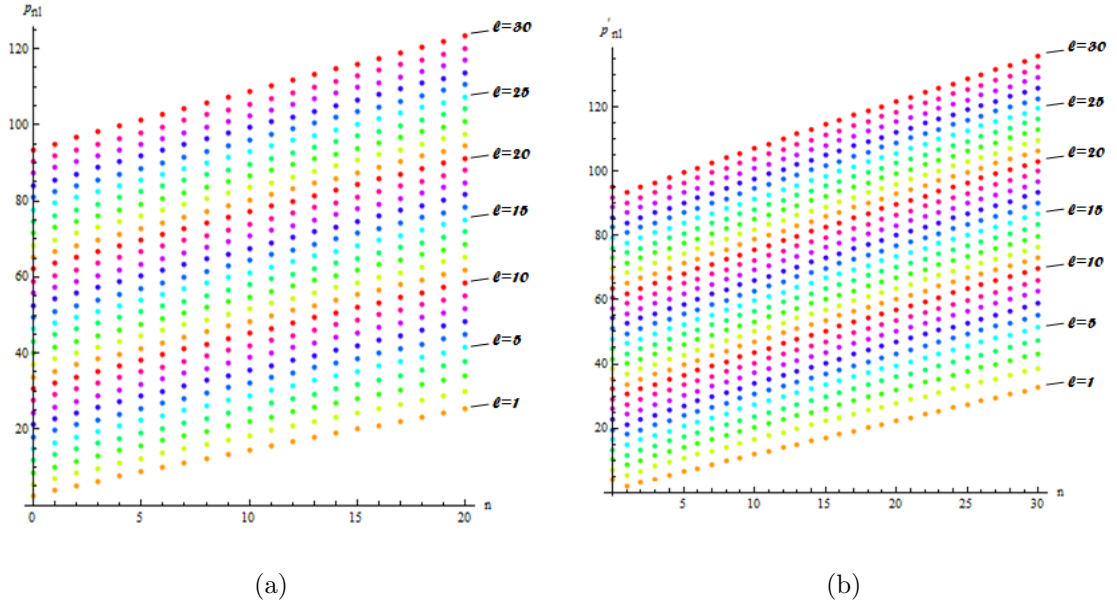


Figure 4.7: Point plot of Zeros of (a) Bessel functions (p_{nl}), and (b) derivatives of Bessel functions (p'_{nl}). Each dot corresponds to the l^{th} root of the n^{th} order Bessel function (as in (a)) or its derivative (as in (b)). The value of the root is represented on the y axis and roots are approximately separated by π for each order and its derivative.

cylindrical waveguide sections we first determine whether each mode is purely propagating or purely evanescent for a particular cylindrical section radius and operating frequency. If the frequency is above a certain critical value (cut-off frequency) or equivalently, if the radius of the section is above a certain critical value that is proportional to the frequency, then the mode will propagate (propagating mode). If on the other hand the radius is below the critical value or the frequency is below the cut-off value for the particular section radius then the mode will decay exponentially as it propagates through the section (evanescent mode). The length of the section in the direction of propagation will determine how much power, if any, will be present in that mode at the end of the section.

The cylindrical mode matching program SCATTER works in a way that analyses power coupling between modes at a junction where there is a change in section radius, then the behaviour of each mode is considered over the length of the section, i.e. whether it is propagating or evanescent. Following propagation through the length of the section the power coupling integrals are then performed again at the next junction. This process is repeated for all sections that make up the horn structure.

The approach taken with conical modes is quite different. No mode is purely propagating or purely evanescent since in a conic section the radius of the cone

is continuously changing, either smoothly increasing or decreasing, depending on whether the wave is propagating toward or away from the apex of the cone. So if a wave is moving away from the apex, and it starts out in a part of the cone where the radius is sufficiently small such that the evanescent behaviour dominates, then the amplitude of the wave will begin to decay exponentially as it travels. But as it does so the radius of the cone is steadily increasing and the rate of decay continuously decreases. If the section is long enough, and if there was enough initial power in the mode, then there will be a certain point where the decay in amplitude will cease and the evanescent behaviour will no longer dominate. As the evanescence continues to decline with increasing radius the mode will begin to resemble a true propagating mode.

This inclusion of evanescence in the propagation of conical modes is a result of the behaviour of the Hankel functions. Figure 4.3 at the beginning of this section shows how the real and imaginary parts of the Hankel function of the second kind behave as the length (r) of the conic section increases. As r goes to very small values (close to the apex) the imaginary part of the Hankel function goes toward minus infinity. This is what leads to the evanescent behaviour of the EM modes when the radius of the conic section is small compared to the wavelength of radiation.

The relationship between wavelength and conic section radius is governed by the fact that the Hankel function operates on kr rather than just r , where k is the free-space wavenumber $k = \frac{2\pi}{\lambda}$. As the length of the section increases, and therefore the radius continuously increases, the Hankel function smoothly changes to a sinusoidally varying waveform that exhibits overall exponential decay (exponential envelope) and then it eventually settles down to a sinusoid of constant amplitude that represents a true propagating mode. In this way the Hankel functions are capable of analytically describing the true nature of an EM field as it propagates through a smooth walled conic section.

4.1.5 Cartesian Field Components

In order to compare the analytical modal fields with the approximate field expressions set out at the beginning of this chapter it was required that the spherical modes be defined in Cartesian coordinates so a comparison could be carried out across a

plane. To find the x , y and z components of the electric field the dot product of the field with the corresponding unit vectors is taken (see Figure 4.2 for coordinate system), which gives:

$$E_x = E_r \sin \theta \cos \phi + E_\theta \cos \theta \cos \phi - E_\phi \sin \phi \quad (4.52)$$

$$E_y = E_r \sin \theta \sin \phi + E_\theta \cos \theta \sin \phi - E_\phi \cos \phi \quad (4.53)$$

$$E_z = E_r \cos \theta + E_\theta \sin \theta \quad (4.54)$$

The above relationships hold true for both the TE modes and the TM modes described earlier. Each of the Cartesian field components are made up of a combination of the spherical components. The electric fields for the TE modes expressed in Cartesian form are shown below. The electric fields for the TM modes and the magnetic fields for both the TE and TM ($H_r = 0$) mode sets can easily be transformed into Cartesian form in the same way.

$$E_x = \left[\left(\frac{m}{\sin \theta} (P_\nu^m(\cos \theta)) \cos \theta \cos \phi - \left(\frac{\partial P_\nu^m(\cos \theta)}{\partial \theta} \right) \sin \phi \right) \frac{B}{kr} H_{\nu+0.5}^{(1)}(kr) e^{im\phi} \right] \hat{i} \quad (4.55)$$

$$E_y = \left[\left(\frac{m}{\sin \theta} (P_\nu^m(\cos \theta)) \cos \theta \sin \phi - \left(\frac{\partial P_\nu^m(\cos \theta)}{\partial \theta} \right) \cos \phi \right) \frac{B}{kr} H_{\nu+0.5}^{(1)}(kr) e^{im\phi} \right] \hat{j} \quad (4.56)$$

$$E_z = \left[\frac{mB}{kr \sin \theta} (P_\nu^m(\cos \theta)) \sin \theta H_{\nu+0.5}^{(1)}(kr) e^{im\phi} \right] \hat{k} \quad (4.57)$$

4.1.6 Example Horn for Comparison

Figure 4.8 below shows the E-plane and H-plane cuts of the electric field intensity for a horn of half angle equal to 5 degrees or 0.087 radians. The length of the horn (r) was set to 2 mm, making the radius at the mouth of the horn $a = 0.175$ mm.

To compare the new results with the approximate method, the same example of a smooth walled horn with $\theta_h = 5^\circ$ and $r = 2$ mm was analysed using equation 4.1. The comparisons of the E-plane and H-plane cuts of the electric field intensity for the conical modes vs. the approximate description are shown in Figure 4.9, and it is clear that there is complete agreement between the two descriptions of

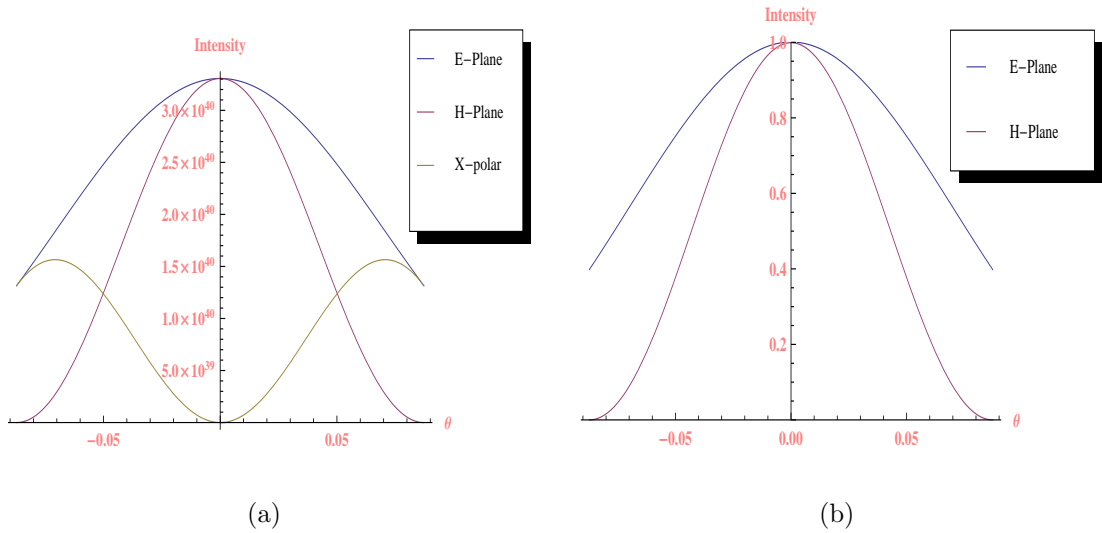


Figure 4.8: (a): E-Plane, H-plane and cross-polar cuts of the electric field at the aperture of a smooth walled conical horn of half angle ($\theta_h = 5^\circ = 0.087$ radians), and (b): The E-Plane and H-plane cuts with the on-axis intensity normalised to unity.

the electric field intensity. This is expected since the horn analysed contained a relatively small half angle of 5 deg. Horns with larger half angles are considered in the next subsection.

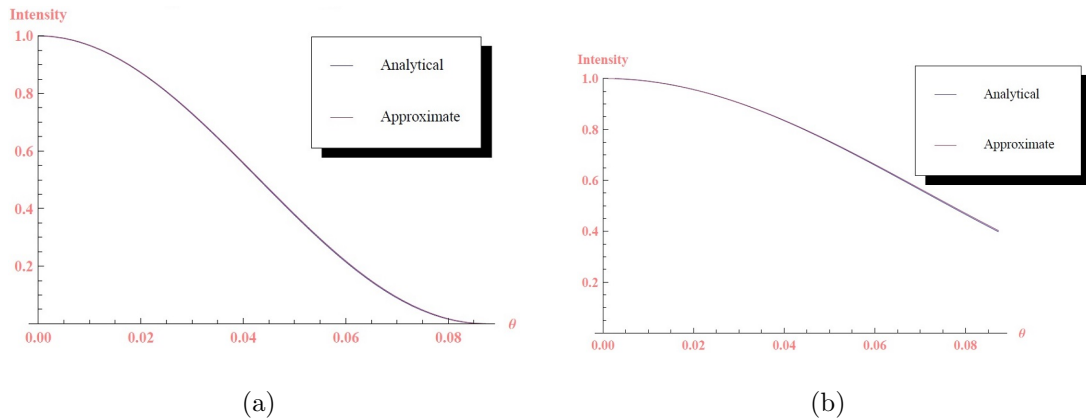


Figure 4.9: Comparison of magnitude of electric field at the aperture of a smooth walled conical horn antenna for analytically derived and semi-analytically derived solutions. (a): E-plane comparison and (b): H-plane comparison.

4.1.7 Limitations of Approximate Method

Spline profiled conical horns have multiple sections with varying flare angles; some of which angles are quite large as can be seen in Figure 4.10, where an example of a multiple conic section spline horn is illustrated. Therefore the limitations of the approximate description for the electric fields must be considered if this method is to be used to model these horns. Multiple examples were analysed and the re-

sults compared for horns with increasing half angle. The example of a horn with a half angle of 5° was already shown to have good agreement for both the approximate and spherical mode approaches. In Figure 4.11 below three cases are shown corresponding to horns with half angles of 10° , 20° and 30° .

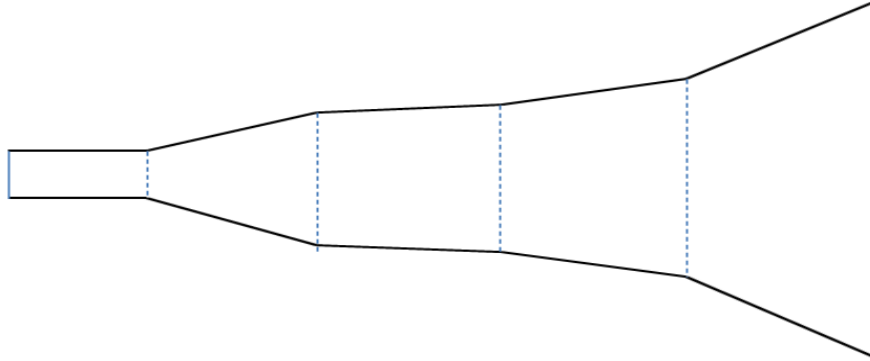
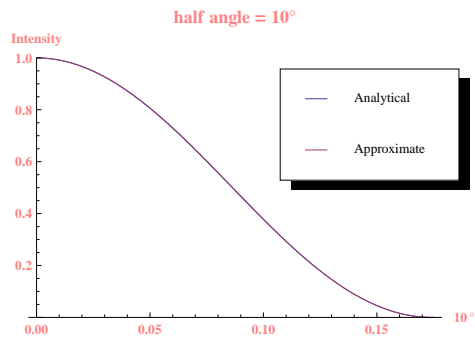
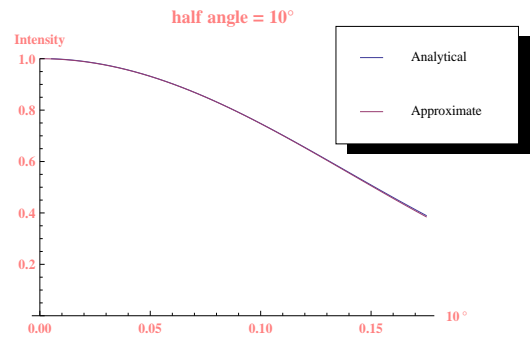


Figure 4.10: Example of a multiple conic section horn. As can be seen some of the section flare angles can be quite large, particularly the final section.

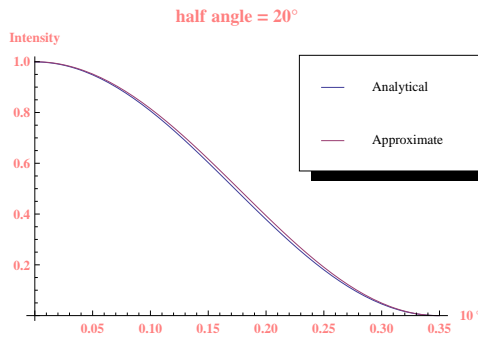
Although only two modes were considered when comparing the approximate and spherical mode approaches, in principle many more higher order modes could propagate in the forward direction through the larger sections of a typical spline horn as the radii of the biggest sections are significantly larger than the wavelength of radiation that the horns are designed for. However the higher order modes will only be present if they are generated through scattering processes since the input waveguide will typically only support the fundamental mode (assuming a single mode system). All higher order modes near the throat of the horn are effectively evanescent and therefore will be attenuated significantly, if not severely, before they reach a radius where they can propagate. As can be seen in 4.11 (a) and (b) there is still excellent agreement for a horn with half angle of 10° . However for 20° there is a small difference in the field structure and for 30° the difference is significant. Therefore to accurately model spline horns with sections of flare angle greater than 20° (half angle = 10°) the full spherical harmonic description will be required. Also, it cannot be guaranteed that even for the case where all flare angles $\theta_h < 20^\circ$ that there won't be some level of scattering into higher order modes at such an interface of changing flare angle. However it should again be pointed out that the angle θ_h is the *half* angle so $\theta_h = 20^\circ$ actually represents a full horn flare angle of 40° which is a relatively large angle in terms of typical horns of this type.



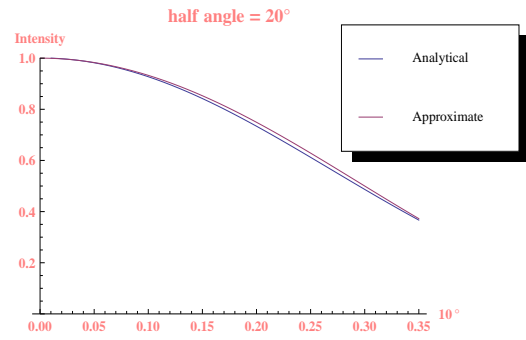
(a)



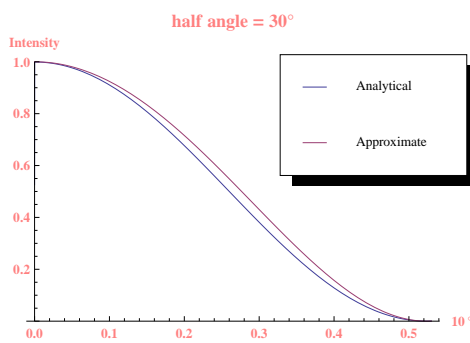
(b)



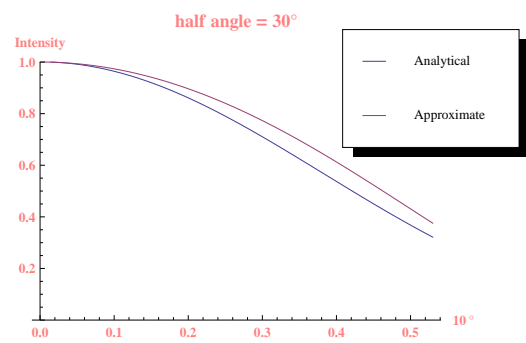
(c)



(d)



(e)



(f)

Figure 4.11: Comparison of TE_{11} electric field patterns inside a smooth walled conical horn antenna for analytically derived and semi-analytically derived solutions. (a) H-plane comparison for $\theta_h = 10^\circ$, (b) E-plane comparison for $\theta_h = 10^\circ$, (c) H-plane comparison for $\theta_h = 20^\circ$, (d) E-plane comparison for $\theta_h = 20^\circ$, (e) H-plane comparison for $\theta_h = 30^\circ$, and (f) E-plane comparison for $\theta_h = 30^\circ$.

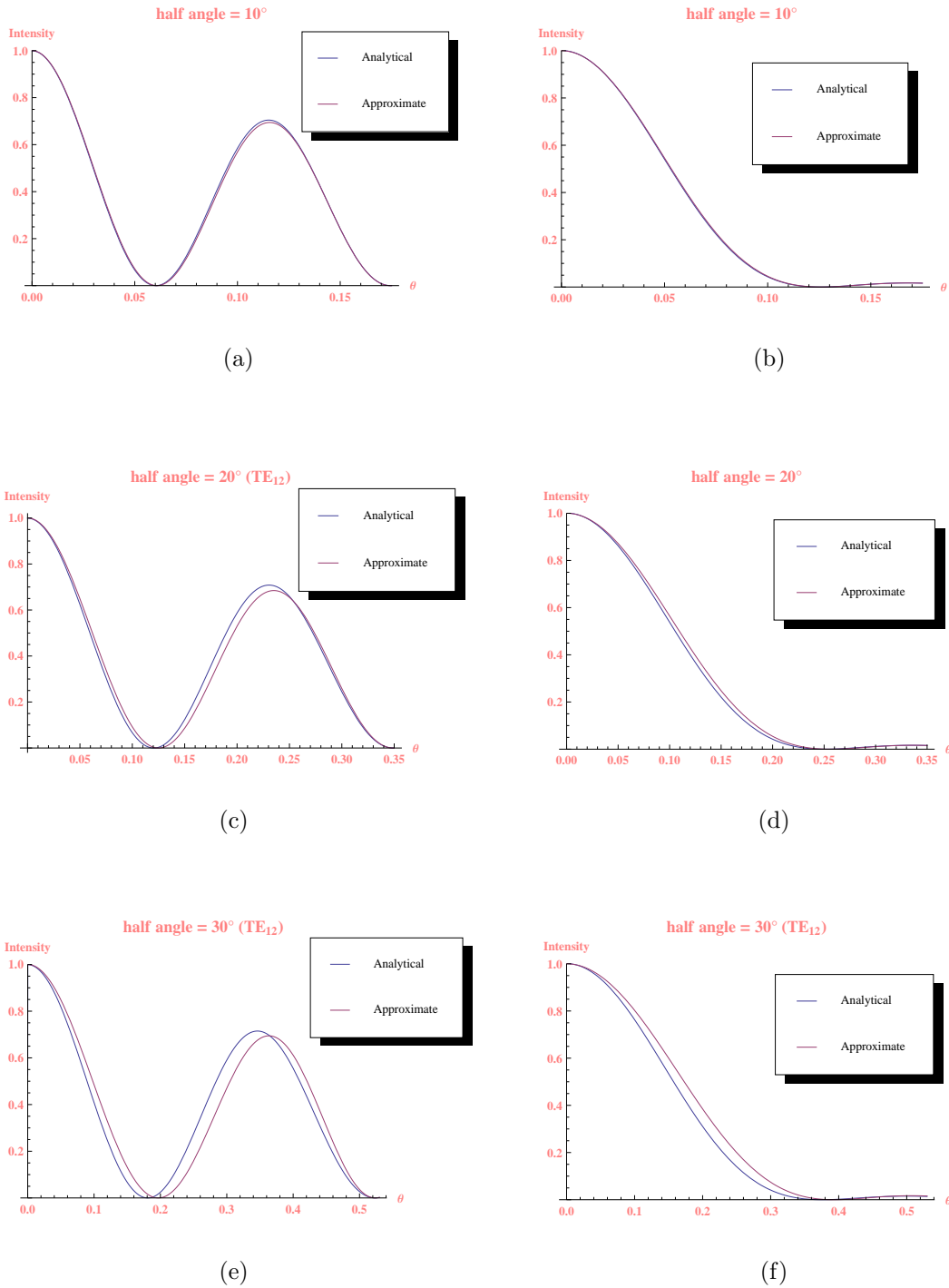


Figure 4.12: Comparison of TE_{12} electric field patterns inside a smooth walled conical horn antenna for analytically derived and semi-analytically derived solutions. (a) H-plane comparison for $\theta_h = 10^\circ$, (b) E-plane comparison for $\theta_h = 10^\circ$, (c) H-plane comparison for $\theta_h = 20^\circ$, (d) E-plane comparison for $\theta_h = 20^\circ$, (e) H-plane comparison for $\theta_h = 30^\circ$, and (f) E-plane comparison for $\theta_h = 30^\circ$.

4.2 Scattering at Conical Horn Junctions (Spherical SCATTER)

With analytical forms now derived for the various components of the TE and TM modes in a conical shaped waveguide or horn, analysis on scattering processes at the interface between horn sections with different flare angles such as in a spline fit horn is now considered in this section.

For constructing the scattering matrices between two conic horn sections the same logic is followed as that for the cylindrical polar and rectangular Cartesian approaches used in the cylindrical and rectangular SCATTER code. The main difference, as will be discussed, is that the power coupling overlap integrals are calculated over a spherical cap, rather than a transverse plane, as was done with the other two cases. The difficulty that arises however is if two conic sections have different flare angles then they both also have different equiphase caps, leading to the question of which phase cap to integrate over. And regardless of which cap is employed for the calculation, the natural mode set on the other section will need to be defined in the coordinate system of the selected one (the two sections have different centres of curvature - or apices in our case). As will be shown this requires a coordinate transformation so that the modes on both sides of the junction can be defined across the same surface.

Another difficulty that arose during this investigation was finding analytical forms for the type of integrals that arise in the power coupling calculations. The integrals involve products of Legendre functions which in free space do have analytical solutions that are defined in much of the literature [Abramowitz and Stegun, 1972], [Lebedev, 1972]. However products of Legendre functions with non-integer eigenvalues (due to the boundary conditions) are not described in any of the literature studied by the author. For this reason all of the integrals over the angle θ were calculated numerically. This process is very computationally demanding, leading to long calculation times for problems involving even a moderate number of modes.

4.2.1 Derivation of S Parameters

The scattering or “S” parameters for the scattering processes involved in EM structures like the conic section spline fit horns discussed above have been explored in some of the texts already mentioned. The texts by both Olver ([Olver *et al.*, 1994]) and Clarricoats ([Clarricoats *et al.*, 1984]) provide some results and definitions for the power coupling integrals and S parameters but the derivations are either not given or are unclear. For the development of the Spherical mode matching code (Spherical SCATTER) it was necessary to revisit their derivations to ensure complete mathematical integrity. Furthermore only the case of single mode systems was considered in any literature that was found on the subject, including the two texts just referenced.

To make the Spherical SCATTER code as flexible as possible the theory was extended to include multi-moded systems. As already mentioned in the introduction to this thesis, multi-moded horn structures are increasingly in demand due to higher throughput requirements for faint signal detection and due to manufacturing limitations on how small components can be made. Therefore multi-moded capability was considered an essential part of the new Spherical SCATTER code requiring that the existing mode matching theory be extended.

It should be made clear that the term multi-moded refers to calculations involving EM modes with higher ϕ dependence. This is represented in the theory by the azimuthal dependence of the associated Legendre functions. When single mode horns are discussed in terms of mode matching only modes of order 1 ($m = 1$ in the associated Legendre functions $P_\nu^m(\cos\theta)$) are considered. Even though there may be multiple modes with higher degree (governed by the ν in the $P_\nu^m(\cos\theta)$) involved in the calculations of power coupling, it is still referred to as a single mode system since the modes are coherent. The main reason for this is due to the fact that modes of a particular order ($m = 1$ for example) do not couple to modes of any other order ($m \neq 1$). This is simply down to the symmetry of the field structure of the modes, and if power coupling overlap integrals are performed between modes of different order the result will always be zero. Due to this orthogonality condition we say that a horn that can only support modes with $m = 1$ (but multiple modes with varying ν) is a single mode system, and a horn that can support modes with $m > 1$ is a truly multi-moded system. Each azimuthal order (m) can be treated

completely separately and then summed in quadrature for calculation of the total field. The sum of squares is used since the azimuthal modes are incoherent, i.e. excited independently of one another.

Considering a particular azimuthal mode order, say $m = 1$, the total electric and magnetic fields within a particular section of a smooth walled conical horn, or conic section of a spline horn, can be defined as being a sum of the spherical modal fields as:

$$\vec{E} = \sum_{n=1}^{\infty} A_n \vec{e}_n + B_n \vec{e}'_n \quad \text{and} \quad \vec{H} = \sum_{n=1}^{\infty} A_n \vec{h}_n - B_n \vec{h}'_n \quad (4.58)$$

where e_n and e'_n represent forward going and backward going waves, respectively, and A_n and B_n are the corresponding amplitude coefficients. The same is true for the magnetic fields h_n and h'_n . Then at the interface (yet to be precisely defined) between two conical sections, the two sets of fields for the two sections are:

$$\begin{aligned} \vec{E}_L &= \sum_{n=1}^{\infty} A_n \vec{e}_{nL} + B_n \vec{e}'_{nL} \quad \text{and} \quad \vec{H}_L = \sum_{n=1}^{\infty} A_n \vec{h}_{nL} - B_n \vec{h}'_{nL} \\ \vec{E}_R &= \sum_{n=1}^{\infty} C_n \vec{e}_{nR} + D_n \vec{e}'_{nR} \quad \text{and} \quad \vec{H}_R = \sum_{n=1}^{\infty} C_n \vec{h}_{nR} - D_n \vec{h}'_{nR} \end{aligned} \quad (4.59)$$

where A_n and B_n are the forward and reflected amplitude coefficients, respectively, of mode n on the left side of the junction. C_n and D_n are the backward and reflected amplitude coefficients, respectively, of mode n on the right side of the junction. e_{nL} and e_{nR} represent forward going waves on the left and right sides respectively, while e'_{nL} and e'_{nR} represent backward going waves. The same is true for h_{nL} , h_{nR} , h'_{nL} and h'_{nR} (see Figure 4.13).

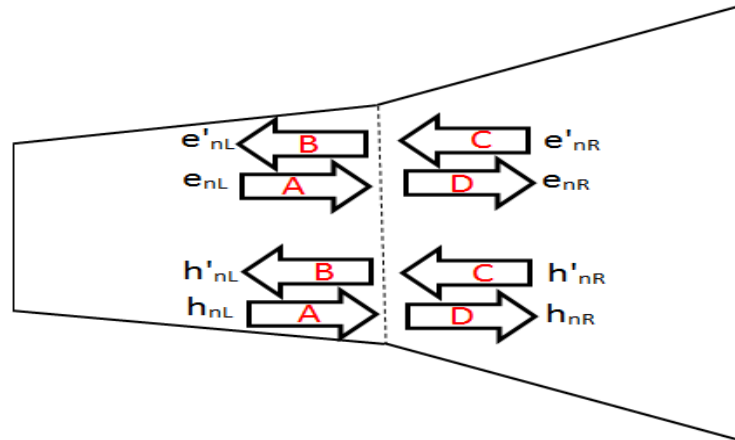


Figure 4.13: Fields on either side of a conical horn flare angle discontinuity.

The SCATTER code calculates the aperture fields of a horn by cascading the S parameters for each section of the horn. The derivation of these parameters begins by considering the modal fields on each side of a spherical surface (yet to be precisely defined) that interfaces two horn sections. The electric field on the left side of the interface must equal the electric field on the right side since the field must be continuous unless there is electric charge present on the interface, which clearly there is not. The same is true for the magnetic field since it too must be continuous across the boundary unless there are electric currents present on the interface, which clearly there is not.

Allowing $\vec{E}_L = \vec{E}_R$ and $\vec{H}_L = \vec{H}_R$, the expressions in 4.59 yields:

$$\begin{aligned} \sum_{n=1}^{\infty} A_n \vec{e}_{nL} + B_n \vec{e}'_{nL} &= \sum_{n=1}^{\infty} C_n \vec{e}'_{nR} + D_n \vec{e}_{nR} & (a) \\ \sum_{n=1}^{\infty} A_n \vec{h}_{nL} - B_n \vec{h}'_{nL} &= \sum_{n=1}^{\infty} -C_n \vec{h}'_{nR} + D_n \vec{h}_{nR} & (b) \end{aligned} \quad (4.60)$$

The next step in this process involves performing an overlap integral for both sides of equation 4.60(a) with the complex conjugate of the magnetic field on the right side of the junction. The requirement is to relate the coefficients B_n and D_n of the transmitted and reflected fields at the two sides of the interface to the incident coefficients A_n and C_n .

$$\begin{aligned} \sum_{n=1}^{\infty} A_n \left(\int \vec{e}_{nL} \times \vec{h}_{mR}^* \right) \cdot d\vec{A} + \sum_{n=1}^{\infty} B_n \left(\int \vec{e}'_{nL} \times \vec{h}_{mR}^* \right) \cdot d\vec{A} \\ = \sum_{n=1}^{\infty} C_n \left(\int \vec{e}'_{nR} \times \vec{h}_{mR}^* \right) \cdot d\vec{A} + \sum_{n=1}^{\infty} D_n \left(\int \vec{e}_{nR} \times \vec{h}_{mR}^* \right) \cdot d\vec{A} \end{aligned} \quad (4.61)$$

Using the Dirak bra-ket notation this can be re-written as:

$$\sum_{n=1}^{\infty} A_n \langle \vec{e}_{nL}, \vec{h}_{mR} \rangle^* + \sum_{n=1}^{\infty} B_n \langle \vec{e}'_{nL}, \vec{h}_{mR} \rangle^* = \sum_{n=1}^{\infty} C_n \langle \vec{e}'_{nR}, \vec{h}_{mR} \rangle^* + \sum_{n=1}^{\infty} D_n \langle \vec{e}_{nR}, \vec{h}_{mR} \rangle^* \quad (4.62)$$

Similarly for 4.60(b), but with the complex conjugate of the *electric* field on the right side of the junction gives:

$$\sum_{n=1}^{\infty} A_n \langle \vec{e}_{mR}, \vec{h}_{nL} \rangle + \sum_{n=1}^{\infty} -B_n \langle \vec{e}_{mR}, \vec{h}'_{nL} \rangle = \sum_{n=1}^{\infty} -C_n \langle \vec{e}_{mR}, \vec{h}'_{nR} \rangle + \sum_{n=1}^{\infty} D_n \langle \vec{e}_{mR}, \vec{h}_{nR} \rangle \quad (4.63)$$

For concise presentation we use some notation for the various overlap integrals just

defined above. It should be noted that the notation used from this point on is the same as that in section 4.7 of Olver [Olver *et al.*, 1994], however there are no derivations of how these authors arrived at the final scatter matrices. Furthermore, the work in that publication deals with *hybrid* spherical modes (i.e. a corrugated conical section) as opposed to the separated TE and TM modes discussed in this work. The following notation will now be used for the various cross products:

$$\begin{aligned}
P_{1mn} &= \langle \vec{e}_{nL}, \vec{h}_{mR} \rangle^* & P_{2mn} &= \langle \vec{e}_{mR}, \vec{h}_{nL} \rangle \\
Q_{1mn} &= \langle \vec{e}'_{nL}, \vec{h}_{mR} \rangle^* & Q_{2mn} &= \langle \vec{e}_{mR}, \vec{h}'_{nL} \rangle \\
R_{1mn} &= \langle \vec{e}'_{nR}, \vec{h}_{mR} \rangle^* & R_{2mn} &= \langle \vec{e}_{mR}, \vec{h}'_{nR} \rangle \\
T_{1mn} &= \langle \vec{e}_{nR}, \vec{h}_{mR} \rangle^* & T_{2mn} &= \langle \vec{e}_{mR}, \vec{h}_{nR} \rangle \\
&& & \Rightarrow T_{2mn} = T_{1mn}^*
\end{aligned} \tag{4.64}$$

Using these definitions equations 4.62 and 4.63 can be rewritten as:

$$P_{1mn} A_n + Q_{1mn} B_n = R_{1mn} C_n + T_{1mn} D_n \tag{4.65}$$

$$P_{2mn} A_n - Q_{2mn} B_n = -R_{2mn} C_n + T_{2mn} D_n \tag{4.66}$$

Or, to account for all modes m and n the above can be written in matrix form as:

$$[P_1][A] + [Q_1][B] = [R_1][C] + [T_1][D] \tag{4.67}$$

$$[P_2][A] - [Q_2][B] = -[R_2][C] + [T_2][D] \tag{4.68}$$

We now wish to relate $[P_1]$, $[P_2]$, $[Q_1]$, $[Q_2]$, etc. to the usual scattering matrices associated with interface junctions. The equation at the start of the previous section describing a two port scattering system is shown again below. Equation 4.69 is equivalent to this and it describes the possible scattering processes that can occur across the spherical boundaries depicted in Figures 4.15 and 4.16 in the next subsection. The transmitted and reflected fields are related to the incident fields at the two boundaries by:

$$\begin{aligned}
\begin{pmatrix} \vec{B} \\ \vec{D} \end{pmatrix} &= \vec{S} \begin{pmatrix} \vec{A} \\ \vec{C} \end{pmatrix} = \begin{pmatrix} \vec{S}_{11} & \vec{S}_{12} \\ \vec{S}_{21} & \vec{S}_{22} \end{pmatrix} \begin{pmatrix} \vec{A} \\ \vec{C} \end{pmatrix} \\
\vec{B} &= \vec{S}_{11}\vec{A} + \vec{S}_{12}\vec{C} & (a) \\
\vec{D} &= \vec{S}_{21}\vec{A} + \vec{S}_{22}\vec{C} & (b)
\end{aligned} \tag{4.69}$$

where \vec{A} and \vec{B} are now column matrices representing the forward and reflected amplitude coefficients, respectively, for all the modes on the left side of the junction. Similarly \vec{C} and \vec{D} are column matrices representing the backward and reflected amplitude coefficients, respectively, for all the modes on the right side of the junction. \vec{S}_{11} , \vec{S}_{12} etc. are sub-matrices that contain the information regarding power coupling between all modes on the input side with all modes on the output side of the interface.

Taking equations 4.67 and 4.68 as a system of simultaneous equations, the coefficient D can be eliminated from the system.

$$[P_1][A] + [Q_1][B] = [R_1][C] + [T_1][D] \quad (a) \quad (4.70)$$

$$[P_2][A] - [Q_2][B] = -[R_2][C] + [T_2][D] \quad (b)$$

Some rearranging gives:

$$\begin{aligned} [B] = & - [[T_1]^{-1}[Q_1] + [T_2]^{-1}[Q_2]]^{-1} [[T_1]^{-1}[P_1] - [T_2]^{-1}[P_2]][A] \\ & + [[T_1]^{-1}[Q_1] + [T_2]^{-1}[Q_2]]^{-1} [[T_1]^{-1}[R_1] + [T_2]^{-1}[R_2]][C] \end{aligned} \quad (4.71)$$

Comparing equation 4.71 above with equation 4.69(a) it is clear that:

$$\begin{aligned} \vec{S}_{11} = & - [[T_1]^{-1}[Q_1] + [T_2]^{-1}[Q_2]]^{-1} [[T_1]^{-1}[P_1] - [T_2]^{-1}[P_2]] \\ \vec{S}_{12} = & [[T_1]^{-1}[Q_1] + [T_2]^{-1}[Q_2]]^{-1} [[T_1]^{-1}[R_1] + [T_2]^{-1}[R_2]] \end{aligned} \quad (4.72)$$

Starting again with equations 4.65 and 4.66 as a system of simultaneous equations, this time the coefficient B can be eliminated from the system. Again, some simple rearranging gives:

$$\begin{aligned} [D] = & [[Q_1]^{-1}[T_1] + [Q_2]^{-1}[T_2]]^{-1} [[Q_1]^{-1}[P_1] + [Q_2]^{-1}[P_2]][A] \\ & - [[Q_1]^{-1}[T_1] + [Q_2]^{-1}[T_2]]^{-1} [[Q_1]^{-1}[R_1] - [Q_2]^{-1}[R_2]][C] \end{aligned} \quad (4.73)$$

Comparing equation 4.73 above with equation 4.69(b) it is clear that:

$$\begin{aligned} \vec{S}_{21} = & [[Q_1]^{-1}[T_1] + [Q_2]^{-1}[T_2]]^{-1} [[Q_1]^{-1}[P_1] + [Q_2]^{-1}[P_2]] \\ \vec{S}_{22} = & - [[Q_1]^{-1}[T_1] + [Q_2]^{-1}[T_2]]^{-1} [[Q_1]^{-1}[R_1] - [Q_2]^{-1}[R_2]] \end{aligned} \quad (4.74)$$

So the four scattering parameters \vec{S}_{11} , \vec{S}_{12} , \vec{S}_{21} , and \vec{S}_{22} have now been derived in terms of combinations of integrals of vector triple products. The integrals represent, in some sense, the flow of complex power across the spherical interface.

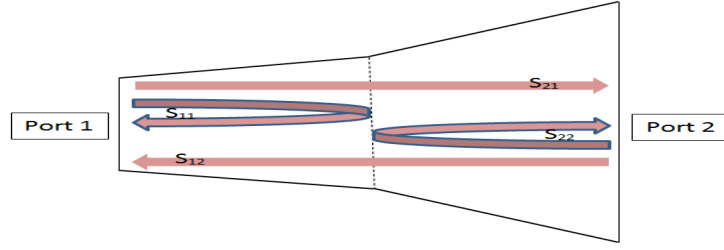


Figure 4.14: Schematic showing the power scattering possibilities for a two port system containing a discontinuity.

4.2.2 Coupling Between Two Conic Sections

As was discussed at the outset of this section if modal power scattering between conic sections of different flare angles is to be analysed then an interface needs to be defined so that the integrals can be calculated over that surface. The appropriate coordinate transformations that are required to enable the fields to be defined over such an interface are discussed in this sub-section for the two possible situations that can arise:

- 1) Going from a section with a smaller flare angle to a section with a larger flare angle.
- 2) Going from a section with a larger flare angle to a section with a smaller flare angle.

The expectation was that the two conditions would be equivalent, but this was checked for verification. So starting with the example of going from a section with a smaller flare angle to a section with a larger flare angle the spherical coordinate systems of both cones were defined as (R_L, θ_L, ϕ_L) for the cone on the left and (R_R, θ_R, ϕ_R) for the cone on the right. For this situation ($\theta_L < \theta_R$) it was decided to perform the power coupling integrations over the equiphase surface of the cone on the right (R_R, θ_R, ϕ_R) . This required expressing the coordinates of the left cone in terms of the coordinates of the right cone, i.e. $R_L(R_R, \theta_R)$ and $\theta_L(R_R, \theta_R)$ so they could be inserted into the expressions for the spherical mode fields of the left hand conic section. The phi component should remain unchanged under the transformation.

As can be seen from Figure 4.15, many parameters require definition due to the virtual extensions of the conic sections back toward the apex of such a full cone for example. Considering the triangle $\angle aR'_R R_L$ in Figure 4.15 and how it would change as the point at the apex of the sides R_L and R'_R traced out the surface C_R . The side

R'_R remains constant, the horizontal length a remains constant, and the angle θ_R rotates through θ_R degrees. The parameter R_L will also slowly vary as θ_R changes, as will the angle θ_L vary from θ_L to zero. The relationship between θ_R and R_L was derived through use of the cosine rule applied to the triangle $\angle aR'_R R_L$, giving:

$$R_L = \sqrt{a^2 + R_R'^2 + 2aR'_R \cos \theta_R} \quad (4.75)$$

where the relationship $\cos(180^\circ - A) = -\cos(A)$ was used. The relationship between θ_R and θ_L was then derived through use of the sine rule applied to the triangle, giving:

$$\theta_L = \sin^{-1} \left[\frac{R'_R \sin(\theta_R)}{\sqrt{a^2 + R_R'^2 + 2aR'_R \cos \theta_R}} \right] \quad (4.76)$$

The situation of going from a larger to a smaller flare angle was dealt with in a very similar manner to that described above. Considering the triangle $\angle aR_L R'_R$ in Figure 4.16 and how it would change as the point at the apex of the sides R'_R and R_L traced out the surface C_R (this time C_R is the inner surface). Again the side R'_R remains constant, and the horizontal length a remains constant but this time it is negative since $a = L_L - \Delta_{LR}$ and $L_L < \Delta_{LR}$ for $\theta_L > \theta_R$. Again the angle θ_R rotates through θ_R degrees. The parameter R_L will again slowly vary (but this time it will get shorter instead of longer) as θ_R changes, as will the angle θ_L vary from θ_L to zero. The relationship between θ_R and R_L was derived through use of the cosine rule applied to the triangle $\angle aR_L R'_R$, giving:

$$\Rightarrow R_L = \sqrt{a^2 + R_R'^2 - 2aR'_R \cos \theta_R} \quad (4.77)$$

which is almost identical to the case of going from smaller to larger angles except for the minus sign. The relationship between θ_R and θ_L was then derived through use of the sine rule applied to the triangle, giving:

$$\theta_L = \sin^{-1} \left[\frac{R'_R \sin \theta_R}{\sqrt{a^2 + R_R'^2 - 2aR'_R \cos \theta_R}} \right] \quad (4.78)$$

which is also almost identical to the transformation derived for the case of smaller to larger angles except for the minus sign.

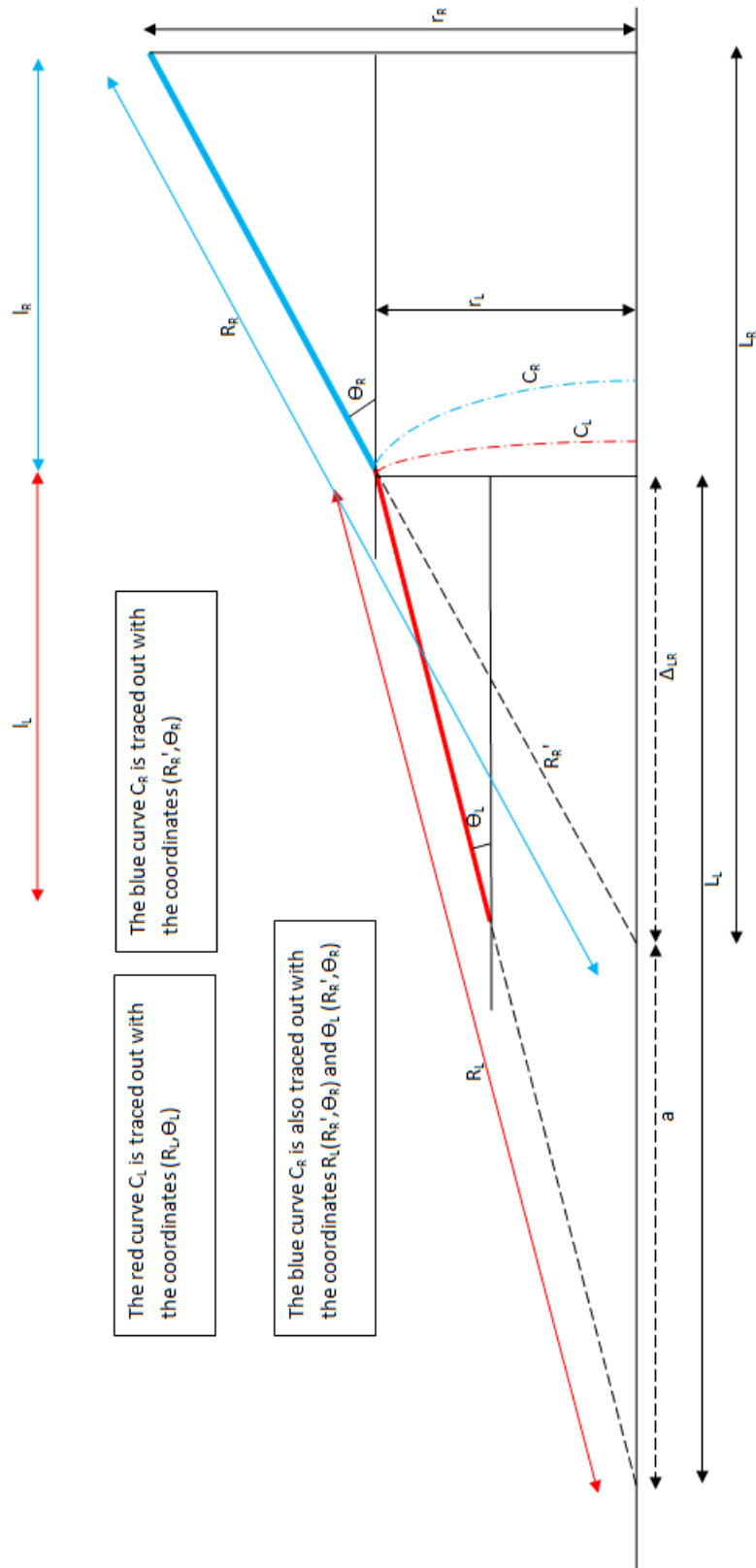
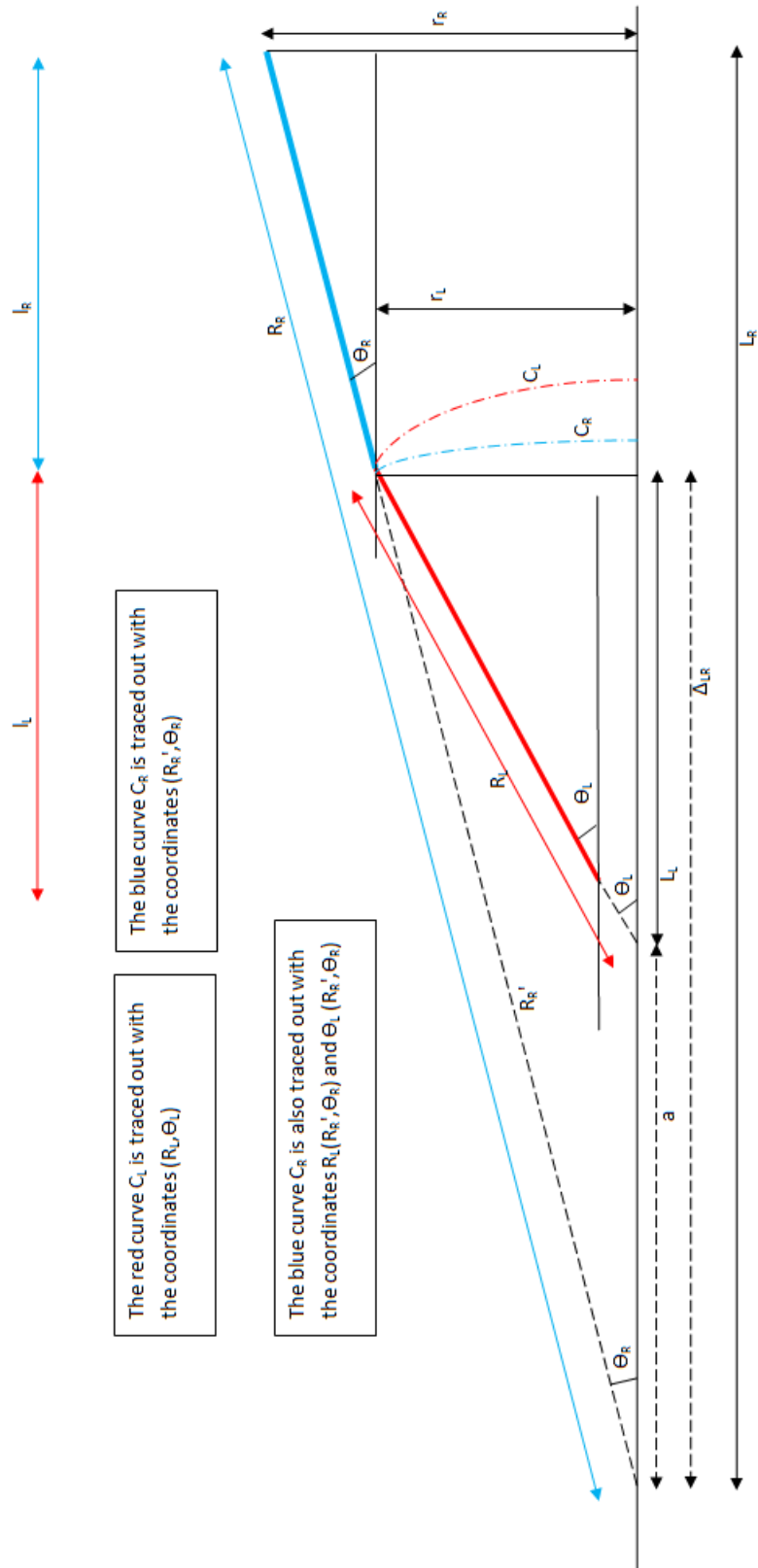


Figure 4.15: Cone-to-cone coordinate transformation for the case of going from a smaller to a larger cone flare angle. The heavy blue and red lines represent the actual horn section boundaries while the dashed black lines trace the virtual extensions of the sections back to their apices.



The red curve C_L is traced out with the coordinates (R_L, θ_L)

The blue curve C_R is traced out with the coordinates (R_R, θ_R)

The blue curve R_L is also traced out with the coordinates (R_R, θ_R) and θ_L (R_R, θ_R)

Figure 4.16: Cone-to-cone coordinate transformation for the case of going from a larger to a smaller cone flare angle. Again the heavy blue and red lines represent the actual horn section boundaries while the dashed black lines trace the virtual extensions of the sections back to their apices.

The coordinate transformations just derived allowed the mode sets on both sides of the junction to be defined across a common surface. This made it possible to perform the power coupling integrals described in section 4.2.1 that are required for construction of the S matrices. In deriving the various \vec{S} matrices account must be taken of all possible left to right and right to left mode couplings including between the TE and TM modes. Table 4.4 shows the possible coupling between the various mode types.

	Transverse Electric	Transverse Magnetic
Transverse Electric	$TE \rightarrow TE$	$TM \rightarrow TE$
Transverse Magnetic	$TE \rightarrow TM$	$TM \rightarrow TM$

Table 4.4: Possible combinations of modal coupling.

The power coupling integrals listed in 4.64 were defined for each combination in Table 4.4. They each had a similar form, for example for a TE mode in the left section coupling to a TE mode in the right section $P_{1_{mn}} = \langle \vec{e}_{nL}^{TE}, \vec{h}_{mR}^{*TE} \rangle = \int_0^{2\pi} \int_0^{\theta_R} \left[\vec{e}_{nL}^{TE} \times \vec{h}_{mR}^{*TE} \right] \cdot \hat{r} \ r^2 \sin \theta d\theta d\phi$, where the fields \vec{e}_{nL}^{TE} in the left section were defined as a function of the coordinates of the right section using the above transformations:

$$P_{1_{mn}} = \int_0^{2\pi} \int_0^{\theta_R} \left[\vec{e}_{nL}^{TE} (R_L (R_R, \theta_R), \theta_L (R_R, \theta_R)) \times \vec{h}_{mR}^{*TE} (R_R, \theta_R) \right] \cdot \hat{r} \ r^2 \sin \theta d\theta d\phi \quad (4.79)$$

Instructions were then defined that stated:

- (a) If $n \leq \frac{N}{2}$ and $m \leq \frac{N}{2}$ then $P_{1_{mn}} = P_{TE \rightarrow TE}$
- (b) If $n \leq \frac{N}{2}$ and $m > \frac{N}{2}$ then $P_{1_{mn}} = P_{TE \rightarrow TM}$
- (c) If $n > \frac{N}{2}$ and $m \leq \frac{N}{2}$ then $P_{1_{mn}} = P_{TM \rightarrow TE}$
- (d) If $n > \frac{N}{2}$ and $m > \frac{N}{2}$ then $P_{1_{mn}} = P_{TM \rightarrow TM}$

where n is the mode number on the left side of the junction, m is the mode number on the right side of the junction, and N is the total number of modes to be calculated and it is split into $\frac{N}{2}$ TE modes and $\frac{N}{2}$ TM modes.

Following this the full $N \times N$ power coupling matrix P_1 was constructed in a manner where it is essentially partitioned into four quadrants with each quadrant

representing one of the four power coupling possibilities.

$$\begin{array}{c}
 TE_{11} \\
 TE_{12} \\
 TE_{13} \\
 TM_{11} \\
 TM_{12} \\
 TM_{13}
 \end{array}
 \begin{array}{c}
 TE_{11} \quad TE_{12} \quad TE_{13} \quad TM_{11} \quad TM_{12} \quad TM_{13} \\
 \left[\begin{array}{cccccc}
 (P_1)_{11} & (P_1)_{12} & (P_1)_{13} & (P_1)_{14} & (P_1)_{15} & (P_1)_{16} \\
 (P_1)_{21} & (P_1)_{22} & (P_1)_{23} & (P_1)_{24} & (P_1)_{25} & (P_1)_{26} \\
 (P_1)_{31} & (P_1)_{32} & (P_1)_{33} & (P_1)_{34} & (P_1)_{35} & (P_1)_{36} \\
 (P_1)_{41} & (P_1)_{42} & (P_1)_{43} & (P_1)_{44} & (P_1)_{45} & (P_1)_{46} \\
 (P_1)_{51} & (P_1)_{52} & (P_1)_{53} & (P_1)_{54} & (P_1)_{55} & (P_1)_{56} \\
 (P_1)_{61} & (P_1)_{62} & (P_1)_{63} & (P_1)_{64} & (P_1)_{65} & (P_1)_{66}
 \end{array} \right]
 \end{array}$$

Similar matrices were constructed for P_2 , Q_1 , Q_2 , etc. But each of the S matrices (S_{11} , S_{12} , etc.) are made up of products of various combinations of the P , Q , R , and T matrices. However the S matrices still have the same partitioned form as that shown above. For example the \vec{S}_{21} matrix that governs how much power will be present in each mode on the right side of the junction (output) for a given input mode set on the left side will have the form:

$$\begin{array}{c}
 TE_{11} \\
 TE_{12} \\
 TE_{13} \\
 TM_{11} \\
 TM_{12} \\
 TM_{13}
 \end{array}
 \begin{array}{c}
 TE_{11} \quad TE_{12} \quad TE_{13} \quad TM_{11} \quad TM_{12} \quad TM_{13} \\
 \left[\begin{array}{cccccc}
 (S_{21})_{11} & (S_{21})_{12} & (S_{21})_{13} & (S_{21})_{14} & (S_{21})_{15} & (S_{21})_{16} \\
 (S_{21})_{21} & (S_{21})_{22} & (S_{21})_{23} & (S_{21})_{24} & (S_{21})_{25} & (S_{21})_{26} \\
 (S_{21})_{31} & (S_{21})_{32} & (S_{21})_{33} & (S_{21})_{34} & (S_{21})_{35} & (S_{21})_{36} \\
 (S_{21})_{41} & (S_{21})_{42} & (S_{21})_{43} & (S_{21})_{44} & (S_{21})_{45} & (S_{21})_{46} \\
 (S_{21})_{51} & \mathbf{(S_{21})_{52}} & (S_{21})_{53} & (S_{21})_{54} & (S_{21})_{55} & (S_{21})_{56} \\
 (S_{21})_{61} & (S_{21})_{62} & (S_{21})_{63} & (S_{21})_{64} & (S_{21})_{65} & (S_{21})_{66}
 \end{array} \right]
 \end{array}$$

where each element $(S_{21})_{ij}$ now represents the quantity of the input mode (along the top of the matrix) that scattered to the output mode (along the vertical of the matrix). For example the amplitude coefficient shown in bold $(S_{21})_{52}$ represents how strongly the input TE_{12} mode on the left side of the junction scattered into the output TM_{12} mode on the other side of the junction. It should be pointed out that the above scatter matrix represents only one azimuthal order and only one junction. Modes of different azimuthal order are treated completely separately as was mentioned previously. The three remaining S matrices (\vec{S}_{11} , \vec{S}_{12} , and \vec{S}_{22}) were constructed in the same format using the relations given in 4.72 and 4.74.

4.2.3 Coupling Between Multiple Conic Sections

For sectional spline horns consisting of multiple conic sections, each with a different flare angle, scatter matrices of the form above must be calculated for each junction of the horn. These scatter matrices take care of mode-to-mode power scattering at each of the section-to-section junctions, but so far there has been no mention of power flow through the length of each conic section. The behaviour of the spherical mode fields through a conic section of constant flare angle is relatively straight forward compared to the scattering that occurs at a discontinuity. In fact as the fields propagate through the section there is no scattering that occurs, so one only needs to consider how each mode changes between the start of the section and the end of the section.

The Legendre functions that govern how the fields behave in the θ and ϕ directions remain unchanged since θ_h remains unchanged and ϕ is always analysed over 2π rad. So the only parameter that changes is the Hankel function since it is dependent on kr , where r is the radial distance along the conic section. Of course the phase front of each mode will change as it propagates through a section, and it would be expected that the amplitude would decrease for the forward going waves as the power spreads out to fill the widening cone.

As was mentioned in the previous subsection, unlike the case for cylindrical waveguides where modes are either purely propagating or purely evanescent, conical modes that begin with dominant evanescent behaviour can become dominantly propagating modes as they move from the narrower to the wider end of a conic section. The opposite is also true for the case of a backward moving wave, i.e. the evanescent behaviour of a mode can begin to dominate as the horn narrows. What is true, however, is that for both forward and backward moving waves the \vec{S}_{11} and \vec{S}_{22} matrices are zero for propagation through a section of constant flare angle, meaning there is no back scatter in either direction, which is also true in the case of cylindrical waveguide mode propagation. In fact the only transformations required for propagation through the uniform sections is to change the value of r in the Hankel function terms contained in the mode descriptions. The r coordinate must be changed from its value relating to the start of the conic section, which corresponds to the length of the full cone including the virtual trace back to the apex, to the value relating to the end of the conic section, also including extension to the apex,

as illustrated in Figure 4.17.

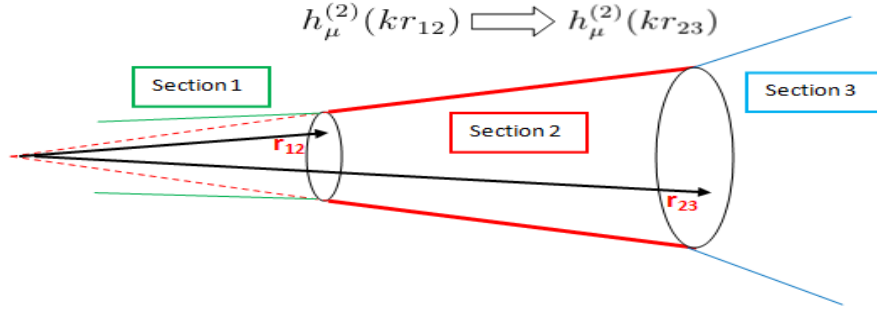


Figure 4.17: Illustration of field transformation from one conic section to the next.

The final step in the scattering process was then to cascade the matrices corresponding to each scattering junction. This is carried out by first cascading the scatter matrices for the first and second sections $[S^a]$ and $[S^b]$ resulting in a third scatter matrix $[S^c]$ that represents the amplitude coefficients in the succeeding section. The algorithm then defines that $[S^b] = [S^a]$ and $[S^c] = [S^b]$ and then calculates a new $[S^c]$ from the new $[S^a]$ and $[S^b]$ for the next succeeding section. The algorithm continues this loop until the last section is reached. The final $[S^c]$ that is calculated from the last two sections is defined as $[S_{total}]$. The method for calculating $[S^c]$ from $[S^a]$ and $[S^b]$ is as follows:

$$\begin{aligned}
 [S_{11}^c] &= [S_{12}^a] [[I] - [S_{11}^b] [S_{22}^a]]^{-1} [S_{11}^b] [S_{21}^a] + [S_{11}^a] \\
 [S_{12}^c] &= [S_{12}^a] [[I] - [S_{11}^b] [S_{22}^a]]^{-1} [S_{11}^b] \\
 [S_{21}^c] &= [S_{21}^b] [[I] - [S_{22}^a] [S_{11}^b]]^{-1} [S_{21}^a] \\
 [S_{22}^c] &= [S_{21}^b] [[I] - [S_{22}^a] [S_{11}^b]]^{-1} [S_{22}^a] [S_{12}^a] + [S_{22}^b]
 \end{aligned} \tag{4.80}$$

The above cascading processes are not derived as they have appeared in many publications including for example [Olver *et al.*, 1994] and [Doherty, 2012]. Again, the above process applies to modes of only one azimuthal order, say $m = 1$. For a single mode system this would be the end of the mode matching process and in order to calculate the aperture field of the sectional spline horn the absolute values of the elements of the $[S_{21}^{total}]$ matrix are used to weight the corresponding TE and TM modes that are defined for the final horn section. The weighted modes are then

simply summed linearly to produce the total aperture field as follows:

$$\vec{E}_{Ap}(r, \theta, \phi) = \sum_{\substack{\{n=N/2\} \\ \{j=N/2\}}}^{\{n=1\} \\ \{j=1\}} [S_{21 \text{ total}}]_{1j} E_{1n}^{\vec{T}E}(r, \theta, \phi) + \sum_{\substack{\{n=N/2\} \\ \{j=N\}}}^{\{n=1\} \\ \{j=\frac{N}{2}+1\}} [S_{21 \text{ total}}]_{1j} E_{1n}^{\vec{T}M}(r, \theta, \phi) \quad (4.81)$$

If a multi-moded system is being considered, where there is more than one azimuthal order being accounted for, then all of the above described steps must be carried out for each order m independently. The behaviour of the fields in the azimuthal direction (ϕ) for the higher order modes is governed by both the order of the Legendre function m for the particular mode and a trigonometric function either of the form $\cos m\phi$ or $\sin m\phi$. In fact it is a product of these two functions that describes the behaviour of the fields, which is clear from Table 4.1. Once the final S matrices have been calculated for each azimuthal order (including that of $m = 0$ for multi-moded horns) then the aperture fields corresponding to each of these independent power channels can be calculated from the $[S_{21 \text{ total}}^m]$ matrix that corresponds to that value of m .

In order to calculate the full aperture field for all modes of degree l and order m that contribute significant power to the fields in the final section of the horn the modes, now weighted by the coefficients encoded in the final $[S_{21 \text{ total}}^m]$ matrices, can be combined. Care must be taken however in the manner in which they are combined. Assuming the horn is illuminated by a blackbody source, and thus each set of azimuthal modes are excited independently, then the modes are clearly incoherent and should be summed in quadrature [Gleeson, 2004]. If modes of common azimuthal dependence are spatially coherent then they should be summed linearly. The full description for the aperture field is then:

$$\vec{E}_{Ap}^{MM}(r, \theta, \phi) = \left[\sum_{m=0}^M \left(\sum_{\substack{\{n=N/2\} \\ \{j=N/2\}}}^{\{n=1\} \\ \{j=1\}} [S_{21 \text{ total}}]_{1j} E_{mn}^{\vec{T}E}(r, \theta, \phi) + \sum_{\substack{\{n=N/2\} \\ \{j=N\}}}^{\{n=1\} \\ \{j=\frac{N}{2}+1\}} [S_{21 \text{ total}}]_{1j} E_{mn}^{\vec{T}M}(r, \theta, \phi) \right) \right]^{\frac{1}{2}} \quad (4.82)$$

The total return power of the horn can also be calculated in a very similar manner but using the $[S_{11 \text{ total}}^m]$ matrices. In this case the actual field structure of

the modes is not required as the field amplitude for each mode (and therefore the power information) is contained in the $[S_{11 \text{ total}}]$ matrices.

4.3 Spherical SCATTER Program

4.3.1 Description of Spherical SCATTER Code

With the full theory for multi-moded conical mode matching described, an account is now given of the structure of the code that was developed by the author. The code is based on heritage from the cylindrical geometry mode matching software SCATTER [Gleeson, 2004], [Colgen, 2001]. The new Spherical SCATTER code was written with the primary aim of calculating aperture field patterns and far-field radiation patterns, specifically for smooth walled structures, in the most computationally efficient way possible. The section-to-section matrix cascading algorithms were similar to those used in cylindrical SCATTER, but the actual power scattering integrals were of a very different form. Spherical SCATTER was written as an alternative solution for modelling smooth walled conical horns with a more exact description of the modal fields. It also has the potential to be much faster computationally due to the fact that the number of calculations is greatly reduced compared to the step-wise smooth wall approximation that cylindrical SCATTER employs.

The first process that is performed in Spherical SCATTER is reading in a geometry file of “*.i.text” format that contains information on operational frequency, maximum azimuthal order, number of conic sections, the length of each section, and the final radius of each section. Table 4.5 shows the layout of the geometry file that is read-in by the code. Figure 4.18 then shows what the r and L values in Table 4.5 represent in terms of the geometry of the horn antenna to be modelled.

The next step involves calculating necessary parameters from the data in the geometry file. These parameters include the flare angle θ_h of each conic section, the slant length R of each section (including the virtual extensions back to the apex), the difference in radial position Δz_{LR} of the apices of each pair of sections, etc. The next section of code then uses these parameters to plot a 2D slice of the horn so the user has a visual representation of the structure.

Using the flare angles θ_h for the various sections the eigenvalues ν_{lm} and μ_{lm} are

Line 1	Frequency (GHz)	Max. Azimuthal Order (m)	Number of Conic Sections (N)
From: Line 2 To: Line N+1	Conic Section Lengths L_n (mm)		
From: Line N+2 To: Line 2N+1	Conic Section End Radii r_n (mm)	Total Number of Modes of Degree l	

Table 4.5: Format of input text file for Spherical SCATTER.

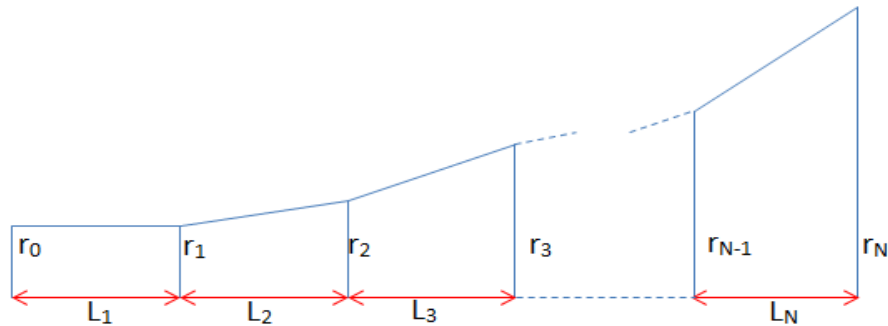


Figure 4.18: Parameters of sectioned spline horn geometry file. The other required parameters for definition of the EM mode fields are derived from r_N and L_n using arithmetic and trigonometric relationships.

then calculated for both the TE and TM modes, respectively. The eigenvalues μ_{lm} correspond to the zeros of the Legendre functions in the mathematical descriptions of the TM_{lm} modes while the eigenvalues ν_{lm} correspond to the zeros of the derivatives of the Legendre functions in the descriptions of the TE_{lm} modes. The calculated eigenvalues are tabulated allowing them to be called by the mode functions during the mode matching calculations. The k parameter is then defined and its value is calculated from the operational frequency that was included in the geometry file.

The mathematical description of the TE and TM modes is then defined for both the forward and backward moving waves. The general definitions are the same for all conic section profiles and therefore are constant for all models. The variables in the TE mode descriptions are ν , m , r , θ , ϕ , and R , where ν is the eigenvalue of mode of degree l , m is the azimuthal order, r is the radial distance along the conic section, θ is the off-axis alt. angle, ϕ is the off-axis az. angle, and R is the full length of the cone from the virtual apex to the spherical cap of the section. The same variables are left free for the TM mode definitions where ν is of course replaced with μ .

The overlap integrals are then defined for each of the power scattering possibilities P_1, P_2, Q_1 , etc. for TE to TE, TE to TM, etc. Using these definitions the scatter matrices are then constructed for each cone-to-cone junction. The mode transformation matrices corresponding to propagation through the uniform conic sections are also now calculated. The cascading process can then be performed comprising of alternating scatter and transformation matrix cascading to account for propagation through a section followed by scattering at a discontinuity, followed by propagation through the succeeding section, etc. until the final section is reached. If a multimoded horn is being analysed then at this point the value of m is incremented and the processes described in this paragraph are repeated. The processes are further repeated for each value of m including $m = 0$.

This is where the mode matching section of the Spherical SCATTER code ends. All further calculations performed by the code such as aperture field description, return power, and horn efficiency involve using the elements of the final \vec{S} matrices. An overview of the structure of the Spherical SCATTER code is shown in Figure 4.19.

FOR EACH AZIMUTHAL ORDER (m)	FOR EACH SECTION (n)	FOR EACH MODE	Calculate eigenvalues V_{lm} and μ_{lm} for all modes of degree l and order m .
			Mode descriptions for forward going and backward going waves.
			Self-coupling and Cross-coupling overlap integrals defined ($Q_1, Q_2, R_1, R_2, T_1, T_2, P_1$, and P_2).
		Coupling coefficients calculated from above overlap integrals are used to construct the scattering matrix for a junction between two sections where flare angle changes.	
		Cascade matrix with overall cascaded matrices representing sections preceding the present one. Output final scatter matrices S_{11}, S_{12}, S_{21} , and S_{22} .	
Scattering matrix S_{21} corresponds to modal transmission.			
Scattering matrix S_{11} corresponds to modal return power.			

Figure 4.19: Overview of how the Spherical SCATTER code performs its algorithms.

4.3.2 Test Horn

As a verification test of the Spherical SCATTER code an example horn was modelled and the resulting aperture fields were compared to those calculated with the well established mode matching code Cylindrical SCATTER which has shown excellent agreement with experiment over many tests and was used to design and analyse the feed horns for the HFI instrument on the PLANCK CMB system [Murphy *et al.*, 2010]. The particular horn consisted of five conic segments, each with a different flare angle, and one initial straight waveguide section (see Figure 4.20). The lengths of the conic sections were all the same at 8.781 mm, the maximum azimuthal order was set to one (single-mode horn), and the frequency was set to 100 GHz.

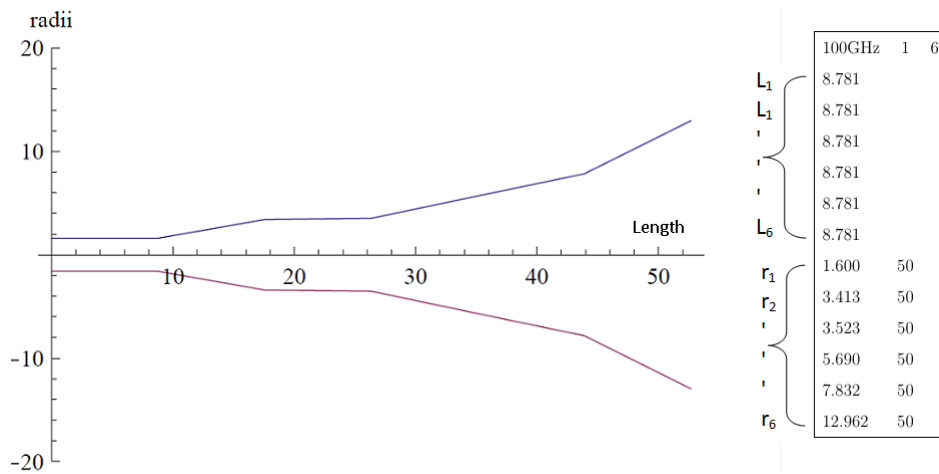


Figure 4.20: Automated plot from the Spherical SCATTER program. A plot of this type (excluding the table of values on the right) is automatically generated after the geometry file is 'read in' to the program.

The design of this horn was optimised through the work of the THz Optics Group at NUIM, with the aim of developing a smooth walled horn that is capable of producing similar beam qualities to that of corrugated structures, as already outlined at the beginning of this chapter [McCarthy *et al.*, 2013]. The particular beam qualities demanded by the design were high Gaussicity and good beam symmetry. High Gaussicity ensures low side-lobe levels in the far-field pattern, while a good level of rotational symmetry in the beam allows for accurate polarisation measurements.

What should be noticed in the table of values in Figure 4.20 is that there are only six lengths and six radii. In contrast, the Cylindrical SCATTER code

typically requires a few hundred lengths and radii for definition of the horn geometry due to the manner in which the smooth walls are approximated by small uniform waveguide sections in a “stairs-like” format. The six sections of the test horn and waveguide indicate that power scattering integrals will need to be evaluated at just five junctions for this example. Table 4.6 shows the eigenvalues for the first six TE and the first six TM modes.

Section (n)	W.G.	1	2	3	4	5
Angle (θ_h)	0°	11.67°	0.72°	13.86°	13.71°	30.29°
ν_{11} (TE_{11})	∞	8.5828	146.487	7.15735	7.24223	3.08647
ν_{12} (TE_{12})	∞	25.6963	425.117	21.549	21.7962	9.6135
ν_{13} (TE_{13})	∞	41.4324	680.967	34.7899	35.1858	15.6634
ν_{14} (TE_{14})	∞	56.9981	934.008	47.8883	48.4313	21.6532
ν_{15} (TE_{15})	∞	72.5052	1186.08	60.9377	61.6271	27.6223
ν_{16} (TE_{16})	∞	87.985	1437.71	73.9641	74.7998	33.5818
μ_{11} (TM_{11})	∞	18.3257	305.391	15.3448	15.5224	6.76452
μ_{12} (TM_{12})	∞	33.9601	559.565	28.5005	28.8259	12.7783
μ_{13} (TM_{13})	∞	49.4686	811.663	41.5511	42.023	18.7479
μ_{14} (TM_{14})	∞	64.94	1063.15	54.5706	55.1886	24.7044
μ_{15} (TM_{15})	∞	80.3956	1314.37	67.5768	68.3408	30.6552
μ_{16} (TM_{16})	∞	95.8428	1565.46	80.5761	81.486	36.6032

Table 4.6: Eigenvalues for the first six TE and TM modes in each of the five horn sections. If the table is analysed closely it will be clear that the larger angles produce smaller eigenvalues while the smaller angles produce the larger eigenvalues.

Figure 4.21 shows the final aperture field through the E-plane and H-plane cuts calculated with the new Spherical SCATTER code. Figure 4.21(a) shows the fields compared to the original input field that was excited through the uniform waveguide section. It is clear that the output aperture field has changed significantly from the input TE_{11} mode, which demonstrates the level of scattering that occurs due to the multiple changes in flare angle throughout the horn. Both the E-plane and H-plane cuts show a high level of Gaussicity, and there is good symmetry in the field, as required. Figure 4.21(b) shows the same aperture field results, this time compared to data that was calculated using the more established Cylindrical SCATTER to

model the same horn. As can be seen there is good agreement between the two approaches.

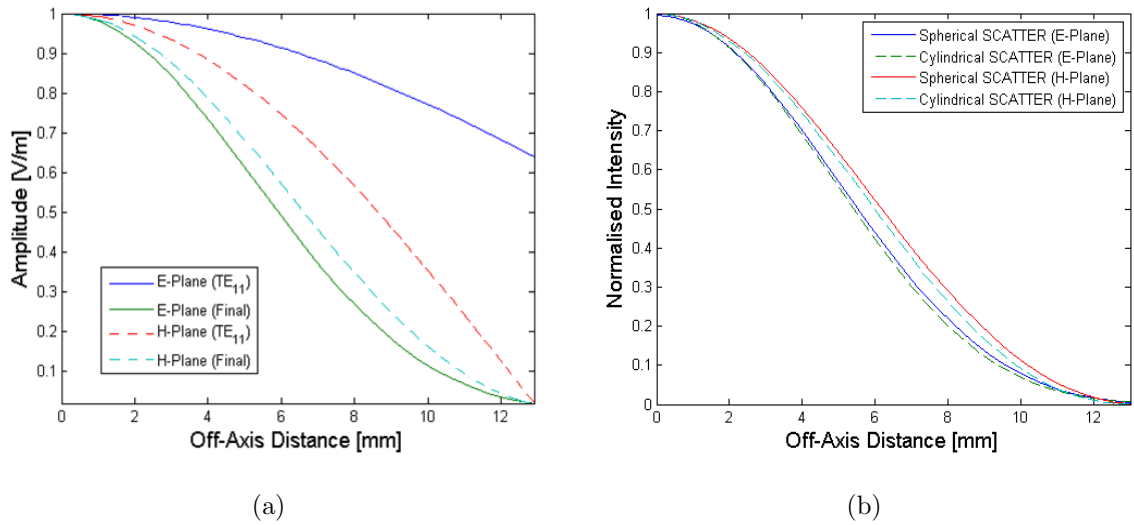


Figure 4.21: Aperture field patterns for the E-plane and H-plane cuts of the electric field intensity through a smooth walled conic section horn. (a): The aperture fields compared to the input TE_{11} waveguide field, which demonstrates the level of scattering that occurs in the horn. (b): The new Spherical SCATTER results compared to Cylindrical SCATTER results.

Since the conic section horn that was used for verification of the new Spherical SCATTER code was a real design that was built for testing, further analysis of the horn using the FEM approach was carried out. A simulation of the induced currents across the adjoining boundary of an array of such horns, similar to the analysis that was performed for the SAFARI horns as presented in chapter 3, was analysed with COMSOL. The effects of any induced currents on the far-field beam pattern were investigated for the conic section test horn. Figure 4.22 shows a screenshot of the FEM model, where the magnitude of the electric field is indicated by the colour variation. Both the E-plane and H-plane symmetry conditions were used to reduce the problem size by a factor of four. The spheric section connected to the exit aperture of the horn, which represents the propagation region, is also visible in screen-shot. Figure 4.23(a) shows E-plane and H-plane linear cuts through the surface current density across the conducting ground plane (GP) that lies in the plane of the exit aperture of the horn. Figures 4.23(b) to 4.23(d) show comparisons of the far-field pattern with and without the conducting ground plane, i.e. the horn in free-space compared to the horn in an array block. It is clear that any induced currents across the ground plane have negligible effects on the far-field pattern. The cross-polar distribution shows some differences for the two cases, although the

maximum levels are roughly the same.

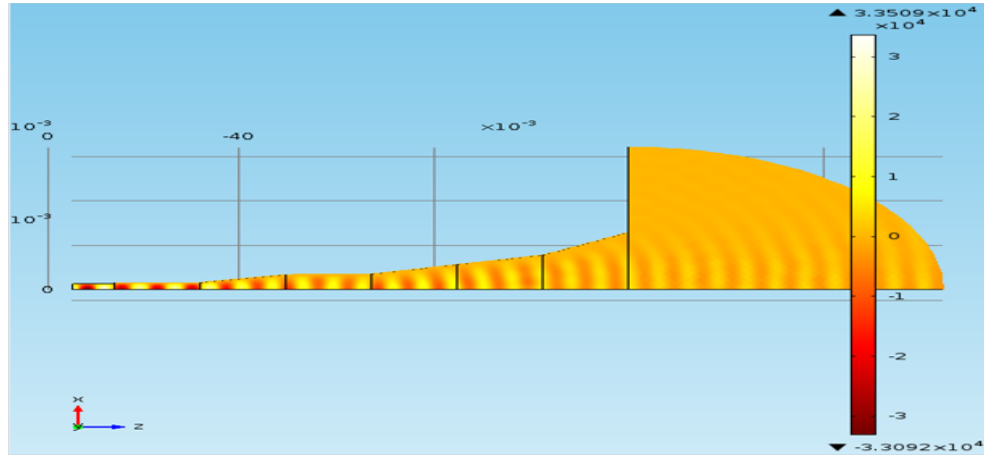


Figure 4.22: Screen-shot of FEM model of smooth walled conic section horn.

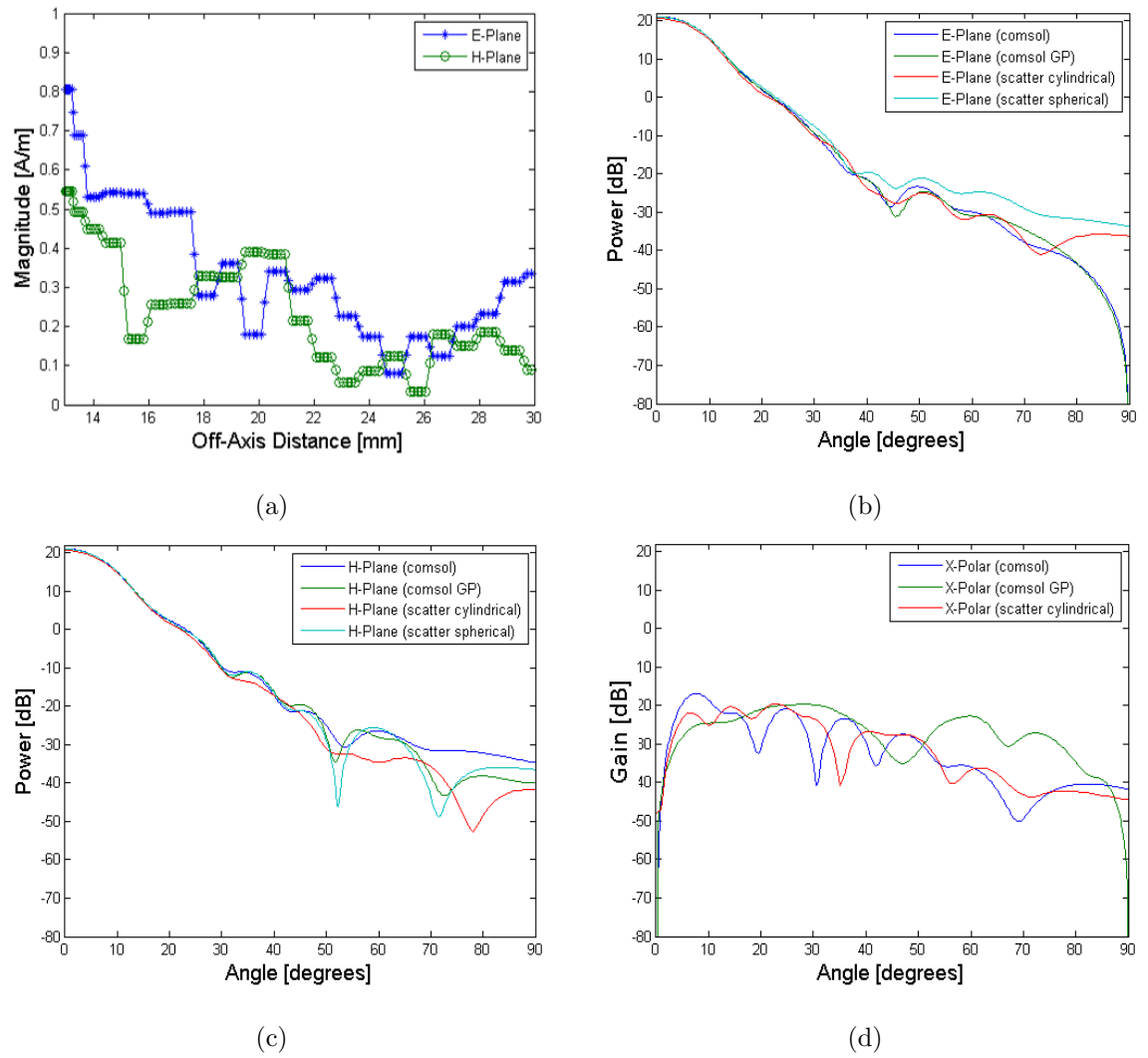


Figure 4.23: Results for a profiled smooth walled conic section horn. (a): The induced surface current density across the conducting ground plane that would separate neighbouring horns, (b): E-plane cut through the far-field pattern, (c): H-plane cut through the far-field pattern, and (d): cross-polar far-field pattern through the $\phi = 45^\circ$ cut.

4.3.3 Experimental Verification

A rigorous set of measurements was carried out by members of the THz Optics Group at NUIM in terms of testing the performance of the test horn described above. The work was primarily driven by Darragh McCarthy, and it involved measuring both the co-polar and cross-polar radiation patterns at various propagation distances, including the far-field. The experimental measurements agreed extremely well with the Cylindrical SCATTER results, and thus Spherical SCATTER, and the full analysis is due to be presented at the SPIE: Millimeter, Submillimeter, and Far-Infrared Detectors and Instrumentation for Astronomy VII conference in Montreal, Canada, in June 2014. A paper on the horn measurements and results will be included in the corresponding conference proceedings [McCarthy *et al.*, 2014].

4.4 Conclusions

In this chapter the theory for EM propagation through smooth walled conical horns and conic sections was described in detail in its full analytical form. Comparisons were made between the exact solutions for TE and TM modes and the approximate solutions that employ cylindrical waveguide modes with a spherical cap correction factor. Good agreement between the two approaches was demonstrated for horns of modest flare angle, and it was shown that the approximations were sufficiently accurate for use as a starting point for a search of roots of the Legendre functions and their derivatives, which were required for determining the eigenvalues of the TE and TM mode solutions.

The results of the new mode matching code, Spherical SCATTER, which was developed by the author, was shown to be in good agreement with the already established and verified Cylindrical SCATTER code, and the FEM software package COMSOL. The verified results of the Spherical SCATTER code demonstrates that it is possible to model the novel smooth walled conic section horns with two orders of magnitude fewer power scattering integrals, compared to the Cylindrical SCATTER approach.

It was explained that some of the theory in this chapter pertaining to spherical mode matching has already been reported on in the literature, most notably by

[Olver *et al.*, 1994] and [Clarricoats *et al.*, 1984]. However since there was little to no derivation of the mathematics it was necessary to revisit the theory with a full and detailed derivation of the most important aspects to ensure mathematical integrity of the new Spherical SCATTER code. Furthermore, the theory in the literature only describes examples of single-mode systems, thus requiring an extension of the theory to account for multi-moded horns. This extended theory was presented in section 4.2.3 of this chapter.

This novel approach to modelling smooth walled conic section spline horns with conical mode matching is an exact solution that relies on approximations only for initial ‘guess’ values for the eigenvalues of the modal fields. All of the fields were derived analytically from Maxwell’s equations. The Spherical SCATTER code, in its present state, ultimately proved to be computationally slower than the Cylindrical SCATTER code. This is due to the numerical integrations used in the analysis of the power scattering calculations. Although modelling a smooth walled horn with Spherical SCATTER requires much fewer power scattering calculations than a similar Cylindrical SCATTER model, the analytical forms employed by Cylindrical SCATTER outweighs the large number of calculations.

Potential future work in this area is the optimisation of the code to increase computational speed. This could be achieved by deriving analytical forms for the integrals involving products of the Legendre functions and their derivatives, and implementing them in place of the numerical integrals used presently. Alternatively the Bessel function approximations that were shown to be accurate for horns of moderate flare angle could be used in place of the Legendre functions. Efficient analytical solutions to integrals involving Bessel functions are well understood and are already used in the Cylindrical SCATTER code.

Chapter 5

The Electromagnetic Design and Analysis of Cavity Coupled Absorbers for SAFARI

“We are at the very beginning of time for the human race. It is not unreasonable that we grapple with problems. But there are tens of thousands of years in the future. Our responsibility is to do what we can, learn what we can, improve the solutions, and pass them on.”

- Richard P. Feynman

5.1 Background

The detectors of the SAFARI instrument will employ a TES [Khosropanah *et al.*, 2012] in each pixel housed in an integrating cavity. Each TES is mounted on a square piece of absorbing material that is relatively large compared to the TES. For example the current design of the SAFARI Short-Wave Band (S-Band) pixel employs a $200 \times 200 \mu\text{m}$ square of Ta (tantalum) film that is only a few nanometres thick coupled to the TES. The TES/absorber combination is cooled to a few milliKelvin and therefore the Ta operates in a superconducting state. A SAFARI test-bed being studied by the SRON currently uses a hemispherical backshort and the system is fed by a smooth walled conical horn. Radiation from the blackbody source is focussed onto the absorber by the feed horn, while the shaped backshort behind the TES/absorber serves to reflect any radiation that is not initially absorbed back toward the absorber (see Figure 5.1). The cavity thus set up between the absorber and the backshort provides a matched impedance for the incoming radiation in order to maximise the radiation that is absorbed. From an optical viewpoint standing waves are set up in the cavity between the absorber and the backshort. A detailed description of the SRON SAFARI S-Band test-bed is given in section 3.3.

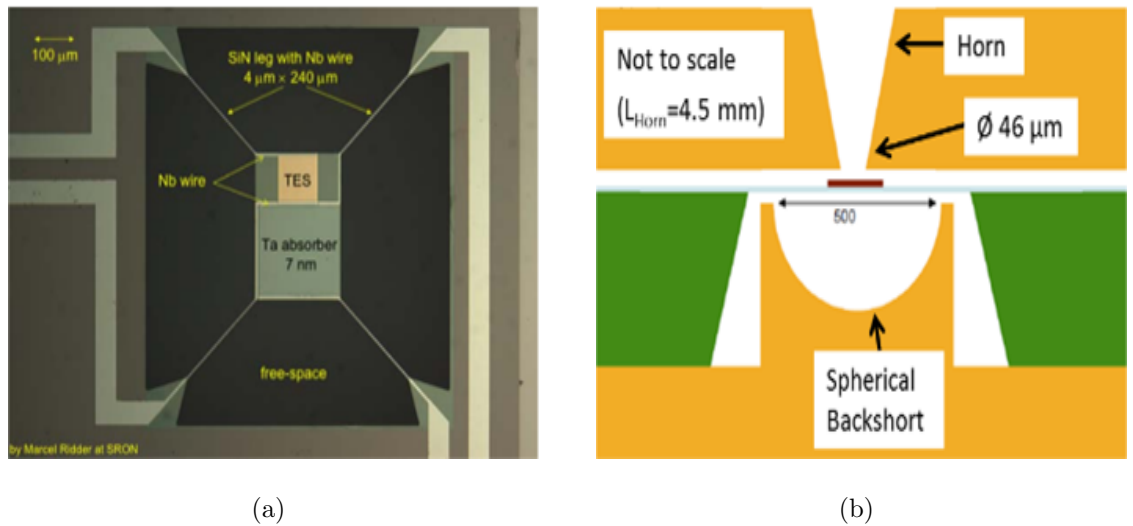


Figure 5.1: Illustration of a SAFARI TES mounted on the Ta absorber. (a): Aerial view showing how the TES and absorber are mounted over the cavity by using thin niobium (Nb) legs. (b): A cut through the SAFARI pixel showing the current design of a hemispherical integrating cavity.

Clearly it is important to be able to predict the optical efficiency of such cavity coupled detectors for the high sensitivities required of far infra-red astronomy and CMB experiments. Efficient computational models are essential for the design

and analysis of these detector systems and the results must be reliable. Modelling such cavity mounted absorbers requires sophisticated EM modelling which tends to be computationally intensive and in the past it was generally not possible to model electrically large cavity structures (in terms of wavelength) without the use of supercomputers.

By analogy with large integrating spheres in infrared systems (based on ray tracing), the assumption was generally made that a hemispherical shaped backshort would refocus in some sense the radiation not absorbed by the absorber in the first pass through it back to the absorber. Now, with more powerful PCs available and employing more efficient simulation techniques, it is possible to include these absorbing cavities in the models (see for example simulations for the SPIRE instrument on the Herschel Space Observatory [Glenn *et al.*, 2003]).

Another assumption during the design of previous systems was often that such cavities (integrating cavities) could be assumed to behave like blackbody cavities, and if feeding multi-mode horn antennas they would excite all the waveguide modes equally (Planck HFI for example [Maffei *et al.*, 2010]). Clearly for achieving the highest sensitivities possible, a more complete understanding of the absorbing cavity is required. Again this is particularly important for multi-mode systems as then it is possible to predict both the multi-mode beam pattern of the horn based on the correct coupling of the individual waveguide modes to the absorbing cavity, and predict an overall optical efficiency or throughput for the system as a whole for both point like and extended source illumination, or indeed the predicted illumination by the FTS output beam for the system on the telescope.

In this chapter we first consider the computational simulation tools available and discuss the validity of various approximate approaches. The original SAFARI Long-wave Band (L-Band) cavity design proposed (based on the hemispherical backshort) is then discussed and simulations using the FEM with the commercially available COMSOL package are described. The redesign of the backshort configuration for improved coupling of the absorber to the cavity is then considered with both FEM simulations and a novel mode matching approach. Finally the SAFARI S-Band is discussed and a redesign of the S-Band multi-moded cavity for improved absorber efficiency is described. The theory of including the Ta absorber in the models is explained, and potential methods for the future for including the vacuum

gap in the mode matching models are discussed.

Modelling cavity structures is very similar to the way waveguides and feed horns are handled as described in chapters 3 and 4, and the absorber material is approximated as an infinitely thin, two dimensional resistive sheet with units of Ohms per square (Ω/\square). The TES itself is omitted from the models as it is the Ta absorbing film that couples to the incoming radiation, and the TES essentially acts as a thermometer to detect the rise in temperature of the Ta. A research team at SRON are attempting to model the TES and the SiN legs on which the TES and absorber are mounted in terms of the heat conductance and the heat capacity in the SiN legs, and the impedance and noise in the TES itself (see for example [Khosropanah *et al.*, 2012]).

The validity of the resistive sheet approximation for the piece of Ta absorber is supported by work carried out by a research group at Cambridge University U.K. [Withington *et al.*, 2013]. They showed that, for a THz beam within the frequency range of approximately 1.4 - 8.8 THz incident on a thin sheet of Ta at moderate angles of incidence, the reactive part of the complex impedance is almost three orders of magnitude smaller than the resistive part, and frequency-independent absorption is possible. They explain that this is true once the thickness of the Ta sheet is less than 10 nanometres ($d < 10\text{nm}$)(See also [Thomas and Withington, 2013]).

5.2 Modelling Approaches

5.2.1 Mode Matching Approach

The theory for modelling waveguide and horn structures with mode matching techniques was discussed in detail in the previous chapter 4. It is an extended version of the mode matching program SCATTER (for cylindrical systems) that was employed in this section to model closed cavities housing resistive sheet absorbers. A summary of the theory that was required for the extension of the code is presented in this section, however the author was not involved in developing the theory or implementing it into the original SCATTER code. The author carried out verification analysis of the code by using it to model a variety of systems, some of which are presented in this chapter, and comparing the results to the same systems modelled with FEM

techniques. The code was validated based upon the good agreement observed in the comparison analysis.

In order to model a closed cavity little modification to the existing code is required. If for example a hemispherical cavity is desired the input geometry text file representing the geometry of the structure is constructed in a manner where the spherical shape is approximated by a series of waveguide sections with increasingly smaller radii where the rate at which the radii reduce is just governed by the equation for a circle. Figure 5.2 illustrates an example of a hemisphere. In the illustration there are only five sections making up the structure for clarity, however there would be a lot more sections in a real model in order to build a smoother, less jagged profile; the minimum number of steps depends on the wavelength of the radiation being simulated.

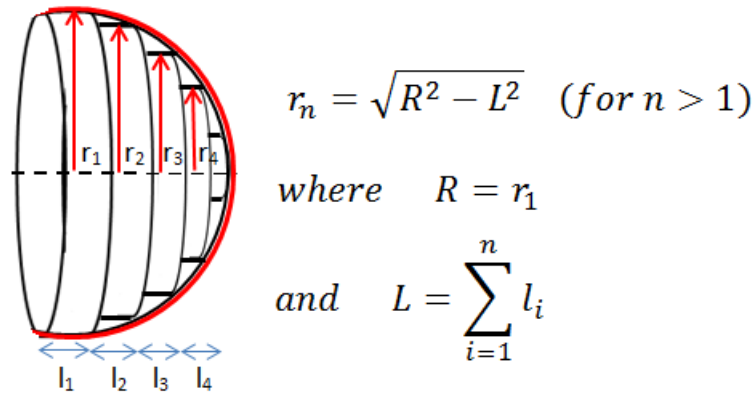


Figure 5.2: Diagram showing how a profiled waveguide structure can be approximated by a series of uniform cylindrical sections. This particular example is for a hemisphere.

Building up cavity geometries in this stepwise manner is clearly a natural extension of how horn structures are modelled with the SCATTER code. The real modification of the SCATTER code was required for including the resistive sheet absorber, and it was the author's role to validate the code by using it to model some simple examples of cavity housed absorbers and then to compare the results to those of FEM models of similar examples. Following validation through testing the author then employed the extended SCATTER code to model various proposed systems such as the SAFARI L-Band, and then to design improved systems as will be shown throughout the chapter. The theory for including a resistive sheet absorber in the SCATTER mode matching code is now summarized.

The TE and magnetic fields in a smooth walled cylindrical waveguide section

were derived and tabulated in chapter 2. The first step in describing the mode matching approach that also takes account of an absorbing resistive sheet begins, as before, by regarding a propagating signal as a sum of such transverse waveguide modes. And considering first the case where the cylindrical symmetry is not broken the modes of the same azimuthal order do not mix. For the sections of the cavity or horn structure where there is no absorber material present, the theory is the same as that described in the mode matching description given in section 2.4. If an absorber is then to be modelled at a particular position/junction between the horn and cavity, or anywhere within the horn or cavity, it can be considered as a resistive current sheet with the electric field constant across the boundary and a drop in the magnetic field due to induced surface currents, leading to the following boundary conditions:

$$\begin{aligned} \vec{E}_L &= \vec{E}_R \\ \vec{H}_L &= \vec{H}_R - \vec{K} \times \hat{k} \\ \text{with } \vec{K} &= \frac{\vec{E}_L}{\eta} = \frac{\vec{E}_R}{\eta} \end{aligned} \quad (5.1)$$

where \vec{K} is the induced current density, η is the sheet resistance defined in units of Ω/\square and \hat{k} is just a unit vector in the direction of propagation (z).

The sheet resistance described in (5.1) is valid for a two-dimensional system when the thickness of the absorber material is negligible. The sheet resistance implies that there is only induced currents in the plane of the sheet and no currents in the perpendicular direction. In S.I. units the more familiar bulk resistivity ρ has units of Ωm (Ohm metres) or alternatively $\Omega\text{m}^2/\text{m}$ since the overall bulk resistance R will depend on a product of the bulk resistivity ρ , the length L in m, and the reciprocal of the area A in m^{-2} of the medium, i.e. $R = \frac{\rho L}{A}$. If we then consider the area A being made up of a width W and a thickness δ as shown in Figure 5.3 then we can write the resistance as $R = \frac{\rho L}{A} = \frac{\rho L}{W\delta}$. Then combining ρ with $1/\delta$ and calling this $R_S = \rho/\delta$, then the resistance can be written as:

$$R = R_S \frac{L}{W} \quad (5.2)$$

where $R_S = \frac{1}{\sigma\delta}$, since $\rho = 1/\sigma$.

Since both L and W have units of metre then the dimensions really cancel out, however the term Ohms per square is used since if $L = W$ (i.e. a square) then such

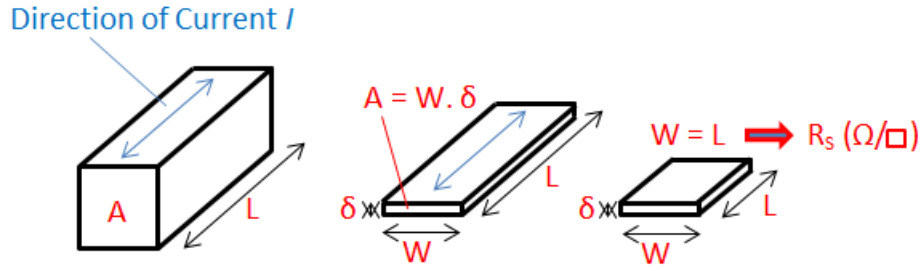


Figure 5.3: Illustration comparing bulk resistance to sheet resistance.

a square with sheet resistance, say 50 Ohms/square, has an actual resistance of 50 Ohms, regardless of the size of the square.

If we want to consider the sheet resistance in terms of induced surface currents due to the jump in the magnetic field as stated in the boundary conditions in 5.1 then we begin by stating Ohm's law:

$$\vec{J} = \sigma \vec{E} \quad (5.3)$$

Then taking Maxwell's fourth equation $\vec{\nabla} \times \vec{H} = \vec{J}$ and integrating it over an area corresponding to the width W and thickness δ from Figure 5.3:

$$\int \int \vec{\nabla} \times \vec{H} \cdot d\vec{A} = \int \int \vec{J} \cdot d\vec{A} \quad (5.4)$$

Applying Stoke's theorem to the left side of 5.4 and substituting $\sigma \vec{E}$ for \vec{J} (Ohm's law) in the right side of 5.4, and then equating both sides yields:

$$\int \vec{H} \cdot d\vec{l} = \sigma \int \int \vec{E} \cdot d\vec{A} \quad (5.5)$$

Integrating the magnetic field around the loop (Figure 5.4) $d\vec{l}$, and again, assuming the thickness δ is negligible, then the left side of 5.5 just becomes $H_L W - H_R W$. Then, assuming E is continuous across the boundary the right side of 5.5 becomes $\sigma E \delta W$, thus:

$$\begin{aligned} H_L W - H_R W &= \sigma E \delta W \\ \Rightarrow H_L - H_R &= \sigma \delta E = \frac{E}{R_S} \end{aligned} \quad (5.6)$$

since it was shown above that $R_S = \frac{1}{\sigma \delta}$.

Following analysis presented in chapter 2, if the incident and reflected fields on the input side of a waveguide junction have mode coefficients A_n and B_n respectively,

and the mode coefficients on the output side for the fields are C_n and D_n for the n th mode, and if a symmetrically placed absorbing disc partially fills the waveguide junction, and assuming $z = 0$ at the position of the absorber, then applying the condition in 5.1 yields:

$$\sum_{n=1}^N [A_n + B_n] \vec{e}_n = \sum_{n=1}^{N'} [D_n + C_n] \vec{e}_n \quad (a)$$

$$\sum_{n=1}^N [A_n - B_n] \vec{h}_n = \sum_{n=1}^{N'} [D_n - C_n] \vec{h}_n - [\eta(r)]^{-1} \sum_{n=1}^N [A_n + B_n] \vec{e}_n \times \hat{k} \quad (b)$$
(5.7)

where $\eta(r) = \infty$ outside the boundary of the absorber ($r > R$) and $\eta(r) = \eta$ across the absorber ($r \leq R$), where R is the radius of the absorbing disk.

Taking the same approach as with scatter matrices at waveguide junctions as presented in chapter 2 we can solve these equations using conservation of complex power to yield the following scatter matrices:

$$S_{11} = - \left[\mathbf{I} + [\mathbf{Q}^*]^{-1} \frac{\mathbf{\Gamma}}{2\eta(\mathbf{r})} \right]^{-1} \cdot \left[[\mathbf{Q}^*]^{-1} \frac{\mathbf{\Gamma}}{2\eta(\mathbf{r})} \right]$$

$$S_{12} = \left[\mathbf{I} + [\mathbf{Q}^*]^{-1} \frac{\mathbf{\Gamma}}{2\eta(\mathbf{r})} \right]^{-1}$$
(5.8)

where $Q_{nm} = \int_S (\vec{e}_n^* \times \vec{h}_m) dS$ and the integration is over the full area of the guide S , $\Gamma_{mn} = \int_S' (\vec{e}_m^* \times \vec{e}_n) dS'$, and $\Gamma_{nm} = \int_S' (\vec{e}_n^* \times \vec{e}_m) dS'$, where S' in the integrals is now the area of the absorber.

Since $[\mathbf{Q}]$ is a diagonal orthogonal waveguide mode set with elements $Q_{mm} = \int_S (\vec{e}_m \times \vec{h}_m^*) dS = \frac{1}{Z_m}$, where Z_m is the impedance of mode m , then 5.8 can be written as:

$$S_{11} = - \left[\mathbf{I} + \frac{\mathbf{Z} \cdot \mathbf{\Gamma}}{2\eta(\mathbf{r})} \right]^{-1} \cdot \left[\frac{\mathbf{Z} \cdot \mathbf{\Gamma}}{2\eta(\mathbf{r})} \right]$$

$$S_{12} = \left[\mathbf{I} + \frac{\mathbf{Z} \cdot \mathbf{\Gamma}}{2\eta(\mathbf{r})} \right]^{-1}$$
(5.9)

where \mathbf{Z} is a diagonal matrix of mode impedances. The Γ_{mn} are real valued as $|\int_{S_{absorber}} \vec{e}_m^* \cdot \vec{e}_n dS| = |\int_{S_{absorber}} e_{m,r} e_{n,r} + e_{m,\phi} e_{n,\phi} dS| = |\int_{S_{absorber}} \vec{e}_m \cdot \vec{e}_n dS|$. It should also be noticed that $S_{11} = S_{22}$ and $S_{12} = S_{21}$ by symmetry, which was not the case for a junction between two waveguide sections, although the S_{11} and S_{12} were very similar to S_{22} and S_{21} respectively, in that case.

We now consider the case of a closed cavity such as the hemispherical example shown in Figure 5.2. Assuming no other losses, the amount of power absorbed by

the resistive sheet can be inferred by analysing the return power through the S_{11} parameter. For no absorber material present the return power will equal the input power so this clearly represents no power absorbed. If the absorbing disk is then included in the closed cavity structure the power absorbed can be calculated by:

$$P_{Abs} = (1 - PowerReturned) = 1 - \left(\sum_{i=1}^N \sum_{j=1}^M S_{11}[i, j]^2 \delta_{ij} \right) \quad (5.10)$$

where N is the maximum radial mode degree that is considered, M is the maximum azimuthal mode order that is excited, and it is assumed unity power is evenly distributed between all propagating modes i, j .

Care must be taken though when dealing with modes that are close to cut-off. If the frequency is below the cut-off frequency of a particular mode then it will decay rapidly through evanescent propagation, thus in that scenario there will be no power reflected back and it will appear that all the power was absorbed. If the return power for a propagating mode is close to zero, say 0.01, then the amount of power absorbed would be $(1 - 0.01) = 0.99$ of the total power contained in that mode. When analysing horns similar concerns with evanescent modes exist at the horn aperture.

5.2.2 3D FEM Approach

The general theory involved in FEM simulation was described in detail in chapter 2 of this thesis, and the specific approaches required for modelling waveguide and horn structures with the COMSOL FEM package was explained in chapters 4 and 3. Thus the only discussion on theory required in this section is how the Ta absorber was treated in the 3D COMSOL models that will be described in this chapter.

The method of instructing COMSOL 3.3 to treat the absorber as a resistive sheet was by using the predefined 'Transition Boundary Condition'. This allows the user to input a value for 'Surface Impedance' and an optional externally applied electric field \vec{E}_s (see equation 5.11). The magnetic field H is analysed on both sides of the transition boundary, and the amount of power absorbed by the sheet can be calculated from the jump in the magnetic field $H_L - H_R$ due to the surface currents this induces. The electric field is continuous across the boundary. The induced current density across the resistive sheet can also be calculated in the post-processing

environment and the 'Surface Resistive Heating' parameter can then be calculated from current density and integrated over the full disk to calculate the amount of power absorbed directly. If we now consider such a resistive sheet situated in the $x-y$ plane and positioned at $z = 0$, and if the field is propagating in the z direction, then the 'Transition Boundary Condition' is defined by COMSOL as:

$$\eta \hat{k} \times (\vec{H}_L - \vec{H}_R) - \hat{k} \times (\vec{E} \times \hat{k}) = \hat{k} \times (\vec{E}_s \times \hat{k}) \quad (5.11)$$

where η is the surface impedance, \vec{H}_L and \vec{H}_R represent the magnetic field on the output and input side of the boundary, respectively (for a wave travelling from right to left), \hat{k} just denotes a unit vector normal to the surface of the resistive sheet, and \vec{E}_s is the optional externally applied electric field which was set equal to zero for these simulations as no external field was applied.

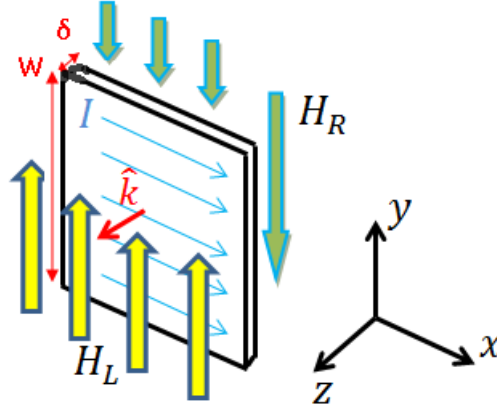


Figure 5.4: Schematic showing the absorber situated in the $x-y$ plane positioned at $z = 0$ with the magnetic field on both sides of the boundary shown. The direction of the induced surface currents is indicated by the blue arrows.

Since $\vec{E}_s = 0$ then,

$$\eta \hat{k} \times (\vec{H}_L - \vec{H}_R) = \hat{k} \times (\vec{E} \times \hat{k}) \quad (5.12)$$

Or,

$$\begin{aligned} \hat{k} \times (\vec{H}_L - \vec{H}_R) &= \frac{\hat{k} \times (\vec{E} \times \hat{k})}{\eta} \\ \Rightarrow H_{||L} &= H_{||R} - \frac{(\vec{E}_{||} \times \hat{k})}{\eta} \end{aligned} \quad (5.13)$$

where the subscript $||$ denotes the component of the field parallel to the surface of the absorber.

If we now label $\frac{\vec{E}}{\eta}$ as \vec{K} , the boundary conditions for the resistive sheet can be written as:

$$\begin{aligned}\vec{H}_R &= \vec{H}_L - \vec{K} \times \vec{k} \\ \text{and } \vec{E}_R &= \vec{E}_L\end{aligned}\tag{5.14}$$

where \vec{K} is the surface current density which is similar to bulk current density $\vec{J} = \sigma \vec{E} = \frac{\vec{E}}{\rho}$. The only difference is that the bulk resistivity ρ is replaced with sheet resistance η .

Clearly the boundary conditions in 5.14 for a resistive sheet as defined in the COMSOL 3D models are identical to those defined in the mode matching approach 5.1. The fraction of power that is absorbed by the resistive sheet in the COMSOL models can be determined in a similar fashion to the method applied with SCATTER where the S_{11} return power was analysed. The post processing environment can be used to analyse the S_{11} parameter, and assuming no other losses the power absorbed by the resistive sheet then is:

$$P_{absorb} = 1 - S_{11}^2\tag{5.15}$$

where in this case S_{11} will be a single value in contrast to the S_{11} matrix in the SCATTER mode matching analysis.

This S_{11} analysis is also the approach that was used by Glenn *et al.* through the use of the Hewlett-Packard High-Frequency Structure Simulator (HFSS) to calculate the fraction of power absorbed by the SPIRE absorbers on the Herschel Space Observatory [Glenn *et al.*, 2003]. Similarly it is the approach taken by Stephen Doherty with the use of the CST Microwave Studio package for similar absorber analysis [Doherty, 2012].

An issue that arises with this indirect approach occurs when there are losses in the system besides the power absorbed by the resistive sheet. This is appropriate in an array system such as SAFARI in which several detectors are fabricated on a single chip and there is an open gap between the detector backshort structure and the horn antenna array block which feeds the detectors. This open gap or 'vacuum gap' as it has come to be called is clearly a source of loss from the cavity structure, and therefore simply analysing the S_{11} parameter will not be sufficient for determining precisely how much power is absorbed by the resistive sheet.

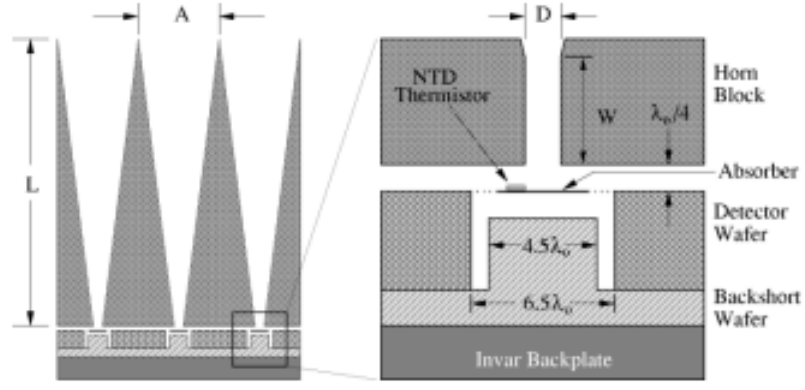


Figure 5.5: *left*: Schematic of three SPIRE pixels for the Herschel Space Observatory. *right*: A single cavity backed detector expanded for clarity. As can be seen a gap must be left between the horn array block and the delicate detector wafer [Glenn *et al.*, 2003].

The solution that both Doherty and Glenn *et al.* applied to this problem was to run the simulation twice; first without the absorber present, and then again with the absorber. The difference in the value of S_{11} for the two separate solutions will then yield an approximate value for the fraction of power absorbed by the Ta. There are of course two assumptions that must be made with this model; first, the presence of the absorber does not affect the amount of power lost through the vacuum gap, and second, any higher-order modes generated as the wave propagates into the cavity are evanescent.

As an alternative approach a method for *directly* calculating the amount of power absorbed by the Ta sheet was formulated by the author. Any induced surface currents on the two dimensional resistive sheet will cause heating (surface resistive heating) across the sheet. Integrating this resistive heating parameter across the area of the absorber will yield the amount of power absorbed by the Ta as follows:

$$P_{absorb} = \int \int Q_{srh} \cdot dS = \int \int \frac{1}{2} Re \left(\vec{J}_S \cdot \vec{E} \right) \cdot dS \quad (5.16)$$

This direct technique allows a more precise calculation of the power absorbed by the resistive sheet. A similar approach is applied for determining the precise amount of power lost through the vacuum gap and this will be discussed in more detail in section 5.4.1 of this chapter.

5.2.3 2D FEM Approach

Such simulations, as described in the previous subsection, can be very time consuming using a 3D solver for an electrically large system such as SAFARI. We therefore also consider a 2D approach that is now described. The approach taken to modelling an absorber in a waveguide with the 2D COMSOL modelling environments is very similar to that outlined above for the 3D case. In the standard 2D option, the 2D plane where the model is built is representative of a 2D planar cut of a model that has translational symmetry in a direction perpendicular to the model plane where the symmetry applies to the geometry and the physics. A depth of one metre is assumed in the transverse direction which can be important if quantities such as fluxes are to be calculated correctly, since the area over which the power will be distributed will be 1 metre times the height that is defined in the model plane. For example the one dimensional line shown in red in Figure 5.6 represents a two dimensional sheet from the three dimensional model, and it has a length of $50\mu\text{m}$ in the x -direction. If 1 Watt of power is defined to flow through the 1D line then the real value for the flux will be $\frac{1W}{(50.10^{-6}\text{m} \times 1\text{m})} = 2 \times 10^4 \text{Wm}^{-2}$.

Once such corrections are applied to the results of any 2D simulations (at least for electrically large systems) we expect very similar results will be true for a 3D environment. This is not strictly speaking true for small systems since Maxwell's equations do mix up the x and y directions. A clear example of this is a narrow waveguide operating at a frequency close to cut-off. The equations governing the waveguide fields in x , y and z are not separate, and changing the size of the guide in one dimension will affect how the field behaves in all three dimensions.

Things are a little bit different in the COMSOL 2D axial symmetry environment. In this option the model is again built in a 2D plane but the geometry is truncated at the axis of rotational symmetry. Rather than assuming a depth of 1 metre in the transverse direction as in the standard 2D option, the post processing mode allows the user to calculate the equivalent values for rotation about the axis of rotational symmetry. Integrals of variables can also be calculated over 2π radians so that the equivalent 3D quantities can be calculated. It is assumed that both the geometry and the physics are symmetric with respect to rotation about the axis of symmetry. The interpretation of the 2D axial symmetry model is illustrated in Figure 5.7.

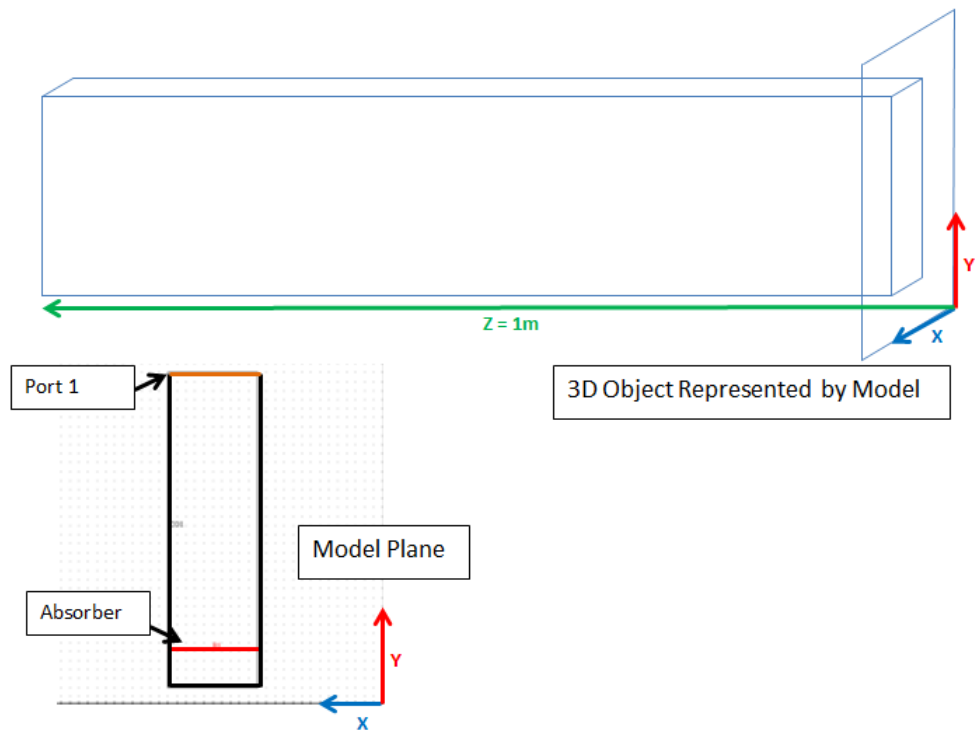


Figure 5.6: Diagram showing what the COMSOL 2D planar symmetry environment represents. The 2D planar model will always represent a 3D model with translational symmetry in the geometry and physics and with a length of 1 metre in the direction perpendicular to the model plane.

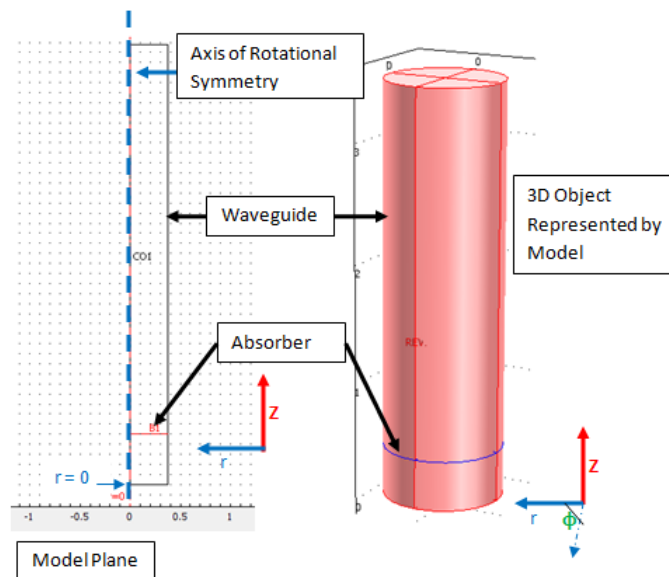


Figure 5.7: Diagram showing what the COMSOL 2D axial symmetry environment represents. The 2D axial symmetry model will always represent a 3D model with rotational symmetry in the geometry and physics rotated through 2π radians.

5.2.4 Comparison of Results

In order to verify the mode matching approach and to investigate the accuracy of the 2D calculation, some simple simulations were run with these two techniques, as well

as with the standard 3D COMSOL mode. The 3D FEM approach is well established and reliable so it served as a good benchmark for validating the other two methods (SCATTER and 2D approach). Mode matching is inherently a different approach to solving EM problems than FEM so agreement between results would be good validation for both FEM and mode matching techniques.

Before considering an absorber in a cavity we began with an analysis of an absorber in a waveguide terminated with a short circuit which could be considered as the simplest kind of "absorber cavity" to be analysed. For example this allowed the multi-mode behaviour to be probed by increasing the waveguide size, and the effect of the "backshort" (i.e. the distance between the absorber and shorted end of the guide) to be examined. Furthermore such a simple, well controlled example provided a trusted set of results that allowed the inclusion of an absorber in the SCATTER code to be verified.

A model was created of a simple circular waveguide structure that was sealed at one end and with an absorber located at $\lambda/4$ from the shorted end of the waveguide. The gap between the absorber and the closed end of the waveguide acted as a simple cavity structure. The waveguide to be modelled was given dimensions of length $L = 0.3\text{mm}$, and radius $r = 50\mu\text{m}$ as shown in Figure 5.8. The first modelling approach applied was the 3D COMSOL RF module, with the waveguide being modelled as a cylinder with perfect electric conducting boundaries, and the absorber material was modelled as an infinitely thin resistive sheet. A similar model was then built in the 2D COMSOL RF module, where the 2D waveguide was given a width equal to the diameter of the 3D cylindrical waveguide ($W = 100\mu\text{m}$). An appropriate geometry file was then written for an input for the mode matching model of the same problem. The maximum absorption was expected to occur at $\lambda_{\text{guide}}/4$ which can easily be calculated by the wave equation [Clarricoats *et al.*, 1984]:

$$\frac{1}{\lambda_g^2} = \frac{1}{\lambda_0^2} - \frac{1}{\lambda_c^2} \quad (5.17)$$

where λ_g is the waveguide wavelength, λ_0 is the free-space wavelength, and λ_c is the cut-off wavelength specific to the particular guide.

Figure 5.9 shows the guide wavelength (relative to the free-space wavelength) plotted as a function of increasing frequency for the fundamental TE_{11} mode in a cylindrical waveguide with the dimensions defined above.

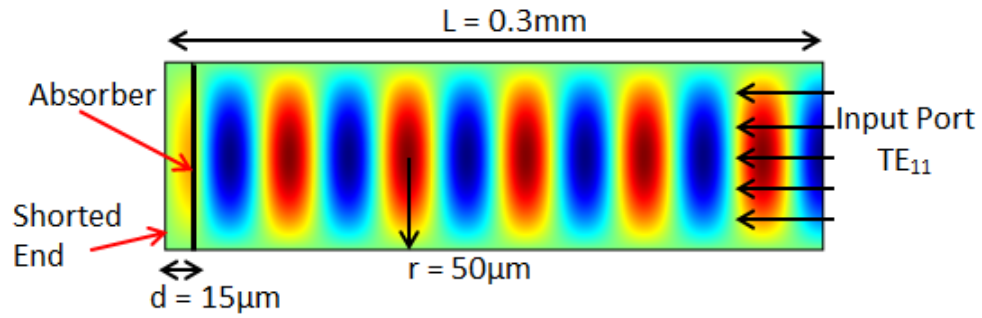


Figure 5.8: Screen shot of a cut through the 3D COMSOL model of a simple shorted waveguide cavity and absorber operating at 5THz.

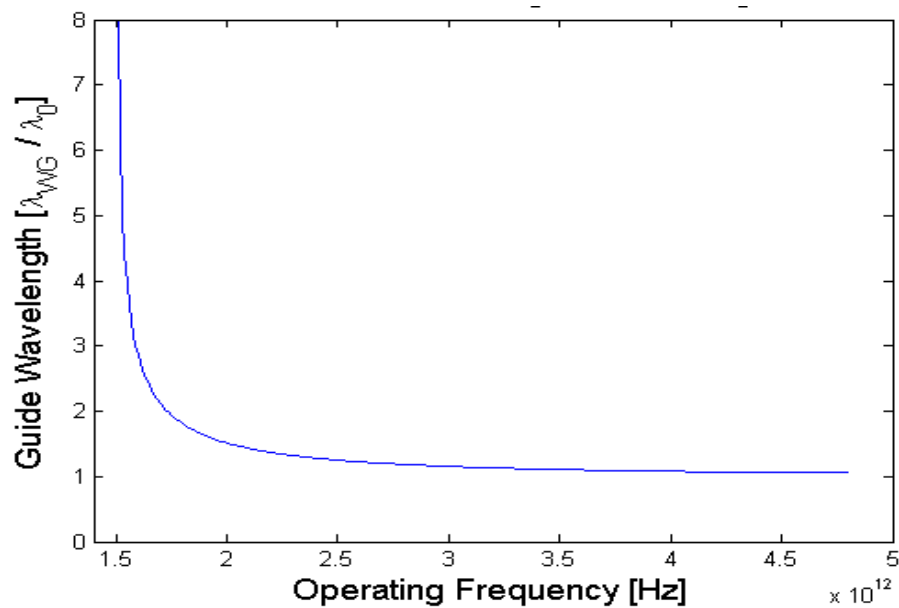


Figure 5.9: Plot of guide wavelength as a function of increasing frequency. As the frequency approaches a few times the cut-off value, the wavelength approaches the free-space value.

The first comparison analysis that was carried out using the waveguide cavity example just described involved varying the surface impedance over a range of 0 to $750 \frac{\Omega}{\square}$ while keeping both the frequency and the absorber position constant. The frequency was just set to a sufficiently high value that the guide wavelength was almost exactly the free-space wavelength, namely 5THz (essentially an oversized guide meaning $\lambda_0 \gg \lambda_c$). This frequency value clearly gives rise to a free-space wavelength of $60\mu\text{m}$ and a guide wavelength approximately the same, therefore the absorber was positioned at $\frac{\lambda_{WG}}{4} = 15\mu\text{m}$ from the shorted end of the guide (Figure 5.8). The absorber was given the same radius as the waveguide thus completely filling the guide. The results are shown in Figure 5.10 and as can be seen there is excellent agreement between all three simulation methods.

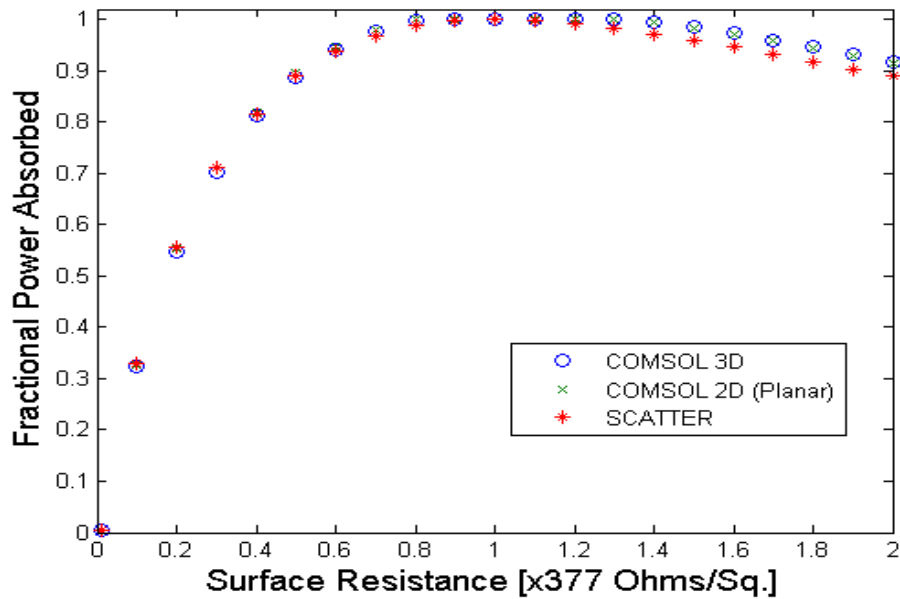


Figure 5.10: Efficiency of a resistive sheet absorber for varying surface resistance. The absorber was placed $15\mu\text{m}$ ($\frac{\lambda_{WG}}{4}$) from the closed end of a cylindrical waveguide $100\mu\text{m}$ in diameter. The values of surface resistance are given in multiples of $377\frac{\Omega}{\square}$. The free-space wavelength (λ_0) of the radiation was $60\mu\text{m}$.

The next step taken with each of the three computational techniques was to simulate the same waveguide and absorber structure across a large frequency range. The range studied was from 1.6THz (which is below the cut-off frequency of the guide for the fundamental mode) to 10THz. What was expected was that maximum absorption should occur when the wavelength was such that the distance between the absorber and the closed end of the guide corresponded to $\frac{\lambda}{4}$, $\frac{3\lambda}{4}$, $\frac{5\lambda}{4}$, etc, and that a minimum amount of power be absorbed when the same distance was equivalent to an integer number of half wavelengths (destructive interference). Any wavelengths in between these should allow for some power to be absorbed following a Fabry-Perot like curve. The results are shown in Figure 5.11.

It is clear that there is again good agreement for the various methods except for the COMSOL 2D results based on axial symmetry, which are labelled as 'COMSOL 2D rot' in the graph. This illustrates the issue with trying to approximate a three dimensional model of this type with the axial symmetry mode in COMSOL. The reason for the disagreement lies in the manner in which the EM modes are excited across the input port boundary in the axial symmetry modelling environment. The fundamental TE mode should have its peak power on axis and decay to zero at the boundary of the waveguide as shown in Figure 5.12. The correct boundary condition to be used for representing symmetry in the electric field is a perfect

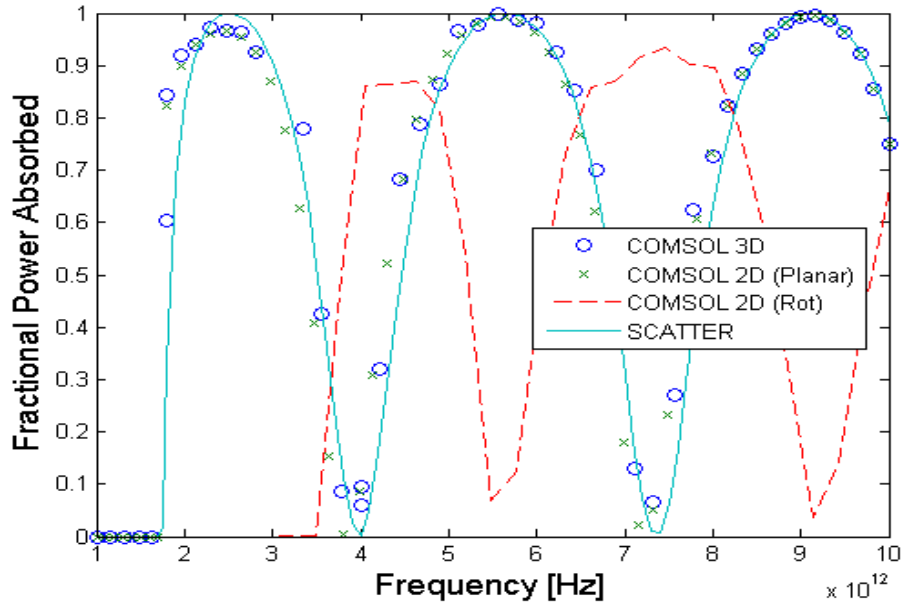


Figure 5.11: Efficiency of a resistive sheet absorber fully filling the guide for increasing frequency. The absorber was again placed $15\mu\text{m}$ ($\frac{\lambda_{WG}}{4}$) from the closed end of a cylindrical waveguide $100\mu\text{m}$ in diameter.

magnetic conductor (PMC) boundary which allows the electric field amplitude to have a maximum at the boundary (whereas a conducting boundary forces the electric field to zero at the boundary). However the COMSOL package only allows for one definition per boundary and the axial symmetry boundary condition is required for what should also be the PMC boundary. Therefore the field is forced to zero at the axis of rotational symmetry which of course represents the central axis of a 3D circular waveguide, thus the field structure is actually representative of some higher order mode like the TE_{21} or in fact a coaxial mode. The much higher cut-off frequency of approximately 3.5THz is clearly evident in the graphed data showing that at the lower frequencies the full mode structure cannot enter the waveguide, except of course in an evanescent form which will decay rapidly within the guide. For this reason the 2D axial symmetry option in the COMSOL package was not used again for simulating these models as clearly it will lead to erroneous results.

Of course for the case when the resistive sheet completely fills the guide, the power scattering integral Γ in the mode matching approach has a simple form. So having found good agreement for this case, the next step taken was comparison between the simulation techniques for the case of a resistive sheet only partially filling the guide. Two examples were examined where the first case was for a sheet radius (r) being 0.8 times that of the guide radius (R) and therefore almost completely filling the guide, and the second example being the case of a sheet diameter only

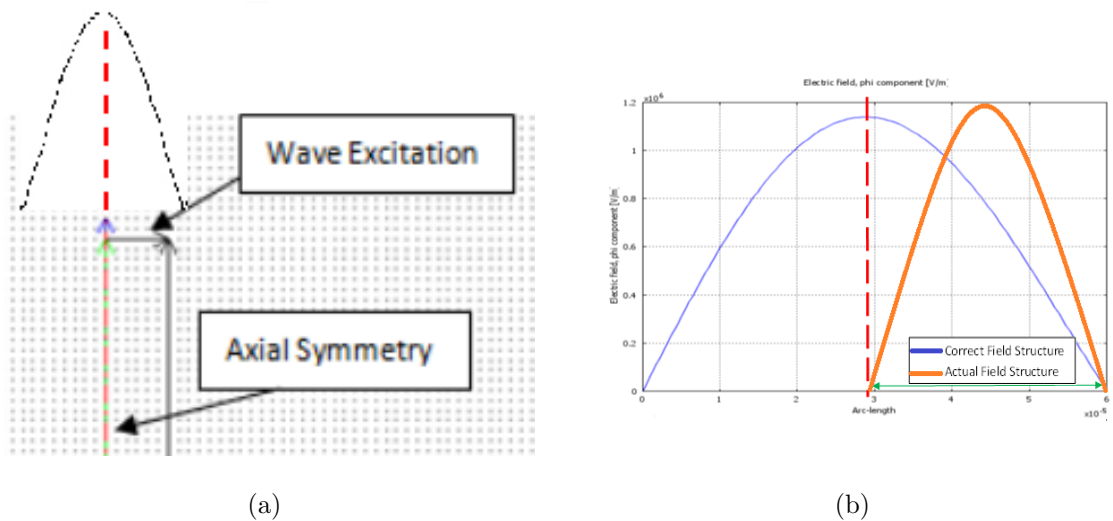


Figure 5.12: Illustration describing the issue with simulating modal problems with the rotational symmetry COMSOL mode. (a): Screen shot showing the axial symmetry boundary condition. (b): The structure of the electric field across the input boundary of the model.

0.1 times that of the guide diameter and therefore allowing a large amount of space for power to flow around the resistive sheet. This test probes how well the Γ term takes this partially filled case into account.

The results for the case of $\frac{r}{R} = 0.8$ are shown in Figure 5.13 and as would be expected there is not much degradation in the amount of power absorbed for any of the simulation methods when compared to the case of the absorber completely filling the guide. However the initial results for the case of $\frac{r}{R} = 0.1$ show a difference of an order of magnitude between the 2D planar symmetry mode and the other two methods. The 3D COMSOL and mode matching results are still in good agreement with each other though, and for this reason it was assumed the error was in the 2D COMSOL planar symmetry method. The results showing the disagreement are shown in Figure 5.14.

With some consideration of what the 2D model represents in the extruded 3D model, the cause of the huge difference in results was obvious. If the 2D model was to be extruded in the third dimension by a length of 1 metre as is assumed by the software, then the ratio of the area of the absorber to the area of the full waveguide cross-section ($\frac{a_1}{A_1}$) would be very different than the case of a circular absorber in a circular waveguide ($\frac{a_2}{A_2}$). This scaling parameter is denoted by Λ and

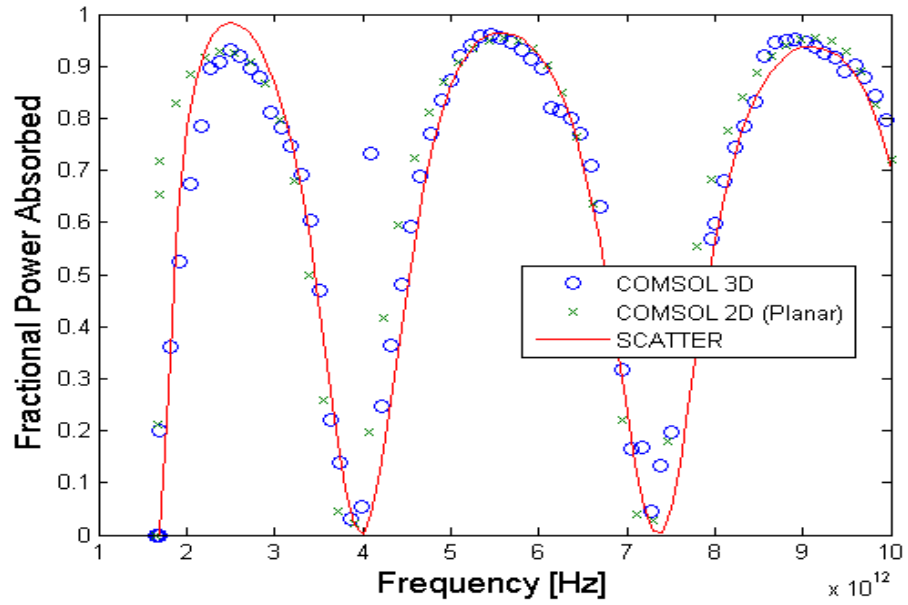


Figure 5.13: Efficiency of a resistive sheet absorber almost completely filling the waveguide for increasing frequency. The absorber was again placed $15\mu\text{m}$ ($\frac{\lambda_{WG}}{4}$) from the closed end of a cylindrical waveguide $100\mu\text{m}$ in diameter. This time the absorber diameter was only 0.8 times that of the waveguide diameter, or $D_{abs} = 80\mu\text{m}$

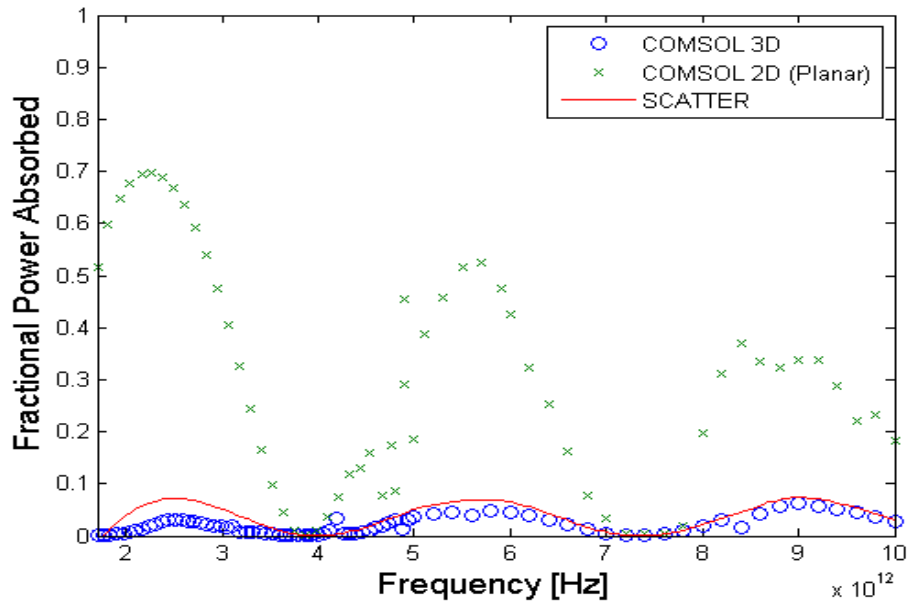


Figure 5.14: Efficiency of a resistive sheet absorber for increasing frequency. The absorber was again placed $15\mu\text{m}$ ($\frac{\lambda_{WG}}{4}$) from the closed end of a cylindrical waveguide $100\mu\text{m}$ in diameter.

it was calculated as follows:

$$\Lambda = \frac{\left(\frac{a_1}{A_1}\right)}{\left(\frac{a_2}{A_2}\right)} = \frac{\left(\frac{\pi r_1^2}{\pi R_1^2}\right)}{\left(\frac{(1m)(r_2)}{(1m)(R_2)}\right)} = \frac{r_1^2 \cdot R_2}{r_2 \cdot R_1^2} = \frac{(1 \times 10^{-4})^2 (10 \times 10^{-4})}{(1 \times 10^{-4}) (10 \times 10^{-4})^2} = 0.1 \quad (5.18)$$

Applying this scaling factor of 0.1 to the 2D COMSOL data shown in Figure 5.14 a new data set was produced and it is shown in Figure 5.15 with the SCATTER results and 3D COMSOL results shown again for comparison. It is clear from the graph

that including the scaling factor brings the 2D results into much better agreement with the 3D FEM and mode matching results, however the symmetry of the 2D and 3D cases is so different it is hard to draw conclusions from the 2D models.

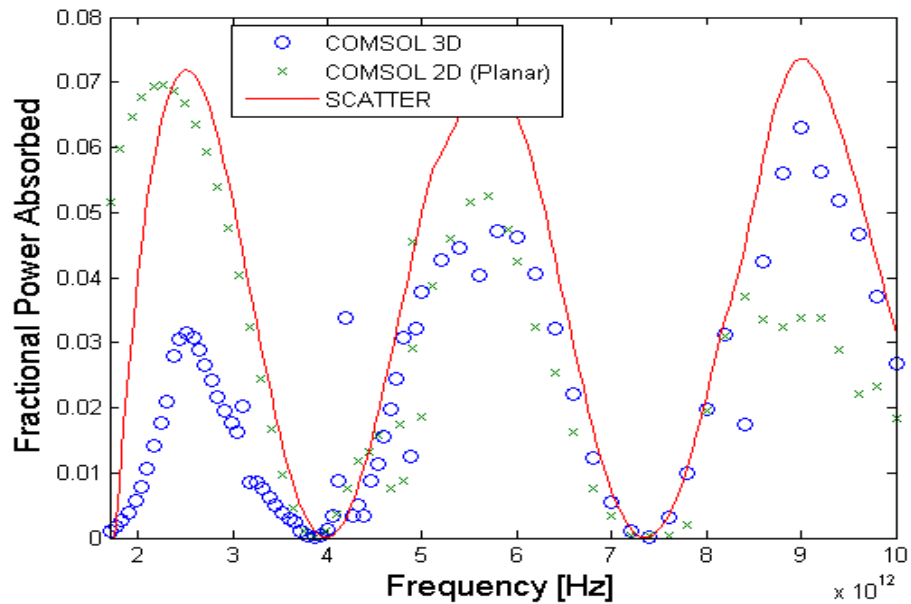


Figure 5.15: Efficiency of a resistive sheet absorber for increasing frequency with the COMSOL 2D results corrected. This graph is just zoomed in on the relatively low power.

It has been shown in this section that the extended mode matching code SCATTER that now allows for a resistive current sheet to be included in the simulations is performing as expected. There is reasonable agreement between SCATTER and the 3D COMSOL results for the case of an absorber filling the waveguide section, and for the case of it only partially filling the guide which is more comparable to a real cavity structure such as a SAFARI detector. An important point to be made here is that the extended SCATTER code was found to be up to three orders of magnitude faster than the 3D FEM approach. For example, the model of a simple cavity containing an absorber that was presented above required 10.81 hours calculation time for one hundred spot frequencies with a FEM analysis. By contrast, the mode matching analysis for the same one hundred spot frequencies took only 15.32 seconds.

It was also shown that the 2D planar symmetry models are not really applicable to these cylindrical waveguide and cavity geometries due to the large differences in symmetry, however with some corrections to the results the 2D approach could be used as a quick method for initial simulations in order to gain approximate results.

The corresponding 3D models would then have to be investigated so that a more reliable final result could be obtained. Of course the 2D axial symmetry approach is a more accurate representation of the 3D cylindrical models in terms of geometry, however the correct symmetry is not employed in the physics, and an example of why it can not be trusted to yield reliable results was described above.

The final discussion in this section regards further verification of the SCATTER absorber code that was carried out by Stephen Doherty as part of Technical Note Three (TN3) for the Irish AO contract commissioned by ESA, and that the author was also involved in [RFQ 3-6418/11/NL/CBi]. The approach taken by Doherty involved simulating a range of different scenarios for an absorber inside a waveguide cavity using the adapted SCATTER code, and then comparing the results to those of similar simulations with the commercially available CST Microwave Studio package. The computational method employed by CST Microwave Studio is FIT, and it is similar to the FEM approach that COMSOL is based on, but it is the integral form of Maxwell's equations that are solved within the meshed problem geometry whereas it is the differential equations that are solved with FEM. As with the good agreement shown in this section for the results from the 3D COMSOL and SCATTER simulations, similarly good agreement was demonstrated for the CST Microwave Studio FIT. An example of the CST/SCATTER results is shown in Figure 5.16.

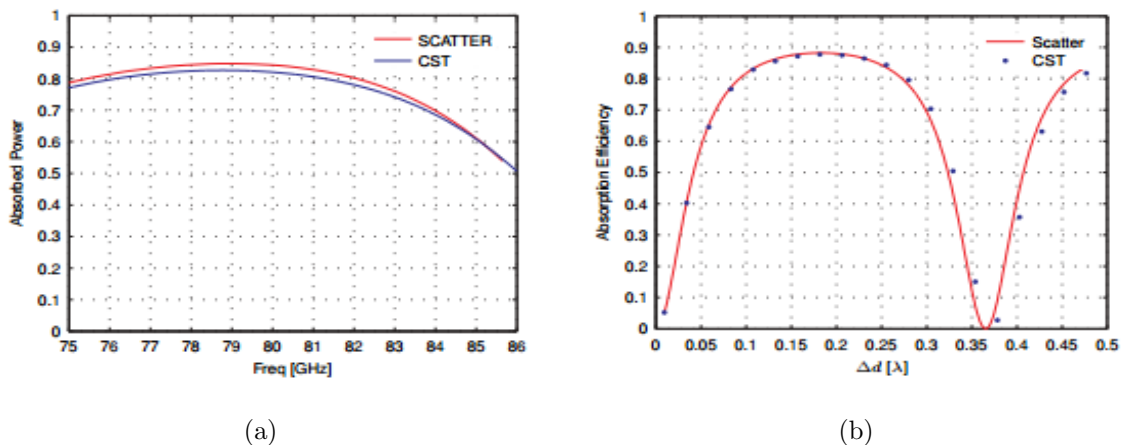


Figure 5.16: Results of CST verification of SCATTER code for modelling an absorber. (a): Absorbed power for varying values of frequency in a single moded circular waveguide with the resistive sheet fully filling the guide and at a fixed position of $\lambda_g/4$. (b): Absorbed power at 80 GHz for varying values of absorber/backshort distance Δd in a single moded circular waveguide with the resistive sheet fully filling the guide [Doherty, 2012].

5.3 Optimisation of Absorber Position and Cavity Geometry

Defining an optimum position for the resistive sheet absorber in a cavity is not a trivial matter as there are a number of factors that one must consider, particularly for a large operational frequency range and an over-moded system such as the case for SAFARI. Since maximum efficiency would be expected when the absorber/backshort distance Δd is equal to a quarter of the guide wavelength as was already demonstrated, then for a signal consisting of a wide band of wavelengths there is no obvious optimum position. Furthermore, in an over-moded cavity structure where even a single frequency is considered, the ideal position of the absorber again is not obvious since the guide wavelength of each mode can differ by significant amounts especially when they are close to cut-off. For these reasons a large number of simulations were carried out in order to determine the absorber/backstop distances that correspond to maximum coupling for both a broad frequency range and for an over-moded system.

5.3.1 Optimising Absorber Position for TE_{11} Mode

With the mode matching code showing good agreement with the FEM results thus far, it was chosen for the purposes of optimisation due to its high computational speed. Both the SCATTER mode matching and COMSOL 2D approaches are highly efficient, with COMSOL 2D being slightly computationally faster (same order of magnitude). Also the mode matching code relies on fewer approximations, and the 2D FEM was shown to disagree with some previous results since strictly speaking it really only applies to systems with Cartesian symmetry.

The aim was to optimise the position of the absorber relative to the backshort for a broad frequency range. The optimum absorber/backshort position is of course expected to vary for different frequencies, so the aim was to determine a position that related to the overall average optimum value for the entire frequency range. The same relatively simple example of a circular waveguide shorted at one end was used for the initial analysis and the frequency range chosen was again 1.8 to 10THz within which the full range of the SAFARI S-Band lies. The length and radius of the

guide were set to $L = 0.3\text{mm}$ and $r = 50\mu\text{m}$ respectively, as shown in Figure 5.17, and the sheet impedance was set to $377\Omega/\square$. The optimisation routine consisted of incrementally moving the absorber away from the backshort in increments of $\Delta d = 1\mu\text{m}$ out to a total of $40\mu\text{m}$. At each absorber position the model was solved for the entire frequency range in steps of 0.1THz .

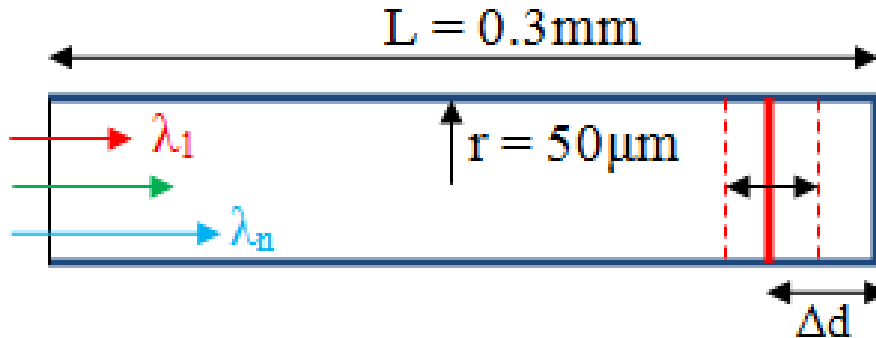


Figure 5.17: Diagram showing the dimensions of a simple waveguide cavity model.

Figure 5.18 shows the contour plot that was generated from the optimisation search procedure. As was expected the optimal position of the absorber clearly depends on frequency. Figure 5.19 then shows the variation in efficiency of the absorber across the band for each position, where the efficiency across the band was calculated by $\frac{1}{N} \sum_{i=1}^N \text{eff}(\nu_i)$, where ν_i is the i^{th} spot frequency and N is the total number of test frequencies. The result was that for a shorted cylindrical waveguide fed by a single-mode waveguide over an operational frequency range of 1.8 to 10THz (30 to $167\mu\text{m}$) the optimum position of the absorber is $11.5\mu\text{m}$. The central wavelength λ_{central} was $98.5\mu\text{m}$, so the distance value of $11.5\mu\text{m}$ corresponds to approximately $\Delta d = \frac{\lambda_{\text{central}}}{8.57}$. What is also evident in Figure 5.19 is that once the absorber is placed at least $6\mu\text{m}$ from the backshort then the average efficiency of the absorber never falls below about 64%. This is highlighted by the red cross hairs placed on the graph and the distance corresponds to $\frac{\lambda_{\text{min}}}{5}$ where λ_{min} is the minimum wavelength of the band, i.e. $30\mu\text{m}$.

5.3.2 Optimisation of Absorber Position for an Over-Moded System

In the previous example it was assumed that only the TE_{11} cylindrical mode propagated, even though a large part of the frequency range was such that higher order

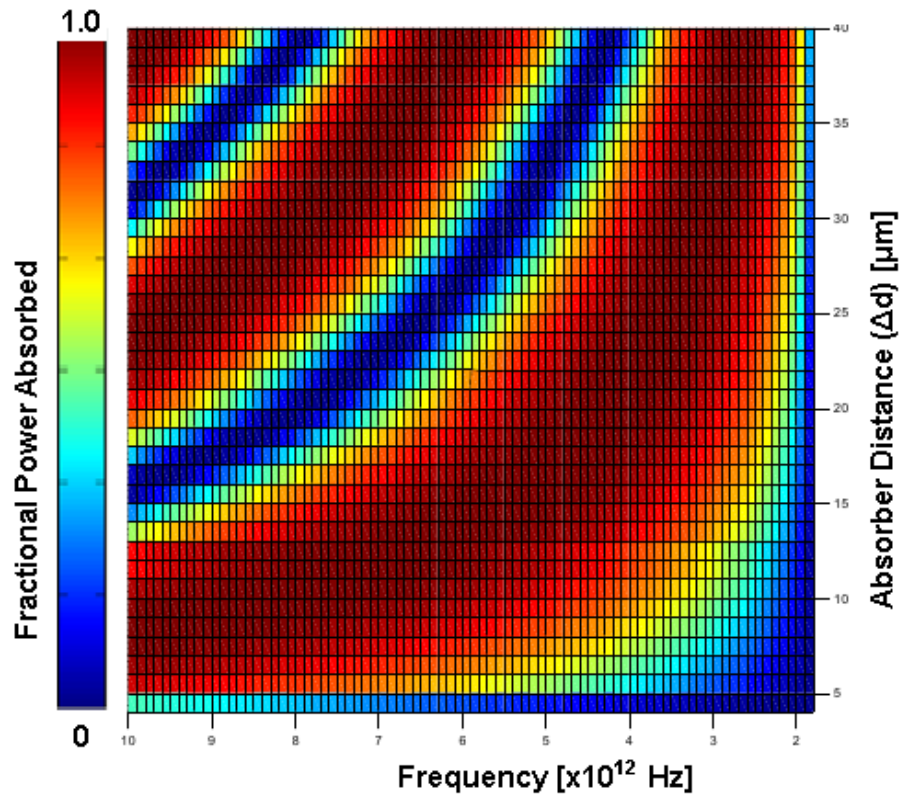


Figure 5.18: Contour plot showing the efficiency of a resistive sheet absorber for varying frequency and backshort distance. The fractional power absorbed is represented by variation in colour with deep blue being minimum and deep red being maximum.

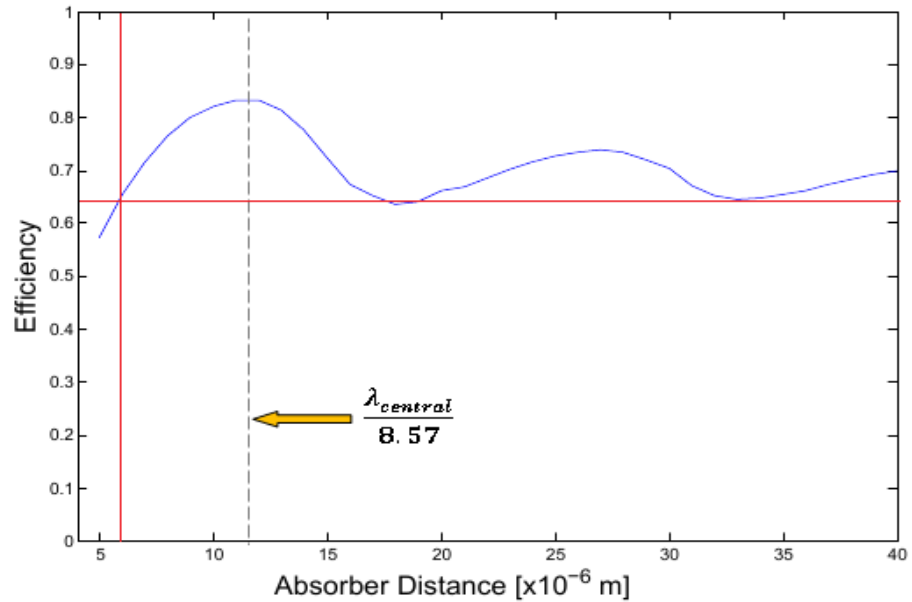


Figure 5.19: Line plot showing the average efficiency across the band ($\Delta f = 1.8 - 10$ THz) of a resistive sheet absorber for varying backshort distance.

modes would propagate if excited. In this subsection the optimum position of an absorber in an over-moded waveguide is investigated by examining the efficiency of the absorber with respect to the various propagating modes. The same waveguide structure as was analysed in the previous example was again used for this study,

i.e. $L = 0.3\text{mm}$ and $r = 50\mu\text{m}$. It was assumed that each mode has equal weight however, in a true blackbody cavity some modes may be more dominant than others. Also, only the $TE_{1,m}$ modes were taken into account since the modes with zero phi dependence are most often the dominant ones.

For this example a single frequency was chosen at the high end of the band so that the higher order modes could also propagate. The frequency was kept at 10THz leading to a free-space wavelength of $30\mu\text{m}$, and since the frequency was so far above the cut-off frequency of 1.87THz then the approximation $\lambda_{WG} = \lambda_0$ could be used. Therefore the expected optimum absorber position relative to the backstop for the TE_{11} mode was $\frac{\lambda_0}{4} = 7.5\mu\text{m}$. However for higher order propagating modes, particularly those close to cut-off, the optimum position would be expected to increase. The absorber/backshort distance was varied from 2 to $35\mu\text{m}$ in steps of $\Delta d = 1\mu\text{m}$ with the efficiency being calculated for each propagating mode at each distance.

Figure 5.20 shows the results of the analysis and it is clear that indeed there is a varying optimum absorber position depending on which mode is being analysed. By calculating the average power absorbed across all modes at each particular distance the plot in Figure 5.21 was generated. As more modes are included in the calculation of average absorbed power the peak average efficiency shifts from $\frac{\lambda_0}{4}$ toward $\frac{\lambda_0}{3}$. Clearly the distribution of modes will affect precisely where the maximum absorption should occur and this will need to be analysed for individual systems.

5.3.3 Cavity and Absorber Size

Having investigated the simplest possible cavity structure where a short circuit was set up by sealing one end of a circular waveguide, thus creating a resonant cavity between the resistive sheet absorber and the shorted end of the guide, an expanded cavity is now considered where 'expanded' refers to the cavity having a larger radius than the waveguide feed. The waveguide is now assumed to be single moded however the step into the larger cavity will almost certainly cause power to scatter into the higher order modes supported by the cavity. Again, building up the complexity of the models in a gradual manner, the first expanded cavity considered was cylindrical in shape, and the radius of the cavity was varied incrementally in order to investigate

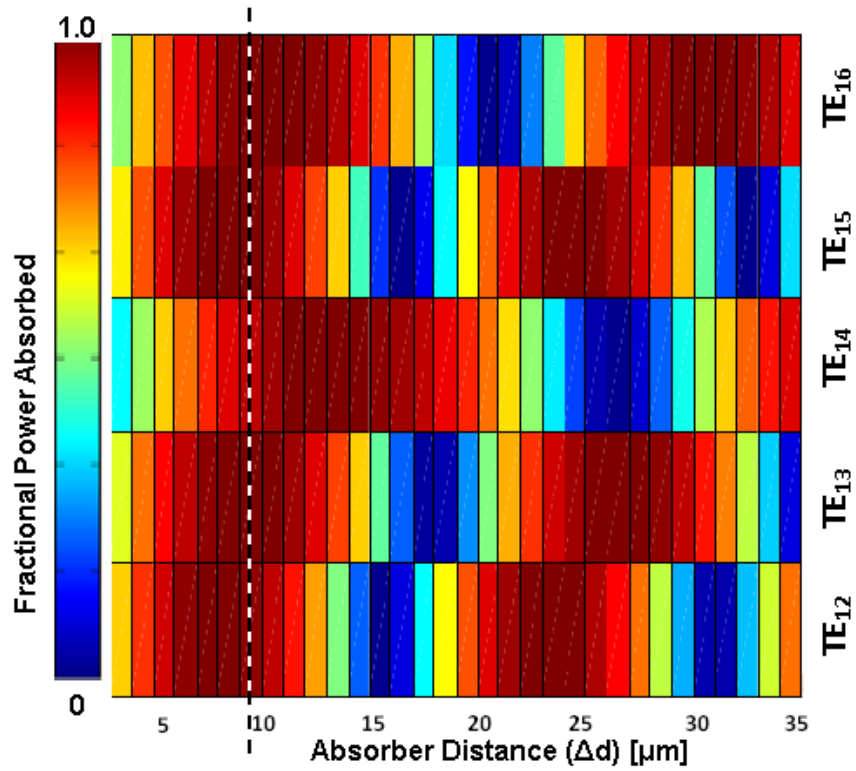


Figure 5.20: Block contour plot showing the efficiency of a resistive sheet absorber for higher order propagating modes and varying backshort distance. The dotted line indicates the optimum absorber position.

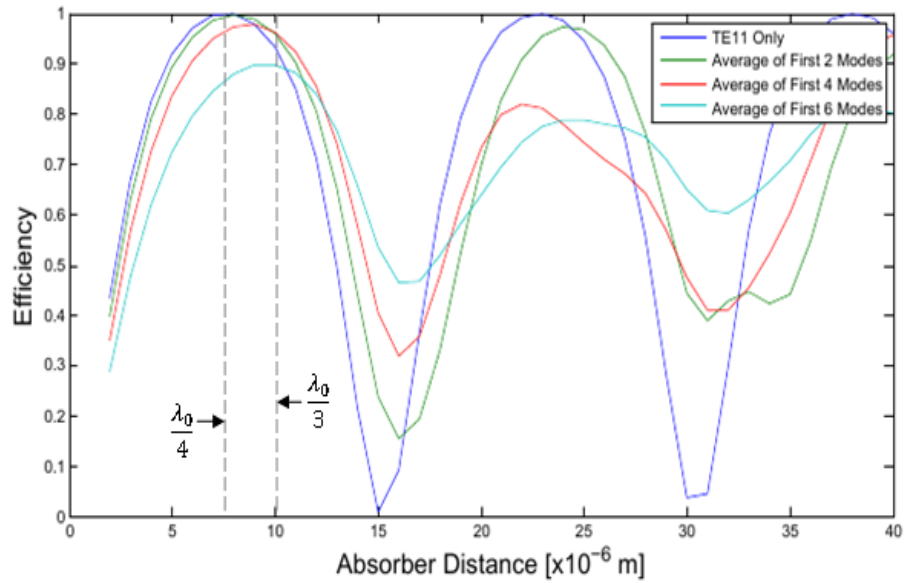


Figure 5.21: Line plot showing the average efficiency of a resistive sheet absorber for varying backshort distance when higher order propagating modes are included. As more modes are considered the optimum distance shifts to slightly larger values.

the ideal size for such a cavity. Starting with a radius equal to that of the waveguide feed ($r = 50\mu\text{m}$) the cavity radius was increased in steps of $5\mu\text{m}$ up to $r = 250\mu\text{m}$ while the absorber radius was kept fixed at $r = 50\mu\text{m}$. The distance between the absorber and backshort was kept fixed at $18.2\mu\text{m}$ and the frequency range was from

4 to 10 THz, approximately the SAFARI S-Band.

Figure 5.22 shows the results of the analysis and it can be seen that the cavity does not affect the absorber efficiency for frequencies that were already coupling well to the absorber in a shorted circular waveguide. However, the cavity does provide improvement in the amount of power absorbed at the frequencies that were experiencing destructive interference due to the standing waves that were set up between the absorber and backshort. At least at some of these frequencies there are particular values for the cavity radius that allow higher coupling of power to the absorber, and what is clear is that a larger cavity is not necessarily better. In fact based on the average power absorbed across the band for each cavity radius the ideal size is $110\mu\text{m}$, or 2.2 times the waveguide feed radius.

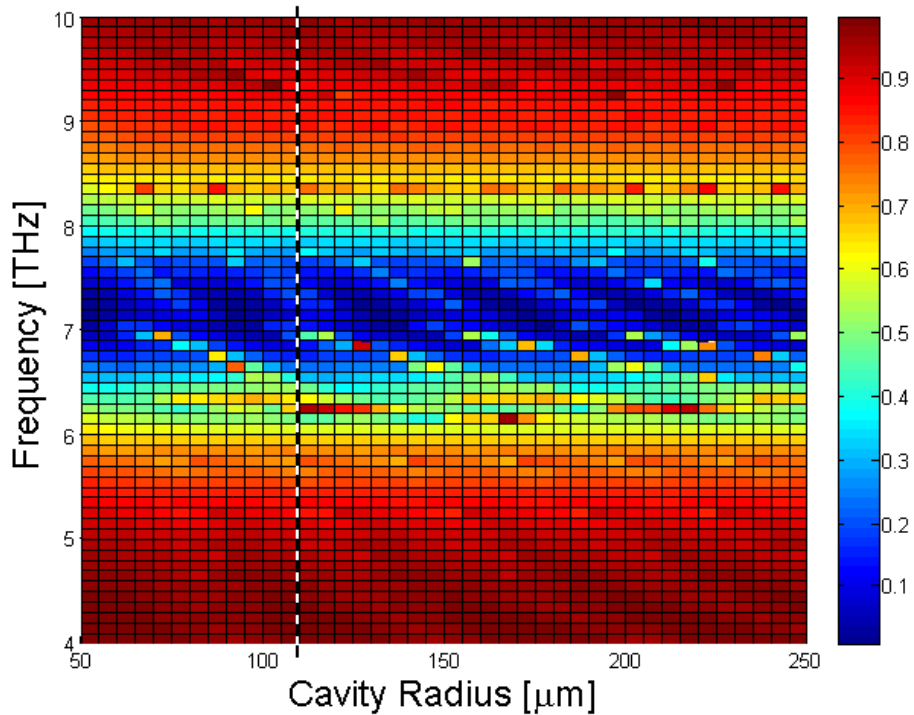


Figure 5.22: Block contour plot showing the efficiency of a resistive sheet absorber for cavities of varying radius. The highest average efficiency is found for a cavity with a radius of $110\mu\text{m}$, or 2.2 times the input waveguide radius ($r_{WG} = 50\mu\text{m}$)

By fixing the radius of the cylindrical cavity to the optimum value of $110\mu\text{m}$, the radius of the absorber was then varied from $5\mu\text{m}$ (0.1 times the waveguide radius) to $110\mu\text{m}$ (completely filling the cavity) in steps of $2.5\mu\text{m}$. Again the distance between the absorber and backshort was kept fixed at $18.2\mu\text{m}$ and the frequency range was from 4 to 10 THz. The results of this analysis are presented in Figure 5.23 and the average absorbed power across the frequency band for each absorber radius is shown in Figure 5.24, where it is clear that while a larger absorber does increase

the amount of power absorbed, there is a point where increasing the radius further has no effect. This value occurs for an absorber radius of approximately $50\mu\text{m}$, or a radius equal to that of the waveguide feed. This is an important result as it is preferred to have a smaller Ta absorber where possible because the level of noise in the absorber is proportional to its volume, and the speed of response (time constant τ) is also related to the absorber volume [Audley *et al.*, 2013]. In fact a discussion is given in section 5.4.3 on techniques for removing portions of the absorber material while maintaining its optical cross section, therefore an understanding of the effects of absorber size in terms of optical coupling is clearly important. It should again be pointed out that these results are specific to the examples chosen for this study, and while the same techniques developed here could be applied to other systems, the results may differ based on the parameters of those systems.

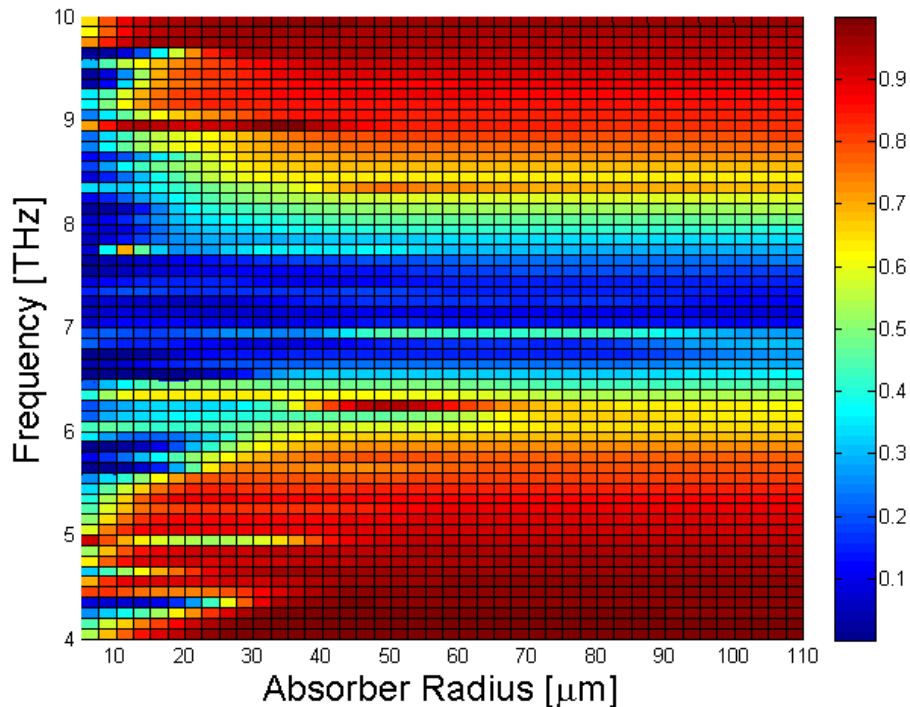


Figure 5.23: Block contour plot showing the efficiency of a resistive sheet absorber in a cavity with a radius of $110\mu\text{m}$ (based on the previous optimisation). The radius of the absorber was varied from $5\mu\text{m}$ to $110\mu\text{m}$ in steps of $2.5\mu\text{m}$.

5.3.4 Cavity Shape

So far in this section only cavities with cylindrical shapes have been considered as they are the simplest geometries due to their similarity to uniform cylindrical waveguides. In fact the standard type of cavity geometry that has been most com-

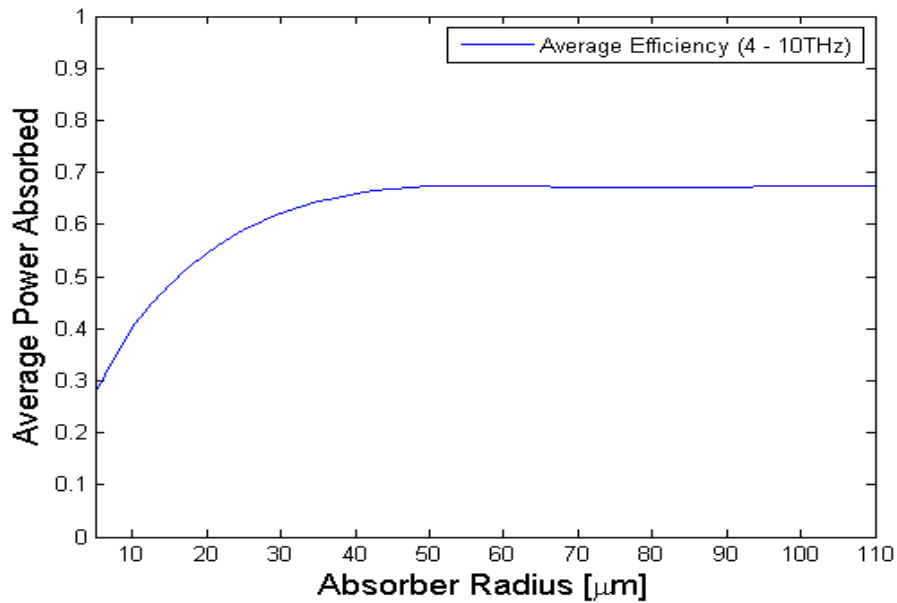


Figure 5.24: Average efficiency across the frequency band for a resistive sheet absorber in a cavity with a radius of $110\mu\text{m}$. The radius of the absorber was varied from $5\mu\text{m}$ to $110\mu\text{m}$ in steps of $2.5\mu\text{m}$.

monly chosen for cavity coupled bolometer type detectors in previous instruments has been the hemispherical cavity since it was assumed to be the best choice for maximising coupling to the bolometer. This assumption is based on ray tracing and the assumption that the cavity is large electrically (many wavelengths in radius). Thus by placing the detector close to the centre of curvature of the hemisphere any power that was transmitted through the absorber was refocussed back onto the absorber. Because of the complex calculations required, clearly the assumption that ray tracing is a valid approach may not be true for such cavities since interference effects need to be taken into account and the cavities are only a modest number of wavelengths in scale size. Until recently modelling the entire pixel with more accurate EM techniques simply was not possible without resorting to super computers. For this reason an investigation was carried out in order to determine if there is a more optimum design for the geometry of the integrating cavity in terms of optical coupling.

A range of different cavity designs were examined and the amount of power absorbed by the resistive sheet was calculated across a frequency range of 1.8THz (just above cut-off for the waveguide) to 10THz . The results for three of these designs are shown in Figure 5.26 and the average absorber efficiency predicted for each design is presented in Table 5.1, together with the maximum and minimum efficiency for each of the three designs. The results of the simple shorted waveguide are shown

again for comparison and the input feed to the cavity was defined as having the same dimensions as that of the cylindrical waveguide used in the comparison study, namely a radius of $50\mu\text{m}$ and a length of 0.30mm . The cylindrical cavity was given a radius twice that of the waveguide radius $R = 2R_{WG}$ and a depth $d = 2R_{WG}$, the hemisphere cavity was also designed with a radius of $2R_{WG}$ which of course results in the same depth of $d = 2R_{WG}$, and the sine profiled cavity was designed with an initial radius of $R_i = 2R_{WG}$ that varied as $R(x) = \sin\left(\frac{\pi}{2}\left(1 - A\frac{x}{R_i}\right)\right)$ where x is the distance from the start of the cavity up to a depth of $d = 2R_{WG}$ (if $A = 1$) meaning that each of the designs had the same depth. Of course the value of A could be allowed to vary in an optimisation analysis for example, however the depth of the cavity was kept the same as the hemisphere and cylinder in this case so that the comparison was balanced. Clearly setting $A = 0.5$ for example will create a cavity with a depth twice that ($d = 4R_{WG}$) as for $A = 1$, with a slower curving profile as shown in Figure 5.25(a). Figure 5.25(b) shows the approximate shapes of the other cavity backshorts that were examined. The absorber was given a radius of $50\mu\text{m}$ and sheet resistance of $377\Omega/\square$, and was positioned at $20\mu\text{m}$ from the start of the cavity for each case.

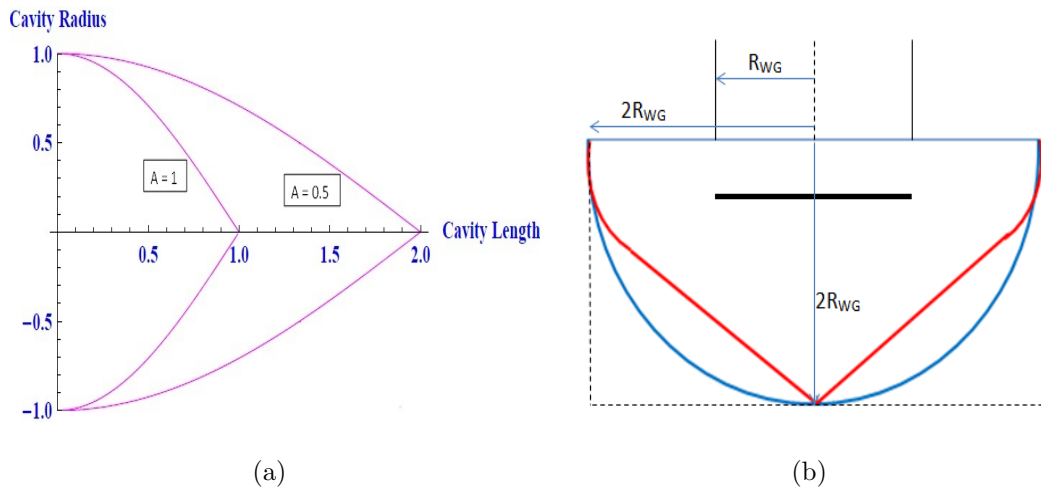


Figure 5.25: Schematic of various cavity backshort geometries. (a): Geometries for sine function profiles with different weighting factors (A), which determines the strength of the curve and the depth of the cavity relative to its radius. (b): Three of the different cavity geometries that were investigated.

What should be clear from both Figure 5.26 and Table 5.1 is that the shape of the cavity does indeed have a significant effect on the coupling of power to the absorber. Both the hemisphere and sine profiled cavity shapes give rise to an average absorber efficiency across the band of 87%, but the sine profiled shape exhibits

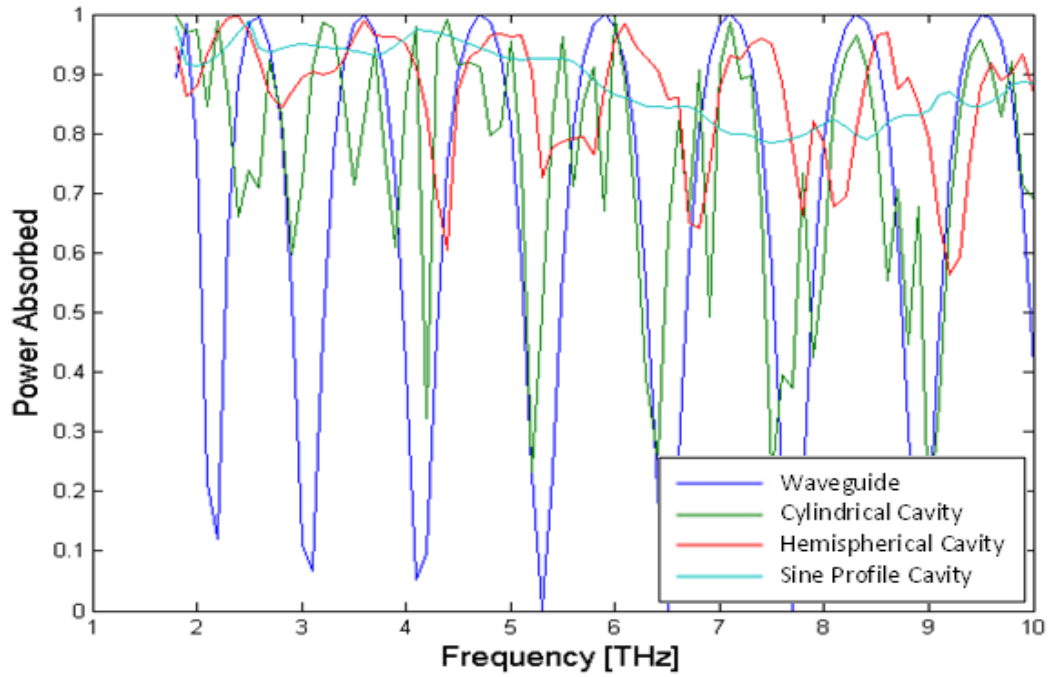


Figure 5.26: Absorber efficiencies for various cavity geometries across the frequency band of 1.8 – 10THz for TE_{11} mode only.

Cavity Design	Maximum Power Absorbed	Minimum Power Absorbed	Average Power Absorbed
Simple Waveguide ($R = 2R_{WG}$)	1.0	0.0	0.69
Cylindrical ($R = 2R_{WG}$)	1.0	0.2	0.76
Hemisphere ($R = 2R_{WG}$)	1.0	0.55	0.87
Sine Profile ($R_i = 2R_{WG}$)	1.0	0.78	0.87

Table 5.1: Absorber efficiency values across the frequency band of 1.8 – 10THz, for TE_{11} mode only, for cavities with varying geometry.

much less variance giving rise to a much smoother frequency dependence compared to the hemisphere example. The conclusion drawn therefore would be that for the cavity examples examined in this case, fed by a single mode waveguide, the ideal cavity geometry for maximising power coupling between the incoming signal and the absorber is the sine profiled cavity. This is surprising considering the almost straight

walls of the cavity in this configuration. There are of course many other geometries that could be examined such as a paraboloid or \sin^2 profile for example, and some of these designs could possibly yield further improved coupling of power to the absorber, however the aim here is to demonstrate the techniques for modelling such systems, and to show that these simulations are important for designing optimised systems.

5.4 SAFARI L-Band Receivers

Having investigated generic systems to gain an understanding of the effects of bandwidth, absorber size, and backshort configuration on the coupling efficiency of a cavity mounted absorber, the next step taken was a model of a realistic system with realistic dimensions and properties. The system chosen was the SAFARI L-Band design that was under investigation by Dr Phil Mauskopf's research team at Cardiff University, Wales where they were carrying out a measurement campaign of the system while also using the software package HFSS (High Frequency Structural Simulator) to model the system [Mauskopf, 2011]. They report very good agreement between the measurements and simulations.

Another member of the NUIM THz Optics research group, Stephen Doherty, carried out a similar analysis using the CST Microwave Studio package [Doherty, 2012] and the results published were in excellent agreement with those of the Cardiff group. Therefore the Cardiff results served as a good comparison for the results of the current study reported in this thesis. At the time of writing the current design for the SAFARI L-Band pixel [Goldie *et al.*, 2012] consisted of a square absorber contained within a hemispherical cavity with a diameter of $500\mu\text{m}$, fed by a single mode cylindrical waveguide with a radius of $60\mu\text{m}$. The absorber was located at $50\mu\text{m}$ from the exit aperture of the input waveguide and had dimensions of $320\mu\text{m} \times 320\mu\text{m}$ (see Figure 5.27). As before the absorber was modelled as an infinitely thin sheet and given a surface resistance of $377\frac{\Omega}{\square}$. The frequency range analysed was from 1.5 to 3.0THz.

The free-space matched sheet resistance of $377\frac{\Omega}{\square}$ used in the L-Band simulations is an idealised value, however the actual sheet resistance in the Cardiff measurement system was thought to be about $90\frac{\Omega}{\square}$. The ideal $377\frac{\Omega}{\square}$ is not unachievable though,

and the SAFARI S-Band research group at SRON, Groningen describe such possible sheet resistances up to about $367\frac{\Omega}{\square}$ [Audley *et al.*, 2013]. If the Ta is below its transition temperature and thus is operating in a superconducting state then the surface resistance will of course be a lot lower. The SRON team report an apparent transition temperature for the film of about 700 mK, which they claim is lower than the expected value of 900 mK [Audley *et al.*, 2013]. The nitride island on which the Ta absorber sits is expected to operate at a higher temperature than this, therefore achieving a $367\frac{\Omega}{\square}$ surface resistance should not be a problem.

Figure 5.27 illustrates the SAFARI L-Band pixel and its various components. As can be seen there is a vacuum gap between the waveguide and cavity which is highlighted in green. This corresponds to a distance of $100\mu\text{m}$ from the exit aperture of the waveguide to the entrance of the cavity backshort. The absorber was placed at the halfway point between the waveguide and cavity. The reason for this vacuum gap arises from the fact that the cavities/backshorts of the pixel array are manufactured on a single substrate (see bottom gold section in Figure 5.1(b) at the beginning of this chapter) with the TES detector array chip then fixed onto it (green section in Figure 5.1(b)). The waveguide/horn array (in the top gold section of the image) that feeds the detector array is a separate block that must be fitted to the detector and backshort array but with a certain amount of space required to be left between the two so as not to damage the delicate electronics and TES detectors. Progress is being made in terms of minimising this gap in order to minimise the amount of power that can potentially leak out through it, but for these simulations a relatively large gap was applied in order to match the Cardiff L-Band set-up, and presumably to consider a worst case scenario. In fact the SRON group have succeeded in reducing the original $230\mu\text{m}$ vacuum gap to $50\mu\text{m}$ in the S-Band test-bed [Audley *et al.*, 2013] so similar reductions should be possible for the SAFARI L-Band also.

5.4.1 Vacuum Gap between Neighbouring Pixel Cavities

The vacuum gap just described brought new challenges in terms of modelling the behaviour of power flow through the pixel with the three simulation techniques described so far, in particular estimating the power lost through the gap. Including the gap with COMSOL was possible with two different approaches. The first approach

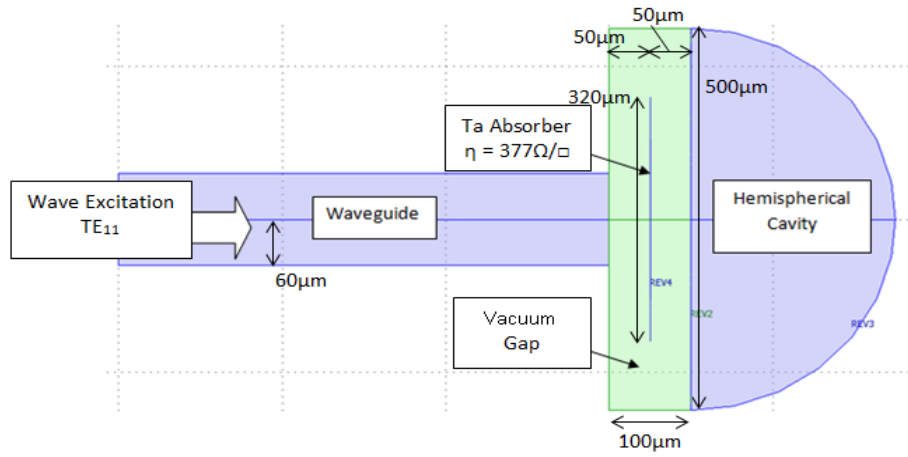


Figure 5.27: Diagram of waveguide fed cavity coupled detector with a vacuum gap of $100\mu\text{m}$. The green coloured section is the vacuum gap.

consisted of employing a boundary condition known as a ‘perfectly matched layer’ where the impedance is perfectly matched at the boundary and therefore simulating propagation into free-space with no reflections.

The second method utilises a ‘scattering boundary condition’ where the scattering coefficients are just set to zero so that no power is reflected and free-space propagation is again simulated. The type of wave expected to be incident on the scattering boundary, say a plane wave or spherical wave, must be defined in the model before calculation of the propagating fields, and an instruction to then reflect zero intensity for any incident plane or spherical waves on the boundary is defined. In both approaches the amount of power lost through the gap is calculated by integrating the power outflow across the surface of the boundary. In the 2D environment the same two techniques are applied but with the integral being of course a line integration across the 1D free-space boundary. The issue again arises as to how to interpret the 2D results. It is a bit more complicated now that there are three surfaces over which power can flow, namely the input waveguide entrance (including back scatter through it (S_{11})), the surface of the absorber (power absorbed due to Joule heating), and the surface that bounds the vacuum gap. Previously the ratio of power flow surface areas was used to correct the differences in the 2D results with some success so a similar approach was applied again. However, this is not expected to yield an accurate result, only an order of magnitude estimate. The results will be discussed following a description of the mode matching approach.

Modelling the vacuum gap with the mode matching code SCATTER proved

much more difficult. In his PhD thesis Stephen Doherty of NUIM attempts to model a vacuum gap with the mode matching technique [Doherty, 2012]. The ‘annular trap’ method he attempted involved defining a waveguide section with a radius larger than the cavity radius and with a length equal to that of the vacuum gap as illustrated in Figure 5.28. Then, by considering what modes were possible to propagate in this annular section based on the cut-off frequencies of the modes, an upper limit to the amount of power that could radiate out through to free-space was calculated. This was achieved by investigating what fraction of power in each mode was contained in the annular section. The results from that study showed that the amount of power that coupled into the annular section was strongly dependent on the radius of the section. It was also shown that as the radius was increased to large values relative to the cavity radius the results tended toward an asymptote. It was concluded that this method would allow for an upper limit to be calculated for the power lost to free-space, but the required large annular radius allowed for a large number of modes and therefore long computation times, and of course this was just an approximation.

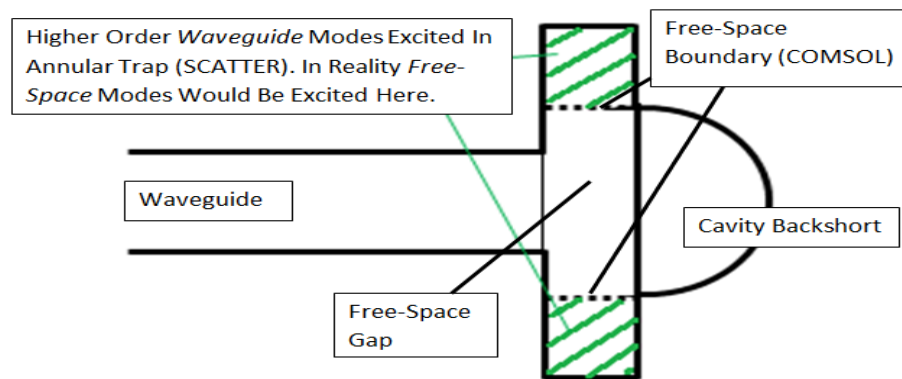


Figure 5.28: Illustration of the ‘annular trap’ method for modelling a vacuum gap in a SAFARI-like detector.

An aim of future work is to model propagation across the vacuum gap using free-space Gaussian beam modes and waveguide modes for the backshort cavity and waveguide entrance aperture. The following theory and discussion relied on heritage from a similar approach taken by Emily Gleeson to model a similar problem in the design of the feed horn array for the HFI instrument on the PLANCK satellite [Gleeson, 2004]. In that case the vacuum gap related to the space between the back-to-back horns and the detector horns and it was the location of the filter stack, as shown in Figure 5.29. The aim here is to allow the free-space modes to propagate

freely across the vacuum gap region until they encounter the cavity entrance. The electric field of the free-space EM waves propagating across the vacuum gap can be described mathematically as a sum of such free-space modes based on the GBM theory that was presented in chapter 2. Of course if the frequency is such that the waveguide feeding the vacuum gap is single-moded then the decomposition of the waveguide field in terms of free-space modes will be straightforward and will be similar to how the corrugated horn aperture fields were decomposed in the examples in chapter 2. However, the waveguide feeds in the SAFARI detectors will be over-moded, and the integrating backshort cavities will certainly be multi-moded, and since each waveguide mode that is present at the waveguide aperture needs to be decomposed in terms of free-space modes then the most convenient approach is to define a transformation matrix $[\mathbf{T}]$ that can account for all possible mode-to-mode coupling. We can represent the loss at the edge of the pixel then as absorbing walls as illustrated in Figure 5.30.

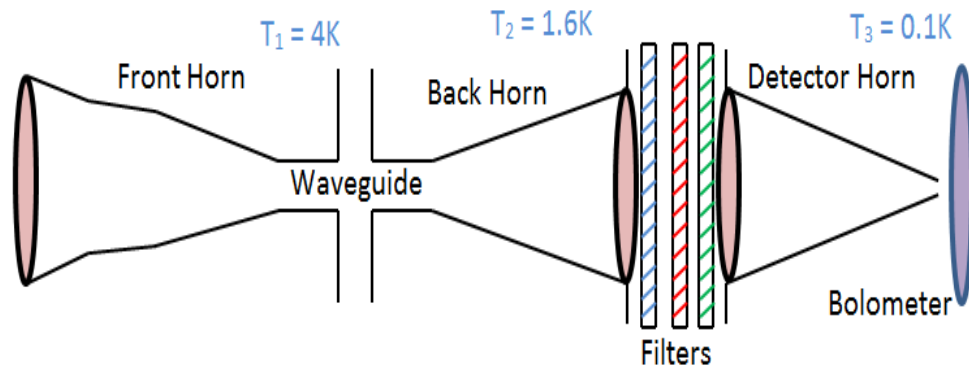


Figure 5.29: Schematic of the optical chain for the HFI channels on the PLANCK satellite. The front horn determines the light collected from the telescope. The back horn launches the CMB radiation through a set of filters into the 100 mK horn which concentrates it onto the bolometer in the detector cavity.

The TE and TM waveguide modes that were described in chapter 2 can be rewritten in terms of combinations of $\hat{\mathbf{i}}$ and $\hat{\mathbf{j}}$ components so that the terms containing Bessel functions of order $n - 1$ and trigonometric functions of $(n - 1)\phi$ are grouped together and similarly terms with Bessel functions of order $n + 1$ and trigonometric functions of $(n + 1)\phi$ also grouped together. The normalised waveguide modes are then written as [Trappe *et al.*, 2005] $\vec{e}_{nl}^{TE} = \vec{e}_{nl}^{TE(n-1)} + \vec{e}_{nl}^{TE(n+1)}$ and $\vec{e}_{nl}^{TM} =$

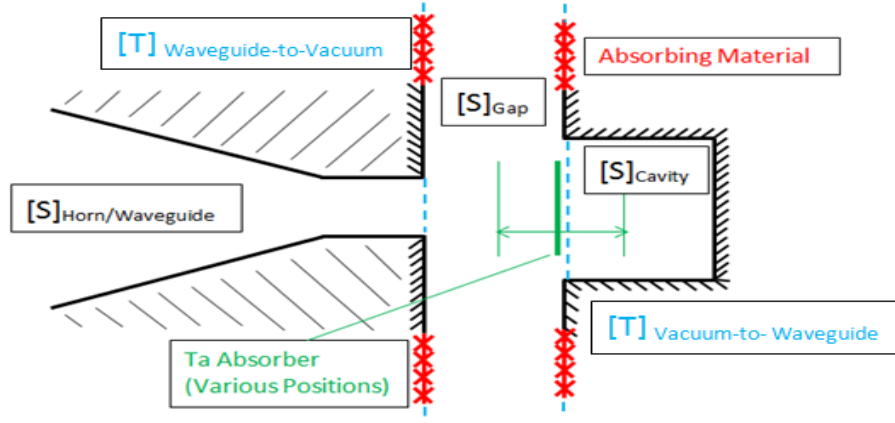


Figure 5.30: Illustration of the waveguide-to-free space transformation method of modelling a vacuum gap.

$\vec{e}_{nl}^{TM(n-1)} + \vec{e}_{nl}^{TM(n+1)}$ where:

$$\vec{e}_{nl}^{TE(n-1)} = \sqrt{\frac{(2 - \delta_{n0})}{\pi a^2 (1 - (n/q_{nl})^2) J_n^2(q_{nl})}} J_{n-1}\left(\frac{q_{nl}r}{a}\right) \left[\begin{matrix} \cos(n-1)\phi \\ -\sin(n-1)\phi \end{matrix} \right] \hat{\mathbf{i}} - \left[\begin{matrix} \sin(n-1)\phi \\ \cos(n-1)\phi \end{matrix} \right] \hat{\mathbf{j}} \quad (5.19)$$

$$\vec{e}_{nl}^{TE(n+1)} = \sqrt{\frac{(2 - \delta_{n0})}{\pi a^2 (1 - (n/q_{nl})^2) J_n^2(q_{nl})}} J_{n+1}\left(\frac{q_{nl}r}{a}\right) \left[\begin{matrix} \cos(n+1)\phi \\ -\sin(n+1)\phi \end{matrix} \right] \hat{\mathbf{i}} + \left[\begin{matrix} \sin(n+1)\phi \\ \cos(n+1)\phi \end{matrix} \right] \hat{\mathbf{j}} \quad (5.20)$$

$$\vec{e}_{nl}^{TM(n-1)} = \sqrt{\frac{(2 - \delta_{n0})}{\pi a^2 J_{n+1}^2(p_{nl})}} J_{n-1}\left(\frac{p_{nl}r}{a}\right) \left[\begin{matrix} \cos(n-1)\phi \\ -\sin(n-1)\phi \end{matrix} \right] \hat{\mathbf{i}} - \left[\begin{matrix} \sin(n-1)\phi \\ \cos(n-1)\phi \end{matrix} \right] \hat{\mathbf{j}} \quad (5.21)$$

$$\vec{e}_{nl}^{TM(n+1)} = \sqrt{\frac{(2 - \delta_{n0})}{\pi a^2 J_{n+1}^2(p_{nl})}} J_{n+1}\left(\frac{p_{nl}r}{a}\right) \left[\begin{matrix} \cos(n+1)\phi \\ -\sin(n+1)\phi \end{matrix} \right] \hat{\mathbf{i}} + \left[\begin{matrix} \sin(n+1)\phi \\ \cos(n+1)\phi \end{matrix} \right] \hat{\mathbf{j}} \quad (5.22)$$

Clearly, because of the orthogonality of the ϕ dependent components of the modes, the waveguide modes couple to normalised vector combinations of two free space Laguerre modes of the form:

$$\vec{\Psi}_m^\alpha(W, R, r, \phi, z) = \psi_m^\alpha(W, R, r, \phi) \exp(-ikz + i\phi_{m,\alpha}(z)) \left[\begin{matrix} \cos \alpha \phi \\ -\sin \alpha \phi \end{matrix} \right] \hat{\mathbf{i}} \pm \left[\begin{matrix} \sin \alpha \phi \\ \cos \alpha \phi \end{matrix} \right] \hat{\mathbf{j}} \quad (5.23)$$

where $\psi_m^\alpha(W, R, r, \phi) = \sqrt{\frac{2m!}{\pi W^{2(m+\alpha)!}}} \exp\left(\frac{-r^2}{W^2}\right) \left(\frac{2r^2}{W^2}\right)^{\frac{\alpha}{2}} L_m^\alpha(2r^2/W^2) \exp(-ik(r^2/2R))$, which are the scalar Associated Laguerre-Gauss modes that were presented in chapter 2, and α is an integer that represents the degree of the Laguerre polynomials. The computation time involved in converting between waveguide modes and free space modes with this method is greatly reduced because when the azimuthal order, n , of the waveguide modes is non-zero both the $\vec{e}_{nl}^{TE(n-1)}$ and $\vec{e}_{nl}^{TM(n-1)}$ waveguide mode components only couple to the $\vec{\Psi}_m^{n-1}(r, \phi, z)$ free-space modes, and the $\vec{e}_{nl}^{TE(n+1)}$ and $\vec{e}_{nl}^{TM(n+1)}$ components only couple to the $\vec{\Psi}_m^{n+1}(r, \phi, z)$. Thus, for each waveguide mode of radial degree l and azimuthal order n we can write:

$$\begin{aligned} \vec{e}_{nl}^{TE} &= \sum_m^M \left(T_{m,l}^{(n)} \vec{\Psi}_m^{n-1} + T_{m+M,l}^{(n)} \vec{\Psi}_m^{n+1} \right) \quad (a) \\ \vec{e}_{nl}^{TM} &= \sum_m^M \left(T_{m,l+L}^{(n)} \vec{\Psi}_m^{n-1} + T_{m+M,l+L}^{(n)} \vec{\Psi}_m^{n+1} \right) \quad (b) \end{aligned} \quad (5.24)$$

where the $T_{i,j}^{(n)}$ can be regarded as the elements of a $2M \times 2L$ transformation matrix $\vec{T}^{(n)}$ for waveguide modes of azimuthal order n . $2M$ is the number of Laguerre modes used in the analysis for a given waveguide mode, and $2L$ is the number of modes of radial degree l that are used for each n (half TE and half TM).

The reason for the $m + M$ in the subscripts in the right hand side terms of 5.24 is related to how the matrix $\vec{T}^{(n)}$ is ordered, i.e. with the first half of the rows corresponding to the $\vec{\Psi}_m^{n-1}$ coefficients and the second half of the rows corresponding to the $\vec{\Psi}_m^{n+1}$ coefficients. The reason then for $l + L$ subscripts in 5.24(b) for the TM waveguide modes is again related to how the matrix $\vec{T}^{(n)}$ is ordered, i.e. with the first half of the columns corresponding to the \vec{e}_{nl}^{TE} TE coefficients, and the second half of the columns corresponding to the \vec{e}_{nl}^{TM} TM coefficients. An example corresponding to waveguide modes with azimuthal order $n = 3$ and radial degree $l = 1$ to $l = 3$ represented by 8 Laguerre-Gauss free-space modes (4 of azimuthal order 2 and 4 of azimuthal order 4) is shown below in the $\vec{T}^{(3)}$ matrix.

$$\begin{array}{c}
\vec{\Psi}_0^2 \\
\vec{\Psi}_1^2 \\
\vec{\Psi}_2^2 \\
\vec{\Psi}_3^2 \\
\vec{\Psi}_0^4 \\
\vec{\Psi}_1^4 \\
\vec{\Psi}_2^4 \\
\vec{\Psi}_3^4
\end{array}
\begin{bmatrix}
TE_{31} & TE_{32} & TE_{33} & TM_{31} & TM_{32} & TM_{33} \\
T_{11}^3 & T_{12}^3 & T_{13}^3 & T_{14}^3 & T_{15}^3 & T_{16}^3 \\
T_{21}^3 & T_{22}^3 & T_{23}^3 & T_{24}^3 & T_{25}^3 & T_{26}^3 \\
T_{31}^3 & T_{32}^3 & T_{33}^3 & T_{34}^3 & T_{35}^3 & T_{36}^3 \\
T_{41}^3 & T_{42}^3 & T_{43}^3 & T_{44}^3 & T_{45}^3 & T_{46}^3 \\
T_{51}^3 & T_{52}^3 & T_{53}^3 & T_{54}^3 & T_{55}^3 & T_{56}^3 \\
\mathbf{T}_{61}^3 & \mathbf{T}_{62}^3 & \mathbf{T}_{63}^3 & \mathbf{T}_{64}^3 & \mathbf{T}_{65}^3 & \mathbf{T}_{66}^3 \\
T_{71}^3 & T_{72}^3 & T_{73}^3 & T_{74}^3 & T_{75}^3 & T_{76}^3 \\
T_{81}^3 & T_{82}^3 & T_{83}^3 & T_{84}^3 & T_{85}^3 & T_{86}^3
\end{bmatrix}$$

One of the elements in the $\vec{T}^{(3)}$ matrix is highlighted in red (T_{62}^3) as an example, and it corresponds to the amount of the TE_{32} waveguide mode that couples to the $\vec{\Psi}_1^4$ free-space mode. Clearly the $\vec{\Psi}_1^4$ free-space mode will also carry power from the other waveguide modes if they are present, and the contributions of each mode to the $\vec{\Psi}_1^4$ are represented in the sixth row of $\vec{T}^{(3)}$ (shown in bold face). It is these $\vec{\Psi}_m^n$ fields that carry the power across the vacuum gap as far as the cavity entrance plane, and due to their formalism they diffract as they propagate. This diffraction causes the intensity of the free-space modes to spread out meaning that not all of the power will be available for coupling to the waveguide modes of the cavity, which are of course truncated at the edge of the cavity. Therefore performing the power coupling integrals over the area corresponding to the cavity aperture will result in a total power available for coupling to the absorber less than the power present before propagation across the vacuum gap. Converting the EM field represented by Laguerre-Gauss modes back into cylindrical waveguide modes appropriate for a cylindrical backshort cavity would be the next step, and the theory is very similar to that just described for the reverse case. Each transformation matrix for each azimuthal order n of waveguide modes will have the form of the complex transpose of the $2L \times 2M$ $\vec{T}^{(n)}$ matrices described above, i.e $2M \times 2L$ $\vec{T}^{\dagger(n)}$.

$$\begin{array}{l}
TE_{31} \\
TE_{32} \\
TE_{33} \\
TM_{31} \\
TM_{32} \\
TM_{33}
\end{array}
\begin{bmatrix}
\vec{\Psi}_0^2 & \vec{\Psi}_1^2 & \vec{\Psi}_2^2 & \vec{\Psi}_3^2 & \vec{\Psi}_0^4 & \vec{\Psi}_1^4 & \vec{\Psi}_2^4 & \vec{\Psi}_3^4 \\
T_{11}^3 & T_{12}^3 & T_{13}^3 & T_{14}^3 & T_{15}^3 & T_{16}^3 & T_{17}^3 & T_{18}^3 \\
T_{21}^3 & T_{22}^3 & T_{23}^3 & T_{24}^3 & T_{25}^3 & T_{26}^3 & T_{27}^3 & T_{28}^3 \\
T_{31}^3 & T_{32}^3 & T_{33}^3 & T_{34}^3 & T_{35}^3 & T_{36}^3 & T_{37}^3 & T_{38}^3 \\
T_{41}^3 & T_{42}^3 & T_{43}^3 & T_{44}^3 & T_{45}^3 & T_{46}^3 & T_{47}^3 & T_{48}^3 \\
T_{51}^3 & T_{52}^3 & T_{53}^3 & T_{54}^3 & T_{55}^3 & T_{56}^3 & T_{57}^3 & T_{58}^3 \\
\mathbf{T}_{61}^3 & \mathbf{T}_{62}^3 & \mathbf{T}_{63}^3 & \mathbf{T}_{64}^3 & \mathbf{T}_{65}^3 & \mathbf{T}_{66}^3 & \mathbf{T}_{67}^3 & \mathbf{T}_{68}^3
\end{bmatrix}$$

The technique described above would be a first order approximation for accounting for losses due to the gap between the horn array block and the detector array. A higher order approximation could include multiple reflections of the free-space Laguerre-Gauss modes within the vacuum gap in a manner similar to modelling a Fabry-Perot etalon environment, and even multiple transformations from waveguide-to-Laguerre-Gauss modes and Laguerre-Gauss-to-waveguide modes to account for the effects of the vacuum gap on return power from the cavity. This could be implemented with a scattering matrix formalism.

Taking account of the resistive sheet absorber would be either straightforward or require even more extra code, depending whether the absorber was to be positioned within the cavity structure or in the vacuum gap between the horn and cavity (see Figure 5.30). If the design consisted of the absorber being located at the aperture of, or within the cavity backshort, then the code to model it already exists as presented in section 5.2.1, where the absorber was treated as an infinitely thin resistive current sheet with a two dimensional sheet resistance in units of Ω/\square . If on the other hand it was located within the vacuum gap (as is the case with past designs), then the absorber could be modelled with the appropriate scattering matrix, where the interaction of free-space Laguerre-Gauss modes with a resistive sheet would need to be considered.

Assuming the absorber is located just after the cavity backshort and not in the vacuum gap, then the overall scattering matrix for an entire pixel system could be calculated by cascading the scatter matrices for each sub-domain of the system as follows:

$$\begin{aligned}
[\vec{S}]_{Total} &= \begin{bmatrix} \vec{S}_{11}^{(n)} & \vec{S}_{12}^{(n)} \\ \vec{S}_{21}^{(n)} & \vec{S}_{22}^{(n)} \end{bmatrix} \boxtimes \begin{bmatrix} 0 & \vec{T}^{(n)} \\ \vec{T}^{\dagger(n)} & 0 \end{bmatrix} \\
&\boxtimes \begin{bmatrix} 0 & \vec{V}^{(n)} \\ \vec{V}^{\dagger(n)} & 0 \end{bmatrix} \boxtimes \begin{bmatrix} 0 & \vec{T}^{\dagger(n)} \\ \vec{T}^{(n)} & 0 \end{bmatrix} \boxtimes \begin{bmatrix} \vec{S}_{11}^{(n)} & \vec{S}_{12}^{(n)} \\ \vec{S}_{21}^{(n)} & \vec{S}_{22}^{(n)} \end{bmatrix}
\end{aligned}$$

where the middle matrix represents propagation across the vacuum gap, and the \boxtimes symbol indicates that the scattering matrices are cascaded [Olver *et al.*, 1994], as opposed to multiplied. The ABCD matrix for propagation through free-space could be used to transform each Laguerre-Gauss free-space mode:

$$\begin{bmatrix} 1 & L \\ 0 & 1 \end{bmatrix}$$

where L is the length of the vacuum gap.

As a first order approximation the TE_{11} mode that can propagate in the waveguide feed of the SAFARI L-Band (see Figure 5.27 above) was decomposed in terms of associated Laguerre-Gauss free-space modes. This TE_{11} mode is the field that is present at the waveguide exit, at the start of the vacuum gap. The higher order TE_{12} mode will only propagate at the highest frequencies of the SAFARI L-Band range, and since the blackbody source used in the measurements at Cardiff [Mauskopf, 2011] produced only faint signal levels at the TE_{12} switch-on frequency, it was ignored in the analysis. Twenty Laguerre-Gauss free-space modes were used in the analysis (ten of $\vec{\Psi}_n^0$ and ten of $\vec{\Psi}_n^2$).

The Laguerre-Gauss free-space modes were then propagated across the vacuum gap by simply using a value for propagation distance equal to that of the gap depth. The power coupling integrals for converting back from Laguerre-Gauss modes to the TE_{11} waveguide mode were then calculated, where the TE_{11} mode is now that corresponding to a cylindrical waveguide with a radius the same as the cavity back-short.

By summing the normalised mode coefficients A_n corresponding to the transformation from the waveguide TE_{11} mode to free-space modes (this of course was equal to unity), and then comparing this to the sum of the normalised mode coefficients A_n^* corresponding to the transformation from free-space modes to the cavity TE_{11} mode, a first order approximation was deduced for the amount of power lost

as a result of the vacuum gap:

$$Loss = \sum_n^N A_n - \sum_n^N A_n^* = 1 - \sum_n^N A_n^* \quad (5.25)$$

The analysis was carried for the SAFARI L-Band frequency range from 1.5 to 3.0THz in steps of 0.1THz, with the results shown in Figure 5.31. The results from a FEM analysis of the SAFARI L-Band detector (to be discussed in the next section 5.4.2) are shown for comparison. As can be seen there is large differences between the two results. In fact it appears that the modal analysis may provide a lower limit on the power radiated through the gap. Since the free-space Laguerre-Gauss mode simulation does not include multiple reflections, and the FEM model of the SAFARI L-Band does, a second FEM model was created which attempted to match the scenario modelled with the modal approach. In this case the vacuum gap was terminated with a perfectly matched layer boundary condition, as shown in Figure 5.32, and as can be seen there is a significant improvement in terms of agreement between the FEM and modal approaches.

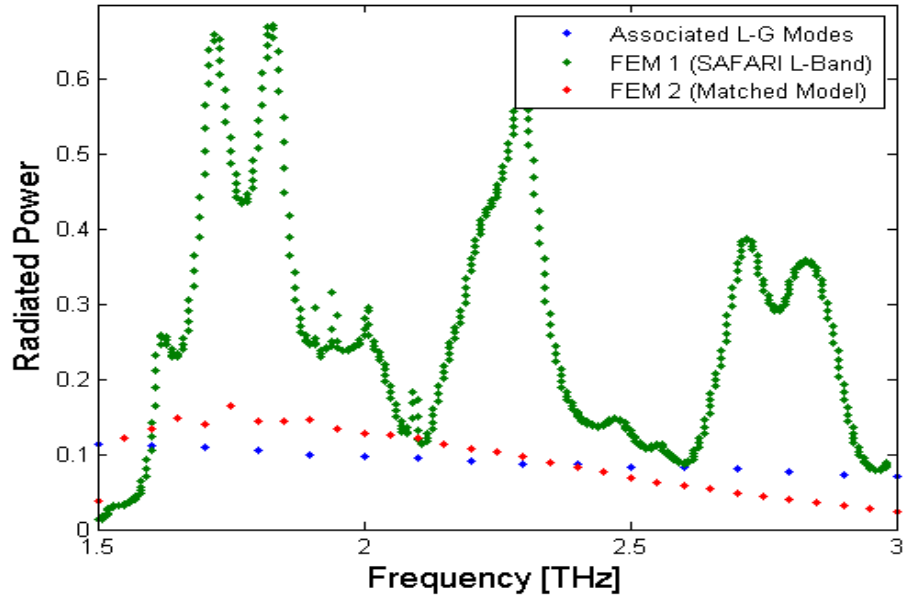


Figure 5.31: Fractional power radiated through the vacuum gap between the horn array and the pixel array chip for the SAFARI L-Band. The analysis involved 20 Laguerre-Gauss free-space modes (10 of $\vec{\Psi}_n^0$ and 10 of $\vec{\Psi}_n^2$). The results from a FEM analysis of the same problem are shown for comparison (see Figure 5.36 in section 5.4.2).

The method described above is a very approximate approach since there are a number of factors not accounted for in the analysis. First, while only the TE_{11} mode was present at the single-mode waveguide feed aperture (at 1.5 THz), the

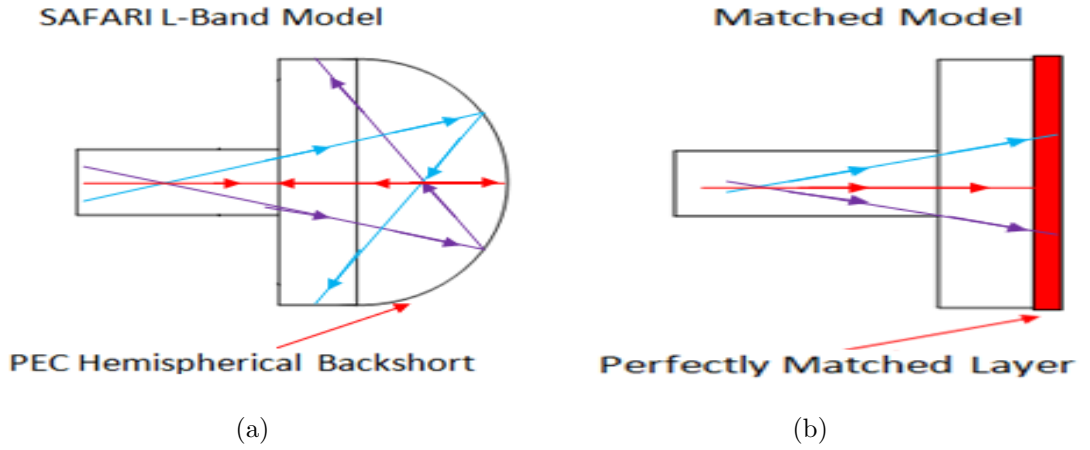


Figure 5.32: Illustration of the matched model for Laguerre-Gauss mode verification. (a): The SAFARI L-Band FEM model illustrates how radiation can be lost due to the hemispherical PEC walls directing signal toward the gap. (b): The matched FEM model depicts the perfectly matched layer that was used in order to try to match what is being simulated in the Laguerre-Gauss mode model.

radius of the cavity aperture is over eight times that of the waveguide meaning that higher order modes can propagate if excited. The Laguerre-Gauss free-space modes with azimuthal dependence $\alpha = 0$ and $\alpha = 2$ can couple to waveguide modes with higher order radial dependence (TE_{1m}), thus an unknown fraction of the observed loss may be coupling to these higher order modes. In fact the Laguerre-Gauss modes with azimuthal dependence $\alpha = 2$ can also couple to waveguide modes with azimuthal dependence $l = 3$ (as discussed earlier in this section), including all possible radial modes of this azimuthal symmetry TE_{3m} . The second point to be made is that multiple reflections will need to be considered for an accurate result, as described above. The hemispherical backshort in the SAFARI L-Band design is likely to direct a large amount of the signal toward the gap (based on ray tracing), leading to the significantly greater levels of loss shown in Figure 5.31 for the FEM model of the SAFARI L-Band detector. Correctly accounting for the vacuum gap using the mode matching approach will clearly require a significant extension of the existing SCATTER code. The FEM modelling approach was therefore employed for the analysis of the SAFARI L-Band and S-Band pixels presented in the following sections.

Ideally the SAFARI receivers would have no gap between the feed aperture and the cavity, but the absorber is typically situated at the entrance of the cavity structure, or even a small distance in front of the entrance, and a minimum distance must be left between the feed horn array block and the sensitive TES detector array

chip. The value for this minimal distance is quoted by the SRON team as $30\mu\text{m}$ and therefore a vacuum gap of this length is required in the current designs. A new design that would allow for the removal of the vacuum gap is discussed in section 5.5 of this chapter, where simulations of the SAFARI S-Band are presented.

5.4.2 COMSOL Model of SAFARI L-Band Detectors

Since including the vacuum gap in the SCATTER mode matching code is still a work in progress in terms of modelling the SAFARI L-Band, the current work focussed on modelling the detector in the most computationally efficient manner achievable with COMSOL. It was possible to model the system with the standard 3D COMSOL approach due to the single mode nature and relatively modest size of the detector, so this is the first method that was used to model the L-Band. However knowing that the SAFARI S-Band is both a multi-moded system, and that the high frequencies involved give rise to the structure being very large in terms of wavelength, the more efficient (but less accurate) 2D COMSOL approach was also used to model the L-Band so that it could be determined if the results could still be used to extrapolate the approximate corresponding 3D behaviour for more complex structures.

A model was created in the COMSOL 3D environment with dimensions corresponding to the L-Band pixel, as illustrated in Figure 5.27 at the beginning of this section. The TE_{11} mode was excited across the entry aperture of the waveguide with a total power of 1 Watt. The surface impedance of the absorber sheet was again set to the idealised value of $377\frac{\Omega}{\square}$ and a frequency sweep was simulated from 1.5 to 3.0THz for 200 spot frequencies. A similar model was then created in the 2D planar symmetry COMSOL environment that represented a 2D cut through the centre of the 3D model in terms of geometry, however in terms of the physics the 2D model actually represented a cut through the model illustrated in 5.33(b). The same frequency sweep was analysed for the 2D model and the results are shown in graphs below. Figure 5.34 shows the fractional power that is absorbed by the resistive sheet for both models and the HFSS data that was produced by Dr. Phil Mauskopf from Cardiff is also shown for comparison [Mauskopf, 2011]. The scaling factor calculated for the 2D data, based on comparing the ratios of areas for the power flow surfaces for both the 2D model and the extruded 3D Cartesian coordinate model, was 0.72 (ratio of absorber areas).

As can be seen there is excellent agreement between the COMSOL 3D and HFSS data. There appears to be a higher level of structure in the COMSOL 3D data compared to HFSS and this may be due to the time-domain approach (transient solver) used for the HFSS analysis in contrast to the frequency domain solver used with COMSOL. If a sufficiently long time period was not allowed for the HFSS calculations then this would transform into lower resolution in the Fourier transformed frequency spectrum and thus less structure. The Cardiff University report good agreement between measurements and their HFSS models [Mauskopf, 2011] and there is clearly very good agreement with the COMSOL results discussed here.

The corrected COMSOL 2D data is in agreement with the general trends seen in the HFSS and COMSOL 3D data sets, with the largest differences occurring at the higher frequencies and certainly less structure observed in the data. Again, since the symmetry in the 3D models is cylindrical, then the 2D model is a gross approximation and we would expect differences between the two models.

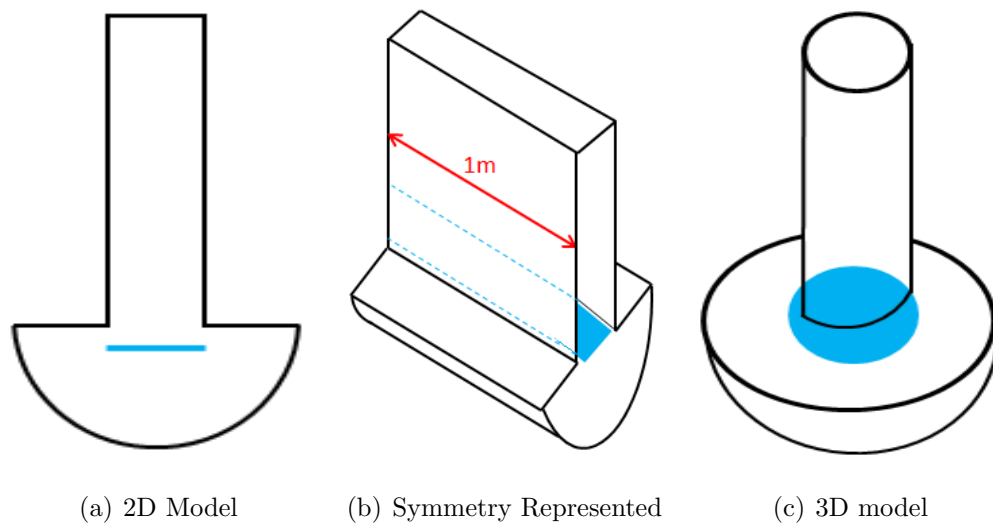


Figure 5.33: Illustration of the 2D COMSOL model of the SAFARI L-Band and what it relates to in terms of its 3D analogue. (a): Illustration of the 2D model, (b): The one dimensional translational symmetry represented in the 2D COMSOL model, and (c): The cylindrical 3D model of the SAFARI L-Band pixel.

It is clear from Figure 5.34 that with a vacuum gap included in the model the efficiency of the absorber is significantly reduced when compared to a closed system, such as those examined in the previous section. For this reason the two sources of loss were separately examined in order to quantify how much power loss is due leakage via the vacuum gap and how much is due to returned power back through the input waveguide. Following the calculations across the frequency range, the post-processing mode in COMSOL was used to first analyse the losses through the

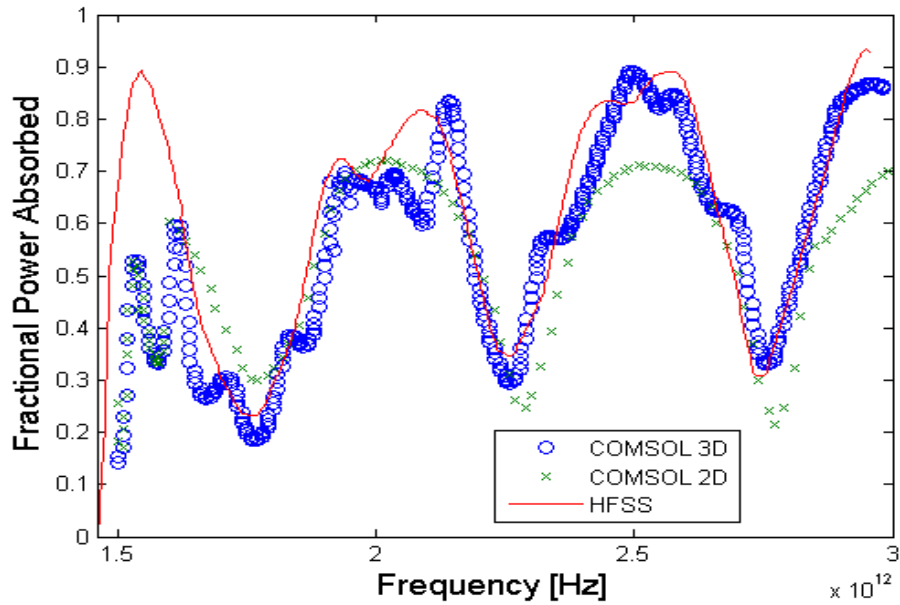


Figure 5.34: Efficiency of the SAFARI L-Band detector with the absorber surface impedance set to $400 \frac{\Omega}{\square}$ in order to match the Cardiff models. There is very good agreement between the COMSOL and HFSS results. The corrected 2D data displays some differences with lower efficiency at the higher frequencies, but the peaks and troughs still align to a good degree of accuracy.

vacuum gap. The time averaged power outflow parameter was integrated over the area that contained the vacuum gap section. This was done for each frequency value and the results are shown in Figure 5.36. Again there is clearly very good agreement between the two 3D models in COMSOL and HFSS, although there is again more structure in the COMSOL data, and there is surprisingly reasonable agreement with the corrected 2D data also. The correction factor used for the vacuum gap loss data was π which again arises due to the 2D model being representative of a slice through a Cartesian geometry model with a length of 1 metre. The result is the vacuum gap power loss being spread over the area of a rectangle of dimensions $2rh$ where r is the distance from the centre to the edge of the cavity and h is the length of the vacuum gap between the horn and cavity (the rectangle highlighted in green in Figure 5.27 shown earlier. The power loss should really be integrated over the area of a cylinder (ignoring the top and bottom circular faces) with dimensions $2\pi r \times h$ where again r is the initial radius of the cavity and h is the vacuum gap length. The ratio of the areas of the power flow surfaces for the two geometries is $\frac{2\pi r \times h}{2rh} = \pi$ as shown in Figure 5.35.

The scaling factor for the amount of power returned back through the waveguide for the 2D model was determined to be 0.4 and it was calculated in a similar

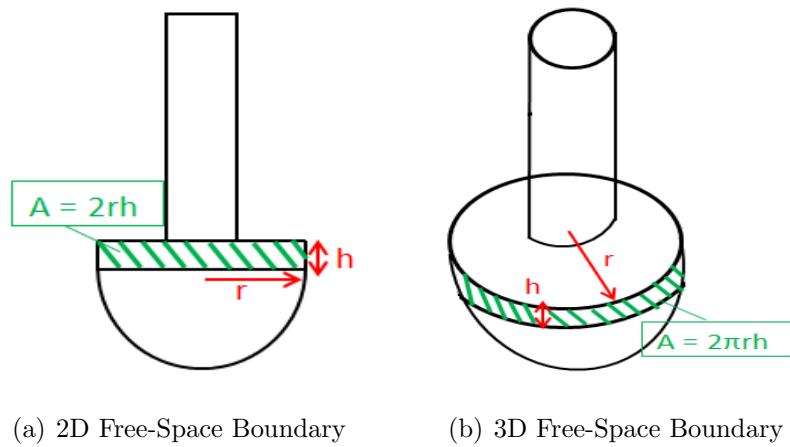


Figure 5.35: Comparison of areas of the free-space boundaries in the 2D and 3D models.

manner to that described earlier for the closed waveguide cavity. The return power is calculated from the S_{11} parameter that analyses the fraction of the electric field that is reflected back onto the input waveguide port where the TE_{11} mode was excited. Again Figure 5.37 shows good agreement between the 3D COMSOL and HFSS results, and some level of agreement with the corrected 2D data. The next step taken was to try to optimise the absorber/cavity configuration of the SAFARI L-Band detector in order to maximise the coupling of power to the absorber.

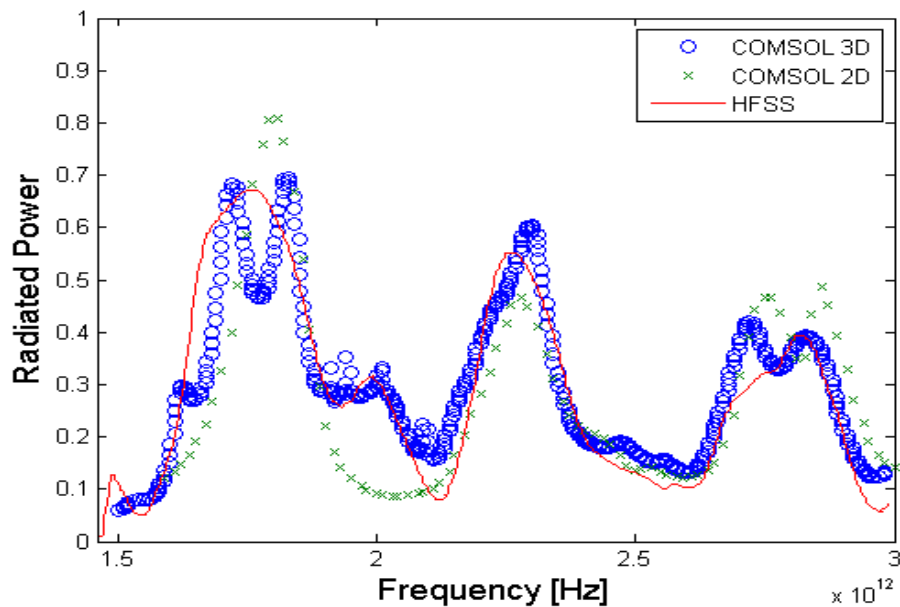


Figure 5.36: Vacuum gap loss of the SAFARI L-Band detector. Again there is very good agreement for all three approaches. The corrected 2D data again shows some differences with slightly higher levels of radiated power at a few of the test frequencies. The general trend is again well aligned with the other two sets of results.

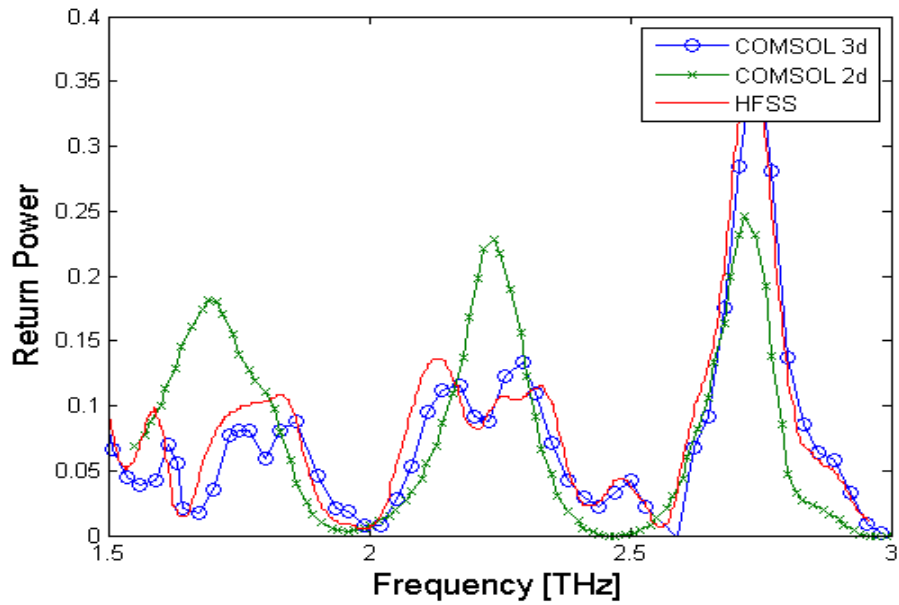


Figure 5.37: Return loss (S_{11}) of the SAFARI L-Band detector. Once again there is very good agreement between all three approaches.

5.4.3 Improving the SAFARI L-Band Design

In the simulations for generic systems presented in section 5.3.4 the cavity backshort geometry that performed best in terms of maximising the amount of power absorbed by the resistive sheet absorber was the sine profiled shape. Based on this result the sine profiled backshort design was substituted for the hemisphere in the SAFARI L-Band model, and using the full 3D COMSOL environment the system was simulated for the same frequency range of 1.5 to 3.0 THz. All other parameters of the model and dimensions of the structure were the same as for the model presented above, and a screen shot of the E-plane cut of the electric field for the sine profiled backshort at 2.2THz is shown in Figure 5.38.

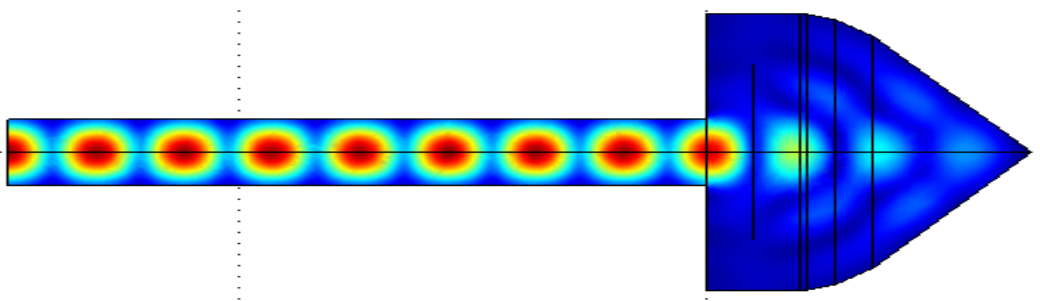


Figure 5.38: Screen shot of the electric field through the E-plane of a SAFARI L-Band pixel at 2.2THz.

By employing the sine profiled cavity backshort the average amount of power

absorbed by the resistive sheet was increased from 0.54 to 0.59. Although this is only an increase in efficiency of 10%, perhaps what is more important is that the standard deviation in the range of efficiency values across the frequency band was reduced from 0.22 to 0.15. This indicates a good improvement in consistency across the band which is also highly beneficial for these detectors. The results are shown in Figure 5.39 with the hemisphere cavity absorber data shown again for comparison.

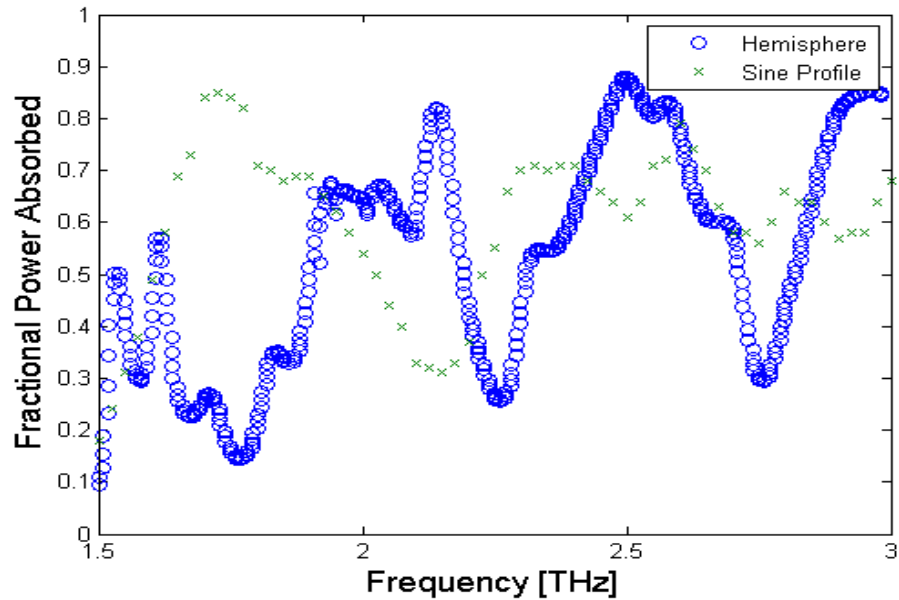


Figure 5.39: Absorber efficiencies for two different SAFARI L-Band cavity designs. It is clear that the sine profiled cavity has overall better performance with less variance across the band. Both systems were modelled with the full 3D EM COMSOL environment.

Figure 5.40 shows the losses through the vacuum gap that connects neighbouring pixels. Again there is clear improvement with the sine profile cavity design over the hemisphere. The peak fractional loss is reduced by half from 0.7 to 0.35, and there is again a significant reduction in how the loss varies across the band with the standard deviation on the data being reduced by more than half from 0.185 to 0.077.

The change in design for the shape of the cavity backshort for the L-Band pixel clearly has an impact on the efficiency of the Ta absorber sheet in terms of coupling to the incoming signal. It should be pointed out that the redesign of the backshort was limited in this case as the depth of the cavity was constrained to $250\mu\text{m}$ for the purposes of maintaining a relative comparison to the hemispherical design of the same depth. If the depth was permitted to vary, or alternatively the particular sine function used was allowed to vary, then the improvements could possibly be

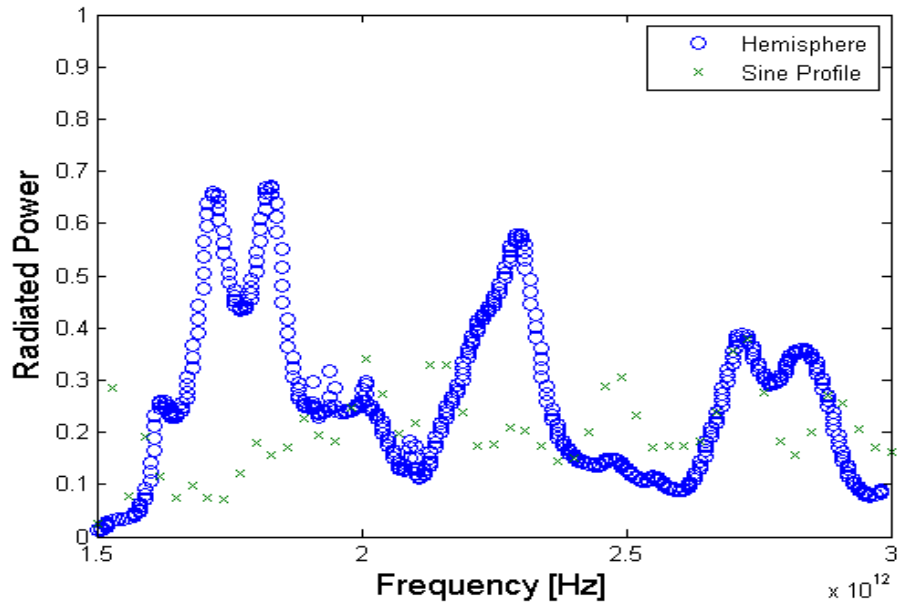


Figure 5.40: Losses through vacuum gap for two different SAFARI L-Band cavity designs. Both systems were modelled with the full 3D EM COMSOL environment.

increased further.

Another improvement to the design of the L-Band receiver is brought about by removing some of the absorber material in a manner that serves to reduce its volume while not significantly impacting on the amount of power it can absorb across the desired frequency range. The reason for wanting to reduce the volume of the absorber has to do with the speed of response of the detector and this was discussed by Stafford Withington in a presentation given to the Virtual Institute of Astroparticle Physics, Paris, at the Workshop on Microwave Spectral Polarimetry in December 2012 [Withington, 2012]. In his presentation he discusses two volume reducing designs they have been working with at his research institute at the Cavendish Laboratory, Cambridge University. One design consists of a mesh of absorber strips in the two perpendicular directions while the other consists of strips in just one direction (see Figure 5.41). The aim is to reduce the overall volume of the absorber whilst maintaining the optical cross section. As the volume is decreased the maximum speed of response of the detector is increased (time constant decreased) and this can be understood by considering how the effective time constant τ_{eff} changes with heat capacity, as can be seen from equation 5.26 [Mauskopf *et al.*, 2010].

$$\tau_{eff} = \frac{C}{G(1 + \Re)} \quad (5.26)$$

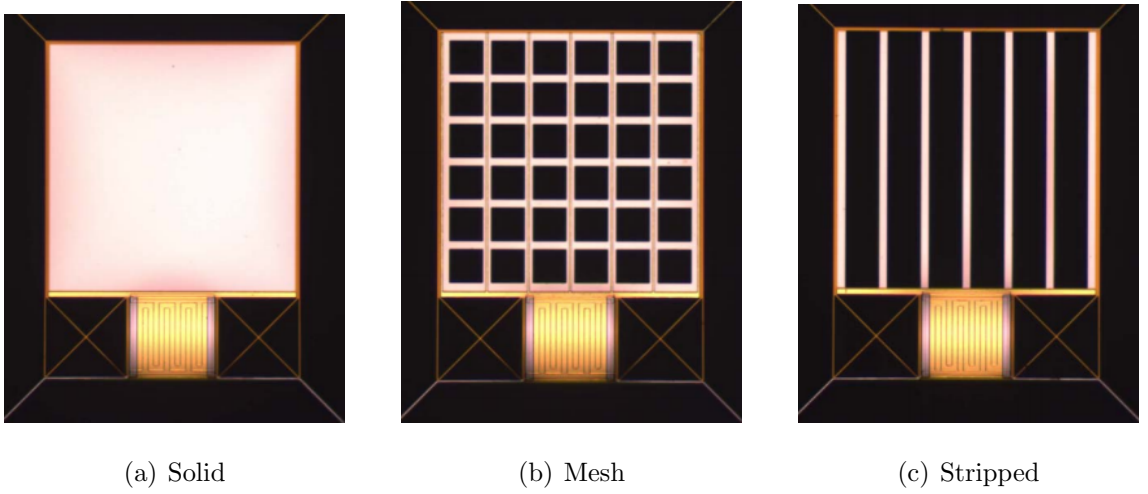


Figure 5.41: Photographs of TES's coupled to the Ta absorbers. (a): A solid sheet of Ta, (b): A mesh design, and (c): A striped design.

where C is the heat capacity of the TES and the absorber, G is the heat conductance to the bath, and \mathfrak{R} is the electro-thermal feedback loop gain.

The heat conductance G also appears in 5.26 and the paper just cited by Mauskopf *et al.* shows that in order to achieve the required detector NEP of $2 - 3 (\times 10^{-19} W/\sqrt{Hz})$, with a detector operating at $100mK$, then the heat conductance must be $G \leq 2 \times 10^{-13} W/K$. This small value calculated for G means that the heat capacity must be kept to a minimal value. The formula used to calculate this value for G is shown in 5.27.

$$NEP = \sqrt{4\gamma k_B T^2 G} \quad (5.27)$$

where T is the operating temperature of the TES, k_B is Boltzmann's constant, and γ is quoted as ≈ 0.5 [Jackson *et al.*, 2012].

The new design for the Ta absorber sheet was basically a two dimensional version of the fractal geometry Menger sponge [El Naschie, 2013]. This 2D format is also known as a Sierpinski carpet [Crownover, 1995] and can be thought of as a slice through the centre of the Menger sponge. Examples of both the Menger sponge and Sierpinski carpet are shown in Figure 5.42. The rules for constructing the 2D Sierpinski carpet are as follows:

- (i) Divide any square into nine equal congruent sub-squares forming a 9×9 grid.
- (ii) Remove the central sub-square.
- (iii) Repeat recursively for each of the remaining sub-squares for as many iterations as desired.

A similar set of rules is defined for constructing a Menger sponge from an ini-

tial cube. An interesting result of the 3D Menger sponge is that as the number of iterations increases to extremely large values the volume of the sponge approaches zero while the surface area approaches infinity. There are many other examples of fractal reduction topologies but it was the Sierpinski carpet that was the obvious choice since the absorber in the SAFARI L-Band is square. In fact fractal geometry structures have been shown to be the ideal solution for broadband receivers where the efficient detection of a large range of frequencies is desired for a relatively small antenna [Kadir, 2007]. Fractal designs can achieve this due to the self-similarity that naturally arises from fractal structures [Hohlfeld and Cohen, 1999]. Some mobile/cell phones now use antennas with either Sierpinski carpet or Sierpinski triangle geometries.

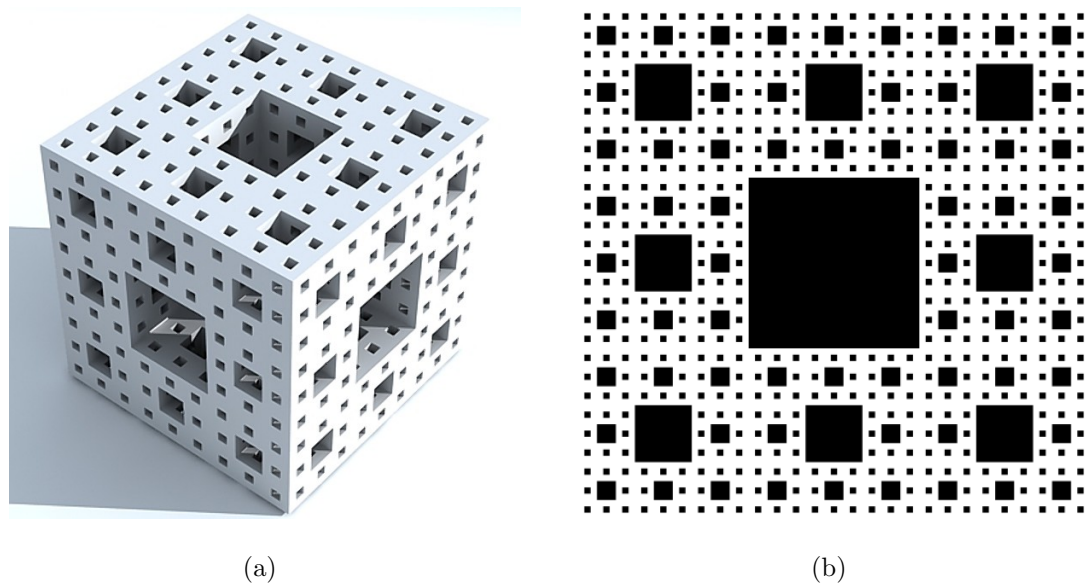


Figure 5.42: Examples of fractal geometry in 2D and 3D cases. (a) A cube having undergone 3 iterations of fractal reduction resulting in what is generally known as a Menger sponge denoted as M_3 . (b) A square having undergone 4 iterations of fractal reduction resulting in what is generally known as a Sierpinski carpet denoted by M_4 . An unaltered cube or square is denoted M_0

The Sierpinski carpet absorber sheet was built in the COMSOL 2D environment and then imported into the 3D model of the SAFARI L-Band in place of the solid 2D absorber that was modelled previously. Absorbers with a range of iterations were designed from one iteration (removal of the central square) to four iterations. Some of the designs are shown in Figure 5.43. The results of the three and four iteration absorbers are shown in Figure 5.44 along with the results from the solid sheet model for comparison. The average power absorbed by the solid sheet across the band was 0.54. The average absorption across the band for the three and four iteration fractal

absorbers was 0.46 and 0.43, respectively. This is a clearly a reduction in absorber efficiency but not a drastic decrease. The equation to calculate how much of the absorber area remains after each iteration is simply $A = \left(\frac{8}{9}\right)^n$ where n is the number of iterations employed. So for the absorber with four iterations of fractal reduction the remaining absorber area is 0.62 times that of the solid sheet. This method of removing material from the absorber appears to be a better choice as the amount of power absorbed by the striped design for example reduces by half [Mauskopf, 2011]. This 50% reduction is a result of only one polarisation of the signal being detected; that which is polarised parallel to the absorber strips.

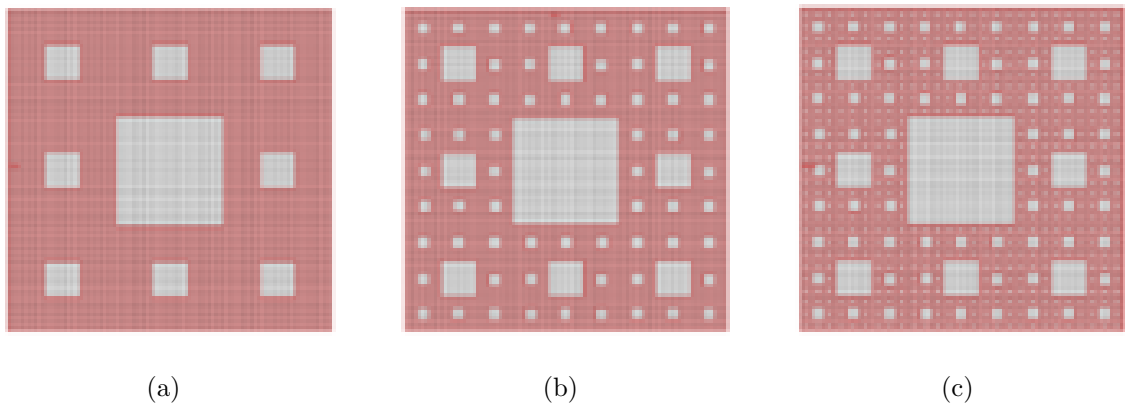


Figure 5.43: A CAD design of a 2D absorber with (a): Two levels of fractal subtraction, (b): three levels of fractal subtraction, and (c): four levels of fractal subtraction.

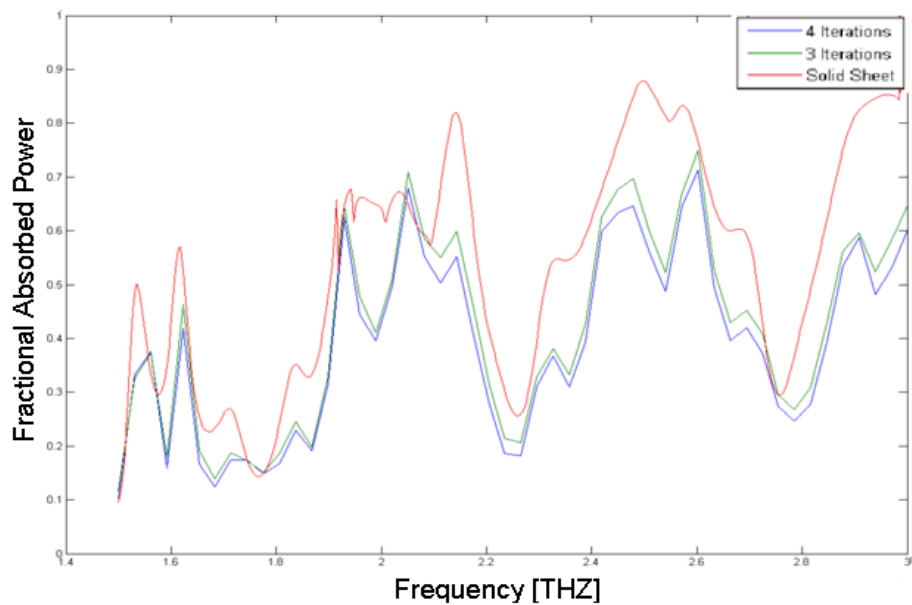


Figure 5.44: Efficiency of the SAFARI L-Band detector with a fractal absorber sheet with various fractal iterations.

5.5 SAFARI S-Band Receivers

A significant collaborative research effort has been ongoing at both NUIM and SRON in terms of the multi-moded SAFARI S-Band (short-wave band) as was described in section 1.2.2 of chapter 1. The research team at SRON led by Dr. Gert de Lange have built a SAFARI testbed and they have undertaken a test campaign with many cool down and warm up cycles where at each warm up they can modify the system and/or add components and then upon re-cooling the measurements can begin again. The current detector configuration employs the traditional hemispherical cavity backshort housing the bolometer being fed by a multi-moded smooth walled conical horn [Audley *et al.*, 2013]. Each bolometer consists of a superconducting TES with a transition temperature of approximately 100 mK coupled to a Ta absorber on a thermally-isolated silicon nitride island. They report base temperatures as low as 8 mK on the mixing chamber, and detector bath temperatures as low as 15 mK for dark measurements, which is significantly lower than the temperatures required for testing the SAFARI detectors. This leaves room for heat loads such as the blackbody source they use to illuminate the detector for optical measurements.

During the three months work placement at SRON the author of this thesis attended regular weekly project progress meetings of the SAFARI testbed team and gained a good understanding of the system. Some of the work performed by the author at SRON during this period concerning characterisation of SAFARI-like THz multi-moded feed horns is discussed in chapter 3. This section is concerned with a new design for the cavity backshort for the S-Band detectors and results of simulations for this new design.

The research team at NUIM has been making significant progress in modelling the current SRON SAFARI testbed, and collaboration between the two institutes is ongoing and funded through an ESA technical development contract [RFQ 3-6418/11/NL/CBi]. Stephen Doherty (post-doctoral researcher at NUIM) has been carrying out most of the simulation work on the current system and the author of this thesis has contributed to this effort through the modelling of alternative geometries for the S-Band cavities.

During the period of work by the author at SRON a concept for a new cavity design was discussed with Dr. Damian Audley and Dr. Gert de Lange, both of SRON.

The concept was to use anisotropic silicon crystal etching as an efficient and accurate method for creating the integrating cavities required for the SAFARI S-Band array. This process uses a chemical etching technique that relies on the different chemical reactivities of different crystal planes in a silicon crystal [Alvi *et al.*, 2008]. This plane dependent reactivity can be exploited through the use of specific chemical agents that etch faster in one direction over others, allowing the user to etch geometrical shapes such as pyramids.

There is a large amount of literature on the topic of anisotropic silicon crystal etching as it is regularly used in the bulk manufacture of micrometer scale electronic components on integrated circuits (see for example [Kovacs *et al.*, 1998]). Whereas isotropic etching will result in a hemispherical shaped cavity being formed on a flat silicon substrate due to the chemical agent reacting in all directions at the same rate, anisotropic etching will typically result in either square shaped trenches being etched into the flat substrate, or pyramidal shaped structures, depending on the nature of the chemical agents, how dilute the reactants are, and a number of other factors such as which crystal plane is exposed on the surface of the substrate, i.e the orientation of the crystal. For example, in his PhD thesis, Samuel Pollock discusses that certain alkali hydroxides exhibit an etch rate significantly higher for the (100) and (110) directions than for the (111) direction [Pollock, 2010]. His work with this etching process involves building atom traps with the aim of performing measurements with cooled trapped atoms, which is obviously a very different application to the work of this thesis. He states that potassium hydroxide (KOH) etches the (100) plane 400 times faster than the (111) plane, while the (110) plane is etched 600 times faster. This results in the etching on the (111) planes being insignificant and the (111) planes are easily revealed and expose themselves as the faces of a pyramidal shaped cavity (see Figure 5.45). The walls of the pyramid make an angle of 54.74° with the flat substrate resulting in a pyramid with an apex angle of approximately 70.5° . The resulting pyramidal cavity has a surface roughness significantly less than can be achieved with any mechanical milling process on these micrometer scales. This is particularly critical given the the small dimensions of the cavities and the short wavelengths involved. The manufacturing process is also a lot easier than other methods.

Another benefit of employing this approach is the possibility of including a

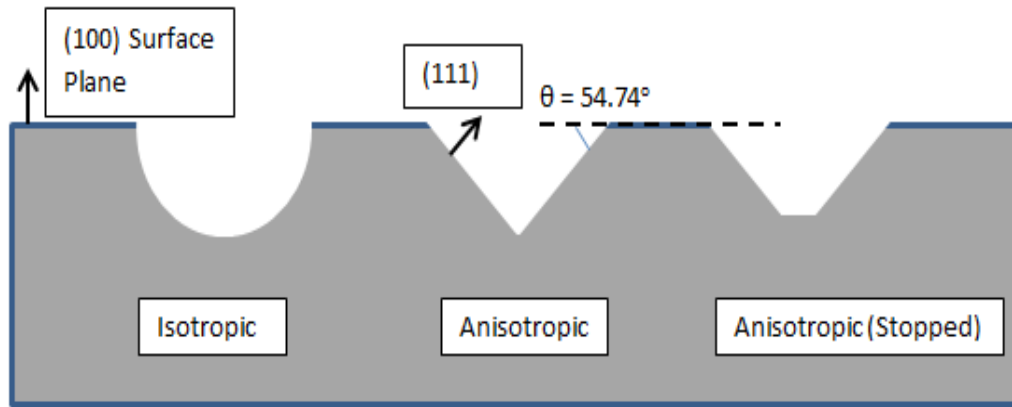


Figure 5.45: Examples of geometries that result from various chemical etching techniques.

second pyramidal or square cavity section above the TES and absorber that would link the integrating cavity with the feed horn array, thus removing the vacuum gap, as shown in Figure 5.46. The overall cavity would therefore have an octahedron geometry if two pyramidal structures were used, or another closed geometry if a pyramid and cuboid were used. The wiring for the TES readout electronics could be located within trenches that could be etched into the silicon wafer through the chemical etching process. The straight, angled walls of the pyramidal cavity would be similar to the almost straight angled sections of the sine profiled cavity design for the SAFARI L-Band detectors discussed in section 5.4.3 of this chapter. In that case the angled walls of the sine profile were shown to be a good solution for coupling radiation to the resistive sheet; the result being an increase in absorber efficiency and with a higher level of consistency across the band while reducing the losses through the vacuum gap between the waveguide feed and the cavity backshort.

Before anything was built it was desired to know how much of an improvement such a design would make over the current hemispherical design with the vacuum gap. A 3D model of the double pyramid design was built in the COMSOL design environment and a range of simulations were performed in order to investigate the efficiency of the absorber sheet within this structure. Various absorber sizes were modelled across the large frequency ranges corresponding to the operational range of the SAFARI S-Band. A screen shot of the COMSOL model is shown in Figure 5.47 where the dimensions of the cavity structure are defined. These dimensions give rise to the $\approx 71^\circ$ angle that would result from appropriate anisotropic etching.

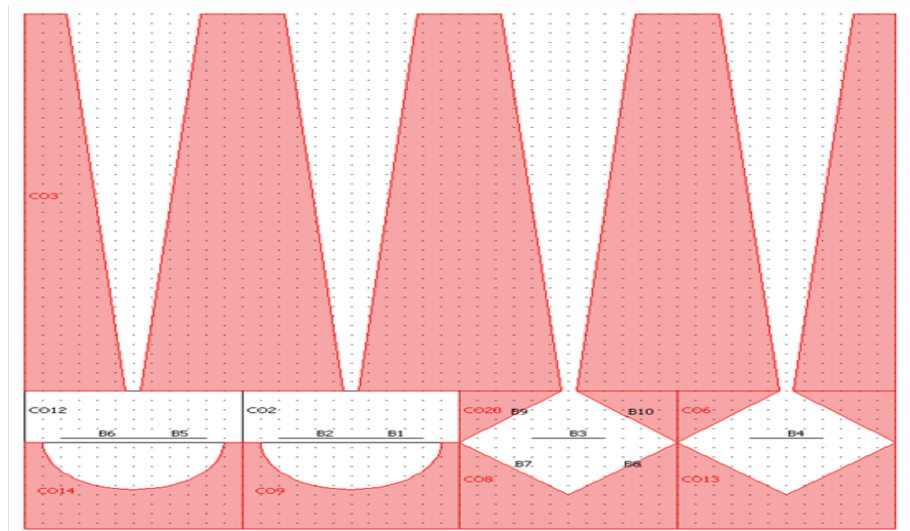


Figure 5.46: Comparison of an open hemisphere cavity and a closed double-pyramid cavity. This CAD drawing clearly shows the vacuum gap in the hemisphere design and how it would be removed in the double pyramid design.

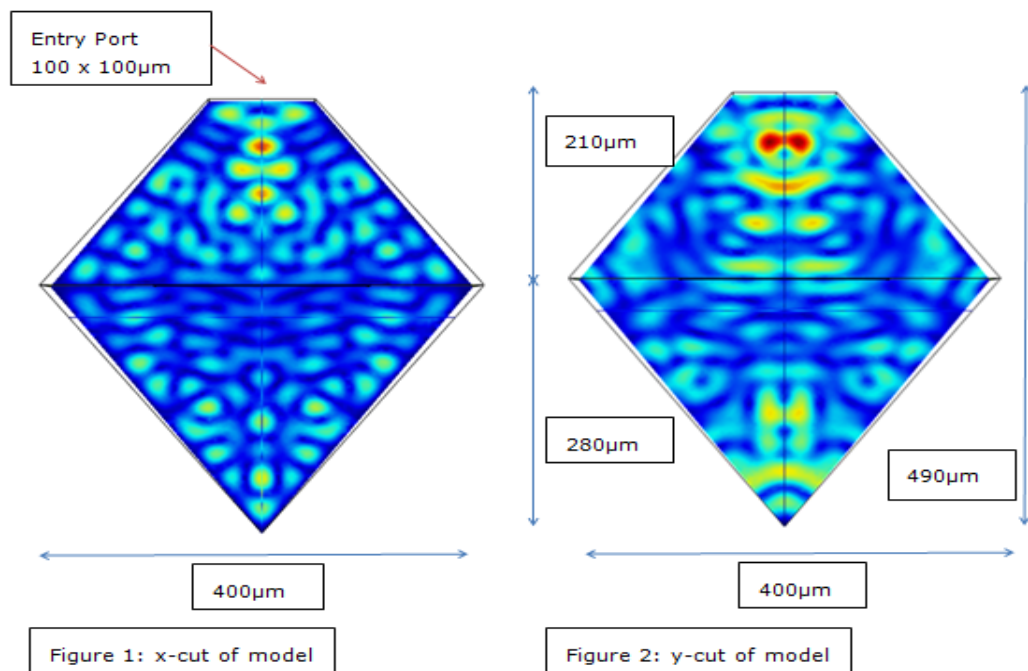


Figure 5.47: Screen shot of pyramidal cavity model showing the dimensions of the structure.

5.5.1 Single Mode Analysis

As a first step the new S-Band cavity design was simulated using only the TE_{10} mode as an input via a square waveguide section with a length of $200\mu\text{m}$ and with the same transverse dimensions as the cavity entrance, i.e. $100 \times 100\mu\text{m}$. Five different absorber sizes were modelled, ranging from $50 \times 50\mu\text{m}$ to $250 \times 250\mu\text{m}$, with the absorber positioned in the centre of the cavity in each case. The fraction

of power absorbed as a function of frequency is shown for three of the absorber sizes in Figure 5.48(a), and the average power across the band is shown in 5.48(b) where it can be seen that there are two values for each absorber size. The blue points represent the average efficiency across a range of 1.8THz (the cut-on frequency of the square waveguide feed) to 10THz. The green points then correspond to the average efficiency across the operational range of the SAFARI S-Band (4.3 - 10THz).

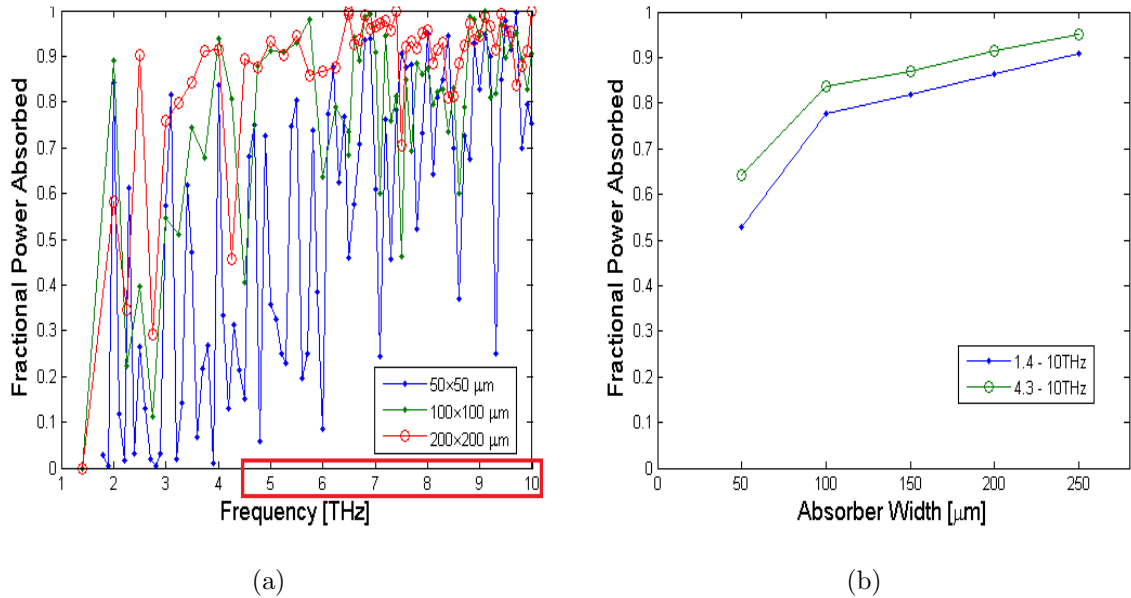


Figure 5.48: Efficiency of the SAFARI S-Band resistive sheet absorber fed by a single mode (TE_{10}) for various absorber sizes. (a): The efficiency of a resistive sheet absorber, for a frequency range of 1.5 to 10THz, for three different absorber sizes. The actual frequency range of SAFARI is indicated by the red box on the x -axis. (b): The average efficiency across the band for five different absorber sizes.

It is clear that the removal of the vacuum gap from the design has a significant impact on the amount of power that couples to the absorber. Also, for an absorber size above $100 \times 100 \mu\text{m}$ there appears to be roughly a linear relationship between absorber area and average power absorbed, while reducing the absorber sheet size to $50 \times 50 \mu\text{m}$ results in a significant reduction in absorbed power. Figure 5.49 then shows the efficiency profile for just two absorber sizes across the SAFARI S-Band range where the frequency dependent behaviour of the absorbers is a bit clearer in this expanded, less cluttered plot.

5.5.2 Analysis of Higher Order Modes

Having found that the resistive sheet absorber behaves well inside the double pyramid cavity when fed by the fundamental TE_{10} mode, the system was then inves-

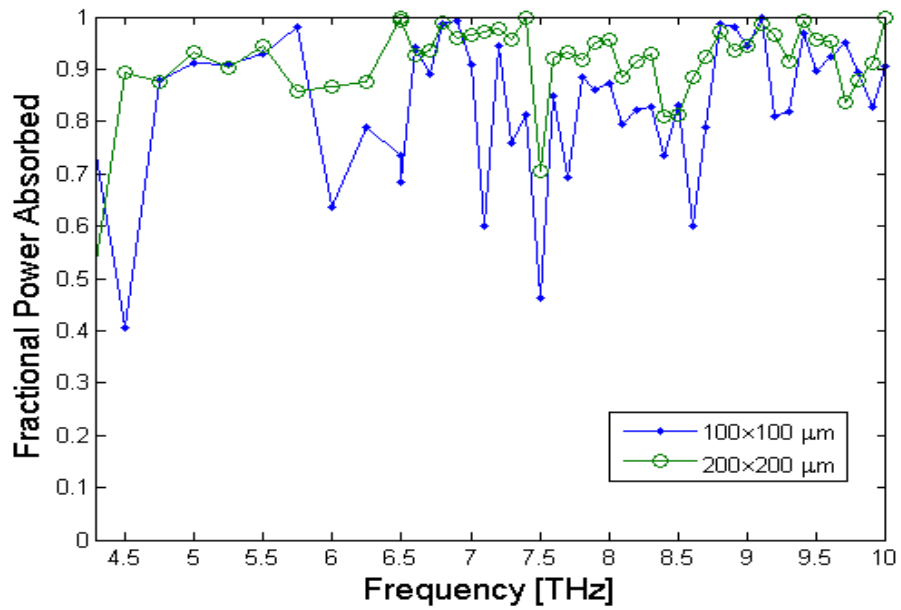


Figure 5.49: Efficiency of the SAFARI S-Band resistive sheet for two different absorber sizes. The behaviour across the frequency range of the SAFARI S-Band (red box in Figure 5.48) is clearer in this graph.

tigated for excitation by the higher order modes that the waveguide feed could support. Average efficiencies for each mode were calculated for an absorber size of $100 \times 100 \mu\text{m}$ across two frequency bands; the first corresponding to the full frequency range of the SAFARI S-Band instrument, and the second range that accounted for the cut-off frequency of each propagating mode. In the second instance the average efficiency was calculated over the range from the switch-on frequency for the particular mode to the high end of the S-Band (10THz), and in this way the evanescent behaviour of the higher order modes at the lower frequencies could be accounted for. In fact this highlights an important question regarding multi-moded systems such as SAFARI, where the efficiency can be ill-defined, and for this reason the band average efficiency was calculated in the two ways just described.

As can be seen in Figure 5.50(b) and Table 5.2 the efficiency of the relatively small $100 \times 100 \mu\text{m}$ absorber in the double pyramid cavity is very reasonable for each higher order mode that the waveguide feed supports. There is of course symmetry in the data with respect to the $m = n$ diagonal of Table 5.2 simply due to the square nature of the waveguide feed which would not be true for a rectangular guide.

TE_{mn}	$n = 0$	$n = 1$	$n = 2$	$n = 3$	$n = 4$	$n = 5$	$n = 6$
$m = 0$	/	0.795	0.653	0.739	0.717	0.850	0.542
$m = 1$	0.795	0.803	0.702	0.753	0.742	0.778	0.651
$m = 2$	0.653	0.702	0.616	0.714	0.666	0.816	0.548
$m = 3$	0.739	0.753	0.714	0.765	0.691	0.777	Cut-Off
$m = 4$	0.717	0.742	0.666	0.691	0.636	0.621	Cut-Off
$m = 5$	0.850	0.778	0.816	0.777	0.621	Cut-Off	Cut-Off
$m = 6$	0.542	0.651	0.548	Cut-Off	Cut-Off	Cut-Off	Cut-Off

Table 5.2: Average absorber efficiencies across the propagation frequency range for higher order modes in a pyramidal cavity. The remaining power is lost as return power back through the waveguide since there is only one port and PEC boundary conditions were in place meaning that no Ohmic heating can take place in the walls.

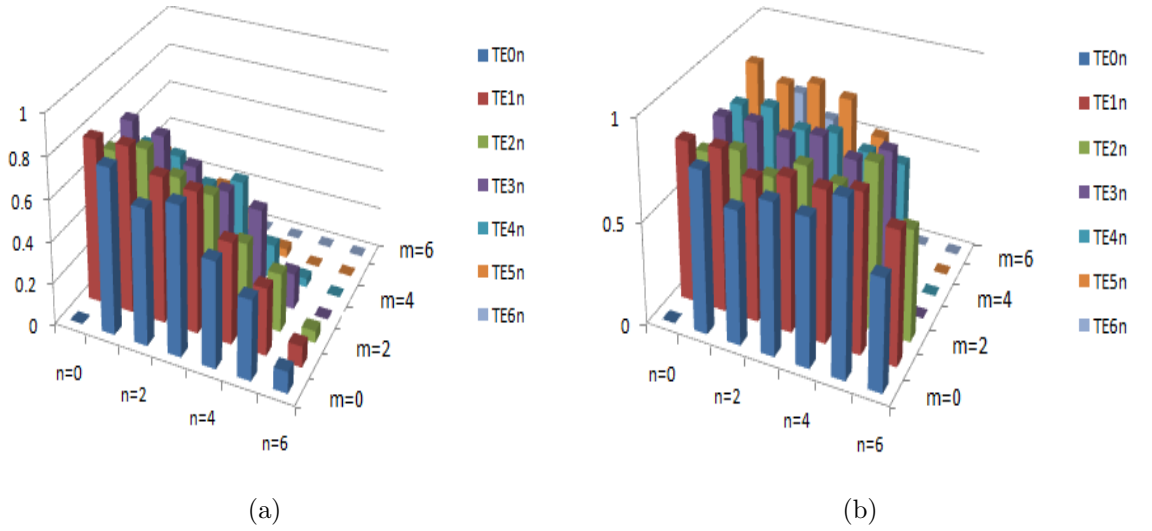


Figure 5.50: Efficiency of the SAFARI S-Band resistive sheet for higher order modes. The size of the absorber chosen was $100 \times 100 \mu\text{m}$. (a): The efficiency of each propagating mode averaged over the entire SAFARI S-Band range (4.3 - 10THz). (b): The efficiency of each propagating mode averaged over a range from the cut-on frequency of each specific mode to 10THz (propagation frequency range).

5.5.3 Experimental Verification

Having found the new S-Band cavity design to be well behaved as predicted by the models, the next step involved designing and building a scaled model of the new SAFARI S-Band pixel for testing at frequencies around 100GHz for verification of the simulation approach. Experimental tests also serve to validate the modelling approaches used for the SAFARI L-Band analysis presented in section 5.4 of this chapter. The system used for the measurements was based on the VNA.

As already indicated in section 1.4 of chapter 1, the VNA system at N.U.I.

Maynooth has a frequency range of 75 - 110 GHz, and a dynamic range that depends on the care taken with the calibration procedure, but with 70dB achievable. The benefits of performing tests at these scaled frequencies is that there is little atmospheric absorption of signal due to the atmospheric window around 100GHz, and of course any thermal emission at these frequencies is greatly dominated by the strength of the VNA signal, thus there is no need for vacuum systems or cryogenic facilities. However, as a precaution, the temperature of the VNA laboratory was kept constant to within $\pm 0.5^\circ$. A further benefit of the scaled tests is based on the dimensions of the scaled cavity and feed structures. Their sizes are clearly larger at longer wavelengths meaning that standard machining processes can be employed for their construction if care is taken and precision is maximised. Also, since the ability of the thin deposit of Ta to absorb radiation is not frequency dependent it was believed that the scaled measurements would provide valid data.

The disadvantage of this approach is that the results on the absorption of power are not obtained by measuring the absorbed power directly. Rather, by measuring the S_{11} parameter (return signal) of a one port VNA set-up, the efficiency of the absorber is deduced. Essentially, any of the input power that is not observed to return is assumed to have been absorbed by the Ta absorber. The Ta absorbers used in the real SAFARI pixel will of course be coupled to ultra-sensitive TES's, which themselves will be coupled to superconducting quantum interference devices (SQUIDs) for amplification, resulting in direct detection of the incoming signal.

Figure 5.51 shows a cut through the CAD design, and a photograph of the scaled cavity that was designed by the author and then built by Mr. David Watson in the departmental workshop at NUIM. The pieces of Ta absorber material shown in Figure 5.52 were provided by the SRON. Each absorber consists of a layer of Ta ($\approx 6nm$) deposited on a 0.25mm thick sapphire substrate. It was possible to sandwich the largest absorber square between the top and bottom parts of the cavity in order to fix it in position. The smaller pieces of Ta had to be mounted in the cavity using fine thread as supporting legs, as shown in Figure 5.52.

Figure 5.53(a) shows the initial results for three different absorber sizes in the cavity, together with a FEM simulation of the 5.0×5.0 mm absorber. Figure 5.53(b) shows the results of two measurements that were performed to investigate if the thread had an effect in terms of absorbing power. Placing thread cross-hairs in the

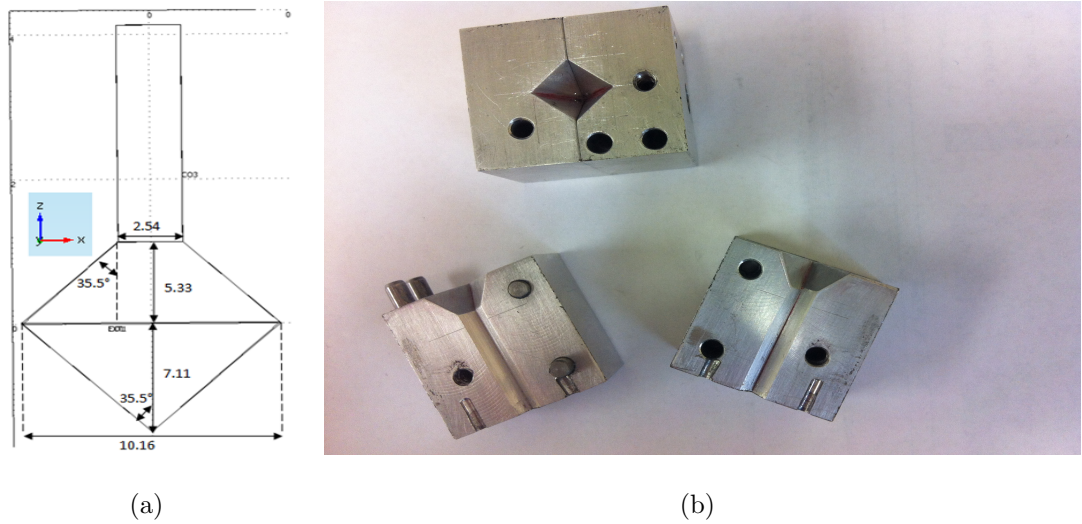


Figure 5.51: The scaled pyramidal SAFFARI S-Band cavity that was designed and built at NUIM. (a): A cut through the CAD design. (b): Some photographs showing how it was manufactured in separate pieces.

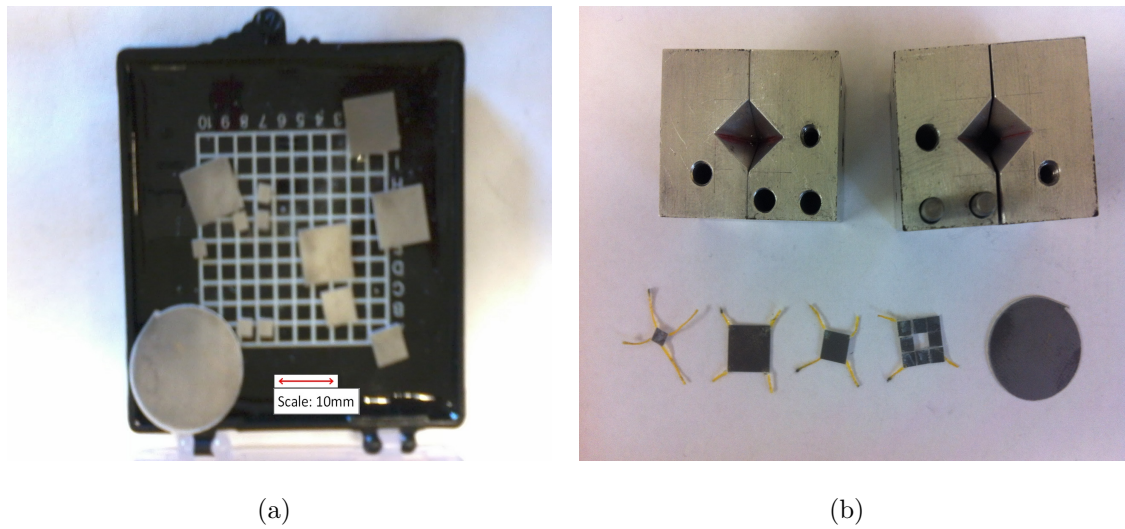


Figure 5.52: Pieces of Ta absorber that were provided by SRON for the scaled VNA measurements at NUIM. (a): The absorber pieces with a scale bar. (b): The absorber pieces showing the thread that was attached to the absorbers for mounting in the cavity.

cavity results in an almost identical profile to an empty cavity as can be seen from the comparison plots.

Although the data in Figure 5.53(b) indicates that the thread has no significant effect on the amount of power absorbed in the cavity, it is clear that the empty cavity is causing significant losses as can be seen from the apparent absorbed power. One would expect to observe almost 100% return power from an empty cavity since the structure is closed apart from the excitation/detection port. The reason for the low return power is thought to be due to the excitation of higher order modes, caused by the shape of the cavity. Only the TE_{01} mode is excited in the input WR-

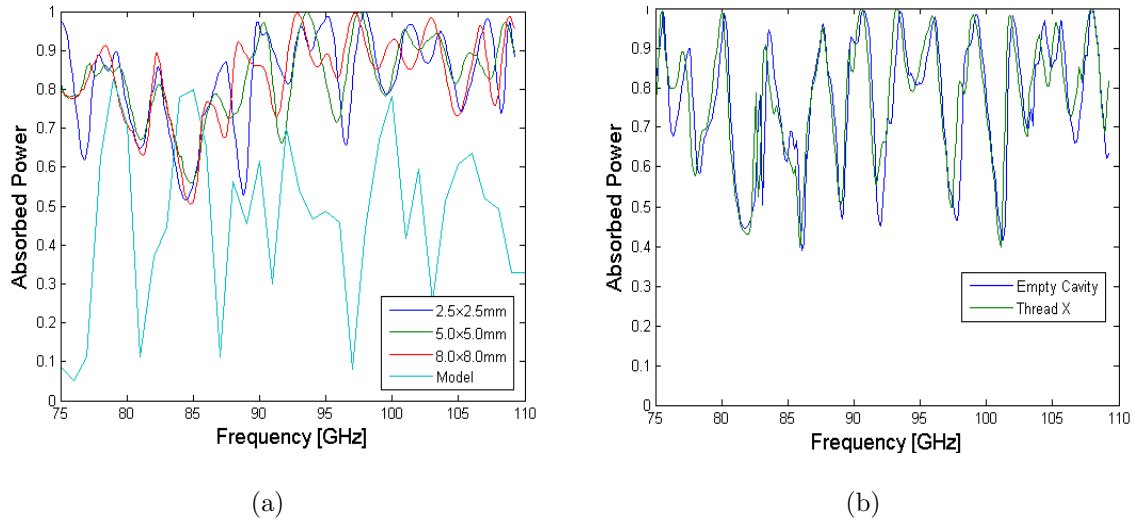


Figure 5.53: Measured efficiency of square Ta absorbers in a double pyramid cavity, and empty cavity excitation. (a): Measured power absorbed for three different absorber sizes. The model results are for a 5.0×5.0 mm absorber. (b): Excitation of empty cavity with and without thread cross-hairs.

10 waveguide, however the break in symmetry inevitably causes power to scatter into higher order modes inside the cavity. The higher order modes cannot return back through the WR-10 guide as the dimensions of the guide give rise to a cut-off frequency of 118GHz for even the first higher order mode (TE_{02}). Since the analysis is being performed for a frequency range of 75 to 110 GHz even the highest operational frequencies cannot propagate back through the guide in the form of higher modes. The multiple reflections from the walls of the cavity for these modes cause them to be absorbed.

The COMSOL model was based on PEC cavity boundaries, meaning that no power could be absorbed by the walls, and an empty cavity returned 100% of the power, as expected. The simulations were performed again, with the PEC cavity walls replaced with boundaries having the properties of aluminium. The difference in the return power with the more realistic boundary conditions was negligible, meaning that the absorption of power observed in the measurement cavity must be due to some other parameter, most likely the surface finish on the cavity walls.

An attempt was made to correct for the cavity losses by using the empty cavity data to rescale the absorber results. It was somewhat successful, although there is still significant disagreement between the simulations and the measured data. The reason for this is due to how the absorber itself affects the behaviour of the fields inside the cavity. The cavity losses in an empty cavity will not be the same as the cavity losses when an absorber is present, since a significant amount of the signal

will be absorbed on its first pass through the Ta sheet. The higher order modes are now preferably absorbed by the Ta absorber rather than the cavity walls. Thus subtracting the losses observed in the empty cavity from the absorber measurements is not an accurate approach.

Figures 5.54(a), 5.54(b) and 5.55(a) show the results for the apparent efficiency of three different sized square Ta absorbers compared to corresponding FEM simulations for each absorber size. As can be seen in each case, the amount of power absorbed in the measured data is significantly higher than that predicted by the simulations. Figures 5.55(b), 5.56(a) and 5.56(b) show the corrected results, again compared to the FEM simulations. In this case a scaled version of the bare cavity data was used to flatten the results, where the scaling factor used was 0.45, which gave rise to the best observed fit.

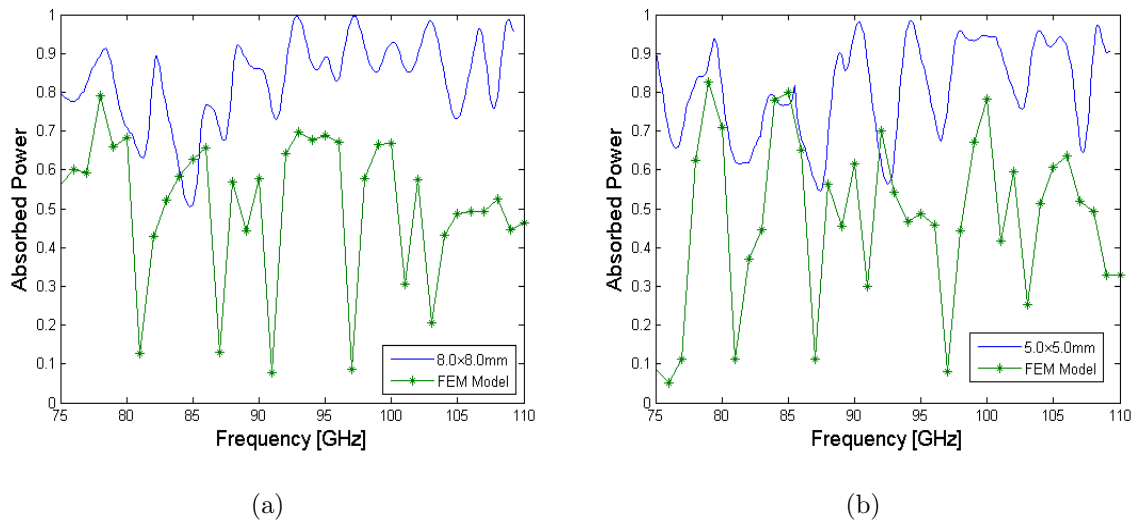


Figure 5.54: Efficiency of square Ta absorbers in a double pyramid cavity. (a): Fractional power absorbed for a large absorber ($8.0 \times 8.0\text{mm}$) filling the cavity cross section. (b): Fractional power absorbed for a medium sized absorber ($5.0 \times 5.0\text{mm}$) partially filling the cavity.

Since the shape of the pyramidal cavity was thought to be the cause of the disagreement between simulation results and those of the particular single mode measurement approach used, another set of absorber measurements were carried out using a more symmetric cavity. A cylindrical cavity that was designed and built previously by the THz Optics Group at NUIM was used, as it was believed that this particular cavity would give rise to fewer higher order modes being generated, and hence physical conditions that are more accurately suited to using the return power as an indicator of power absorbed by the Ta sheet. The cylindrical cavity is shown in Figure 5.57. A variety of similar rings as those shown in Figure 5.57(a) can be

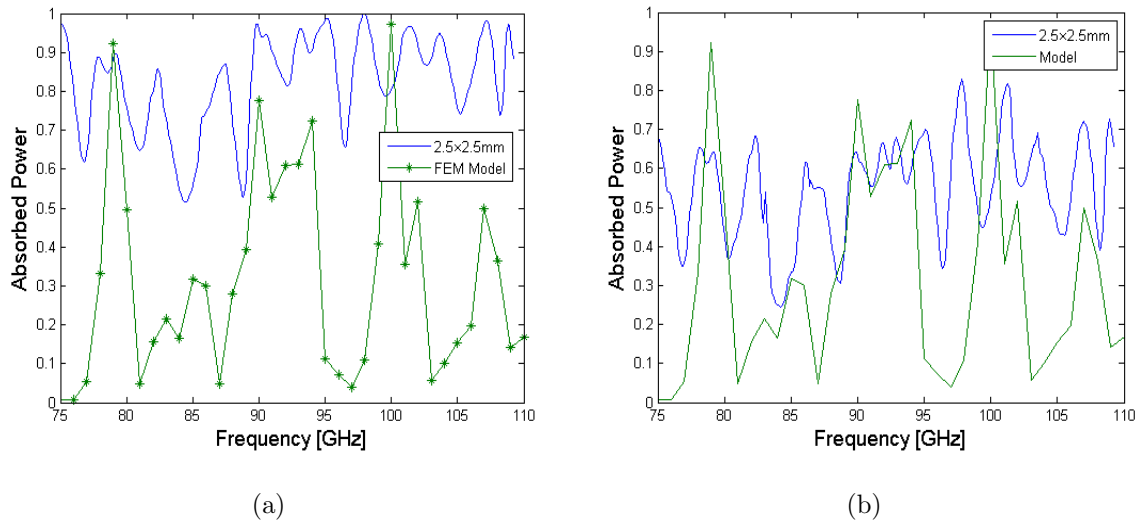


Figure 5.55: Efficiency of a small square Ta absorber in a double pyramid cavity. (a): Fractional power absorbed for a small absorber ($2.5 \times 2.5\text{mm}$) partially filling the cavity cross section. (b): Fractional power absorbed for a small absorber ($2.5 \times 2.5\text{mm}$) corrected with data from an empty cavity measurement.

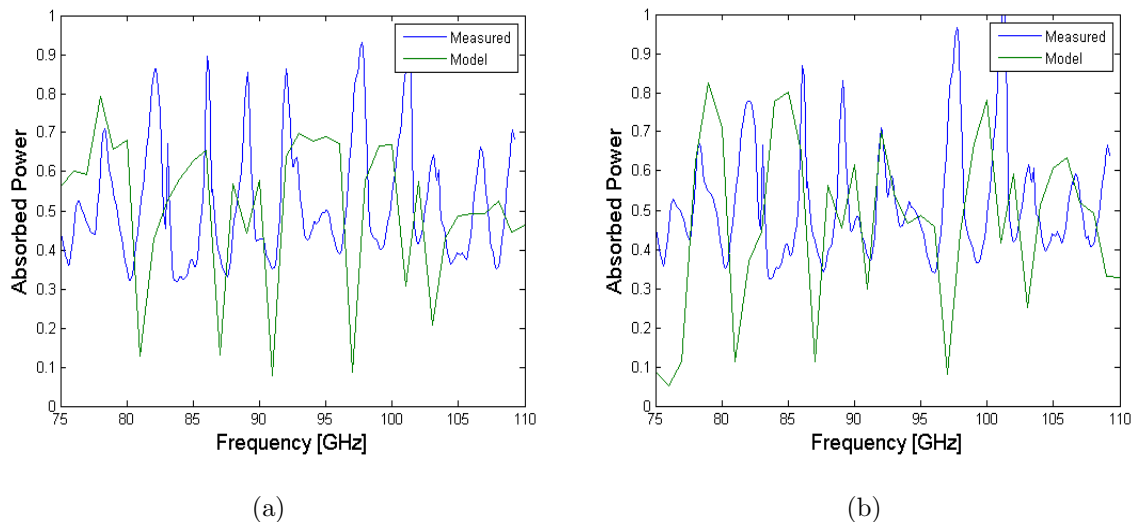


Figure 5.56: Normalised efficiency of square Ta absorbers in a double pyramid cavity normalised with data from an empty cavity measurement. (a): Fractional power absorbed for a large absorber ($8.0 \times 8.0\text{mm}$) filling the cavity cross section. (b): Fractional power absorbed for a medium sized absorber ($5.0 \times 5.0\text{mm}$) partially filling the cavity.

used to construct cylindrical cavities of a variety of depths and radii. The rings are held in place in the holding tube also visible in the top left of Figure 5.57(a). The absorber pieces can then be held in place by sandwiching the thread between two of the rings as shown in Figure 5.57(b), where the carpet absorber [Crownover, 1995] is shown mounted above a ring.

The dimensions of the particular cavity assembly that was used is illustrated in Figure 5.58(a), and a screen shot of the COMSOL FEM model is shown in Figure 5.58(b) indicating the symmetry conditions used in order to reduce the problem size. Figure 5.59 then shows the model following the meshing procedure, and finally the



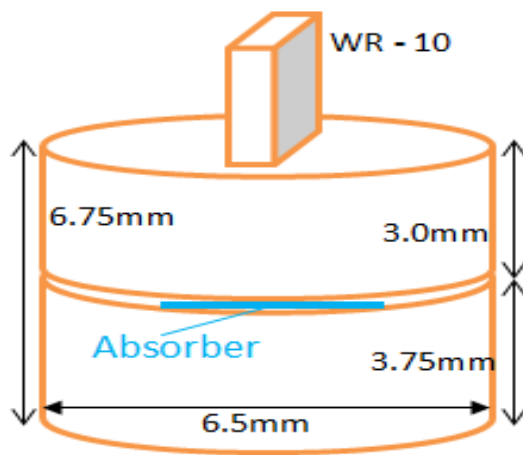
(a)



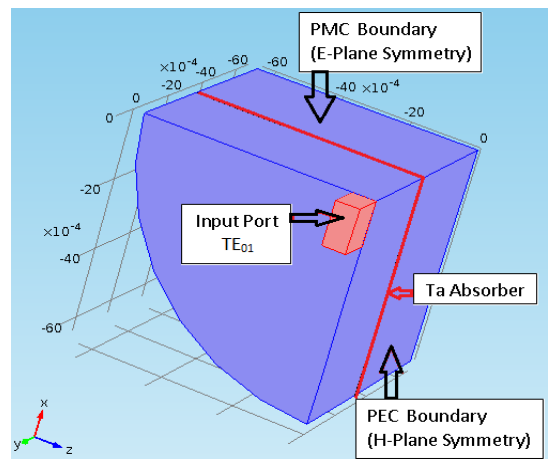
(b)

Figure 5.57: Photographs of the cylindrical cavity used for the VNA absorber measurements. (a): The cavity, rings, and front face showing the WR-10 waveguide input and screw holes for attachment. (b): The carpet absorber mounted above one of the rings.

electric field magnitude through the structure. Figure 5.59(c) shows a comparison between the apparent power absorbed by the empty pyramidal cavity and the empty cylindrical cavity. It is clear that there are significantly lower losses in the cylindrical cavity compared to the double pyramid cavity, although the levels are still relatively high.



(a)



(b)

Figure 5.58: Schematic and screen-shot of the COMSOL FEM model of the cylindrical cavity and absorber set-up. (a): Schematic showing dimensions of cavity and waveguide feed structures. (b): The geometry of the model showing the E-plane and H-plane symmetry conditions that were employed.

The results of the absorber measurements in the cylindrical cavity are shown in Figures 5.60 and 5.61, where Figure 5.60(a) shows the results of a circular absorber completely filling the cavity cross section, and as can be seen there is a much higher

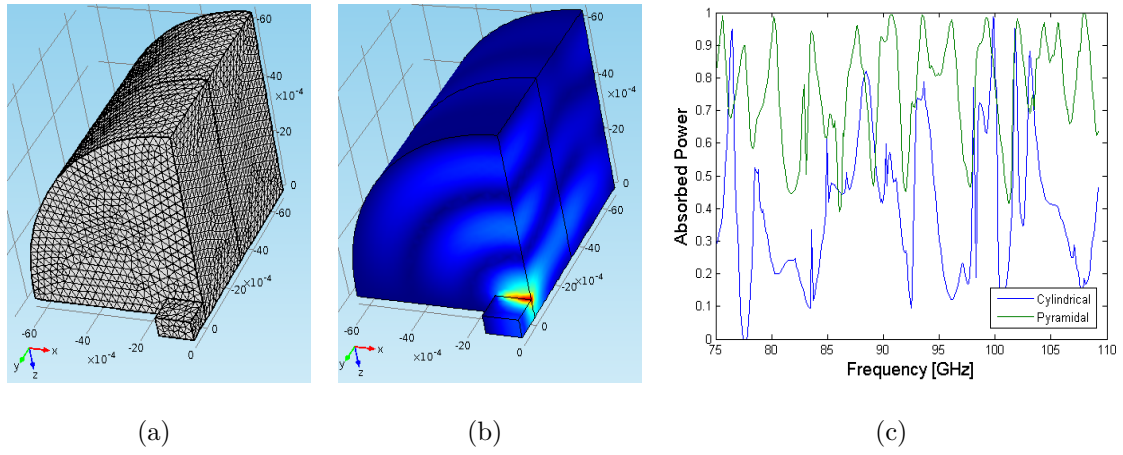


Figure 5.59: Screen-shot of the meshed model and the electric field from the cylindrical cavity and absorber FEM model. (a): The model geometry following meshing, and (b): The electric field. (c): A comparison between the apparent power absorbed by the empty pyramidal cavity and the empty cylindrical cavity.

level of agreement between measurement and model. Figures 5.60(b), 5.61(a), and 5.61(b) show the results of the 8.0×8.0 , 5.0×5.0 , and 2.5×2.5 absorbers, respectively, in the cylindrical cavity. Again, although there is some disagreement between measurement and model, the agreement is significantly better than for the pyramidal cavity, as predicted.

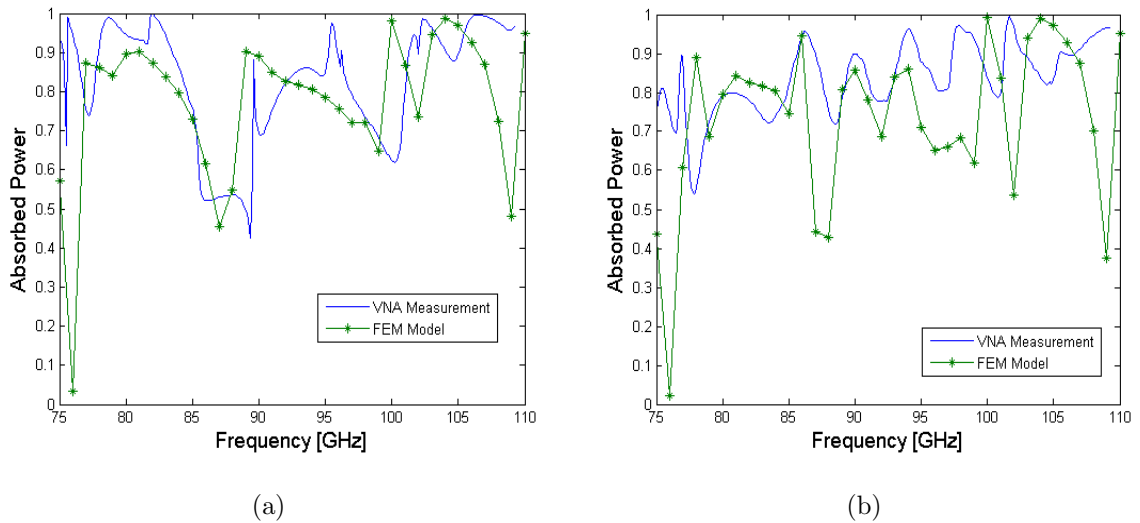


Figure 5.60: Efficiency of square Ta absorbers in a cylindrical cavity. (a): Fractional power absorbed for a large circular absorber filling the cavity cross section. (b): Fractional power absorbed for a large square absorber (8.0×8.0 mm) partially filling the cavity.

The carpet absorber, where a central square (2.66×2.66 mm) was removed from the 8.0×8.0 mm Ta square in its construction, was tested and compared to the efficiency of the solid 8.0×8.0 mm Ta square. The reasons for wanting to remove some of the absorber volume were discussed in section 5.4.3 of this chapter. Figure 5.62(a) shows the measurement results, with the corresponding FEM simulation

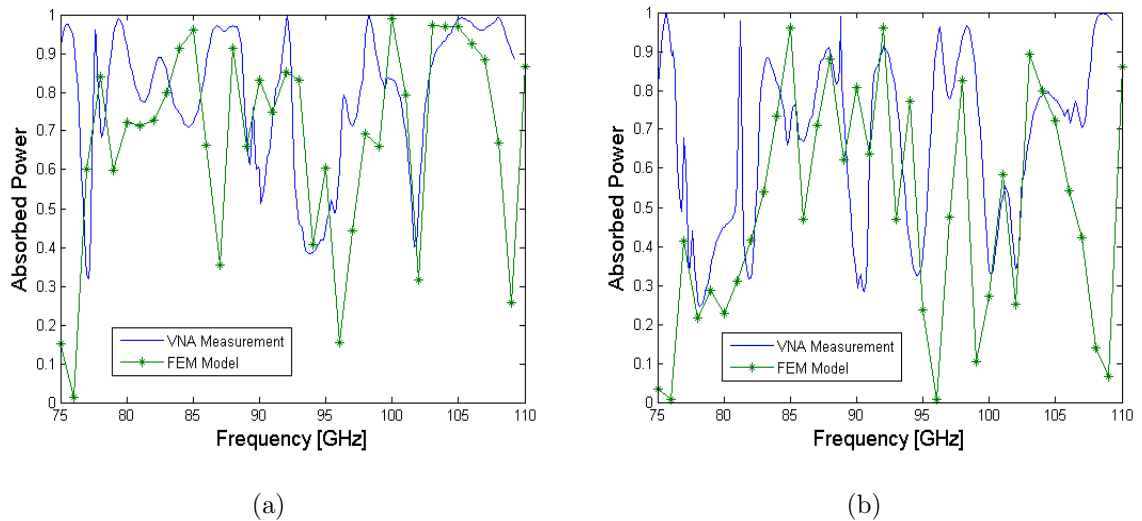


Figure 5.61: Efficiency of square Ta absorbers in a cylindrical cavity. (a): Fractional power absorbed for a medium square absorber ($5.0 \times 5.0\text{mm}$) partially filling the cavity. (b): Fractional power absorbed for a small square absorber ($2.5 \times 2.5\text{mm}$) partially filling the cavity.

results also shown, and the measurement results for the solid absorber are shown again for comparison. It is clear that removing some of the absorber material in this manner has very little effect in terms of reducing the efficiency of the absorber. This was also found in the simulations presented in section 5.4.3 of this chapter.

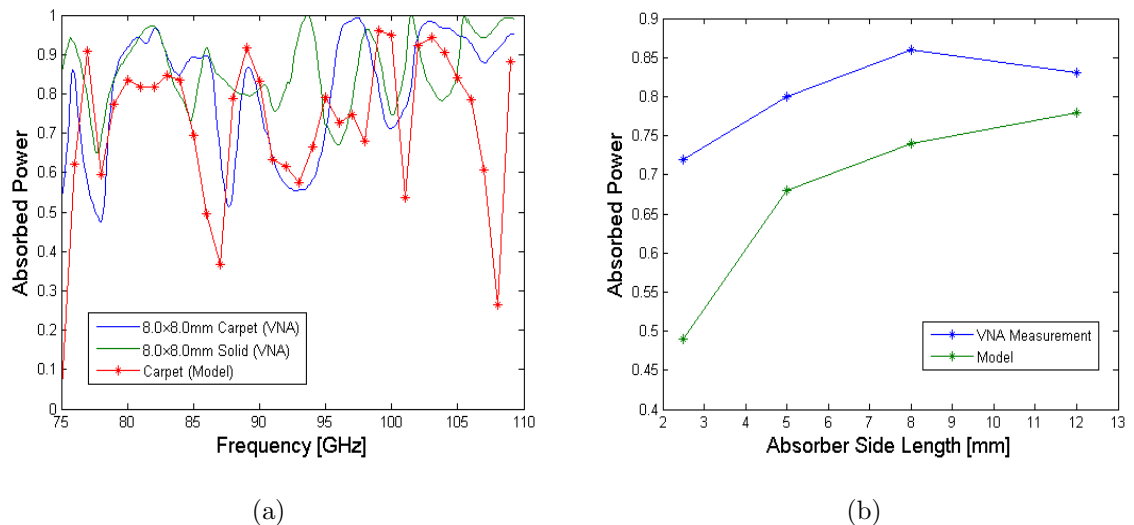


Figure 5.62: (a): Efficiency of a large square carpet absorber in a cylindrical cavity, where the carpet has dimensions of $8.0 \times 8.0\text{mm}$ with the central square ($2.66 \times 2.66\text{mm}$) removed. (b): Average power absorbed across the band as a function of absorber size.

Figure 5.62(a) then shows the average power absorbed across the frequency band plotted against increasing absorber size. As is expected the average absorbed power typically increases with absorber size, with the VNA measurements again showing a higher level of apparent absorption, indicating other losses as already

discussed above. Interestingly the largest absorber, which was the circular piece filling the cavity cross section ($\approx 12\text{mm}$ in diameter) shows a reduction in measured absorption compared to the smaller $8.0 \times 8.0\text{mm}$. This also brings the result into closer agreement with the model than for the other absorber sizes. This is further evidence that it is the break in symmetry that is causing the cavity losses, since the largest absorber clearly has the same symmetry as the cylindrical cavity, whereas the square absorber pieces of course differ from the symmetry of the cavity. Thus, power losses in the walls of the cavity dominate when multiple reflections occur, whereas the losses occur in the absorber when it is placed in the cavity.

5.6 Conclusions

It was shown in this chapter that in order to fully model a complete SAFARI L-Band or S-Band pixel, multiple simulation methods are currently required. The progress being made by the THz Optics Group at N.U.I. Maynooth in terms of developing an integrated mode matching software was discussed. Such an integrated program should be able to account for the conducting waveguide structures of the pixel, the resistive sheet absorber housed in an integrating cavity, and any vacuum gaps within the pixel. The extension of the Cylindrical SCATTER mode matching code to include a resistive sheet absorber in the models was shown to agree well with the conventional FEM simulation approach. The extended SCATTER code was also shown to be up to three orders of magnitude faster than FEM simulations.

The particular shape of the integrating cavity backshort in a far-IR pixel was shown to be very important in terms of detector efficiency. Using the extended SCATTER code, a cavity backshort with a sine profile was demonstrated as being a good improvement compared to the conventional hemisphere design. The efficiency of the SAFARI L-Band pixel was then shown to increase significantly when the hemisphere backshort was replaced with the sine profiled backshort. A reduction in power leakage through the vacuum gap was also observed with the new L-Band design, and thus potential cavity cross-talk was reduced.

A new design for the SAFARI S-Band was shown to be a significant improvement over the current design. As was discussed in section 5.5, the primary cause of the increased pixel efficiency was the removal of the cavity-to-cavity vacuum gap

from the design.

Finally, it was shown that it is possible to use a scaled measurement system to verify the results of the simulations of cavity mounted Ta absorbers, although there are restrictions in terms of using structures that do lead to too much power being scattered into higher order propagating modes. Choosing a structure with high symmetry and smoothly varying boundaries, such as a cylindrical cavity, was shown to produce results that are in reasonable agreement with those from the FEM modelling approach. The FEM results in turn were shown to agree well with the more efficient mode matching approach in section 5.2.4 of this chapter.

Chapter 6

Summary and Conclusions

The primary aim of this thesis was to demonstrate that it is possible to model and characterise the full structure of a SAFARI-like pixel comprising the over-moded input feed, the absorbing resistive sheet, and the multi-moded cavity backshort, using a single computer with moderate processing power. This was achieved by employing multiple simulation techniques, combining the commercially available packages such as COMSOL for FEM analysis with novel mode matching code. Use was made of the available in-house mode matching code SCATTER, and further mode matching code was developed by the author for increased efficiency for specific horn geometries.

The work of this thesis was primarily driven by two technical research programs (TRPs). The first was a TES TRP funded by ESA, and led by SRON, with involvement from Cambridge University and RAL in the UK, Cardiff University in Wales, and NUIM in the Republic of Ireland [TRP AO/1-5922/08/NL/EM, 2011]. The TES TRP was a research program contract to investigate transition edge superconducting bolometers toward development of detectors for the SAFARI instrument for SPICA with sensitivities approaching $1 \times 10^{-19} \text{ W}/\sqrt{\text{Hz}}$. The TRP was from 2010 until 2012 and the author contributed to characterising optical cross-talk (horn-to-horn) between SAFARI horns as required by the contract, and as presented in chapter 3 of this thesis. Other work that was carried out by the author as required by the TES TRP contract involved characterising cavity cross-talk between SAFARI pixels, and determining the optical efficiency of the Ta absorbers suggested for SAFARI-like detectors. Although the TES TRP has now officially ended (as of January 2012), a strong collaboration still exists between the research institutes in the Netherlands, the UK, and Ireland, and work continues on the TES detector technology toward the SAFARI instrument.

The second TRP that the author was involved in was an Irish AO (Announcement of Opportunity) and was again funded by ESA (Strategic Initiative by ESA for Ireland) [RFQ 3-6418/11/NL/CBi]. This TRP was specifically aimed at the development of new technology horn antennas for CMB and far-IR astronomy, with the goal of producing a profiled smooth walled horn antenna consisting of multiple straight smooth walled conic sections that could match the beam control of simi-

lar corrugated structures. Producing such a horn antenna design required the use of optimisation routines such as genetic algorithms, which must cycle through the simulation code many hundreds or even thousands of times, to iteratively converge on an optimum design solution [McCarthy *et al.*, 2013]. As part of this work the author developed and tested a new conical mode matching code in spherical coordinates that reduced the number of calculations required for each simulation loop by up to two orders of magnitude. This work is presented in chapter 4 with a description of the new code given and the results of some examples shown. The Irish AO contract also involved continued work on detector development with SRON for SPICA/SAFARI, including an extended visit by the author to SRON, Groningen from June to August of 2013. The measurement work carried out by the author while at SRON is reported on in chapter 3 of this thesis, and it involves the characterisation of the multi-mode behaviour of SAFARI-like horns at THz frequencies. Other modelling work performed by the author during the SRON visit is discussed in chapter 5. This work involved the design and multi-mode analysis of a new twin pyramid cavity for the highest frequency SAFARI band (SAFARI S-Band). Upon returning to Ireland, the author then designed a scaled model of the new S-Band cavity for testing at frequencies around 100GHz with NUIM's in-house VNA apparatus. The scaled cavity was built by Mr. David Watson of the Experimental Physics Department of NUIM, and samples of Ta absorber material were provided for the tests by SRON, Groningen.

The majority of the work in this thesis was carried out by the author. Anywhere others were involved is clearly indicated, and credit is given as such. The two-port VNA set-up described in section 1.4 was already in place (see [Yurchenko *et al.*, 2014], for example), and the precise alignment procedures that were used in preparation for horn antenna far-field beam pattern measurements described in section 3.1.10 were developed by Dr. Marcin Graziel and Mr. Niall Tynan, B.Sc., both of the department of experimental physics at NUIM. Assistance was provided by Mr. Niall Tynan, B.Sc. and Miss Niamh Tobin, B.Sc., in performing the cavity and absorber measurements described in section 5.5.3. Dr. Stephen Doherty provided assistance with the use of the SCATTER absorber code that was used for analysis presented in chapter 5, and with the use of the Rectangular SCATTER code that is discussed in section 3.2.1. Parts of the Spherical SCATTER mode matching code

developed by the author used the established Cylindrical SCATTER as heritage [Murphy *et al.*, 2010].

The series of horn throughput measurements that were carried out at SRON, and described in section 3.3, were carried out under the supervision of Dr. Gert de Lange, and large assistance was provided by Dr. Damien Audley and Mr. Willem Jan Vreeling, B.Sc. The measurement system used at SRON was already in place, and the work carried out by the author built on previous research by Mr. Chris de Jong, B.Sc., and Dr. Manisha Ranjan. The design concept for the SAFARI S-Band cavity, and the corresponding FEM simulations, discussed in section 5.5, were the result of collaborative work by the author, Dr. Gert de Lange, and Dr. Damien Audley.

In chapter 3 it was shown that the far-field beam patterns of the current SAFARI horn design can be efficiently calculated using the Pyramidal SCATTER mode matching code [Doherty, 2012], since the electrically large size of the rectangular SAFARI horns leads to a FEM model that is very large computationally. However, the characterisation of horn-to-horn optical crosstalk required the use of the FEM simulation approach, since the current mode matching code does not allow for analysis in the near-field, nor for horn-to-horn interactions. It was shown that while the level of crosstalk in the E-plane of two neighbouring horns can be orders of magnitude larger than that in the H-plane, the predicted levels of crosstalk in the SAFARI array are sufficiently low as to not overwhelm the detectors. The FEM simulation approach for crosstalk analysis was verified using experimental measurements carried out using a two-port VNA system.

It was demonstrated that the frequency dependent throughput of SAFARI-like feed horns can be characterised using an FTS, provided care is taken with proper calibration of the data. It was shown that the propagating modes can be observed to switch-on in a step-like manner, as predicted by the geometrical analysis of the switch-on frequencies of the rectangular waveguide section in the back-to-back horn configuration. Further work is required in terms of refining the measurement technique, as described in section 3.3.7.

Chapter 4 focussed on the theory of conical waveguide modes, and by developing the new mode matching code Spherical SCATTER it was shown how new technology smooth walled conic section horn antennas can be modelled in an al-

ternative manner to the approximate cylindrical mode matching approach, where the number of power scattering integrals required to be performed can be reduced by up to two orders of magnitude. To date, however, analytical solutions to the scattering integrals have not been found in the literature or independently, leading to long calculation times due to numerical integrals. Thus, the Spherical SCATTER code is currently less efficient than the Cylindrical SCATTER approach. The theory for the new code was verified by comparing the results of a test horn modelled with both Spherical SCATTER and the established SCATTER for cylindrical geometries. Good agreement was demonstrated between the two approaches, and similar good agreement was shown for a FEM model of the same horn.

Finally, in chapter 5, new designs for far-IR cavity backshorts were investigated, with the aim of improving the SAFARI detector cavity design. By using a combination of FEM and mode matching analyses the efficiency of the Ta absorbers for both the SAFARI L-band and S-Band were predicted. It was shown that the particular shape of the cavity backshort can have a significant effect on the amount of power absorbed by the Ta sheet when housed in the cavity. The amount of power lost through the vacuum gap between the horn array block and the detector array chip was shown to be significant if the gap is too large, resulting in up to 65% loss of signal for some frequencies of the L-Band. Again, the shape of the cavity was shown to affect this parameter, with a sine profiled backshort providing a significant reduction of this loss. Removal of the vacuum gap with a new cavity design was shown to provide an improvement in the fraction of the signal absorber by the Ta sheet, and of course removal of any free-space-gap losses, and thus elimination of any cavity-to-cavity crosstalk. The simulation techniques were then verified through experimental measurements using a one-port VNA set-up and small absorber pieces mounted in conducting cavities. The measurement technique that was employed, where analysis of the return power (S_{11}) was used to infer the amount of power absorbed by the Ta sheet, was shown to work only in special conditions. As was discussed in section 5.6 care must be taken in choosing the profile of the cavity structure to be used. The S_{11} parameter will only inform on the amount of power returned in the fundamental TE_{01} mode, and therefore any power that is scattered into higher order cavity modes will appear to have been completely absorbed by the Ta, and hence lead to inaccurate inference of absorber efficiency.

A list of publications and conference proceedings related to the work presented in this thesis, and contributed to by the author, can be found below. It is envisaged that further papers relating to work presented in this thesis will be submitted for publication in appropriate academic journals, following submission of this thesis for examination.

Publications

[Audley *et al.*, 2013] M. Audley, G. de Lange, and C. Bracken, *Detector and Calibration-source Models for the SAFARI Detector Test Facility*, COMSOL Conference Proceedings, WTC Rotterdam, the Netherlands, October 23-25, 2013.

[McCarthy *et al.*, 2013] D. McCarthy, N. Trappe, J.A. Murphy, C. Bracken, S. Doherty, M.L. Gradziel, and C. O’Sullivan, *Efficient Horn Antennas for Next-Generation THz and Millimeter-Wave Space Telescopes*, Proc. SPIE 8624, Terahertz, RF, Millimeter, and Submillimeter-Wave Technology and Applications VI, 862413. doi:10.1117/12.2001268. March 27, 2013.

[Murphy *et al.*, 2012] J.A. Murphy, S. Doherty, N. Trappe, C. Bracken, T. Peacocke, and C. O’Sullivan, *New Developments in Waveguide Mode-Matching Techniques for Far- Infrared Astronomy*, Proc. SPIE 8261, Terahertz Technology and Applications V, 82610F. doi:10.1117/12.908068. February 9, 2012.

[Murphy *et al.*, 2011] J.A. Murphy, S. Doherty, N. Trappe, C. Bracken, and C. O’Sullivan, *Efficient Modeling of Detectors for Far-IR Astronomy*, SPIE Newsroom. doi: 10.1117/2.1201112.004039. December 9, 2011.

[Trappe *et al.*, 2012] N. Trappe, C. Bracken, S. Doherty, J. R. Gao, D. Glowacka, D. Goldie, D. Griffin, R. Hijmering, B. Jackson, P. Khosropanah, P. Mauskopf, D. Morozov, J.A. Murphy, C. O’Sullivan, M. Ridder, and S. Withington, *Optical Modeling of Waveguide Coupled TES Detectors Towards the SAFARI Instrument for SPICA*, Proceedings of the SPIE, Vol. 8452, pp. 84520L-84520L-6, 2012.

[Dirkx *et al.*, 2013] D. Dirkx, T. Bocanegra, C. Bracken, *et al.*, *Unveiling the Evolution and Formation of Icy Giants*, EPSC Abstracts, Vol. 8, EPSC2013-745-2, 2013, European Planetary Science Congress. 2013.

[Bracken *et al.*, 2014] C. Bracken, J.A. Murphy, S. Doherty, N.A. Trappe, *Efficient Modeling of Cavity Coupled Detectors for Terahertz Frequencies*, Proceedings of the 24th International Symposium on Space Terahertz Technology, (In press, 2015).

[McCarthy *et al.*, 2014] D. McCarthy, J.A. Murphy, C. O’Sullivan, N. Trappe, M.L. Gradziel, S. Doherty, C. Bracken, N. Tynan, and Arturo Polegre, *Efficient algorithms for optimising the optical performance of profiled smooth walled horns for*

future CMB and Far-IR missions, Proceedings of SPIE 9153, Millimeter, Submillimeter, and Far-Infrared Detectors and Instrumentation for Astronomy VII, 915316, 23 July 2014. doi: 10.1117/12.2056336.

References

- [Abramowitz and Stegun, 1972] M. Abramowitz and I.A. Stegun, *Handbook of Mathematical Functions with Formulas, Graphs, and Mathematical Tables*, New York: Dover Publications, ISBN 978-0-486-61272-0 (1972).
- [Ade *et al.*, 2009] P.A. Ade, R.J. Wy1de, and J.Zhang, *Ultra-Gaussian Horns for CLOVER - a B-Mode CMB Experiment*, Proceedings of the 20th International Symposium on Space Terahertz Technology (ISSTT), April 20-22, 2009, Charlottesville, VA, USA, pp. 128-137.
<http://adsabs.harvard.edu/abs/2009stt..conf..128A>
- [Ade *et al.*, 2013] P.A.R. Ade *et al.*, *Planck 2013 Results. I. Overview of Products and Scientific Results*, Astronomy and Astrophysics manuscript no. PlanckMission2013. March 21, 2013.
http://planck.caltech.edu/pub/2013results/Planck_2013_results_01.pdf
- [Alvi *et al.*, 2008] P. A. Alvi, V. S. Meel, K. Sarita, J. Akhtar, K. M. Lal, A. Azam, and S. A. H. Naqvi, *A Study on Anisotropic Etching of (100) Silicon in Aqueous KOH Solution*, International Journal of Chemistry Science: 6(3), pp. 1168-1176, 2008.
- [Anwane, 2007] S. W. Anwane, *Fundamentals of Electromagnetic Fields*, Infinity Science Press, 2007.
- [Audley *et al.*, 2013] M. Audley, G. de Lange, and C. Bracken, *Detector and Calibration-source Models for the SAFARI Detector Test Facility*, COMSOL Conference Proceedings, WTC Rotterdam, the Netherlands, October 23-25, 2013.
http://www.comsol.de/paper/download/182113/audley_abstract.pdf

- [Audley *et al.*, 2013] M.D. Audley, A. Detrain, L. Ferrari, J.R. Gao, D. Hayton, G. de Lange, P.D. Mauskopf, D. Morozov, M. Ranjan N.A. Trappe, and W.J. Vreeling, *Optical Measurements of TES Bolometers for SAFARI*, ISSTT 2013 Proceedings, International Symposium for Space Terahertz Technology, April 2013, Groningen, the Netherlands.
<http://www.nrao.edu/meetings/isstt/papers/2012/2012194202.pdf>
- [Baumann *et al.*, 2009] D. Baumann *et al.*, *CMBPol Mission Concept Study, Probing Inflation with CMB Polarization*, arXiv:0811.3919v2 [astro-ph], 2009.
<http://arxiv.org/pdf/0811.3919.pdf>
- [Beattie, 1958] C.L. Beattie, *Table of First 700 Zeros of Bessel Functions - $J_1(x)$ and $J_1'(x)$* , The Bell System Technical Journal, Vol. 37, pp 689-697, May 1958.
- [Bennett *et al.*, 1993] C.L. Bennett, N.W. Boggess, E.S. Cheng, M.G. Hauser, T. Kelsall, J.C. Mather, S.H. Moseley JR., T.L. Murdock, R.A. Shafer, R.F. Silverberg, G.F. Smoot, R. Weiss, and E.L. Wright, *Scientific Results from the Cosmic Background Explorer (COBE)*, Proceedings of the National Academy of Sciences USA. Vol. 90, pp. 4766-4773, June 1993. Colloquium Paper.
<http://www.pnas.org/content/90/11/4766.full.pdf>
- [Blain *et al.*, 1999] A.W. Blain, R.J. Ivison, J-P. Kneib, and I.Smail, *Galaxy Counts at $450\mu m$ and $850\mu m$* , Proceedings of a conference held in Berkeley, CA, 21-24 June, 1999. ASP Conference Proceedings, Vol. 193, pp. 246-249, 1999. ISBN: 1-58381-019-6.
<http://adsabs.harvard.edu/full/1999ASPC..193..246B>
- [Born and Wolf, 1999] M. Born and E. Wolf, *Principles of Optics: Electromagnetic Theory of Propagation, Interference and Diffraction of Light*, (Seventh Edition), Cambridge University Press, 1999. ISBN: 0 521 642221 Hardback.
- [Bracken *et al.*, 2014] C. Bracken, J.A. Murphy, S. Doherty, and N.A. Trappe, *Efficient Modelling of Cavity Coupled Detectors for Terahertz Frequencies*, Proceedings of the 24th International Symposium on Space Terahertz Technology (ISSTT), in press (2015). <https://www.sron.nl/proceedings>
- [COMSOL, 2011] COMSOL Multiphysics, *COMSOL Support Literature for RF Module*, 1998–2011 COMSOL, May 2001.

<http://nf.nci.org.au/facilities/software/COMSOL/4.2/doc/pdf/rf/RFModuleUsersGuide.pdf>

- [Chen and Zhang, 2001] Q. Chen and X.C. Zhang, *Semiconductor Dynamic Aperture for Near-Field Terahertz Wave Imaging*, IEEE J. Select. Topics Quant. Electron. Vol. 7, Issue 4, pp. 608-614, July 2001.
http://www.eleceng.adelaide.edu.au/thz/documents/chen_2001_stq.pdf
- [Chervenak *et al.*, 2002] J. Chervenak, J. Staguhn, D. Benford, R. Shafer, H. Moseley, *Absorber Coupled Transition-Edge-Sensor Bolometer Arrays for Submillimeter Imaging*, Far-IR, Sub-mm & MM Detector Technology Workshop, Monterey, CA, 1-3 April 2002. Organized and Sponsored by NASA/Ames & USRA/SOFIA.
http://www.sofia.usra.edu/det_workshop
- [Clarricoats *et al.*, 1984] P.J.B. Clarricoats and A.D. Olver, *Corrugated Horns for Microwave Antennas*, Peter Peregrinus Ltd., 1984.
- [Colgan, 2001] R. Colgan, *Electromagnetic and Quasi-optical Modelling of Horn Antennas for Far-IR Space Applications*, PhD Thesis from the Department of Experimental Physics, NUI Maynooth, Maynooth, Co.Kildare, Ireland, 2001.
- [Cox and Hodge, 2006] C. Cox and P. Hodge, *Point-Spread Function Modeling for the James Webb Space Telescope*, Proc. SPIE 6265, Space Telescopes and Instrumentation I: Optical, Infrared, and Millimeter, 62650W, June 2006; doi: 10.1117/12.672010.
<http://spie.org/Publications/Proceedings/Paper/10.1117/12.672010>
- [Crownover, 1995] R. M. Crownover, *Introduction to Fractals and Chaos*, Sudbury, MA: Jones & Bartlett, 1995.
- [De Marchi *et al.*, 2010] G. De Marchi, N. Panagia, and M. Romaniello, *Photometric Determination of the Mass Accretion Rates of Pre-Main-Sequence Stars. I. Method and Application to the SN 1987A Field*, The Astrophysical Journal, Vol. 715, Issue 1, doi:10.1088/0004-637X/715/1/1, 2010.
<http://iopscience.iop.org/0004-637X/715/1/1>
- [Deming *et al.*, 2007] D. Deming, E. Agol, D. Charbonneau, N. Cowan, H. Knutson, and M. Marengo, *Observations of Extrasolar Planets During the non-Cryogenic*

Spitzer Space Telescope Mission, arXiv:0710.4145v1 [astro-ph], 2007.

<http://arxiv.org/abs/0710.4145>

[Denny *et al.*, 2013] S. P. Denny, J. Y. Suen, and P. M. Lubin, *Fundamental Limits of Detection in the Far Infrared*, *New Astronomy*, Vol. 25, pp. 114-129, December 2013.

<http://adsabs.harvard.edu/abs/2013NewA...25..114D>

[Doherty, 2012] S. Doherty, *Optical and Quasi-Optical Design and Analysis of Astronomical Instrumentation including a Prototype SAFARI Pixel*, PhD Thesis from the Department of Experimental Physics, NUI Maynooth, Maynooth, Co.Kildare, Ireland, 2012.

[Dole *et al.*, 2001] H. Dole *et al.*, *FIRBACK: III. Catalog, Source Counts, and Cosmological Implications of the 170 μm ISO Deep Survey*, *Astronomy and Astrophysics*, vol. 372, pp. 364-376, 2001.

http://link.springer.com/chapter/10.1007%2F3-540-45553-1_8

[Dole *et al.*, 2006] H. Dole, G. Lagache, J-L. Puget, K.I. Caputi, N. Fernández-Conde, E. Le Floch, C. Papovich, P.G. Pérez-González, G.H. Rieke, and M. Blaylock, *The cosmic Infrared Background Resolved by Spitzer: Contributions of Mid-Infrared Galaxies to the Far-Infrared Background*, *Astronomy & Astrophysics*, Vol. 451, Issue 2, pp. 417-429, May IV 2006, DOI:10.1051/0004-6361:20054446.

<http://www.aanda.org/articles/aa/full/2006/20/aa4446-05/aa4446-05.html>

[Dowell *et al.*, 2003] C.D. Dowell, C.A. Allen, S. Babu, M.M. Freund, M.B. Gardner, J. Groseth, M. Jhabvala, A. Kovacs, D.C. Lis, S. Harvey Moseley, Jr., T.G. Phillips, R. Silverberg, George Voellmer, and H. Yoshid, *SHARC II: a Caltech Submillimeter Observatory Facility Camera with 384 Pixels*, *Proc. SPIE 4855, Millimeter and Submillimeter Detectors for Astronomy*, (17 February 2003); doi: 10.1117/12.459360

<http://spie.org/Publications/Proceedings/Paper/10.1117/12.459360>

[Duncan, 1990] W. D. Duncan, *SCUBA: A Submillimetre Common-User Bolometer Array for the James Clerk Maxwell Telescope*, *Submillimetre Astronomy*,

Astrophysics and Space Science Library, Vol. 158, pp. 51-52, 1990.

http://link.springer.com/chapter/10.1007%2F978-94-015-6850-0_17

[Eggen *et al.*, 1962] O.J. Eggen, D. Lynden-Bell, A.R. Sandage, *Evidence from the Motions of Old Stars that the Galaxy Collapsed*, The Astrophysical Journal Vol. 136, pp. 748-766, November 1962.

<http://adsabs.harvard.edu/abs/1962ApJ...136..748E>

[El Naschie, 2013] M. S. El Naschie, *A Fractal Menger Sponge Space-Time Proposal to Reconcile Measurements and Theoretical Predictions of Cosmic Dark Energy*, International Journal of Modern Nonlinear Theory and Application, Vol. 2, pp. 107-121, 2013.

[Elbaz *et al.*, 2011] D. Elbaz *et al.*, *GOODS-Herschel: An Infrared Main Sequence for Star-Forming Galaxies*, Astronomy and Astrophysics, Vol. 533, pp. 1-26, id.A119, September 2011.

<http://adsabs.harvard.edu/abs/2011A%26A...533A.119E>.

[Enya *et al.*, 2008] K. Enya, L. Abe, K. Haze, S. Tanaka, T. Nakagawa, H. Kataza, S. Higuchi, T. Miyata, S. Sako, T. Nakamura, M. Tamura, J. Nishikawa, N. Murakami, Y. Itoh, T. Wakayama, T. Sato, N. Nakagiri, O. Guyon, M. Venet, and P. Bierden, *Mid-Infrared Coronagraph for SPICA*, Proceedings of SPIE 7010, Space Telescopes and Instrumentation 2008, Optical, Infrared, and Millimeter, 70102Z, 12 July 2008. doi: 10.1117/12.788509.

<http://spie.org/Publications/Proceedings/Paper/10.1117/12.788509>

[Evans *et al.*, 2002] R. Evans, D. A. Harper, S. Casey, J. A. Davidson, I. Gatley, J. Kastner, R. Loewenstein, S. H. Moseley, R. Pernic, J. Wirth, R. Evans, D. A. Harper, S. Casey, J. A. Davidson, I. Gatley, J. Kastner, R. Loewenstein, S. H. Moseley, R. Pernic and J. Wirth, *SOFIA and its facility Far Infrared Camera HAWC*, EAS Publications Series, 4, pp. 239-239, 2002. doi:10.1051/eas:2002082.

<http://dx.doi.org/10.1051/eas:2002082>

[Ferlet *et al.*, 2010] M. Ferlet, N. Geis, J. Goicoechea, D.K. Griffin, A.M. Heras, K. Isaak, T. Nakagawa, T. Onaka, N. Rando, B. Swinyard, N. Takahashi, S. Vives, *SPICA Revealing the Origins of Planets and Galaxies*, ESA/SRE(2009)6,

Assessment Study Report.

<http://arxiv.org/ftp/arxiv/papers/1001/1001.0709.pdf>

- [Figueroa-Feliciano, 2001] E. Figueroa-Feliciano, *Theory and Development of Position-Sensitive Quantum Calorimeters*, PhD Thesis, Department of Physics, Stanford University, 2001.
- [Fixsen *et al.*, 1998] D.J. Fixsen, E. Dwek, J.C. Mather, C.L. Bennett, and R.A. Shafer, *The Spectrum of the Extragalactic Far Infrared Background from the COBE FIRAS Observations*, *The Astrophysical Journal*, vol. 508, pp. 123-128, 1998
<http://adsabs.harvard.edu/abs/1998ApJ...508..123F>
- [Geers *et al.*, 2006] V.C. Geers, J-C. Augereau, K.M. Pontoppidan, C.P. Dullemond, R. Visser, J.E. Kessler-Silacci, N.J. Evans II, E.F. van Dishoeck, G.A. Blake, A.C.A. Boogert, J.M. Brown, F. Lahuis, and B. Merin, *C2D Spitzer-IRS spectra of disks around T Tauri stars*, *Astronomy and Astrophysics* Vol. 459, pp. 545-556, 2006.
<http://authors.library.caltech.edu/13771/1/GEEaanda06.pdf>
- [Gleeson, 2004] E. Gleeson, *Single and Multi-moded Corrugated Horn Design for Cosmic Microwave Background Experiments*, Ph.D. thesis, National University of Ireland, Maynooth, Ireland, 2004.
- [Glenn *et al.*, 2003] J. Glenn, J.J. Bock, B.K. Rownd, M. Caldwell, and M.J. Griffin, *Feed Horn Coupled Bolometer Arrays for SPIRE: Design, Simulations, and Measurements*, *IEEE Transactions on Microwave Theory and Techniques*, Vol. 51, Issue 10, October 2003.
http://www.submm.caltech.edu/~goutam/ps_pdf_files/mtt_spire.pdf
- [Goicoechea *et al.*, 2009] J.R. Goicoechea, K. Isaak and B. Swinyard, *Molecules in the Atmospheres of Extrasolar Planets*, ASP Conference Series, Volume: The Astronomical Society of the Pacific, 2009.
- [Goicoechea and Nakagawa, 2011] J. R. Goicoechea, and T. Nakagawa, *SPICA: the Next Generation Infrared Space Telescope*, arXiv:1101.1418v1 [astro-ph.IM], 2011.
<http://arxiv.org/abs/1101.1418>

- [Goldie *et al.*, 2012] D. J. Goldie, J. R. Gao, D. M. Glowacka, D. K. Griffin, R. Hijmering, P. Khosropanah, B. D. Jackson, P. D. Mauskopf, D. Morozov, J. A. Murphy, M. Ridder, N. Trappe, C. O’Sullivan, and S. Withington, *Ultra-Low-Noise Transition Edge Sensors for the SAFARI L-Band on SPICA*, Proceedings of SPIE 8452, Millimeter, Submillimeter, and Far-Infrared Detectors and Instrumentation for Astronomy VI, 84520A, 27 September 2012. doi: 10.1117/12.925861
- [Goldsmith, 1992] P. F. Goldsmith, *Quasi-Optical Techniques*, Proceedings of the IEEE, Vol. 80, Issue 11, pp. 1729-1747, November 1992.
<http://ieeexplore.ieee.org/stamp/stamp.jsp?arnumber=175252>
- [Goldsmith, 1998] P.F. Goldsmith, *Quasioptical Systems*, The Institute Of Electrical And Electronics Engineers, Inc., New York, NY. 10017-2394, 1998.
- [Golub and Kahan, 1965] G.H. Golub, and W. Kahan, *Calculating the Singular Values and Pseudo-Inverse of a Matrix*, Journal of the Society for Industrial and Applied Mathematics Series B Numerical Analysis, Vol. 2, Issue 2, pp. 205-224, 1965.
<http://epubs.siam.org/doi/abs/10.1137/0702016>
- [Hacking *et al.*, 1987] P. Hacking, J.J. Condon, J.R. Houck, *A Very Deep IRAS Survey - Constraints on the Evolution of Starburst Galaxies*, Astrophysical Journal, Part 2-L, Vol. 316, pp. L15-L19, May 1987.
http://adsabs.harvard.edu/cgi-bin/bib_query?1987ApJ...316L..15H
- [Hall *et al.*, 2014] L.J. Hall, Y. Nomura, and S. Shirai, *Grand Unification, Axion, and Inflation in Intermediate Scale Supersymmetry*, High Energy Physics-Phenomenology, arXiv:1403.8138 [hep-ph]. 3 Apr 2014.
<http://arxiv.org/abs/1403.8138>
- [Hand, 2009] E. Hand, *Cosmology: The Test of Inflation*, Nature 458, pp. 820-824, 2009. doi:10.1038/458820a.
- [Hanson *et al.*, 2013] D. Hanson *et al.*, *Detection of B-mode Polarization in the Cosmic Microwave Background with Data from the South Pole Telescope*, arXiv:1307.5830v2 [astro-ph.CO], 2013.
<http://arxiv.org/abs/1307.5830>

- [Hayward *et al.*, 2014] C.C. Hayward, L. Lanz, M.L.N. Ashby, G. Fazio, L. Hernquist, J.R. Martínez-Galarza, K. Noeske, H.A. Smith, S. Wuyts, and A. Zezas, *The Total Infrared Luminosity May Significantly Overestimate the Star Formation Rate of Recently Quenched Galaxies*, The Royal Astronomical Society, pp. 1-6, 2014.
<http://arxiv.org/pdf/1402.0006v1.pdf>.
- [Hippelein *et al.*, 1996] H. Hippelein, D. Lemke, R. J. Tuffs, M. Haas, H. J. Voelk, and U. Klaas, *Far Infrared Mapping of the Galaxies M51 and M101 with ISOPHOT.*, Astronomy and Astrophysics, Vol. 315, pp. L79-L81, September 1996.
<http://articles.adsabs.harvard.edu//full/1996A%26A...315L..79H/L000079.000>
- [Hohlfeld and Cohen, 1999] R.G. Hohlfeld and N. Cohen, *Self-Similarity and the Geometric Requirements for Frequency Independence in Antennae*, Fractals: Complex Geometry, Patterns, and Scaling in Nature and Society, Vol. 07, Issue 01, pp. 79-84, March 1999. doi: 10.1142/S0218348X99000098.
<http://www.worldscientific.com/doi/abs/10.1142/S0218348X99000098>
- [Holland *et al.*, 2013] W.S. Holland, *et al.*, *SCUBA-2: The 10000 pixel bolometer camera on the James Clerk Maxwell Telescope*, Instrumentation and Methods for Astrophysics (astro-ph.IM), arXiv:1301.3650 [astro-ph.IM].
<http://arxiv.org/abs/1301.3650>
- [Homes *et al.*, 2007] C.C. Homes, G.L. Carr, J.D. LaVeigne and D.B. Tanner, *Silicon Beam Splitter for Far-Infrared and Terahertz Spectroscopy*, Applied Optics, Vol. 46, Issue 32, pp. 7884-7888, 10 November 2007.
<http://www.phys.ufl.edu/~tanner/PDFS/Homes07AO-SiBms.pdf>
- [Hubble, 1926] E.P. Hubble, *Extra-Galactic Nebulae*, Astrophysical Journal, Vol. LXIV, pp. 321-369, 1926.
- [Hulbert and Jones, 1955] J. A. Hulbert and G. O. Jones, *The Superconducting Bolometer as a Detector of Thermal Radiation from Low-Temperature Sources*, Proceedings of the Physical Society, Section B, Vol. 68, Issue 11, pp. 801-804, 1955. doi:10.1088/0370-1301/68/11/301.
<http://iopscience.iop.org/0370-1301/68/11/301>

- [Hyde, 2000] E. McKay Hyde, *The Validity of a Paraxial Approximation in the Simulation of Laser-Plasma Interaction*, Student Symposium 2000, Albuquerque, NM, 10/08/2000. U.S. Department of Energy, 2000.
<https://e-reports-ext.llnl.gov/pdf/238356.pdf>
- [IAU, 2006] IAU 2006 General Assembly, *Result of the IAU Resolution votes*, (International Astronomical Union), IAU 2006 General Assembly.
- [IRAP, 2014] IRAP, *A New Start for the SPICA Mission*, IRAP Press Release, 2014.
<http://www.irap.omp.eu/en/actualites/actu-spica>.
- [Irwin and Hilton, 2005] K.D. Irwin and G.C. Hilton, *Transition-Edge Sensors*, Topics in Applied Physics Vol. 99, pp 63-150, 2005.
- [Isaak and Withington, 1993] K.G. Isaak and S. Withington, *Phase Retrieval at Millimetre and Submillimetre Wavelengths using a Gaussian-Beam Formalism*, ISSTT 1993 Proceedings, Fourth International Symposium on Space Terahertz Technology, pp. 199-210, March 1993.
<http://www.nrao.edu/meetings/isstt/papers/1993/1993199210.pdf>
- [Iyomoto *et al.*, 2008] N. Iyomoto, S.R. Bandler, R.P. Brekosky, A.-D. Brown, J. A. Chervenak, F.M. Finkbeiner, R.L. Kelley, C.A. Kilbourne, F.S. Porter, J.E. Sadleir, and S.J. Smith, *Close-Packed Arrays of Transition-Edge X-ray Microcalorimeters with High Spectral Resolution at 5.9keV*, Applied Physics Letters, Vol. 92, Issue 1, pp. 013508-1 to 013508-3, 2008.
- [Jackson *et al.*, 2012] B. D. Jackson, P. A. J. de Korte, J. van der Kuur, P. D. Mauskopf, J. Beyer, M. P. Bruijn, A. Cros, J-R. Gao, D. Griffin, R. den Hartog, M. Kiviranta, G. de Lange, B-J. van Leeuwen, C. Macculi, L. Ravera, N. Trappe, H. van Weers, and S. Withington, *The SPICA-SAFARI Detector System: TES Detector Arrays with Frequency Division Multiplexed SQUID Readout*, IEEE Transactions on Terahertz Science and Technology, Vol. 2, Issue 1, pp. 12-21, January 2012. doi: 10.1109/TTHZ.2011.2177705
- [Jaffe *et al.*, 2004] W. Jaffe *et al.*, *The Central Dusty Torus in the Active Nucleus of NGC 1068*, Nature, Vol. 429, pp. 47-49, 2004. doi:10.1038/nature02531.
<http://www.nature.com/nature/journal/v429/n6987/full/nature02531.html>

- [James and Ring, 1967] D.J. James and J. Ring, *The Efficiency of Beamsplitters in the Far Infra-Red Michelson Interferometer*, Journal De Physique. Colloque C 2, supplkment uu no 3-4, Tome 28, mars-avril1967, pp. 2-150.
- [Jeans, 1928] Sir J. Jeans, *Astronomy and Cosmogony*, pp. 337, Cambridge University Press.
- [Jenness *et al.*, 2010] T. Jenness, D. Berry, E. Chapin, F. Economou, A. Gibb, D. Scott, *SCUBA-2 Data Processing*, arXiv:1011.5876v1 [astro-ph.IM], 2010.
<http://arxiv.org/abs/1011.5876>
- [Justin Mullins, 2010] Justin Mullins, *Full-Body Scanners: We Reveal All*, New Scientist On-line Article, 18:08, 18 November 2010.
<http://www.newscientist.com/article/dn19746-fullbody-scanners-we-reveal-all.html>
- [Kadir, 2007] M. Kadir, *Sierpinski Carpet Fractal Antenna*, Asia-Pacific Conference on Applied Electromagnetics, pp. 1-4, 4-6 December, 2007. doi: 10.1109/APACE.2007.4603961
- [Khosropanah *et al.*, 2011] P. Khosropanah, R.A. Hijmering, M. Ridder, M.A. Lindeman, L. Gottardi, M. Bruijn, J. van der Kuur, P.A.J. de Korte, J.R. Gao, and H. Hoevers, *Low Noise Transition Edge Sensor (TES) for the SAFARI Instrument on SPICA*, Proceedings from the 12th International Symposium on Space Terahertz Technology, pp. 125-129, 2011.
- [Khosropanah *et al.*, 2012] P. Khosropanah, R.A. Hijmering, M. Ridder, M.A. Lindeman, L. Gottardi, M. Bruijn, J. van der Kuur, P.A.J. de Korte, J.R. Gao, H. Hoevers, *Distributed TES Model for Designing Low Noise Bolometers Approaching SAFARI Instrument Requirements*, Journal of Low Temperature Physics, Vol. 167, pp. 188-194, January 2012. doi: 10.1007/s10909-012-0550-6.
- [Kovacs *et al.*, 1998] G.T.A. Kovacs, N.I. Maluf, and K.E. Petersen, *Bulk Micromachining of Silicon*, Proceedings of the IEEE, Vol. 86, Issue 8, pp. 1536 - 1551, August 1998.
<https://ece.umd.edu/class/enee416.S2004/Bulk-Micromachining.pdf>.

- [Kulesa, 2011] C. Kulesa, *Terahertz Spectroscopy for Astronomy: From Comets to Cosmology*, IEEE Transactions Terahertz Science and Technology, Vol. 1, Issue 1, pp. 232-240, September 2011.
<http://ieeexplore.ieee.org/stamp/stamp.jsp?arnumber=6005336>
- [Kuo *et al.*, 2009] C.L. Kuo, J.J. Bock, J.A. Bonetti, J. Brevik, G. Chattopadthyay, P.K. Day, S.Golwala, M. Kenyon, A.E. Lange, H.G. LeDuc, H. Nguyen, R.W. Ogburn, A. Orlando, A. Trangsrud, A. Turner, G. Wang and J. Zmuidzinas, *Antenna-Coupled TES Bolometer Arrays for CMB Polarimetry*, SPIE Proceedings Vol. 7020, Marseille, 2008. arXiv:0908.1464 [astro-ph.IM]
<http://arxiv.org/abs/0908.1464>
- [Lavelle and O'Sullivan, 2010] J. Lavelle and C. O'Sullivan, *Beam Shaping Using Gaussian Beam Modes*, Journal of the Optical Society of America A, Vol. 27, Issue 2, pp. 351-357, February 2010. Doc. ID 118881.
<http://eprints.nuim.ie/4438/1/CO-Beam-Shaping.pdf>
- [Lebedev, 1972] N. N. Lebedev, *Special Functions & their Applications*, Revised English Edition, Dover Publications Inc., 1972. ISBN:0-486-60624-4.
- [Lee, 1979] Y-S. Lee, *Principles of Terahertz Science and Technology*, Proceedings of the International Conference, Mainz, Germany, June 5-9, 1979, Springer Science & Business Media, pp. 162, Mar 2009.
- [Leeks *et al.*, 2003] S.J. Leeks, B.M. Swinyard, T.L. Lim, and P.E. Clegg, *The In-Orbit Performance of the LWS Detectors*, Published as ESA Publications Series, ESA SP-481, pp. 251-260, European Space Agency, 2003.
<http://adsabs.harvard.edu/full/2003ESASP.481..251L>.
- [Leisawitz *et al.*, 2006] D. Leisawitz, *et al.*, *The Space Infrared Interferometric Telescope (SPIRIT): High Resolution Imaging and Spectroscopy in the Far-Infrared*, Advances in Space Research, Vol. 40, pp. 689-703, 2007.
- [Lonsdale, 1990] Carol J. Lonsdale, *Galaxy Evolution in the Far Infrared*, Astrophysics and Space Science Library Vol. 160, pp 121-124, 1990.
http://link.springer.com/chapter/10.1007%2F978-94-009-0543-6_17

- [Lucci *et al.*, 2004] L. Lucci, R. Nesti, G. Pelosi, and S. Selleri, *Phase Centre Optimization in Profiled Corrugated Circular Horns with Parallel Genetic Algorithms*, Progress In Electromagnetics Research, Vol. 46, pp. 127-142, 2004. doi:10.2528/PIER03090501.
<http://www.jpier.org/PIER/pier.php?paper=0309051>
- [Maffei *et al.*, 2010] B. Maffei, F. Noviello, J.A. Murphy, P.A.R. Ade, J-M. Lamarre, F.R. Bouchet, J. Brossard, A. Catalano, R. Colgan, R. Gispert, E. Gleeson, C.V. Haynes, W.C. Jones, A.E. Lange, Y. Longva, I. McAuley, F. Pajot, T. Peacocke, G. Pisano, J-L. Puget, I. Ristorcelli, G. Savini, R. Sudiwala, R.J. Wylde and V. Yurchenko, *Pre-Launch Status: HFI Beam Expectations from the Optical Optimisation of the Focal Plane*, Astronomy and Astrophysics, Vol. 520, A12, pp. 1-15, September 2010.
<http://www.aanda.org/articles/aa/pdf/2010/12/aa12999-09.pdf>
- [Maillard, 2005] J-P Maillard, *Recent Results with FTS in Astronomy*, Proceedings from the OSA/FTS Conference, Alexandria, Virginia, pp. 780-786, January 2005. ISBN: 1-55752-780-6.
<http://www.opticsinfobase.org/abstract.cfm?uri=FTS-2005-FMC1>
- [Math Works, 1994] Math Works, *Matlab*, The Math Works, Natick, Massachusetts, 1994.
<http://www.mathworks.co.uk/help/matlab/ref/fminsearch.html>
- [Mauskopf *et al.*, 2010] P.D. Mauskopf, P.A.R. Ade, J. Beyer, M. Bruijn, J.R. Gao, D. Glowacka, D. Goldie, D. Griffin, M.J. Griffin, H.F.C. Hoevers, P. Khosrapanah, P. Kooijma, P.A.J. De Korte, D. Morozov, A. Murphy, C. O'Sullivan, M. Ridder, N. Trappe, H. Van Weers, J. Van Der Kuur, S. Withington, *A TES Focal Plane for SPICA-SAFARI*, 21ST International Symposium on Space Terahertz Technology, Oxford, UK. pp. 23-25, March 2010.
<http://www.nrao.edu/meetings/isstt/papers/2010/2010246255.pdf>
- [Mauskopf, 2011] P. Mauskopf, *Single mode simulations of L-band absorber efficiency*, Circulated document within the SAFARI group (un-published), 1/12/2011.

- [Mayer *et al.*, 2005] Lucio Mayer, James Wadsley, Thomas Quinn and Joachim Stadel, *Gravitational Instability in Binary Protoplanetary Discs: New Constraints on Giant Planet Formation*, MNRAS, Vol. 363, pp. 641-648, 2005. doi:10.1111/j.1365-2966.2005.09468.x.
- [McCabe *et al.*, 1992] C. McCabe, G. Duchêne and A. M. Ghez, *The First Detection of Spatially Resolved Mid-Infrared Scattered Light from a Protoplanetary Disk*, The Astrophysical Journal, Vol. 588, pp. 113-116, 10/05/2003.
- [McCarthy *et al.*, 2013] D. McCarthy, N. Trappe, J.A. Murphy, C. Bracken, S. Doherty, M.L. Gradziel, C O'Sullivan, *Efficient Horn Antennas for Next-Generation Terahertz and Millimeter-Wave Space Telescopes*, Proc. SPIE 8624, Terahertz, RF, Millimeter, and Submillimeter-Wave Technology and Applications VI, 862413 (March 27, 2013); doi:10.1117/12.2001268. <http://proceedings.spiedigitallibrary.org/proceeding.aspx?articleid=1673574>.
- [McCarthy *et al.*, 2014] D. McCarthy, J.A. Murphy, C. O'Sullivan, N. Trappe, M.L. Gradziel, S. Doherty, C. Bracken, N. Tynan, and Arturo Polegre, *Efficient algorithms for optimising the optical performance of profiled smooth walled horns for future CMB and Far-IR missions*, Proceedings of SPIE 9153, Millimeter, Submillimeter, and Far-Infrared Detectors and Instrumentation for Astronomy VII, 915316, 23 July 2014. doi: 10.1117/12.2056336. <http://spie.org/Publications/Proceedings/Paper/10.1117/12.2056336>
- [Melbourne *et al.*, 2005] J. Melbourne, D.C. Koo, E. Le Floch, *Optical Morphology Evolution of Infrared Luminous Galaxies in GOODS-N*, The Astrophysical Journal, Vol. 632, Issue 2, pp. L65-L68, October 2005. <http://adsabs.harvard.edu/abs/2005ApJ...632L..65M>.
- [Milligan, 2005] T. A. Milligan, *Modern Antenna Design, Second Edition*, pp. 336-340, John Wiley & Sons, Inc. 2005.
- [Morgenthaler, 2011] F. R. Morgenthaler, *The Power and Beauty of Electromagnetic Fields*, IEEE, John Wiley and Sons, Inc., Hoboken, New Jersey, 2011.
- [Murphy *et al.*, 1997] J. A. Murphy, M. McCabe, and S. Withington, *Gaussian Beam Mode Analysis of the Coupling of Power between Horn Antennas*, International Journal of Infrared and Millimeter Waves, Vol. 18, Issue 2, pp.

501-518, February 1997.

<http://link.springer.com/article/10.1007%2F02677936>

[Murphy *et al.*, 2001] J.A. Murphy, R. Colgan, C. O'Sullivan, B. Maffei, P. Ade, *Radiation Patterns of Multi-Moded Corrugated Horns for Far-IR Space Applications*, Infrared Physics Technology, Vol. 42, Issue 6, pp. 515-528, 2001.

[Murphy *et al.*, 2010] J.A. Murphy, T Peacocke, B Maffei, I McAuley, F Noviello, V Yurchenk, P.A.R. Ade, G Savini, J-M Lamarre, J Brossard, R Colgan, E Gleeson, A E Lange, Y Longval, G Pisano, J-L Puget, I Ristorcelli, R Sudiwala, and R.J. Wylde, *Multi-Mode Horn Design and Beam Characteristics for the Planck Satellite*, Journal of Instrumentation, Vol. 5, Issue: T04001, pp. 1-21, 2010.

<http://iopscience.iop.org/1748-0221/5/04/T04001>.

[Murphy *et al.*, 2011] J.A. Murphy, S. Doherty, N. Trappe, C. Bracken, and C. O'Sullivan, *Efficient Modeling of Detectors for Far-IR Astronomy*, SPIE Newsroom. doi: 10.1117/2.1201112.004039. December 9, 2011.

<http://spie.org/x84428.xml>

[Murphy and Egan, 1993] J.A. Murphy and A. Egan, *Examples of Fresnel Diffraction using Gaussian Modes*, European Journal of Physics, Vol. 14, Issue 3, 121, (May 1993), doi:10.1088/0143-0807/14/3/005

<http://iopscience.iop.org/0143-0807/14/3/005/pdf/ej930305.pdf>

[Nagar *et al.*, 2003] N.M. Nagar, A.S. Wilson, H. Falcke, S. Veilleux, and R. Maiolino, *The AGN Content of Ultraluminous IR Galaxies: High Resolution VLA Imaging of the IRAS 1 Jy ULIRG sample*, Astronomy and Astrophysics, Vol. 409, Issue 1, pp. 115-121, October 2003.

<http://www.aanda.org/articles/aa/pdf/2003/37/aa3871.pdf>

[Nagelberg, 1967] E.R. Nagelberg, *Phase Progression in Conical Waveguides*, The Bell System Technical Journal, Vol. 46, Issue 10, pp. 2453-2466, December 1967.

[Nakagawa, 2010] T. Nakagawa, *The Next-Generation Space Infrared Astronomy Mission SPICA*, Proceedings of SPIE, Vol. 7731, Space Telescopes and Instrumentation, 2010: Optical, Infrared, and Millimeter Wave, 77310O, August 05,

2010.

<http://proceedings.spiedigitallibrary.org/proceeding.aspx?articleid=749917>.

[Naylor *et al.*, 2006] D.A. Naylor, B.G. Gom, and B. Zhang, *Preliminary Design of FTS-2: an Imaging Fourier Transform Spectrometer for SCUBA-2*, Proceedings of SPIE, Astronomical Telescopes and Instrumentation Vol. 6275, 2006.
<http://adsabs.harvard.edu/abs/2006SPIE.6275E..64N>

[Naylor *et al.*, 2013] D.A. Naylor, B.G. Gom, M.H.D. van der Wiel, and G. Makiwa, *Astronomical Imaging Fourier Spectroscopy at Far-Infrared Wavelengths*, Canadian Journal of Physics, Vol. 91, Issue 11, pp. 870-878, 2013.
<http://adsabs.harvard.edu/abs/2013CaJPh..91..870N>

[Nichols and Tear, 1923] E.F. Nichols and J.D. Tear, *Short Electric Waves*, Physical Review, Vol. 21, Issue 6, pp. 587-610, June 1923.

[Nichols and Tear, 1925] E.F. Nichols and J.D. Tear, *Joining the Infra-Red and Electric Wave Spectra*, Astrophysical Journal. Vol. 61, pp. 17-37, 1925.

[Nichols, 1897] E.F. Nichols, *A Method for Energy Measurements in the Infrared Spectrum and the Properties of the Ordinary Ray in Quartz for Waves of Great Wavelength*, Physical Review Vol. 4, pp. 297-311, 1897.

[O'Dell *et al.*, 1992] C.R. O'Dell, Z. Wen and X. Hu, *Discovery of New Objects in the Orion Nebula on HST Images*, The Astrophysical Journal, Vol. 410, pp. 696-700, 20/06/1993.

[Oliver *et al.*, 2010] S.J. Oliver *et al.*, *HerMES: SPIRE Galaxy Number Counts at 250, 350 and 500 μ m*, Astronomy and Astrophysics, Vol. 518, L21-L25, August 2010.
http://www.aanda.org/articles/aa/full_html/2010/10/aa14697-10/aa14697-10.html

[Olver *et al.*, 1994] A.D. Olver, P.J.B. Clarricoats, A.A. Kishk, and L. Shafai, *Microwave Horns and Feeds*, The Institution of Electrical Engineers, IEEE Press 1994.

- [Oppenheim *et al.*, 1999] A. V. Oppenheim, R. W. Schaffer, and J. R. Buck, *Discrete-Time Signal Processing, 2nd Edition*, Englewood Cliffs, NJ: Prentice-Hall, 1999.
- [Optics.org, 2002] Optics.org, *Terahertz Waves Penetrate the World of Imaging*, Taken from proceedings of Opto & Laser Europe, October 2002.
<http://optics.org/article/9937>
- [Orfanidis, 2002] S. J. Orfanidis, *Electromagnetic Waves and Antennas*, pp. 800-805, Rutgers University, 2002. ISBN: 0130938556.
- [Pampaloni and Enderlein, 2004] F. Pampaloni and J. Enderlein, *Gaussian, Hermite-Gauss, and Laguerre-Gauss Beams: A Primer*, arXiv:physics/0410021v1 [physics.optics], 2004.
<http://arxiv.org/abs/physics/0410021>
- [Patel *et al.*, 2009] K. Patel, P. S. Negi, and P. C. Kothari, *Complex S-parameter Measurement and its Uncertainty Evaluation on a Vector Network Analyzer*, Elsevier, Vol. 42, Issue 1, pp. 145-149, January 2009.
<http://www.sciencedirect.com/science/article/pii/S0263224108000766>
- [Plume *et al.*, 2007] R. Plume *et al.*, *The James Clerk Maxwell Telescope Spectral Legacy Survey*, Astronomical Society of the Pacific, Vol. 119, pp. 102-111, January 2007.
http://www.jach.hawaii.edu/JCMT/surveys/docs/SLS_PASP.pdf
- [Pollock, 2010] Samuel Pollock, *Integration of Magneto Optical Traps in Atom Chips*, PhD Thesis from the Centre for Cold Matter, Department of Physics, Imperial College London.
<https://workspace.imperial.ac.uk/ccm/Public/Sam%20Pollock%20Thesis.pdf>.
- [Pozela *et al.*, 2013] J. Pozela, E. Sirmulis, K. Pozela, A. Silenas, and V. Juciene, *SiC and GaAs Emitters as Selective Terahertz Radiation Sources*, Lithuanian Journal of Physics, Vol. 53, Issue 3, pp. 163-167, 2013.
<http://www.itpa.lt/ lfd/Lfz/533/06/Ljp53306.pdf>
- [RFQ 3-6418/11/NL/CBi] J.A. Murphy, N. Trappe, C. Bracken, D. McCarthy, S. Doherty, M.L. Gradziel, C O'Sullivan, *New Technology High Efficiency Horn*

Antennas for Microwave Background Experiments and Far-Infrared Astronomy, European Space Agency Announcement of Opportunity 2012, RFQ 3-6418/11/NL/CBi.

[Rosenthal *et al.*, 2007] D. Rosenthal, F. Bertoldi, and S. Drapatz, *ISO-SWS Observations of OMC-1: H₂ and Fine Structure Lines*, *Astronomy and Astrophysics*, Vol. 356, pp. 705-723, February 2000.

<http://adsabs.harvard.edu/abs/2000A%26A...356..705R>

[Rubens and Nichols, 1897] H. Rubens and E.F. Nichols, *Certain Properties of Heat Waves of Great Wave-Length*, *Physical Review (Series I)* Vol. 5, pp. 152-169, 1897.

[Savini, 2013] Giorgio Savini, *Far-Infrared Space Interferometer Critical Assessment (FISICA): A Double-Fourier Space Technology Development*, Conference Paper: Fourier Transform Spectroscopy, Arlington, Virginia United States, June 23-24, 2013. ISBN:978-1-55752-975-6. Satellite Astronomy I (FM3D).

<http://www.opticsinfobase.org/abstract.cfmuri=FTS-2013-FM3D.4>

[Schot, 1992] S. H. Schot, *Eighty Years of Sommerfeld's Radiation Condition*, *Historia Mathematica*, Vol. 19, Issue 4, pp. 385-401, November 1992.

<http://www.sciencedirect.com/science/article/pii/031508609290004U>

[Schwan *et al.*, 2011] D. Schwan, P.A.R. Ade, K. Basu, A.N. Bender, F. Bertoldi, H-M. Cho, G. Chon, J. Clarke, M. Dobbs, D. Ferrusca, R. Gusten, N.W. Halverson, W.L. Holzapfel, C. Horellou, D. Johansson, B.R. Johnson, J. Kennedy, Z. Kermish, R. Kneissl, T. Lanting, A.T. Lee, M. Lueker, J. Mehl, K.M. Menten, D. Muders, F. Pacaud, T. Plagge, C.L. Reichardt, P.L. Richards, R. Schaaf, P. Schilke, M.W. Sommer, H. Spieler, C. Tucker, A. Weiss, B. Westbrook, O. Zahn, *Millimeter-Wave Bolometer Array Receiver for the Atacama Pathfinder Experiment Sunyaev-Zel'dovich (APEX-SZ) Instrument*, *Review of Scientific Instruments*, 82, 091301 (2011). arXiv:1008.0342 [astro-ph.IM]

<http://arxiv.org/abs/1008.0342>

[Seymour *et al.*, 2010] N. Seymour, M. Symeonidis, M.J. Page, M. Huynh, T. Dwelly, I.M. McHardy, and G. Rieke, *The Comoving Infrared Luminosity Density: Domination of Cold Galaxies Across $0 < z < 1.$* , *The Royal Astronomical*

Society, Vol. 402, pp. 2666-2670, 2010.

<http://iopscience.iop.org/0004-637X/640/2/784/fulltext/63477.text.html>.

[Shitov *et al.*, 1998] S.V. Shitov, A.B. Ermakov, L.V. Filippenko, V.P. Koshelets, W. Luinge, A.M. Baryshev, J.-R. Gao, P. Lehtikainen, *Recent Progress on the Superconducting Imaging Receiver at 500 GHz*, Proceedings of the 9th International Symposium on Space Terahertz Technology, pp. 263-272, March 1998.
<http://adsabs.harvard.edu/abs/1998stt..conf..263S>

[Shumyatsky and Alfano, 2011] P. Shumyatsky and R. R. Alfano, *Terahertz Sources*, Journal of Biomedical Optics, Vol. 16, Issue 3, 033001, March 22, 2011. doi:10.1117/1.3554742.
<http://biomedicaloptics.spiedigitallibrary.org/article.aspx?articleid=1166729>

[Soifer *et al.*, 2008] B.T. Soifer, G. Helou, and M. Werner, *The Spitzer View of the Extragalactic Universe*, Annual Review of Astronomy and Astrophysics, Vol. 46, pp. 201-240, September 2008.
<http://www.annualreviews.org/doi/abs/10.1146/annurev.astro.46.060407.145144>

[Spergel *et al.*, 2007] D.N. Spergel, R. Bean, O. Doré, M.R. Nolta, C.L. Bennett, J. Dunkley, G. Hinshaw, N. Jarosik, E. Komatsu, L. Page, H.V. Peiris, L. Verde, M. Halpern, R.S. Hill, A. Kogut, M. Limon, S.S. Meyer, N. Odegard, G.S. Tucker, J.L. Weiland, E. Wollack, and E.L. Wright, *Three-Year Wilkinson Microwave Anisotropy Probe (WMAP) Observations: Implications for Cosmology*, The Astrophysical Journal Supplement Series, Vol. 170, Issue 2, pp. 377-408. June 2007.
<http://adsabs.harvard.edu/abs/2007ApJS..170..377S>

[Springel *et al.*, 2005] V. Springel, S.D.M. White, A. Jenkins, C.S. Frenk, N. Yoshida, L. Gao, J. Navarro, R. Thacker, D. Croton, J. Helly, J.A. Peacock, S. Cole, P. Thomas, H. Couchman, A. Evrard, J. Colberg, and F. Pearce, *Simulations of the Formation, Evolution and Clustering of Galaxies and Quasars*, Nature, Vol. 43, pp. 629-636, March 2005.
<http://www.nature.com/nature/journal/v435/n7042/full/nature03597.html>

- [Springel *et al.*, 2006] V. Springel, C.S. Frenk, Carlos S.D.M. White, *The large-scale structure of the Universe*, Nature, Vol. 440, Issue 7088, pp. 1137-1144, 2006.
<http://adsabs.harvard.edu/abs/2006Natur.440.1137S>
- [Steinmetz and Navarro, 2003] M. Steinmetz and J.F. Navarro, *The Hierarchical Origin of Galaxy Morphologies*, New Astronomy, Vol. 7, pp. 155-160, 2002.
- [Sturm *et al.*, 2011] E. Sturm, E. Gonzalez-Alfonso, S. Veilleux, J. Fischer, J. Gracia-Carpio, S. Hailey-Dunsheath, A. Contursi, A. Poglitsch, A. Sternberg, R. Davies, R. Genzel, D. Lutz, L. Tacconi, A. Verma, R. Maiolino, and J. de Jong, *Massive Molecular Outflows and Negative Feedback in ULIRGs Observed by Herschel-PACS*, Astronomy and Astrophysics Outflow Letter 3, February, 2011. https://www.mpe.mpg.de/381044/outflow_letter3.pdf.
- [Sugitaa *et al.*, 2008] H. Sugitaa, Y. Satoa, T. Nakagawa, H. Murakami, H. Kaneda, K. Enya, M. Murakami, S. Tsunematsud, M. Hirabayashi, SPICA Working Group, *Development of Mechanical Cryocoolers for the Japanese IR Space Telescope SPICA*, Cryogenics Vol. 48, pp. 258-266, March, 2008.
http://www.submm.caltech.edu/BLISS/decadal/references/Sugita_08.pdf.
- [Swinyard *et al.*, 2003] B.M. Swinyard, K. Dohlen, D. Ferand, J-P Baluteau, D. Pouliquen, P. Dargent, G. Michel, J. Martignac, P.A.R. Ade, P.C. Hargrave, M.J. Griffin, D.E. Jennings, and M.E. Caldwell, *Imaging FTS for Herschel SPIRE*, Proceedings of SPIE, Vol. 4850, IR Space Telescopes and Instruments, pp. 698, March 2003.
<http://proceedings.spiedigitallibrary.org/proceeding.aspx?articleid=875521>
- [Swinyard *et al.*, 2009] Swinyard *et al.*, *The European Contribution to the SPICA Mission*, Proceedings of SPIE, Vol. 7010, Space Telescopes and Instrumentation, pp. 70100I-70100I-8, 2009.
http://www.submm.caltech.edu/BLISS/decadal/references/Swinyard_Nakagawa
- [TICRA, 2012] TICRA, *GRASP User's Manual*, TICRA, Copenhagen, 2012, pp. 689-702.
- [TRP AO/1-5922/08/NL/EM, 2011] N. Trappe, C Bracken, S Doherty, J.R. Gao, D. Glowacka, D. Goldie, D. Griffin, R. Hijmering, B. Jackson, P. Khosropanah, P. Mauskopf, D. Morozov, A. Murphy, C. O'Sullivan, M. Ridder, S. Withington,

European Space Agency Transition Edge Sensor Technical Research Programme (TRP), European Space Agency (ESA) 2012, RFQ 3-6418/11/NL/CBi.

- [Tan *et al.*, 2012] B-K. Tan, J. Leech, G. Yassin, P. Kittara, M. Tacon, S. Wangsuya, and C. Groppi, *A High Performance 700 GHz Feed Horn*, Journal of Infrared, Millimeter, and Terahertz Waves, January 2012, Vol. 33, Issue 1, pp. 1-5.
<http://link.springer.com/article/10.1007>
- [Thomas and Withington, 2013] C.N. Thomas and S. Withington, *Optical Modeling Techniques for Multi-Mode Horn-Coupled Power Detectors for Submillimeter and Far-Infrared Astronomy*, Journal of the Optical Society of America A, Vol. 30, Issue 8, pp. 1703-1713, August 2013.
- [Tio *et al.*, 2004] L. Y. Tio, A. A. P. Gibson, B. M. Dillon and L. E. Davis, *Weak Form Finite Element Formulation for the Helmholtz Equation*, International Journal of Electrical Engineering Education Vol. 41, Issue 1, pp. 1-9, January 2004.
- [Tomasino *et al.*, 2013] A. Tomasino, A. Parisi, S. Stivala, P. Livreri, A. C. Cino, A. C. Busacca, M. Peccianti, and R. Morandotti, *Wideband THz Time Domain Spectroscopy based on Optical Rectification and Electro-Optic Sampling*, Scientific Reports 3, Article number: 3116, doi:10.1038/srep03116, 31 October 2013.
<http://www.nature.com/srep/2013/131031/srep03116/full/srep03116.html>
- [Trappe *et al.*, 2003] N. Trappe, J.A. Murphy, S. Withington, *The Gaussian Beam Mode Analysis of Classical Phase Aberrations in Diffraction-Limited Optical Systems*, European Journal of Physics, Vol. 24, pp. 403-412, 2003.
- [Trappe *et al.*, 2005] N. Trappe, R. Mahon, W. Lanigan, J.A. Murphy, and S. Withington, *The Quasi-Optical Analysis of Bessel Beams in the Far Infrared*, Infrared Physics & Technology Vol. 46, pp. 233-247, 2005.
- [Trappe *et al.*, 2005] N. Trappe, S. Withington, and W. Jellema, *Gaussian Beam Mode Analysis of Standing Waves Between Two Coupled Corrugated Horns*, IEEE Transactions on Antennas and Propagation, Vol. 53, Issue 5, pp. 1755-1761, May 2005.
<http://ieeexplore.ieee.org/stamp/stamp.jsp?arnumber=1427934>

- [Trappe *et al.*, 2012] N. Trappe, C Bracken, S Doherty, J.R. Gao, D. Glowacka, D. Goldie, D. Griffin, R. Hijmering, B. Jackson, P. Khosropanah, P. Mauskopf, D. Morozov, A. Murphy, C. O’Sullivan, M. Ridder, S. Withington, *Optical Modeling of Waveguide Coupled TES Detectors towards the SAFARI Instrument for SPICA*, Millimeter, Submillimeter, and Far-Infrared Detectors and Instrumentation for Astronomy VI. Proceedings of the SPIE, Vol. 8452, pp. 84520L-84520L-6, 2012.
<http://adsabs.harvard.edu/abs/2012SPIE.8452E..0LT>
- [Van Kempen *et al.*, 2010] T.A. van Kempen *et al.*, *Dust, Ice, and Gas In Time (DIGIT) Herschel Program First Results, A full PACS-SED Scan of the Gas Line Emission in Protostar DK Chamaeleontis*, Astronomy and Astrophysics, Vol. 518, L128-L132, 2010.
<http://peggysue.as.utexas.edu/DIGIT/>
- [Van der Valk and Planken, 2004] N.C.J. van der Valk and P.C.M. Planken, *Towards Terahertz Near-Field Microscopy*, Philosophical Transactions of the Royal Society A, Vol. 362, pp. 315-321, February 2004.
- [Volakis and Sertel, 2012] J.L. Volakis and K. Sertel, *Integral Equation Methods for Electromagnetics*, The Ohio State University, SciTech Publishing, Raleigh, NC, 2012.
http://www.scitechpub.com/Explore/9781891121937_Volakis.pdf
- [WIKIMEDIA Commons, 2014] WIKIMEDIA Commons, *Atmospheric electromagnetic transmittance or opacity.jpg*, WIKIMEDIA Commons, Public Domain Material.
http://commons.wikimedia.org/wiki/File:Atmospheric_electromagnetic_transmittance_or_opacity.jpg
- [Wesson *et al.*, 2010] R. Wesson, J. Cernicharo, M.J. Barlow, M. Matsuura, L. Decin, M.A.T. Groenewegen, E.T. Polehampton, M. Agundez, M. Cohen, F. Daniel, K. M. Exter, W.K. Gear, H.L. Gomez1, P.C. Hargrave1, P. Imhof, R.J. Ivison, S.J. Leeks, T.L. Lim, G. Olofsson, G. Savini, B. Sibthorpe, B.M. Swinyard, T. Ueta, D.K. Witherick, and J.A. Yates, *Herschel-SPIRE FTS spectroscopy of the carbon-rich objects AFGL 2688, AFGL 618 and NGC 7027*,

Astronomy and Astrophysics, Vol. 518, id.L144, July 2010.

<http://adsabs.harvard.edu/abs/2010A%26A...518L.144W>

[Wexler, 1967] A. Wexler, *Solution of Waveguide Discontinuities by Modal Analysis*, IEEE Transactions on Microwave Theory and Techniques, Vol. 15, pp. 508-517, 1967

http://ieeexplore.ieee.org/xpls/abs_all.jsp?arnumber=1126521

[Wilsher *et al.*, 1999] D. S. Wilsher, J. J. Spencer, C. M. Mann, M. C. Gaidis, *A Moderate Cost 2.5 THz High Performance Feedhorn*, Proceedings from the Tenth International Symposium on Space Terahertz Technology, Charlottesville, pp 429-435, March 1999.

<http://library.nrao.edu/isstt/catalog/1999429435>

[Withington *et al.*, 2013] S. Withington, C.N. Thomas, and D.J. Goldie, *Partially Coherent Optical Modelling of the Ultra-Low-Noise Far-Infrared Imaging Arrays on the SPICA Mission*, arXiv:1307.7278 [astro-ph.IM], July 2013.

[Withington, 2012] Stafford Withington, *Realising Ultralow-Noise Multimode Far Infrared Detectors for Space Science*, Workshop on Microwave Spectral Polarimetry, Virtual Institute for Astroparticle Physics, Paris, France, December 11-12, 2012.

http://viavca.in2p3.fr/workshop_on_microwave_spectral_polarimetry/realizing_ultralow_noise_multimode_far_infrared_detectors_fos_space_science.

[Wylde and Martin, 1993] R.J. Wylde and D.H. Martin, *Gaussian beam-mode analysis and phase-centers of corrugated feed horns*, IEEE Transactions on Microwave Theory and Techniques, Vol. 41, Issue 10, pp. 1691-1699, October 1993.

<http://ieeexplore.ieee.org/stamp/stamp.jsp?arnumber=247912>

[Yuana *et al.*, 2014] Z. Yuana, J. Suna, R. Zhaib, X. Lib, and Z. Shao, *Mercury Arc Lamp Based Super-Resolution Imaging with Conventional Fluorescence Microscopes*, Micron, Vol. 59, pp. 24-27, April 2014.

<http://www.sciencedirect.com/science/article/pii/S0968432813001960>

[Yurchenko *et al.*, 2014] V. B. Yurchenko, M. Ciydem, J. A. Murphy, M. Gradziel, and A. Altintas, *Double-Sided Split-Step MM-Wave Fresnel Lenses: Design*,

Fabrication and Focal Field Measurements, Journal of European Optical Society
Rap. Public. 9, 14007, pp. 1-5, 2014.

http://www.jeos.org/index.php/jeos_rp/article/viewFile/14007/1153

[Zapata *et al.*, 2013] L.A. Zapata, L. Loinard, L.F. Rodríguez, V. Hernández-Hernández, S. Takahashi, A. Trejo, and B. Paris, *ALMA 690 GHz Observations of IRAS 16293–2422B: Infall in a Highly Optically Thick Disk*, The Astrophysical Journal Letters Vol. 764, Issue 1, pp. 1-5, February 2013.

<http://iopscience.iop.org/2041-8205/764/1/L14>

[Zetie *et al.*, 2000] K. P. Zetie, S. F. Adams, and R. M. Tocknell, *How Does a Mach-Zehnder Interferometer Work*, Physics Education 35(1), pp. 46-48, January 2000.

[Zheng *et al.*, 2006] X.Z. Zheng, E.F. Bell, H-W. Rix, C. Papovich, E. Le Floch, G.H. Rieke, and P.G. Pérez-González, *Detecting Faint Galaxies by Stacking at 24 μ m*, The Astrophysical Journal, Vol. 640, pp. 784-800, April 2006.

<http://iopscience.iop.org/0004-637X/640/2/784/fulltext/63477.text.html>

[Zheng *et al.*, 2012] W. Zheng, P. Bo, Y. Liu, and W. Wang, *Fast B-spline curve fitting by L-BFGS*, Computer Aided Geometric Design 29, pp. 448-462, 2012.